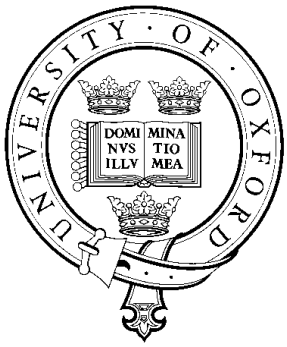
A thesis submitted for the degree
Doctor of Philosophy
in Engineering Science

Characterisation of microbubble–membrane interactions in ultrasound mediated drug delivery

Valerio Pereno
Keble College

supervised by Professors
Eleanor Stride and
Constantin Coussios



Oxford
Trinity term 2018

Abstract

Cancer imposes a significant disease burden and constitutes a major societal challenge. Despite being widely used, chemotherapy suffers numerous disadvantages, including off-target drug toxicity, poor tumour penetration, and drug resistance. The use of ultrasound in combination with contrast agents has shown promise in enhancing outcomes in the treatment of cancerous and non-cancerous diseases. However, the underlying biophysical processes that underpin their interactions with tissues remain poorly understood. The aim of the research presented in this thesis is to develop methods to elucidate these processes.

Development is hindered by the difficulties involved in isolating cellular parameters, non-invasively quantifying biological features at the molecular scale, and recreating a predictable and repeatable ultrasound field. To overcome these challenges, giant unilamellar vesicles made with 1,2-dioleoyl-*sn*-glycero-3-phosphocholine and cholesterol were used initially as cell models and exposed to therapeutically relevant conditions in a purpose-built acoustofluidic device. The resulting effects on the hydration and permeability of the vesicle membranes and the dynamics of their intravesicle milieu were characterised *in situ* using quantitative microscopy.

Results show that flow, ultrasound, and microbubbles led to an increase in vesicle membrane hydration, while dehydration was seen only in the presence of microbubbles. An increase in permeability was observed for all exposure conditions, and was accentuated when microbubble shell fragments were incorporated in the vesicle bilayer. These findings thus indicate that ultrasound-mediated delivery is governed by a combination of physical and chemical mechanisms that influence the permeation of molecules through lipid membranes.
Further, it was shown that exposure to the same conditions led to the onset of streaming flows within the vesicles' lumen. An experimental proof-of-concept for extending the study in vitro was also presented. Actuating the motion of cytoplasmic constituents may potentially induce a broad range of underexplored and therapeutically relevant bioeffects.

Statement of Originality

I hereby declare that this submission is my own work and, to the best of my knowledge, it contains no materials previously published or written by another person, or substantial proportions of material which have been accepted for the award of any other degree or diploma at the University of Oxford or any other educational institution, except where due acknowledgement is made in the thesis. Any contribution made to the research by others, with whom I have worked at the University of Oxford or elsewhere, is explicitly acknowledged in the thesis. I also declare that the intellectual content of this thesis is the product of my own work, except to the extent that assistance from others in the project's design and conception or in style, presentation and linguistic expression is acknowledged.

Valerio Pereno
Oxford, May 2018

To my family: past, present, and future

Acknowledgements

First and foremost, I would like to thank Professor Eleanor Stride for providing me with unwavering academic guidance, personal support, and friendship throughout the most difficult stages of this journey. I would also like to express sincere gratitude to Professor Constantin Coussios for his encouragement, mentorship, and guidance throughout the past three years. A huge debt of thanks goes to Dr. Dario Carugo for being there at every moment of awe and agony; and to Dr. Luca Baù, for his vast patience in challenging my deepest convictions. I am indebted to Jim Fisk and Dave Salisbury, for turning my abstract ideas into reality. I am also thankful to Daphne Cunningham and Graham Brown, for their incessant support throughout my degree.

I also would like to thank Kya Shoar for flipping the rimless wheel, a true stroke of genius. I further extend my gratitude to Fabio Bianchi for his culinary abilities and for enchanting our journey with his melodic voice.

I thank the University of Oxford and the Engineering and Physical Science Research Council for the award of a doctoral studentship.

Finally, I would to truly thank my friends for the delightful times together: Adam, Aldo, Carlo, Eduardo, Elizabeth, Erica, Federico, Francesco, Giulia, Marie, Patrick, Riccardo, Seamus, and Tim.

Dissemination

Peer reviewed publications

1. Pereno, V. et al. Electroformation of Giant Unilamellar Vesicles on Stainless Steel Electrodes. **ACS Omega** 2, 994–1002 (2017)

2. Layered acoustofluidic resonators for the simultaneous optical and acoustic characterisation of cavitation dynamics, microstreaming and biological effects. **Biomicrofluidics** 12, 034109 (2018)

3. Investigating the role of membrane hydration as a mediator of permeability in microbubble mediated drug delivery. **J. Roy. Soc. Interface** *(in preparation)*

4. Ultrasound and microbubble-mediated microstreaming inside cellular models. **Biomaterials** *(in preparation)*

Conference presentations

1. Pereno, V. et al. Cell-microbubble interaction in ultrasound mediated drug delivery: using giant vesicles as models to quantify bio-effects. 30th Conference of The European Colloid and Interface Society, Rome, Italy, September 2016.
2. Pereno, V. et al. Ultrasound mediated intracellular streaming. The 22nd European Symposium on Ultrasound Contrast Imaging, Rotterdam, The Netherlands. January 2017.

Poster sessions

1. Pereno, V. et al. *In vitro* neural activity modulation using ultrasound. BioEngenuity Keynotes, Oxford, UK, February 20, 2016

Table of Contents

i Acronyms 9

ii List of Symbols 13

I. Introduction 14

1.0 Background and motivation 15

1.1. Medical ultrasound 15

1.1.1. Ultrasound imaging 15

1.1.2. Contrast agents 18

1.1.3. Therapeutic ultrasound 19

1.2. Introduction to drug delivery 20

1.2.1. Pharmacological strategies 22

1.2.2. Barriers to therapeutic outcomes 24

1.2.3. Drug delivery vehicles 25

1.2.4. Targeting strategies 26

1.2.5. Release strategies 28

1.3. Ultrasound and microbubbles 32

1.3.1. Physical principles and definitions 32

1.3.2. Ultrasound contrast agents 36

1.3.3. Microbubble cavitation 39

1.3.4. Acoustic radiation force 41

1.3.5. Acoustic streaming 42

1.3.6. Cavitation microstreaming 43

1.4. Bioeffects of ultrasound 46

1.4.1. Physical 46

1.4.2. Chemical 47

1.4.3. Thermal 48

1.5. Research challenges 49

1.6. Approach 50

1.6.1. Advanced microscopy techniques 53

1.6.2. Lipid packing and hydration 54

1.6.3. Spectral imaging 55

1.6.4. Generalised polarisation 56

1.7. Thesis aims and objectives 57

1.8. Thesis outline 65

II. Electroformation of Giant Unilamellar Vesicles on Stainless Steel Electrodes 60

2.0 Abstract 61

2.1. Introduction 61

2.2. Materials and methods 65

2.2.1. Electroformation chamber 65

2.2.2. Material cost 66

2.2.3. Electroformation protocol 67

2.2.4. GUV detection and sizing 69

2.2.5. Lipid order measurements 69

2.2.6. Inductively coupled plasma optical emission spectrometry 70

2.2.7. Lipid extraction and NMR experiments 70

2.2.8. Limit of detection of oxidised DOPC 71

2.2.9. Vesicle unilamellarity 72

2.2.10. Statistical analyses 72

2.3. Results and discussion 73

2.3.1. Giant unilamellar vesicles production and imaging 73
2.3.2. Lipid order and size of vesicles composed of binary lipid mixtures 74
2.3.3. Leaching of metals from the electrodes 76
2.3.4. Lipid oxidation and hydrolysis 77
2.3.5. Unilamellarity of electroformed vesicles 78
2.4. Conclusions 80

III. Layered Acoustofluidic Resonators for the Simultaneous Optical and Acoustic Characterisation of Cavitation Dynamics, Microstreaming, and Biological Effects 81

3.0 Abstract 82
3.1. Introduction 83
3.1.1. Cavitation in ultrasound therapy 83
3.1.2. Existing devices 94
3.1.3. Challenges 86
3.2. Device design and fabrication 87
3.2.1. The piezoelectric transducer 88
3.2.2. The carrier 89
3.2.3. The thin reflector 89
3.2.4. Construction 90
3.3. Device characterisation 91
3.3.1. Acoustic field 91
3.3.1.1. 1D mathematical model 91
3.3.1.2. 2D mathematical model 93
3.3.1.3. Acoustic pressure 95
3.3.2. Acoustic streaming 96
3.3.3. Transducer temperature 97

3.3.4. Resonance frequency verification 98
3.3.5. Cell culture and sample preparation 99
3.3.5.1. Fluorescent labelling of cells and microbubbles 100
3.3.5.2. Preparation of DSPC-PEG40s microbubbles 100
3.3.5.3. Preparation of magnetic perfluorocarbon droplets 101
3.3.5.4. Preparation of polymeric cups 102
3.4. Measurements 102
3.4.1. Imaging of microbubble dynamics 103
3.4.2. Quantification of cavitation microstreaming velocities 104
3.4.3. Particle streak velocimetry 104
3.4.4. Microstreaming from different US-RAs 104
3.4.5. Monitoring from acoustic emissions 106
3.4.6. Monitoring of biological effects 108
3.4.6.1. Bubble-cell interactions 109
3.4.6.2. Quantification of cell membrane properties 109
3.4.6.3. Quantification of intracellular delivery 110
3.5. Limitations and future perspectives 110
3.6. Conclusions 113

IV. Investigating the Role of Membrane Hydration as a Mediator of Permeability in Microbubble Mediated Drug Delivery 114

4.0 Abstract 115
4.1. Introduction 116
4.2. Materials and methods 119
4.2.1. Giant unilamellar vesicles characterisation 119
4.2.1.1. GUV formation protocol 119
4.2.1.2. Glass functionalisation and vesicle fixation 119

4.2.1.3. Vesicle-glass binding strength 120
4.2.2. Preparation of microbubble solution 120
4.2.2.1. DSPC-PEG40s microbubbles 120
4.2.2.2. DSPE-PEG2000-Rhodamine microbubbles 121
4.2.3. Generalised polarisation measurements 121
4.2.3.1. Effect of photobleaching on generalised polarisation 122
4.2.4. Acoustofluidic device 122
4.2.4.1. Frequency and pressure field characterisation 122
4.2.4.2. Acoustic streaming 123
4.2.4.3. Temperature changes as a result of US exposure 123
4.2.5. Vesicle excitation modes and protocols for GP quantification 123
4.2.5.1. Shear flow only 124
4.2.5.2. Ultrasound only 124
4.2.5.3. Microbubbles only 125
4.2.5.4. Ultrasound and microbubbles combined 125
4.2.5.5. Free PEG40s 125
4.2.6. Visualisation of microbubble shell material deposition 125
4.2.7. Modulation of the uptake of a model drug during treatment 126
4.2.8. Excitation protocols for the quantification of fluorescein uptake 126
4.2.8.1. No exposure 126
4.2.8.2. Blank injection 126
4.2.8.3. Ultrasound only 126
4.2.8.4. Pressure-driven flow 126
4.2.8.5. Microbubbles only 126
4.2.8.6. Ultrasound and microbubbles combined 128
4.2.8.7. Free PEG40s 128
4.2.8.8. Microbubble shell debris 128

4.2.8.9. Temperature 128
4.2.9. Data and statistical analyses 130
4.3. Results and discussion 130
4.3.1. Setup characterisation 131
4.3.1.1. Microbubble properties 131
4.3.1.2. Acoustic pressure measurements 131
4.3.1.3. Avidin-biotin assay binding strength 131
4.3.1.4. Temperature changes as a result of ultrasound exposure 132
4.3.1.5. Effect of photobleaching on generalised polarisation 132
4.3.1.6. Acoustic streaming 132
4.3.2. Changes in membrane lipid order as a result of varying exposure conditions 133
4.3.2.1. Ultrasound only 133
4.3.2.2. Pressure-driven flow 135
4.3.2.3. Microbubbles only 138
4.3.2.4. Ultrasound and microbubbles combined 139
4.3.2.5. Exposure to PEG40s 140
4.3.3. Effect of cholesterol molar fraction 143
4.3.4. Microbubble-shell lipid deposition on DOPC vesicles 144
4.3.5. Vesicle permeabilisation 144
4.3.6. Fluorescence uptake 146
4.3.6.1. No exposure 146
4.3.6.2. Black injection control 148
4.3.6.3. Exposure to ultrasound only 149
4.3.6.4. Exposure to pressure-driven flow 150
4.3.6.5. Exposure to microbubbles 151
4.3.6.6. Exposure to ultrasound and microbubbles 151

4.3.6.7. Exposure to microbubble shell debris 152
4.3.6.8. Exposure to PEG40s 152
4.3.6.9. Exposure to heat 152
4.3.7. Relationship between lipid packing changes and permeability 153
4.3.8. Relevance to cells 154
4.3.9. Limitations 156
4.4. Conclusions 157

V. Ultrasound and microbubble-mediated luminal movement 159

5.0 Abstract 160
5.1. Introduction 161
5.2. Materials and methods 164
5.2.1. Production of giant vesicles and encapsulation of flow tracers 164
5.2.2. Vesicle fixation to glass slide 165
5.2.3. Production and characterisation of microbubbles 165
5.2.4. Exposure conditions 166
5.2.4.1. Imaging and controls 166
5.2.4.2. Pressure-driven shear flow 168
5.2.4.3. Ultrasound exposure 168
5.2.4.4. Ultrasound and microbubble exposure 168
5.2.5. Bead velocity analysis 169
5.2.6. Statistical analysis 170
5.3. Results and discussion 170
5.3.1. No exposure 170
5.3.2. Pressure-driven flow 171
5.3.3. Ultrasound exposure 173
5.3.4. Ultrasound and microbubbles 174

5.3.5. Biological implications 175
5.4. Intracellular trafficking 176
5.4.1. Materials and methods 176
5.4.1.1. Cell culture 177
5.4.1.2. Image analysis 179
5.4.1.3. Statistical analysis 179
5.4.2. Results 181
5.4.3. Conclusions 181

VI. Conclusions and Future Work 183

6.0 Overview 184
6.1. Summary of experimental findings 185
6.2. Limitations and future work 186
6.3. Final remarks 199

Appendix A 191

1.0 Uncertainty analysis on layer thickness (1D simulations) 191
2.0 Particle streak velocimetry 191
3.0 Particle streak velocimetry algorithm performance 193

Appendix B 196

1.0 Link to Supporting Videos 196

References 198

Acronyms

^{1}H-NMR	Proton nuclear magnetic resonance
5FU	Fluorouracil
A	Amplitude
A549	Adenocarcinomic human basal epithelial cells
ANOVA	Analysis of variance
BBB	Blood brain barrier
BSA	Bovine albumin serum
$CDCl_3$	Deuterated chloroform
CH	Channel
Chol	Cholesterol
CNC	Computer numerical control
CW	Continuous wave
Da	Dalton
DiI	1,1'-dioctadecyl-3,3,3',3'-tetramethylindocarbocyanine perchlorate
DMEM	Dulbecco's modified eagle's medium
DMPC	1,2-Dimyristoyl-sn-glycero-3-phosphorylcholine
DMSO	Dimethyl sulfoxide
DOPC	1,2-dioleoyl-sn-glycero-3-phosphocholine

DOX	Doxorubicin
DPPC	1,2-dipalmitoyl-sn-glycero-3-phosphocholine
DPPE-biotin	1,2-dipalmitoyl-sn-glycero-3-phosphoethanolamine-N-(cap-biotinyl) sodium salt
DSPC	Distearoyl-sn-glycero-3-phosphocholine
EPR	Enhanced permeability and retention effect
FDA	Food and drug administration
FITC	Fluorescein isothiocyanate
FLIM	Fluorescence lifetime imaging Microscopy
GPMV	Giant plasma membrane vesicle
GUV	Giant unilamellar vesicle
HIFU	High intensity focused ultrasound
HUVEC	Human umbilical vein endothelial cells
IARC	International agency for research on cancer
ICP-OES	Inductively coupled plasma atomic emission spectroscopy
ITO	Indium tin oxide
IV	Intravenous
LMV	Large unilamellar vesicle
MB	Microbubble

MDR	Multidrug resistance
MPS	Mononuclear phagocyte system
mRNA	Messenger RNA
NBD-PE	N-(7-Nitrobenz-2-Oxa-1,3-Diazol-4-yl)-1,2-dihexadecanoyl-sn-Glycero-3-Phosphoethanolamine, Triethylammonium salt
Np	Neper
NP	Nanoparticle
Pa	Pascal
PBS	Phosphate-buffered saline
PC	Phosphatidylcholine
pDNA	Plasmid DNA
PDT	Photodynamic therapy
PEG	Polyethylene glycol
PEG40s	Polyethylene 40 stearate
pH	Potential of hydrogen
PI	Propidium iodide
PIV	Particle image velocimetry
P-NMR	P-31 NMR spectroscopy
PRF	Pulse repetition frequency
PRP	Pulse repetition period
PSV	Particle streak velocimetry
PTV	Particle tracking velocimetry
PZT	Piezoelectric transducer

RBC	Red blood cell
ROI	Region of interest
ROS	Reactive oxygen species
RP	Rayleigh-Plesset
SD	Standard deviation
SDT	Sonodynamic therapy
siRNA	Small interfering RNA
T	Temperature
UCA	Ultrasound contrast agents
US	Ultrasound
VCAM	Vascular cell adhesion molecules

List of Symbols

λ	Wavelength
τ	Period
ω_n	Natural frequency
v	Velocity of sound
f	Frequency of sound
Ω	Acoustic impedance
ρ	Density
α	Acoustic attenuation coefficient
ρ_L	Density of liquid
r	Radius
p_0	Hydrostatic pressure
r_0	Initial microbubble radius
κ	Gas polytropic constant
μ_c	Viscosity of the microbubble coating
G_c	Elasticity of the microbubble coating
μ_L	Viscosity of the fluid
ρ_0	Density of the medium
c_0	Acoustic velocity in the medium
Φ	Acoustophoretic contrast factor
τ_w	Shear stress at wall boundary
α_d	Thermal diffusivity

I

Introduction

This chapter provides a contextual overview of the clinical motivation for the research, and an introduction to drug delivery, and the current state-of-the-art. Furthermore, it describes the advantages of using ultrasound and microbubble agents in combination for treatment, and outlines the theoretical foundations of acoustic cavitation and associated physical phenomena. The literature concerning the interaction between microbubbles and cells is evaluated, emphasising the need for simple, microscopy-based approaches to investigate this process *in vitro*. The thesis overview, motivation, aims, and structure are also presented in this chapter.

1.0 Background and motivation

Cancer imposes a significant disease burden worldwide, with considerable variation in incidence, mortality, and overall morbidity. According to the International Agency for Research on Cancer (IARC), there were 14.1 million new cancer cases and 8.2 million cancer deaths in 2012.[1] In the United Kingdom alone, 331,487 new cases and 161,823 deaths were reported in 2011.[2] Clearly cancer prevention, diagnosis, and and treatment constitutes a major challenge, placing significant pressure on scientists and clinicians to develop more effective treatments.

One of the most common cancer therapies involves intravenously injecting chemotherapeutic drugs into the bloodstream.[3] Despite being widely used, this method suffers from numerous disadvantages. These include systemic toxicity, low drug concentration at tumour site, and development of drug resistance.[4] While numerous novel cancer therapies attempt to simultaneously address these needs, they are limited by an inherent trade-off between the amount of therapeutic agent delivered to the target tissue, its specificity, and treatment invasiveness.

Ultrasound (US) transducers induce a localised oscillatory motion that propagates through tissue, triggering several phenomena that may facilitate intracellular drug uptake. The mechanisms that govern this process include enhanced molecular transport and diffusion induced by acoustic streaming [5], cell sonoporation [6], heating[7], and acoustic cavitation. Ultrasound enhanced permeation of therapeutic agents through an initially impermeable cell membrane has been observed widely in the past.[7–10] Likewise, delivery of genetic material (pDNA, siRNA, mRNA), peptides, and proteins *via* a transient permeabilisation of the cell membrane has been performed both *in vitro* and *in vivo*.[11]

The bio-effects of ultrasound may be further enhanced by the presence of cavitation nuclei such as microbubbles (MBs). They comprise an echogenic gaseous core and a biocompatible phospholipid, protein or polymer shell to stabilise the gas content of the bubble. Microbubbles are used routinely as ultrasound contrast agents (UCAs) to enhance blood-tissue contrast in ultrasonography and more recently have been investigated as ultrasound-activated vehicles of bioactive compounds.[12] UCA typically range between 1-10 μm in diameter and are delivered *via* intravenous (IV) injection.[13] The inert gas contained in the microbubbles typically dissolves into the blood stream after ten minutes and is exhaled through the lungs, while the microbubble shell is filtered by the kidneys, and eliminated by the liver.[14]

While exposed to an ultrasound field, microbubbles undergo cavitation, i.e. a repetitive volumetric contraction and expansion, as the gaseous core is exposed to an oscillatory pressure field. Cavitation dynamics can be influenced by varying the properties of the driving pressure field and can be monitored using techniques such as passive acoustic mapping.[15] The direction and focus of the ultrasound beam can be also adjusted to localise and trigger a range of therapeutic effects within the body. Microbubbles offer the potential to enhance existing treatment modalities by inducing mechanical[16], thermal[15] and chemical effects[17], at both the cellular and bulk tissue scale.

The bioeffects of ultrasound and microbubbles are characterised by their multiscale nature: changes in cell membrane properties occur on the molecular scale, cell deformation and vesicular transport take place microscopically, while acoustic radiation forces and fluid transport due to streaming constitute aggregate (macroscopic) effects on tissue. Timescales also vary considerably, ranging from the microsecond scale for microbubble oscillations to several milliseconds for the bulk movement caused by acoustic radiation forces.

Nonetheless, the underlying biophysical processes that underpin cell microbubble interactions are still poorly understood.[11] Progress in the field is inhibited by the by the difficulties in isolating cellular features such as membrane and intracellular properties, non-invasively quantifying biological characteristics down to the molecular scale, and exposing samples to a known and repeatable ultrasound field.

To overcome these challenges, giant unilamellar vesicles were employed as a cell mimic to characterise the effects of ultrasound and microbubbles on the properties of phospholipid membranes and the dynamics of their intracellular lumen.

1.1 Medical ultrasound

1.1.1 Ultrasound imaging

Ultrasound is a convenient, fast, and cost-effective way to observe a patient's internal tissues. By measuring the time of travel of a given ultrasound pulse from and back to the transducer, the distance of the object can be inferred from the relationship between speed, distance, and time. When the ultrasound wave is incident to an interface between media having different acoustic impedance, part of it is reflected back to the transducer and is detected as an echo. The magnitude of the echo is proportional to the difference in acoustic impedance at the interface. To generate a two dimensional image, the beam is swept across an area to reconstruct a slice.[18] Over the past two decades, improvements in computing power have also enabled three dimensional imaging[19].

Ultrasound scanners have become ubiquitous in large parts of the world; and are generally accessible even in resource constrained settings. Techniques such as magnetic resonance imaging (MRI), computerised tomography (CT), single photon emission computed tomography (SPECT), and positron emission tomography (PET) may provide better spatial resolution, tissue contrast, and/or functional information. However, this is often off-set, however, by the cost and size of equipment, the need for specialised training, long scan times,

toxicity of the relevant contrast agents and/or ionizing radiation.[20]A further advantage of ultrasound is the speed with which images can be acquired and displayed. This enables concurrent monitoring and therapy with real-time feedback and excellent temporal resolution, without the need for additional probes[21]. However, ultrasound imaging is limited by three factors. First, the contrast that can be achieved with ultrasound between tissue-blood interfaces is limited and inferior to other techniques, such as MRI. Second, the imaging depth inside the body is limited by attenuation, which increases with ultrasound frequency; and third, spatial resolution, which is inversely proportional to the frequency. Ultrasound imaging is therefore afflicted with a trade-off between depth of imaging and resolution.

1.1.2 Contrast agents

The quality of ultrasound images has been improving steadily since the 1970s, owing to the advances in computational power, miniaturization of integrated circuits, and image forming algorithms.[22] Image contrast, however, is ultimately determined by the acoustic impedance mismatch of different tissues within the body. To increase the image contrast of blood vessels, a solution composed of gaseous microbubbles may be injected into the bloodstream to increase its echogenicity. Microbubbles are highly reflective to ultrasound due to their high compressibility and therefore produce a larger echo signal compared to their surroundings. As a result, the vessels can be readily imaged, revealing vascular signatures that could not previously be detected. The technique was first observed at a catheter tip by Dr. Raymond Gramiak in 1968 followed by Kremkau in 1970, leading to the development of the first commercially available contrast agent, Albunex® (Mallinckrodt Inc., Hazelwood, MO, USA).[23]

1.1.3 Therapeutic ultrasound

Both in the presence and absence of microbubbles, ultrasound may be used to deliver energy deep inside the body with a high degree of spatial and temporal control. This enables both mechanical and thermal effects to be produced locally, at a desired location. Mild temperature increases (up to 38 - 40 ˚C) have been associated with immunogenic responses, tissue healing for physiotherapeutic applications, and improved transport of drugs, nutrients, and oxygen. Moderate temperature rises (up to <43ºC) in tissue have been demonstrated to further increase tumour perfusion, sensitising tumours to chemotherapy[24]. Recent studies[25] have also demonstrated that heat generated by ultrasound triggers the release of therapeutic payload from thermosensitive liposomes[25]. At higher temperatures, the heating generated by high intensity focused ultrasound (HIFU) can be used to cause cell death and tissue coagulation, and has been applied successfully to the treatment of uterine fibroids[26], benign prostate hyperplasia[27], and in eye treatments. Ablation of malign tissue can also be achieved at high ultrasound intensities (100-10 000 W/cm^2)[28], allowing the treatment of various types of cancer including prostate (FDA approved), liver (approved outside the USA), breast (approved outside the USA), and bone cancer (FDA approved). Treatment speed and efficacy have been shown to be enhanced by the presence of microbubbles, which nucleate cavitation in the target volume[29]. Currently, ultrasound is being investigated as treatment for neurological conditions such as essential tremor[30]. The ability to ablate specific regions in the brain non-invasively and modulate the neural activity of specific parts of the brain could potentially open new avenues for treatment of conditions such as chronic pain, epilepsy, and mental health disorders[31].

This thesis will focus on the effects of ultrasound in combination with microbubbles at low acoustic pressures in the context of drug delivery. A wide range of therapeutic bioeffects have been reported, including enhanced tissue sensitisation, modulation of membrane properties, and delivery of drugs, all of which will be discussed in more detail in Section 1.4.

1.2 Introduction to drug delivery

1.2.1 Pharmacological strategies

The efficacy of an anticancer therapeutic is determined by its ability to induce targeted cell death in diseased tissue. The most common form of cancer chemotherapy involves the systemic administration of cytotoxic small molecule drugs to inhibit the growth and reproduction of malignant cells. Chemotherapeutic molecules such anthracyclines have been used previously to treat various forms of cancer, including liver, lung, breast, ovary, and prostate[32]. One of the most common anthracycline drugs is doxorubicin, a highly toxic compound that has been shown to be effective but to have very low specificity. As a result, anthracyclines are often associated with severe side effects, such as a compromised immune system, nausea and alopecia (hair loss), which arise as the result of chemotherapy drugs affecting healthy tissue. To improve targeting and concentration at the tumour site, anthracyclines are often co-injected with UCAs[33] or encapsulated in carriers[34] engineered to release their contents at a specific location following an external stimulus. However, the long term efficacy of chemotherapy diminishes with time, as cells develop drug resistance mechanisms.

Novel oncological strategies that attempt to mitigate the limitations of chemotherapy without compromising the efficacy of treatment include: antibodies, gene-based therapies, and immunotherapy. Antibodies selectively bind to receptors expressed on tumour cell membranes, limiting their action to malignant cells. Gene-therapy molecules such as small interfering RNA (siRNA) and messenger RNA (mRNA) have also been used to suppress specific genes, which in turn regulate the expression and mutation of proteins specifically in tumour tissue. However, the efficacy of these strategies is limited by the molecular weight of the therapeutics, which translates in low extravasation, limited diffusion and ultimately diminished delivery. Viruses have shown promise as anti-cancer therapies[35], given their ability to infect and replicate selectively in diseased tissue, while triggering an immune response.

Recent successful clinical trials[36] have led to fervour in the cancer research community, due to the prospect of harnessing a patient's immune response to target malignant cell growth. Yet, the efficacy of a particular viral therapy is highly dependent on the specific patient's immune reaction.

Despite the availability of therapeutic agents, progress in developing efficacious treatment for cancer has been slower than hoped. As a result, much research effort has shifted from designing therapeutic agents to developing efficient carriers, targeting approaches, and release strategies, in order to identify and overcome factors that limit treatment efficacy.

1.2.2 Barriers to successful therapeutic outcomes

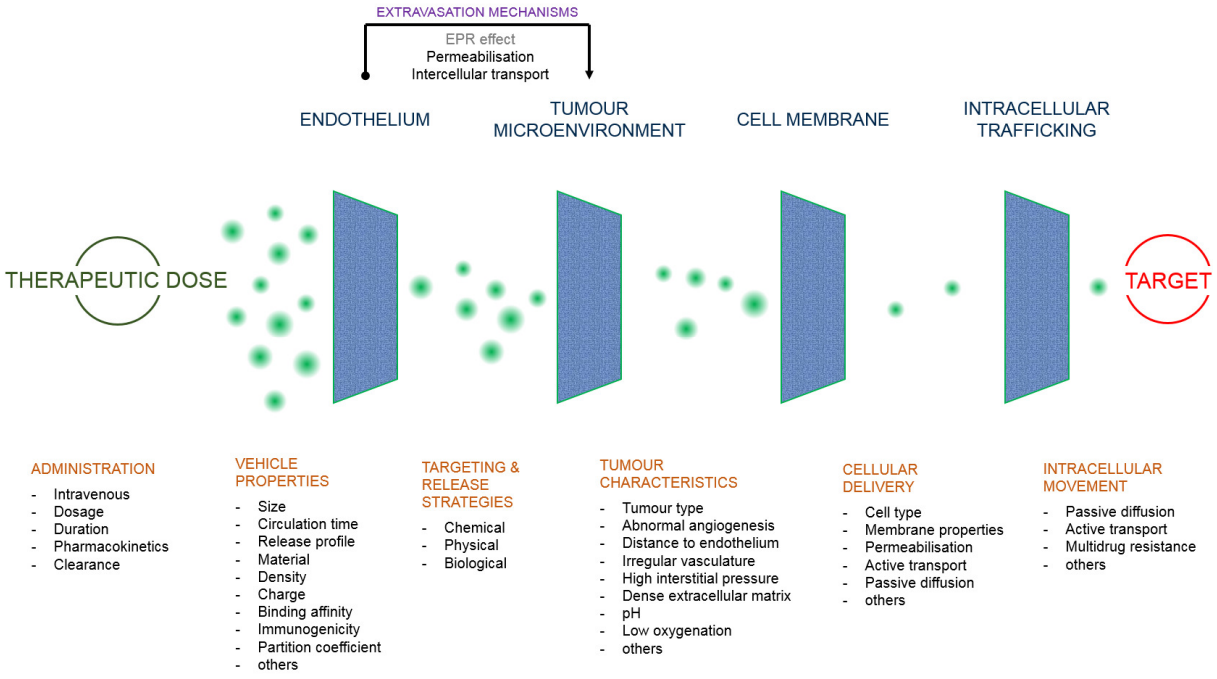


Figure 1 – Schematic illustrating the barriers that injected therapeutic doses face before reaching the target tissue. A summary of factors involved in dose administration, physicochemical properties of delivery vehicles, payload targeting and release strategies, and cellular and intracellular factors are briefly outlined. The Enhanced Permeability and Retention (EPR) effect is a disputed concept whereby particles are able to accumulate more readily in cancer tissue compared to healthy tissue, as a result of malformed and leaky vasculature in the tumour. The letters EPR are displayed in grey to highlight the controversy of EPR as an effective extravasation mechanism to achieve therapeutic outcomes.

Despite the concerted efforts and considerable advances in the design of cancer therapeutics, chemical-based treatment strategies still suffer from low drug bioavailability at the malignant tissue. The effective delivery of the injected therapeutic dose is hindered by multiform biological, chemical, and physical barriers, hence limiting therapeutic outcomes[37].

While a myriad of formulations have been engineered to exhibit favourable physicochemical properties, the complexity of tumour tissues still represents a major challenge[38]. Existing treatment modalities have the scope for significant improvement, particularly in overcoming the physical obstacles that separate the circulatory system and the tumour core. In this respect, recent efforts have been directed in investigating the use of physical stimuli to overcome

physiological barriers such as the vascular endothelium, the tumour extracellular matrix, and the cell plasma membrane. In particular, ultrasound in combination with cavitation agents have received considerable attention for their ability to propel and extravasate therapeutics up to hundreds of micrometres away from the cavitation source, and into the tumour interstitium[39].

The first obstacles therapeutics encounter are in the blood. Here, drugs are affected by non-specific passive extravasation, protein binding, non-specific adherence[40], and are subject to immunological responses by the mononuclear phagocytic system (MPS)[41]. Moreover, excretion mechanisms such as renal clearance also play a role in determining the destination and concentration of the therapeutic[42]. To address these challenges, chemical strategies have been implemented to reduce the immunogenicity and binding affinity of therapeutics; however, these modifications simultaneously adversely affect the ability of the therapeutic to cross the endothelial barrier.

The endothelium represents a considerable obstacle separating the blood and the tumour interstitium. To overcome this barrier, therapeutics may either penetrate the cell membrane of endothelial cells, or permeate through the intercellular junctions. To facilitate this process, therapeutics may be targeted to specific areas of the endothelium using chemical adhesion strategies[43], or may be directed to closely adhere to the endothelium using physical approaches such as magnetic targeting or ultrasound in combination with gaseous contrast agents. Another mechanism that can potentially facilitate extravasation is known as the enhanced permeability and retention effect (EPR). The EPR effect is a controversial concept whereby particles are able to accumulate more readily in cancer tissue compared to healthy tissue, as a result of malformed and leaky vasculature in the tumour. While this effect could in principle be exploited to deliver therapeutics and nanoparticles to the tumour in a targeted manner, there is little evidence demonstrating that it enhances therapeutic outcomes[44]. Moreover, according to a literature survey by Wilhelm et al. in 2016[45], only 0.7% (median) of the injected

nanoparticle dose reaches target site. Among the causes cited in this study, the physicochemical alterations of the particles, MPS, and renal clearance were hypothesised to be the most dominant in limiting the accumulation of particles at the desired location. The paper also shows how, in the past thirteen years, little improvement has been made in nanoparticle delivery efficiency, despite the titanic efforts and investment that have been directed towards developing carrier particles.

Following successful translocation across the endothelium, therapeutics encounter further challenges before reaching the cancerous tissue. The accumulation of solid stress caused by uncontrolled cell growth[40] and a tortuous and dense extracellular matrix[46], coupled with a comparatively higher interstitial fluid pressure[47], restrict convective transport of therapeutics throughout the target site. In addition, the low oxygenation and the distance that separates the vasculature and the tumour further limit drug delivery and treatment[37].

The plasma membrane also constitutes a major delivery obstacle, as the efficacy of treatment depends on the ability of therapeutic agents to penetrate and remain in the intracellular environment. The physicochemical properties of the therapeutic have perhaps the highest influence on the ability of molecules to penetrate the plasma membrane. In particular, the lipophilicity of a substance is a good indicator of its ability to penetrate through tissue. To quantify the lipophilicity of a molecule, the partition coefficient of a substance, or logP, is calculated. The logP refers to the ratio of concentrations of a molecule in a mixture of two immiscible aqueous and lipophilic phases at equilibrium.

Lipinski et al.[48] in 1997 outlined five characteristics that influence the permeation of particles through the lipid-rich plasma membrane. Ideal properties for permeation include: a i. partition coefficient above five, ii. molecular weight below 500 Da, iii. no more than five hydrogen bond donors, iv. no more than ten hydrogen bond acceptors. These criteria are still widely used in the design of new therapeutics[49]. Larger particles may also be internalised by other mechanisms such as endocytosis. However, depending on the type of endocytic

pathway, chemotherapy drugs can be sequestered into endosomes, deflecting the therapeutic from its target and enabling drug resistance[50].

The intracellular environment also presents challenges for effective delivery. Tumour cells are able to develop drug resistance mechanisms to prevent the action of chemotherapy, such as selectively decreasing drug uptake, increasing efflux through exocytosis, DNA repair systems, and a wide range of detoxification processes[51]. The combination of these mechanisms is more commonly known as multi-drug resistance (MDR), and is particularly relevant in patients that undergo long exposure to chemotherapy. MDR mitigation strategies have been developed to inhibit this phenomenon by suppressing specific transporters that exhibit MDR phenotype, with positive results in a colorectal cancer cell line exposed to doxorubicin.[52]
The heterogeneous nature of the barriers encountered by cancer therapeutics emphasises the need for holistic delivery strategies that combine chemical, biological and physical approaches in combination with external stimuli, to increase the therapeutic dose and successful treatment of the target tissue.

1.2.3 Drug delivery vehicles

To increase the *in vivo* circulation time, target therapy, and modulate release profiles, drugs have been encapsulated in numerous nanoscopic delivery vehicles. Much effort[53] has been directed in creating the optimal drug carrier, with characteristics that span size, density, surface chemistry, biocompatibility, biodegradability, encapsulation efficiency, release sensitivity, stimuli responsiveness, production scale-up potential, susceptibility to drug resistance, and ability to trigger an immune response.

Among all drug carriers, liposomal formulations and nanoparticles represent the most researched vehicles. Carriers such as polymeric and carbon nanoparticles have also received considerable attention due to ease of production and the ability to fabricate hollow and porous structures that enable facile drug encapsulation and effective payload release. However, their

size still hinders extravasation, thence limiting convection towards throughout the tumour mass.

Liposomes represent one of the most versatile delivery platforms. They are lipid bi-layers that enclose a liquid phase within a 25 nm – 2.5 μm spherical assembly[54]. Depending on the lipid mixture, liposomes can be designed to efficiently encapsulate a wide range of hydrophilic drugs and their surface can be effectively modified to incorporate targeting ligands. Moreover, drug-loaded liposomes have shown to increase the drug circulation time, reduce systemic toxicity, and diminish immunological responses.[54] Furthermore, liposomal drug release can be passively tuned by altering the liposome shell composition, or can be actively triggered by various non-invasive modalities, such as magnetic stimulation, ultrasound, hyperthermia, and pH gradients[55]. The combination of these characteristics has led to the clinical approval of many liposomal formulations for the treatment of prostate, pancreatic, head and neck, liver, and colorectal cancers.[56] However, due to their soft and fusogenic nature, liposomes suffer from short half-life compared to hard particle formulations, and are prone to undesired interactions that lead to leakage of the payload.

The *in vivo* carrier circulation time may be further enhanced by functionalising the shell with polyethylene glycol (PEG). The hydrophilic PEG brush-like chains encompass the particle shell, protecting it from lysis, undesired chemical interactions, and the immune system[57]. Nevertheless, the properties and chain length of the PEG must be tuned to strike the fine balance between limited *in vivo* circulation and excessive stealth of the carrier.

While the encapsulation of therapeutics in vehicles has shown significant improvement in delivery of chemotherapeutics, the comparably larger size of carriers compared to their content still hampers extravasation. Even following successful extravasation, carrier systems still face significant barriers, such as the extracellular matrix and dense stromal and tumour cellular architecture before they reach the tumour core. Indeed, only a tiny fraction of the injected nanoparticle dose reaches the desired location.[45] Following successful delivery, carriers

must be engineered to allow efficient payload release upon stimulus. A more detailed account on the obstacles to successful drug delivery is discussed in Section 1.2.2.

1.2.4 Targeting strategies

Targeting therapeutics to a specific site is particularly useful in the context of chemotherapy. Many oncolytic drugs are either highly toxic or are cleared too quickly from the body; hence, targeting would be beneficial in partially overcoming these limitations by increasing the drug concentration at the tumour. Moreover, if a higher drug concentration is achieved at the tumour, the undesired effects on off-target sites will also be reduced, potentially limiting the occurrence of side-effects in patients. While the design of vehicles plays an important role in therapeutic efficacy, the pharmacokinetics of the drugs is also a major bottleneck. In fact, despite the availability of effective therapeutic agents, improvements to the clinical outcomes in cancer therapy have been slower than expected. As a result, a trend is emerging in drug delivery where the focus is shifting from designing potent therapeutics to the development of drug delivery platforms that intersect therapeutic design, delivery approaches, targeting and release strategies.

Targeting strategies can be broadly divided in two categories: active and passive. Among passive strategies, the most prevalent is passive diffusion and accumulation. Passive diffusion refers the free drug permeating the endothelium driven by concentration gradients, with the hope that the dose at the target will be sufficient to inhibit growth and cause the tumour to recede. Accumulation refers to the passive gathering of particles in tumours through abnormal and leaky vasculature. Due to their rapid growth, tumour vessels exhibit pores in the range of 0.2-1.2 μm[58–60] compared to 5-10 nm in healthy tissue[55]. This creates the opportunity to encapsulate drugs into vehicles in the order of 100 nm, in order to simultaneously increase circulation time, maximise passive accumulation, and minimise immunogenic response. However, the effective increase in accumulation due to EPR is still limited (~2%)[55], and in many cases particles are often too stable to release the payload following extravasation[61].

Active targeting involves the preferential action of therapeutics on, or in proximity of, malignant cells. This can be achieved by either chemical, biological, and physical approaches. Chemical strategies involve altering the surface chemistry of the particles by functionalising the surface with ligands such as antibodies that selectively bind to tumour cell antigens. For example, particles can be functionalised with vascular cell adhesion molecules 1 (anti VCAM-1) to adhere and endocytose in endothelial cells that express VCAM-1 proteins.[62] Biological approaches, for example, involve harnessing a patient's immune response by reprogramming immune cells to scavenge tumour cells. Physical approaches relate to the use of magnetic forces and ultrasound to direct and foster endothelial acceptor-ligand interactions and accumulation of functionalised carriers at a desired target location. Moreover, targeting may be achieved through the pumping action of ultrasound in combination with microbubbles, which has been shown to cause endothelium permeabilisation and drug extravasation.[63]

The action of active and passive targeting mechanisms cannot be decoupled and may be exploited in combination. Physical approaches such as ultrasound and magnetic forces may be used to direct particles towards the endothelium, promote extravasation, and permeabilise cells, within tight spatial boundaries. Chemical approaches may be used to promote specific adhesion, endocytosis, and interactions with cancer cells. Both can be used to release the payload at the desired site.

1.2.5 Release strategies

A further challenge in achieving positive therapeutic outcomes is the targeted release of the drug payload from the carrier to its surroundings, at desired time points during treatment. Even when successful accumulation in the tumour is accomplished, the efficacy of the treatment is inhibited by the inadequate release of the carrier cargo[64]. There is thus the need to develop strategies to release and diffuse the encapsulated drug selectively in proximity of the target site. This constitutes an opportunity in both the design of responsive carriers as well as in the development of devices for delivering physical stimuli within the body.

The surface chemistry of carriers may be tuned to release the encapsulated drug upon exposure to specific physicochemical conditions. The challenge involves the identification of conditions particular to the tumour interstitium, in order to avoid non-specific release. Conditions such as altered pH levels and enzymatic activity have been proposed as in-tumour release mechanisms. While it has been shown that tumours exhibit lower pH compared to healthy tissue[65], the pH levels in tumours are heterogeneous and depend on vascular perfusion and local hypoxia within a given site. Other triggers such as specific enzymatic activity have been exploited chemically to induce cytotoxicity from prodrugs[66], as well as prompting drug release.[67]

Among externally triggered mechanisms, hyperthermia, photo/sonodynamic therapy, and ultrasound in combination with microbubbles, have shown the greatest potential. Hyperthermia, which can be caused by alternating magnetic fields[68], radio frequency[69], and ultrasound[70], has shown positive effects in the context of cancer treatment. In particular, heating tissue has been linked to tissue sensitisation, increased cell permeability, and drug release from thermosensitive carriers[71].

Photodynamic therapy (PDT) involves exposing a particular class of drugs, referred to as *photosensitisers,* to a specific wavelength of light to produce reactive oxygen species (ROS)[72]. As light can be focused in a very narrow beam, the production of ROS can be achieved within tight spatial resolution. ROS have been shown to cause plasma membrane disruption and poration, promoting the delivery of drugs[73]. Recent studies have shown that sensitisers used in photodynamic therapy also respond to exposure to ultrasound waves[74], in a process referred to as sonodynamic therapy (SDT). This constitutes an opportunity to achieve deeper targeting into the body, as light is attenuated readily in tissue. Cavitating microbubbles containing oxygen have been shown to enhance this effect; however, the underlying mechanisms are still under investigation.[75] SDT is a nascent field and further understanding of the relationship between mechanisms of action, dosimetry, and therapeutic response, is required.

The mechanical effects caused by the combination of ultrasound and microbubbles have been shown to cause vigorous mixing, microstreaming, and stresses resulting from the microbubbles' radial vibrations[76] (Figure 2). In turn, these have been related to doxorubicin-containing liposome lysis[77] and drug release from micelles[78] to achieve targeted release of therapeutic payload. Notably, ultrasound provides significant advantages in promoting drug release, due to its ability to target energy within the body up to tens of centimeters deep at tight spatial locations. Its action has been related to effects that include sensitisation of tissue, sensitiser activation, and cavitation, all using a single treatment modality. Using ultrasound, a wide range of tumours can be targeted, including liver, pancreatic, kidney, and brain[79]. Moreover, it is cost effective and has a superior safety profile compared to other physical stimuli. The following sections provide an overview of the physical principles of ultrasound and the characteristics of contrast agents, and introduce the phenomena that underpin ultrasound-mediated, microbubble-based, drug delivery (Figure 2).

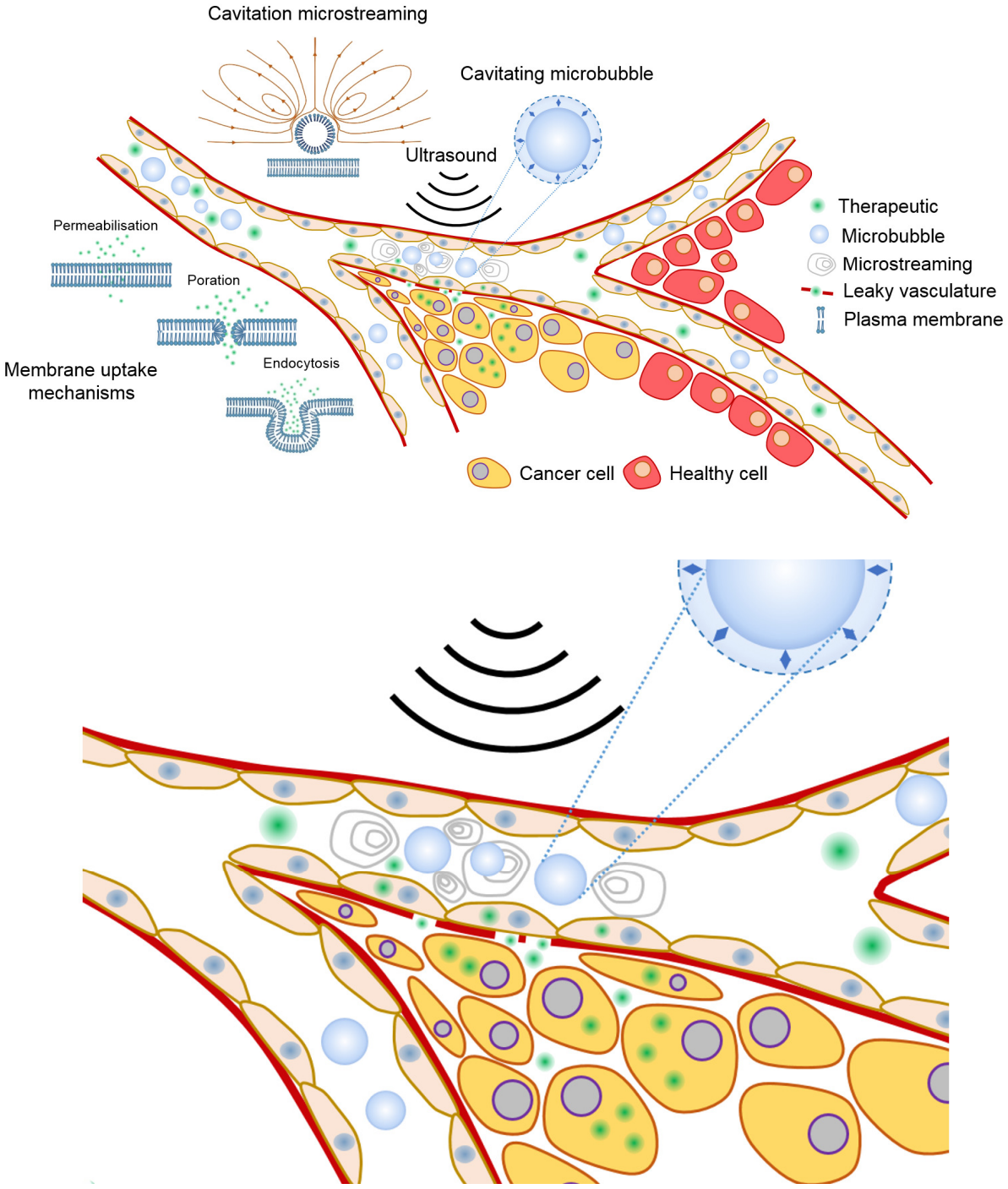


Figure 2 - Schematic representation of the approach underlying ultrasound-mediated drug delivery. It illustrates a capillary network with healthy and diseased tissue with circulating therapeutic molecules and microbubbles. The therapeutic is able to cross the endothelial barrier by EPR effect. Microbubble cavitation also enhances the extravasation of particles beyond the endothelium. The insets show possible mechanism of membrane internalisation; a cavitating microbubble; and cavitation microstreaming fields.

1.3 Ultrasound and microbubbles

1.3.1 Physical principles and definitions

Sound waves are longitudinal perturbations in pressure and density that propagate energy within a medium. When the frequency of the wave exceeds the human audible limit of 20 kHz, the waves are commonly referred to as *ultrasound*. The waves can be defined by their frequency, f [Hz], wavelength, λ [m], amplitude [Pa], and propagation speed, c [m/s].

$$v = f \cdot \lambda \qquad \textit{Equation 1}$$

Ultrasound is typically produced by piezoelectric elements, which consist of materials, such as lead zirconate titanate (PZT), that are able to generate mechanical strain in response to an input electric field. To produce ultrasound, an alternating potential difference is applied on the surface of the piezoelectric, causing a repetitive expansion and contractions of the material. The etymological origin of the word piezoelectric is Greek, and stems from the terms πιέζειν (piezein), which means to press or squeeze, and elēkrŏn, which means amber. The effect was discovered in 1880 by the French physicists Jacques and Pierre Curie.

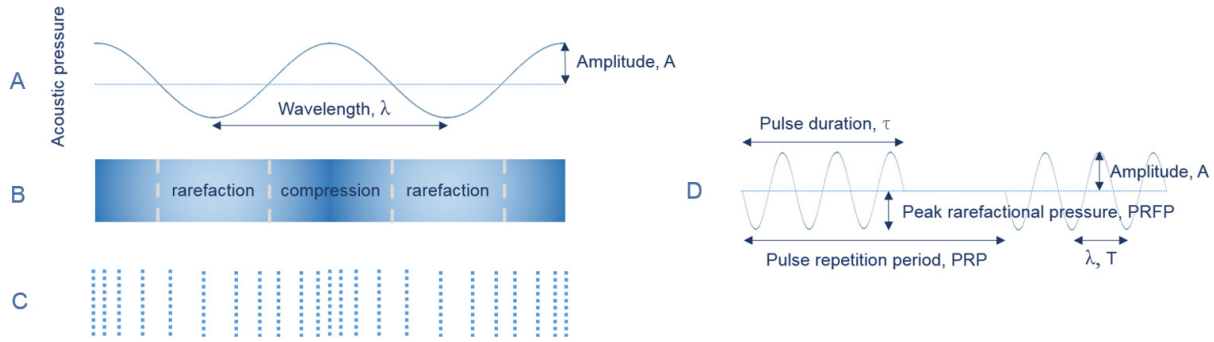


Figure 3 - Schematic representation of a single frequency ultrasound continuous wave. A. the wave is characterised by its frequency, wavelength, and amplitude. B. the dark shaded regions represent areas of compression, when the ultrasound pressure is greater than its average value. The lightly shaded regions represent areas of rarefaction. C. representative particle displacement as a result of ultrasound propagation. All areas are aligned vertically in time and space. D. representation of a series of ultrasound pulses, defined by their duration, pulse repetition period, and peak rarefactional pressure.

Figure 3 shows a schematic of an ultrasound wave, with labels to show amplitude and wavelength, cycles of compression and rarefaction, and a particle representation to illustrate density fluctuations. For both imaging and therapeutic applications, the amount of energy delivered to the body is modulated by pulsing the ultrasound wave. This can be achieved by applying a voltage on the transducer surface over short intervals separated by delay where no stimulus is applied.

This regime is represented in Figure 3b, where a repetition of three cycles, followed by a pause, represents an exemplary pulsed wave configuration. The pulse duration is defined by the time of one pulse, the pulse repetition frequency by the number of pulses in one second, and the duty factor is the fraction of the time the ultrasound is active within the pulse repetition period. The pulse repetition period is the time between two equivalent time points within a pulse. Table 1 summarises the definition of terms commonly used throughout the thesis.

Table 1 – Terms, abbreviations, units and description of terms commonly used to characterise ultrasound waves and the media they penetrate.

Parameter	Abbreviation	Units	Description
Pressure amplitude	A	Pa	Peak positive acoustic pressure of the ultrasound wave
Peak rarefactional pressure	PRFP	Pa	Peak negative pressure of the ultrasound wave
Frequency	f	Hz	Number of times per second a waveform experiences a full compressional and rarefactional cycle
Period	T	s	Duration of one full compressional and rarefactional cycle
Wavelength	λ	m	Distance between two equivalent points on a waveform
Pulse duration	τ	s	Duration of one ultrasound pulse
Pulse repetition Frequency	PRF	Hz	Number of pulses in one second
Pulse repetition period	PRP	m	Time between the start of one pulse and the start of the next
Duty Factor	DF	%	Fraction of time the ultrasound is activated
Characteristic impedance	Ω	kg/(s·m^2) MRayls	The product of density and speed of sound in an unperturbed medium

When the ultrasound travels through the body at low acoustic pressures, the frequency of the wave remains unaltered, whereas its velocity and wavelength adjust upon the changes in characteristic impedance of the medium, according to the following relation:

$$\Omega = \rho \cdot c \qquad \textit{Equation 2}$$

where ρ is the density of the medium and c is the speed of sound in the medium. It can therefore be inferred that ultrasound travels faster in denser tissues, such as bone, and slower in low density and compressible mediums such as air. As ultrasound travels through the body, it encounters media with a diverse range of acoustic properties, causing it to reflect, refract

and diffract within the body. Table 1 summarises the typical acoustic properties of tissue (density, speed of sound, and acoustic impedance).

Table 2 - Typical acoustic properties of tissues relevant to ultrasound imaging and therapy. Adapted from Azhari, Basics of Biomedical Ultrasound.[80]

Tissue	**Density** (g·cm^3)	**Speed of sound** (m/s)	**Acoustic impedance** (MRayls)
Water	1	1480	1.48
Blood	1.055	1575	1.66
Fat	0.95	1450	1.38
Liver	1.06	1590	1.69
Kidney	1.05	1570	1.65
Brain	1.03	1550	1.60
Heart	1.045	1570	1.64
Muscle (along fibres)	1.065	1575	1.68
Muscle (across fibres)	1.065	1590	1.69
Skin	1.15	1730	1.99
Bone (longitudinal)	1.9	4080	7.75

As ultrasound wave propagates through tissue, its amplitude decreases with penetration depth due to absorption and scattering, which are dependent on the frequency of the wave and the acoustic properties of the tissue. This phenomenon is referred to as attenuation. It is characterised by an exponential decrease in pressure with travelling distance z in the body:

$$p(z) = p_0 \cdot e^{-\alpha z} \quad \textit{Equation 3}$$

where p is the acoustic pressure, p_0 is the acoustic pressure at penetration depth z = 0, and α is the frequency dependent attenuation coefficient, expressed in Np · cm^{-1} · MHz. In tissue, the value is approximately comprised between 0.5-1 dB · cm^{-1} · MHz. Attenuation is therefore more pronounced at higher frequencies, which explains why lower frequencies are used in treatment across the skull. Table 3 provides a summary of the attenuation of tissues, which are commonly expressed in dB / cm. One decibel approximately equals 0.115129255 Nepers.

Table 3 - Summary of attenuation constant α for various tissues. Adapted from Azhari, Basics of Biomedical Ultrasound.[80]

Tissue	α [dB/cm] @ 1 MHz
Water	0.002
Blood	0.15
Fat	0.6
Muscle (average along and across the fibres)	2.3
Bone	2-20

1.3.2 Ultrasound contrast agents

Microbubbles consist of a 1-10 μm inert gas core enclosed by a protein, polymer, or lipid shell to stabilise the inert gas core in physiological conditions and slow down gas diffusion (Figure 4). Microbubble are usually injected through a constant infusion spanning several minutes, or through a bolus injection; however, there is no consensus on what constitutes an ideal microbubble dose. Claudon et al.[81] provide guidelines for the administration of microbubbles in contrast enhanced ultrasound. In the case of SonoVue® (Bracco, Italy), the UCA is injected intravenously as a bolus of 1-2 mL (up to 4.8 mL) followed by 10 mL injection of saline. Considering a microbubble concentration between 100 and 500 million per mL[82] and a dilution in 5 litres of blood, this yields a concentration of $5x10^5$ microbubbles/mL. The microbubbles are cleared by the liver and the gas exhaled through the lungs with an elimination half-life of approximately 6 minutes[82].

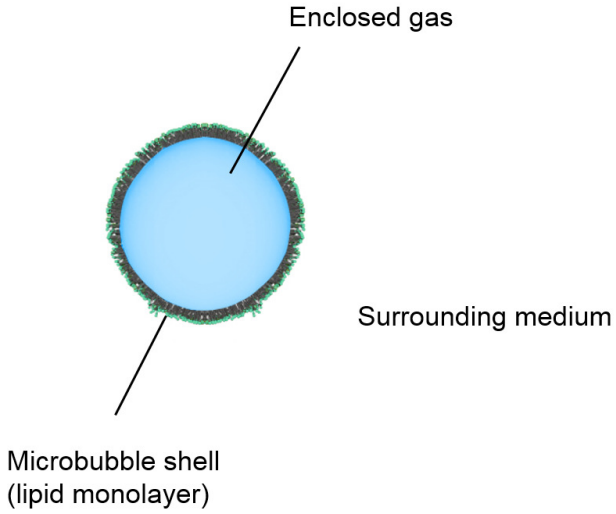


Figure 4 - Schematic of a coated microbubble indicating the shell coating, the enclosed gas and the surrounding medium

The shell material composition, thickness, charge, and incorporated ligands can be tailored to suit specific applications. The most common microbubble shells are composed of proteins, polymers, and lipids. Protein microbubbles, such as Albunex® and Optison™, have a relatively stiff shell, making them long-lived; however, they are prone to irreversible rupture upon exceeding a threshold expansion ratio. Polymer microbubbles exhibit the highest shell stiffness among all shell materials, yet this limits their echogenicity.

Phospholipid shells offer the best compromise between stability and echogenicity, while providing an ideal scaffold for ligand binding. The phospholipid shells also have the added benefits of biocompatibility and dye affinity. Moreover, the stability and circulation time may be further improved by incorporating polyethylene glycol (PEG) chains of varying length within the shell, which act as steric brushes protecting the microbubble. This further reduces protein absorption and microbubble aggregation. However, the reduction in immunogenicity of particles coated with PEG *in vivo*[83] is subject to debate, as there is an increasing body of evidence[84,85] that emphasises the presence of antibodies produced by the immune system that recognise and bind to PEG, potentially limiting the therapeutic efficacy of the coated carrier.

Both polymer and protein microbubbles have the ability to encapsulate payload within their shell, nonetheless, the therapeutic load will be orders of magnitude lower than those administered through co-injection[86].

Table 4 – Microbubble shell composition, thickness, stability, and drug payload and ultrasound effects. Adapted from Sirsi et al.[86]

Shell type	Thickness	Stability	Drug payload	Ultrasound effects
Protein	15-20 nm	Medium	Medium	High echogenicity; shell does not reseal after rupture
Lipid	3 nm	Low-medium	Low-medium	High echogenicity; shell reseals after rupture
Polymer	100 – 200 nm	High	High	Low echogenicity; shell does not reseal after rupture

Table 4 summarises the microbubble properties, highlighting the correlation between thickness and echogenicity. For thicker shells, the compliance of the microbubble decreases, inhibiting the ability to adsorb and reradiate the incident ultrasound waves, hence reducing echogenicity.

Currently, three UCAs are approved by the FDA for intravascular administration[87]. Optison™ (albumin shell, octafluoropropane gas core), Definity® (lipid shell, octoafluoropropane gas core) are only approved for electrocardiography and off-label in the abdomen. SonoVue® (lipid shell, sulphur hexafluoride gas core), also known as Lumason® in the U.S., was approved for the first time for specific non-cardiac uses in 2016. Outside the US, specifically in the Asia, Europe, and Canada, SonoVue® was approved in the early 2000s and its use is supported by widely accepted

guidelines, as published by the European federation of societies for ultrasound in medicine and biology.[81] In Japan, Sonazoid (lipid shell, perfluorobutane gas core) is approved for liver imaging, but is not FDA approved.[87]

1.3.3 Microbubble cavitation

The term *cavitation* describes the formation and dynamics of gas and/or vapour filled bubbles. When exposed to an ultrasound field, the pressure inside the bubble oscillates between positive and negative cycles, causing the enlargement and shrinkage of the bubble. The nature of the bubble response depends on the its size and coating properties, as well as the ultrasound field's frequency, acoustic pressure, duty cycle, and pulse repetition frequency.

At very small excitation pressures, a bubble oscillates linearly and symmetrically (Figure 5). In this scenario, the bubble re-radiates acoustic energy in the form of acoustic emissions at the frequency at which it is being driven. At higher acoustic pressures, the oscillations become increasingly non-symmetrical, leading to harmonic, sub-harmonic, and ultra-harmonic emissions. When the pressure amplitude is increased even further, the bubble pressure is no longer able to withstand the inertia of the surrounding fluid, leading to the violent collapse of the microbubble, which is associated with a broadband acoustic spectra.

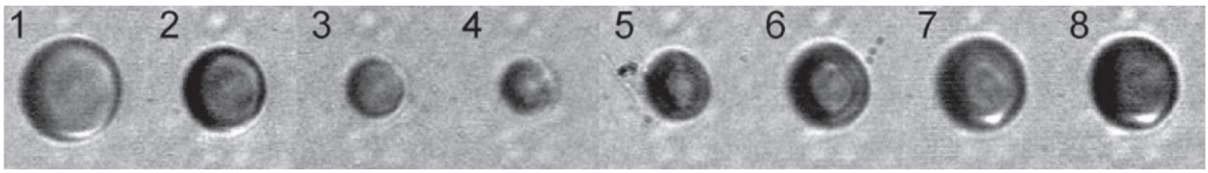


Figure 5 - Optical images of the bubble during 2 cycles of the ultrasound pulse in a cellulose tube. Top panels show top view images at an interframe time of 138 ns. Ultrasound parameters were 1 MHz, 140 kPa peak negative pressure. Adapted from Vos et al.[88]

The dynamic behaviour of bubbles is a multivariate continuum, making classification challenging and controversial. Studies have attempted to classify cavitation by their radial excursion and emission signatures, however, in many cases these definitions overlap. Throughout the thesis, prolonged cavitation that is dominated by the gas pressure of the microbubble core is termed *non-inertial*, whilst regimes in which the fluid inertia dominates over the microbubble gas pressure will be referred to as *inertial* cavitation[89]. At the frequencies and acoustic pressures used throughout this thesis, unless otherwise stated, the microbubble behaviour is expected to be non-inertial.

The equation that describes the radial oscillation of a single spherical adiabatic ideal-gas bubble, with an infinitely thin and linear viscoelastic coating, in an infinite volume of Newtonian non-compressible fluid, subject to an ultrasound field whose wavelength is much greater than the bubble diameter, is the Rayleigh-Plesset equation (RP):

$$\rho_L \left(\ddot{r}r + \frac{3\dot{r}^2}{2} \right) = p_0 \left[\left(\frac{r_0}{r} \right)^{3\kappa} - 1 \right] - p(t) - \frac{12\mu_c r_0^2 \dot{r}}{r^4} - \frac{12G_c r_0^2}{r^3} \left(1 - \frac{r_0}{r} \right) - \frac{4\mu_L \dot{r}}{r}$$

Equation 4

Here, ρ_L is the density of the fluid, r is the bubble radius, p_0 is the hydrostatic pressure, r_0 is the initial microbubble radius, κ is the polytropic constant of the gas, $p(t)$ is the driving frequency, μ_c is the viscosity and G_c is the elasticity coefficient of the bubble coating, and μ_L is the viscosity of the fluid. The equation assumes the density of the gas to be much smaller than the density of surrounding fluid, a uniform pressure within the bubble, and a constant gas content.

At low acoustic pressures, the RP equation can be linearised and expressed as a second order linear differential equation[90,91]:

$$m\ddot{z} + b\dot{z} + kz = F(t) \qquad \textit{Equation 5}$$

where m represents the inertia of the surrounding fluid, b represents the damping from viscous and radiation losses, k represents the elastic component of the gas, z represents the radial excursion of the bubble, and $F(t)$ represents the incident acoustic pressure.

$$m = \rho_L r_0^2 \qquad \textit{Equation 6}$$

$$b = 4\mu_L + \frac{12\mu_s}{r_0} \qquad \textit{Equation 7}$$

$$k = 3\kappa p_0 + \frac{12G_s}{r_0} \qquad \textit{Equation 8}$$

It follows when the equation is written in its singular form, the natural frequency of the system (ω_n) can be inferred.

$$\ddot{r} + 2b\dot{r} + \omega_n^2 = \frac{F(t)}{m} \qquad \textit{Equation 9}$$

Therefore, the natural frequency of bubble is the square root of the ratio between the elastic and viscous forces acting on it.

$$\omega_0 = \sqrt{\frac{k_{\text{eff}}}{m_{\text{eff}}}} = \sqrt{\frac{3\kappa p_0 + 12G_s}{\rho_L r_0^3}} \qquad \textit{Equation 10}$$

1.3.4 Acoustic radiation force

As an ultrasound wave travels through a medium, it transfers energy to both the medium and any particles within it. The resulting force, which acts along the axis of ultrasound propagation, is known as the primary radiation force[92].

In a standing wave field, which consists of a series of pressure nodes and antinodes fixed in position as the acoustic pressure oscillates in time, particles and bubbles migrate towards the nodes or antinodes depending on their physical and acoustic properties and the frequency of the ultrasound field.

The driving force for this migration is a radiation force *F(r)*. Assuming a particle of volume V at a position r in an ultrasound field with wavelength λ, it can be expressed as[93,94]:

$$F(z) = \frac{\pi}{2\rho_0 c_0^3}\left[\left(1 - \frac{\rho_0 c_0}{\rho c^2}\right) + \frac{6(\rho - \rho_0)}{4\rho + 2\rho_0}\right] V p_0^2 \sin\left(4\pi\frac{z}{\lambda}\right) \qquad \textit{Equation 11}$$

where ρ_0 and c_0 are the sound density and velocity in the medium, while ρ and c are the density and speed of sound in the particle. The acoustophoretic acoustic contrast factor[95] may be used to determine the direction of propagation of a single particle. Particles that are characterised by a positive contrast factor (ϕ>0) migrate towards the pressure node(s), and *vice versa*.

$$\phi = \left(\frac{3(\rho - \rho_0)}{\rho_0 + 2\rho} + \frac{\beta_0 - \beta}{\beta_0}\right) \qquad \textit{Equation 12}$$

where β and β_0 are the compressibility of the medium and particle, respectively.

Particles and microbubbles in the ultrasound beam also scatter the incident ultrasound wave, which in turn also generates an acoustic force on nearby particles and microbubbles, referred to as the secondary radiation force. Secondary radiation force has been shown to cause attraction/repulsion of particles, depending on their physical properties. It is of particular relevance in cavitating microbubble clouds[96], as the attraction and repulsion may cause microbubble aggregation and/or translation.

In microfluidic systems, the effects of acoustic radiation force have been used for a number of applications such as particle trapping[97], cell concentration[98], and food analysis[99]. Through the design of appropriate standing wave fields, the separation of particles based on mechanical properties such as size, shape, density, and compressibility can be achieved. This technique is referred to as acoustophoresis[100].

1.3.5 Acoustic streaming

The attenuation of ultrasound as it propagates through a fluid causes steady flow in the direction of ultrasound propagation known as acoustic, or Eckart, streaming. The effect is associated with acoustic energy gradients which result in Reynolds stresses[101] within the medium of propagation.

Streaming may also occur due to the attenuation of the acoustic wave near fluid boundaries. When a wave encounters a solid boundary comparable or greater in length than a quarter of its acoustic wavelength, the steep velocity gradients perpendicular to the boundary lead to viscous dissipation in the boundary layer.[102]

This leads to the formation of circular vortex patterns that in turn lead to the formation of counter-rotating streams outside the boundary layer. Various studies[102] have reported acoustic streaming within acoustofluidic devices with confined fluid layers. The resulting streaming vortexes, both parallel and perpendicular to the transducer plane[103], however, are not likely to be Eckart streaming driven, due to the small length scales and low driving frequencies.

There is large heterogeneity in acoustic streaming velocities reported in the literature. The wide parameter space, which includes factors such as driving frequency and acoustic pressure, channel geometry, and local acoustic pressure field, limits the merit of direct comparisons. Nonetheless, previous studies have reported acoustophoretic velocities in the order of tens to thousands micrometres per second[103,104].

1.3.6 Cavitation microstreaming

Cavitation microstreaming is the result of cavitation, which leads to fluid flow in the vicinity of cavitating microbubbles. When microbubbles oscillate periodically as a result of an applied ultrasound field, the radial excursions of the microbubble shell transfer momentum to the surrounding fluid, causing localised eddying motion within and outside the microbubble's shell[105]. Cavitation streaming is also characterised by the viscous absorption of the high-frequency components of the re-radiated signal from microbubbles, which are more readily attenuated by the surrounding medium. There have been a few studies attempting to quantify the microstreaming flows in the vicinity of microbubbles, both theoretically and experimentally. The experimental consensus, in agreement with theoretical models, is that cavitating microbubbles, even when driven at acoustic pressure in the order of only tens of Pa, are able to induce flows in the order of hundreds of micrometres per second that extend millimetres away from the bubble.

However, there is wide variation in experimental conditions such as microbubble properties and acoustic field characteristics. Wu et al.[106] estimated the microstreaming flows arising from the cavitation of an uncoated 33 μm microbubble driven at 53 kPa and 100 kHz to be 580 μm/s in the tangential and 450 μm/ in the radial direction. Gormley and Wu[107] used streak velocimetry to estimate the cavitation microstreaming velocity in Albunex microbubbles driven at a pressure amplitude of 0.5 MPa and a frequency of 160 kHz, reporting a velocity range of 50-100 μm/s. Collis et al.[108] used particle image velocimetry to measure the cavitation microstreaming velocity in the proximity of single air bubbles with sizes ranging

from 30-300 μm driven at acoustic frequencies of 28 or 40 kHz, reporting velocities up to 680 μm/s (Figure 6). Tho et al.[109] analysed the microstreaming flows around bubbles of sizes between 232 and 250 μm excited at frequencies ranging from 2.4-13 kHz, also reporting streaming velocities of hundreds of micrometres per second. The cavitation streaming velocities of ultrasound responsive agents is explored in Chapter III, 3.4.2 of this thesis.

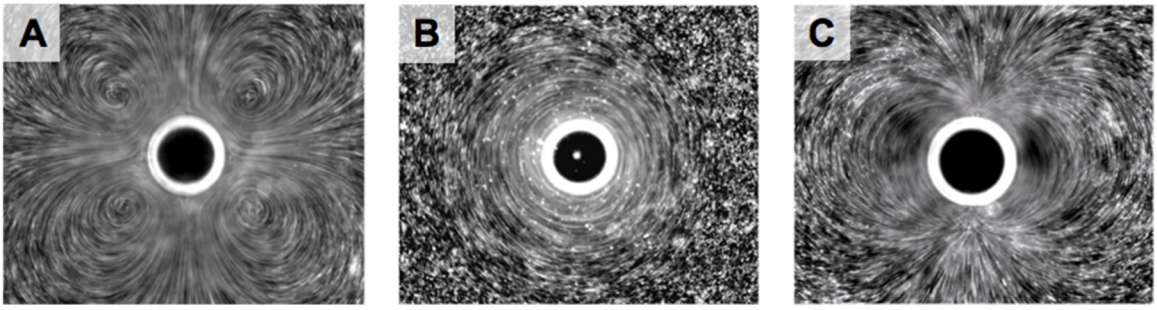


Figure 6 - A. Quadrupole microstreaming pattern created by linear translation of a 232 μm radius bubble attached to a horizontal surface and exposed to 2.422 kHz US; B. Circular vortex microstreaming pattern created by circular translation of a 224 μm radius bubble on surface driven at 1.188 kHz; C. Dipole microstreaming pattern created by radial oscillation of a 267 μm radius bubble on surface forced at 8.658 kHz. Adapted from Collis et al.[108]

The mechanical properties of the rigid boundary can affect the microbubble dynamics and associated microstreaming patterns. De Jong et al.[91] studied the influence of a nearby wall on the dynamics of bubble cavitation, showing asymmetrical vibrations in the plane normal to the boundary. The asymmetric vibration and the resulting surface waves are likely to have an influence on the direction, magnitude, and frequency spectrum of the re-radiated waves, thereby affecting the microstreaming flows contiguous to the bubble. These effects are particularly relevant in *in vivo* applications, where the compliant vessel wall has been shown have an effect on the resonant frequency and dynamics of microbubbles[110]. Cavitation in compliant walls has been studied numerically[111,112], with direct observation in capillaries *ex vivo* [113–115].

The fluid flow generated by cavitation microstreaming has been hypothesised to be a contributing cause of cell membrane poration. Wu et al.[116] investigated the role of cavitation microstreaming by attaching a PZT transducer to a Mason horn in order to induce

microstreaming-like flow in a suspension of Jurkat cells. Through experimental observations and numerical models, it was determined that the threshold shear stress required to porate cells was 12 Pa; however, this value has not been supported by other studies[117].

1.4 Bioeffects of ultrasound

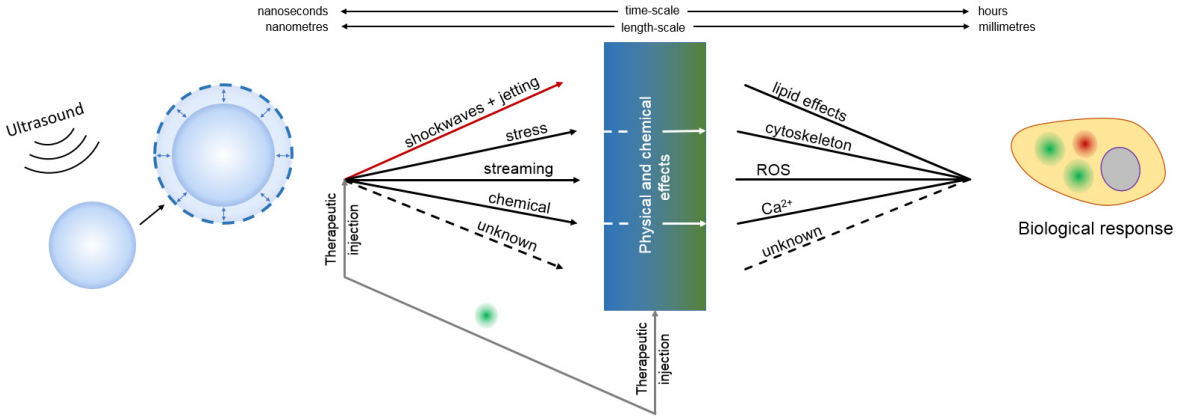


Figure 7 – Illustrative schematic of the biological effects resulting from exposure to cavitating microbubbles. The length and time scales over which these effects occur are also indicated on the diagram. The red arrows indicate effects that are not expected in the exposure conditions used throughout this thesis. Adapted from De Jong et al.[91]

1.4.1 Physical

The mechanical perturbations caused by non-inertially cavitating microbubbles on tissue have been shown to cause distinct physical effects, which include primary and secondary acoustic radiation forces[118], mechanical stresses imparted by the radial vibration of microbubble shells[119], and fluid shear stress associated with cavitation microstreaming[120].

Primary acoustic radiation forces are responsible for the translation of microbubbles in the direction of ultrasound propagation, thereby decreasing the distance between the endothelium and the cavitation source. This effect has been shown to amplify the effects of cavitation activity[118], as the push-pull action of microbubbles occurs in closer proximity to the cell membrane. The mechanical stress caused by the microbubble's radial excursions on the cell membrane have been linked to disparate effects, including changes in membrane potential[121], permeabilisation[122], and modifications in the cytoskeletal organisation[123,124].

In addition, stresses imparted by cavitating microbubbles are capable of opening pores up to hundreds of nanometers in diameter which reseal in the order of tens of seconds[125]. The ability of microbubbles to transiently induce pores within the cell membrane without

compromising viability is one of the most clinically attractive effects, as it provides therapeutic access to previously impenetrable targets. However, sonoporation studies are plagued with low delivery efficiency and variable therapeutic outcomes[126], prompting further mechanistic studies on the underlying mechanisms. A large number of sonoporation studies[127–131] have demonstrated the uptake of fluorescently labelled impermeant molecules of various sizes, as well as the uptake of large nanoparticles (>100 nm[132]), by the stimulation of clathrin-mediated endocytosis. In addition, small compounds such as calcium ions have been shown to be internalised *via* the mechanical stimulation of ion channels, resulting in the triggering of a cascade of downstream bioeffects such as signaling, membrane blebbing[133], and exocytosis.[134] The streaming flows resulting from microbubble oscillation can also impose significant fluid shear stress on the surrounding biological tissue, up to several hundreds of micrometers away from the cavitation source (Chapter III). This effect has been shown to enhance drug transport and delivery of conventional systemic therapies in tissue and across the cellular membrane.[135] Cavitation microstreaming is also often associated with sonoporation, despite the limited evidence that fluid shear stress is able to create pores within the cell membrane without causing cell death[136,137]. The flow set up by cavitation microstreaming has also been shown to be responsible for secondary effects such as endothelial cell membrane fluidisation[5–27] (Chapter III). In addition, cavitation microstreaming at low acoustic pressure was shown to attract, repel, deform, and rupture suspended phospholipid lipid vesicles (employed as cell models)[138].

1.4.2 Chemical

Relatively recently, chemical interactions have also been shown to play an important role in sonoporation. Various *in vitro* studies have reported material transfer from microbubble shells to cell membranes in the presence and absence of cavitation[139,140], leading to the fusion and internalisation of exogenous lipid species. The alteration of plasma membrane properties may potentially lead to undesired anomalies in fundamental cellular processes, such as signaling[141]

and endocytosis[142]. On the other hand, the effect could potentially be exploited as a targeting and delivery mechanism for lipid-conjugated therapeutics.

The generation of free radicals such as reactive oxygen species (ROS) has also been reported as a potential mechanism for sonoporation. It has been shown that ROS modulate the intracellular Ca^{2+} balance and trigger membrane lipid peroxidation[73], which in turn leads to membrane disruption and poration[143].

A promising new treatment strategy involves the use of microbubbles to carry and deliver oxygen to hypoxic tumours such as pancreatic cancer[144]. By increasing tissue oxygenation, it has been shown that the tumours respond more readily to treatments such as photo/sonodynamic therapy and radiation, following the formation of reactive oxygen species.

1.4.3 Thermal

The viscous absorption of acoustic energy produces a heating effect. The extent to which heating is produced *in vivo* will depend on exposure parameters such microbubble concentration, frequency, acoustic pressure, repetition frequency, duty cycle, and microbubble proximity to blood vessels. In the studies presented in this thesis, however, due to the low US frequency coupled with comparatively low acoustic pressures, thermal effects have not been considered. Thermal effects, however, play a more prominent role in hyperthermia-mediated ultrasound treatment and sensitisation.

1.5 Research challenges

The adoption of ultrasound contrast agents used in ultrasound imaging for therapeutic applications is an active field of research. The prospect of enhancing and targeting therapeutic delivery deep inside the body non-invasively holds great promise in improving the efficacy of treatment of several conditions. However, despite the extensive body of *in vitro* and *in vivo* studies, the underlying biophysical mechanisms remain elusive.

The complex behaviour of microbubbles subject to ultrasound, coupled with the complexity of biological tissues, and the broad spatial and temporal scales over which effects occur, make experimental investigations extremely challenging. In practice, the complications relate to recreating a well-defined and spatially uniform acoustic field in physiologically relevant dimensional confinement; as well as isolating, visualising, and quantifying cell-microbubble interactions *in situ* controllably and in real time.

Moreover, the quantity and variety of the interactive elements that compose a living cell – such as the constituents of the plasma membrane, intracellular organelles, and an abundance of biochemical reactions – impede the disassociation of individual effects of microbubbles on biological tissue. Thus, there exists a trade-off between increasing experimental complexity to better mimic physiological conditions, and the ease at which variables can be controlled, visualised, and quantified.

It is therefore desirable to integrate various measurement techniques within a single *in vitro* platform that allows high throughput mechanistic investigations of the mechanisms involved in microbubble-based treatment. A multidisciplinary approach involving *in vitro* and *in vivo* testing will enable the characterisation of the effects of microbubble-based treatment, allowing the potential development efficient and effective protocols to widen the impact in the clinic.

1.6 Approach

The complex and multifactorial nature of cell-microbubble interactions calls for simpler experimental approaches that allow the isolation, observation, and measurement of the underlying phenomena. To accomplish this in the work reported in the subsequent chapters, an experimental platform that allows repeatable high-throughput sample exposure to a known ultrasound field, while enabling real time non-invasive monitoring, was developed. Second, the complex cellular structures were replaced by a minimal cell model to study the individual biological effects of ultrasound and microbubble exposure.

Current ultrasound exposure systems rely on the custom integration of commercial analytical and optical instrumentation with water-tank based ultrasound stimulation rigs. These configurations pose significant practical challenges, which limit large-scale study of biological samples. This creates the necessity to develop an experimental platform able to produce an ultrasound field at therapeutic frequencies and pressures, that is compatible with high magnification fluorescence and quantitative microscopy, and that allows acoustic monitoring of acoustic emissions. To allow high throughput mechanistic studies, the device also needs to be simple to operate, economical, and reusable; and allow the injection and extraction of material for analysis. The design and characterisation of a device that meets such criteria is the subject of Chapter III.

The ability to reconstitute fundamental cellular functions in a minimal cell model would allow the study of specific parameters independently from active cell functions. The plasma membrane is a complex patchwork of heterogeneous lipid species and proteins, as shown in Figure 8a. Lipids are the most abundant molecule by number, and can be divided into three major categories: phospholipids, glycolipids, and cholesterol. Cholesterol and phospholipids are the most common, and can be found in similar numbers within the membrane. The plasma membrane is also rich in proteins, which account for 50% of the weight[145]. Proteins are embedded within the 5 nm thick lipid bilayer, and execute important functions such as ion

balancing[146], signaling[147], and ion transport[148]. The components of the plasma membrane are highly dynamic as they laterally diffuse and rearrange along the contours of the cell membrane, which effectively acts as a two dimensional fluid surface, as first described by Singer and Nicholson[149].

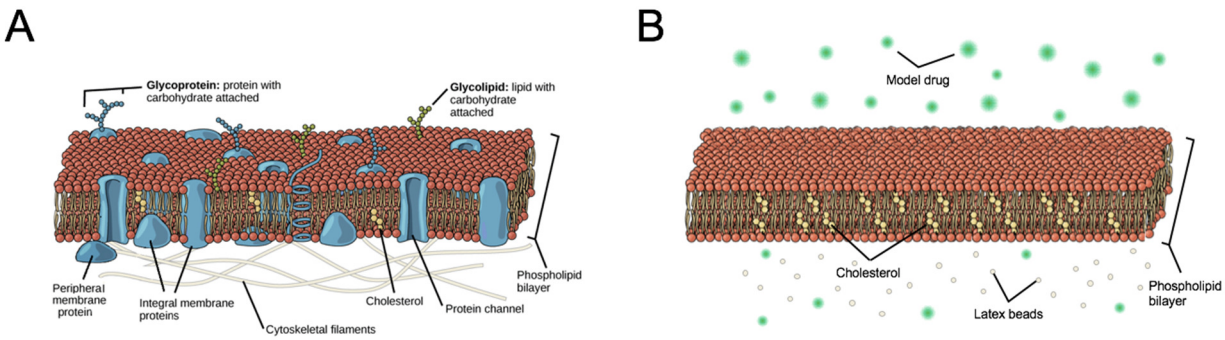


Figure 8 - Lipid membranes diagram. A. Mammalian cell plasma membrane, including membrane components and cytoskeletal filaments. B. Single phospholipid bilayer model including the illustration of a model drug and encapsulated beads for flow tracing. Adapted from Khan et al.[150]

Investigating the effects of microbubble exposure on singular cell elements, such as plasma membrane phospholipids and the intracellular milieu, would be effective in aiding the understanding of the fundamental mechanisms that underpin cell-microbubble interactions. Indeed, a cellular model that can be tuned with specific phospholipids, cholesterol, proteins, cytoskeleton, and encapsulated solutions would be an ideal investigative tool.

The use of cellular models to understand biological phenomena is a growing field within the biophysical community[151]. The spherical and invariant shape of membrane models such as giant unilamellar vesicles (GUVs) allows the non-invasive observation and quantification of biophysical processes in a cell-free environment.

GUVs are the most prevalent model for such biomimetic studies, as they provide a suitable platform for investigating cell membrane behaviour.[152] They have been used as a model to study fluid-fluid and gel-fluid phase coexistence in lipid bilayers[153–156], membrane transport phenomena,[157–160] and as erythrocyte models[161]. Also referred to as giant liposomes, GUVs are cell-sized (1-100 μm[162]) lipid pouches that consist of a spherical phospholipid bilayer and an

encapsulated fluid solution. Vesicles may also be produced to enclose particles within their lumen[163]. Their fabrication protocols are relatively simple, however, the high cost of platinum limits large scale experimentation. Chapter III describes a novel method of GUV production on stainless steel needles, which can be achieved at a fraction of the cost compared to conventional electroformation techniques.

In the context of drug delivery, vesicles allow the study of the effects of various stimuli on the properties of lipid bilayers, the transport phenomena across their membranes, and the dynamics of the intracellular milieu. Throughout this thesis, vesicles formed with a single species of phospholipid, doped with increasing molar fractions of cholesterol, and containing a sucrose solution with latex beads in suspension, were employed as cell models (Figure 8). DOPC was chosen as a common non-raft biomimetic lipid used in membrane studies as a model for the fluid phases of the plasma membrane. Its bilayer hydration and packing characteristics are comparable to those of natural lipid mixtures such as porcine brain phosphatidylcholine (PC) and bovine liver PC[164]. Cholesterol also plays an important role in modulating the fluidity of the plasma membrane, and is abundant in membrane rafts such as caveolae[165]. A non-ionic solution of sucrose was encapsulated within the vesicles to facilitate formation, maintain osmotic balance, and promote sedimentation in water. More complex vesicles have been formed in physiological solutions to incorporate native membrane lipids[166], proteins[167], and cytoskeletal filaments[168]. Exhaustive surveys on the advancements in the application of GUVs in the study of cell behaviour were conducted by Fenz et al.[162] and Schwille et al.[169]

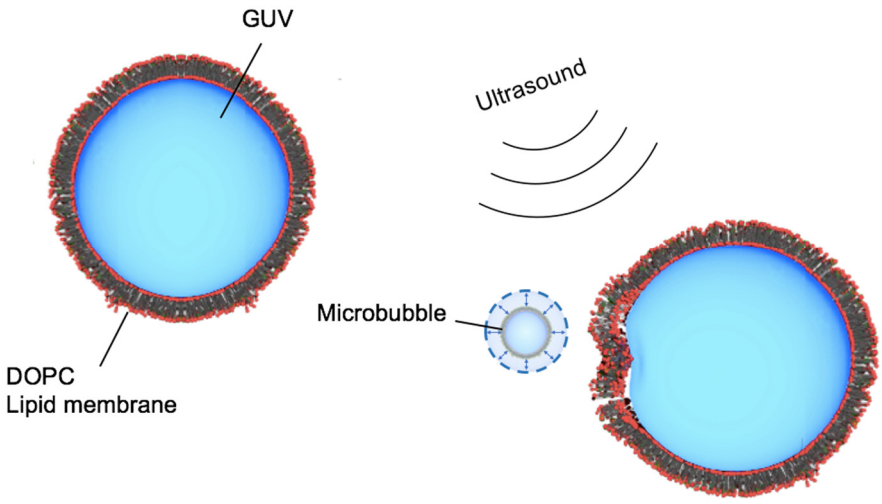


Figure 9 - Experimental approach used throughout the thesis. The diagram shows an unperturbed GUV, which includes a DOPC phospholipid membrane and an encapsulated sucrose solution. On the right, the GUV membrane is disrupted by the cavitation of a nearby microbubble in an ultrasound field.

The minimal model studied in this thesis, shown in Figure 9, represents the early building block of a series of potential experiments to elucidate the complex mechanisms involved in microbubble-cell interactions using giant vesicles. Throughout this thesis, reference to three distinct regions will be made when describing GUVs: the inner core, the lipid bilayer, and the external environment. These regions will be referred to as intravesicular, membrane and extravesicular, respectively.

1.6.1 Advanced microscopy techniques

The challenges associated with probing the lipid membrane nano-environment, and quantifying the membrane property changes resulting from exposure to different stimuli, may be addressed through the use of advanced microscopy techniques such as spectral imaging[170]. Through the incorporation of environment-sensitive fluorophores with an emission spectrum that changes depending on the phase-state of the membrane, the properties of the membrane can be inferred optically through the use of appropriate image processing techniques[171]. Novel fluorophores have been developed that are able to sense the chemical[172], physical[173], and

electrical[174] properties of lipid membranes at the sub-micron scales. However, finding direct relationships between the emission characteristics and the physical properties of the membrane is inherently challenging due to the concurrent interaction of dye and membrane specific properties. Studies have also shown that the characteristics of the external environment such as polarity[175] and viscosity[73] also affect the emission spectrum of environment sensitive probes.

Advanced microscopy techniques such as fluorescence lifetime microscopy (FLIM)[176] and fluorescence correlation spectroscopy (FCS)[177] are increasingly used to quantify the mechanical properties of model and plasma[178,179] membranes. Quantities such as viscosity and diffusion coefficient can be determined optically by analysing the fluorescence intensity, lifetime, and spectral changes in time. In the experiments presented in this thesis, a technique based on spectral imaging and the calculation of generalised polarisation (GP)[180] will be employed to determine the degree of membrane packing and hydration of giant unilamellar vesicles.

1.6.2 Lipid packing and hydration

For many years the measurements of membrane properties using membrane dyes were carried out in cuvette spectrophotometers, which only allowed to infer membrane properties through bulk measurements. Recent advances[181] in microscopy techniques and versatile spectral detectors that allow the entire emission spectrum of a fluorophore to be captured from a single image, have allowed pixel-based analysis of membrane properties up to the optical diffraction limit.

Membrane hydration has been used in the past as a proxy to quantify the degree of lipid packing in plasma and membrane bilayers[181]. The emission spectrum of Laurdan and its derivatives (i.e. c-Laurdan), a lipophilic environment-sensitive fluorescent probe, varies as a function of the dipolar relaxation of water, which is related to the level of hydration and order

of its surrounding microenvironment. Generalised Polarisation (GP)[182] was employed in this thesis as a relative measure to quantify lipid packing.

1.6.3 Spectral imaging

Spectral imaging involves the analysis of the emission characteristics of a fluorophore. Exciting the molecular probe at its excitation wavelength and measuring the emission intensity as a function of 25 wavelengths reveals information on the membrane properties not apparent in single wavelength detection.

Laurdan, for example, is a polarity sensitive molecular probe that is commonly used to determine the structural properties of phospholipid and cell membranes. The lipophilic moiety of the molecule resides within the hydrophobic section of the bilayer, shown in Figure 10a, which restricts the probe's rotational and translational ability, as shown in Figure 10c. The degree at which this occurs is related to the hydration of the membrane. When the membrane is more hydrated and more fluid, the dye is able to rotate freely, affecting its emission characteristics.

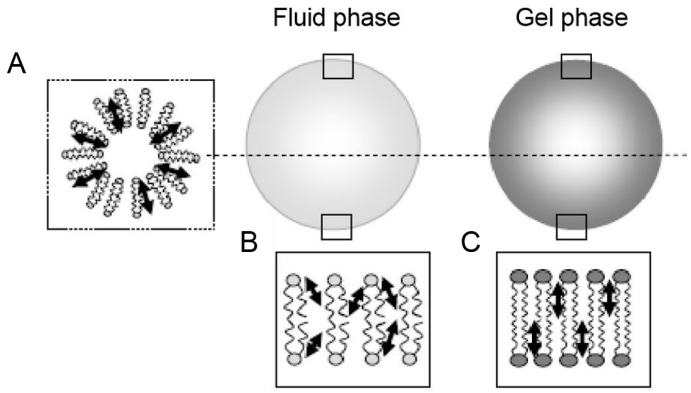


Figure 10 - A. Laurdan intercalates in the lipid bilayer. B. Membrane in the fluid phase that allows the rotational movement of the Laurdan molecule B. Membrane in the gel phase that restricts the rotational movement of the Laurdan molecule. Adapted from Sanchez et al.[181]

1.6.4 Generalised polarisation

The emission spectrum of c-Laurdan, a modified version of Laurdan with superior photostability, shifts as a function of the dipolar water relaxation, and thus the level of hydration within its surrounding microenvironment, which in turn is indicative of lipid packing in membranes. Generalised Polarisation (GP)[183] is employed as a relative measure of lipid packing on a scale of -1 to 1, where -1 represents the least packed and 1 represents the most packed membrane.

Equation 13 describes the GP relative to the intensities at two specific wavelengths of the emission spectrum of c-Laurdan: 440 (I_{440}) and 490nm (I_{490}) when excited with a 405 nm laser.

$$GP = \frac{I_{440} - I_{490}}{I_{440} + I_{490}} \qquad \textit{Equation 13}$$

Figure 11 shows the steps taken in order to determine the GP from a given sample. This method was employed in Chapter II to validate the properties of phospholipid membranes fabricated with a novel electroformation technique, and in Chapter III to probe the changes in membrane characteristics when exposed to therapeutically relevant exposure conditions.

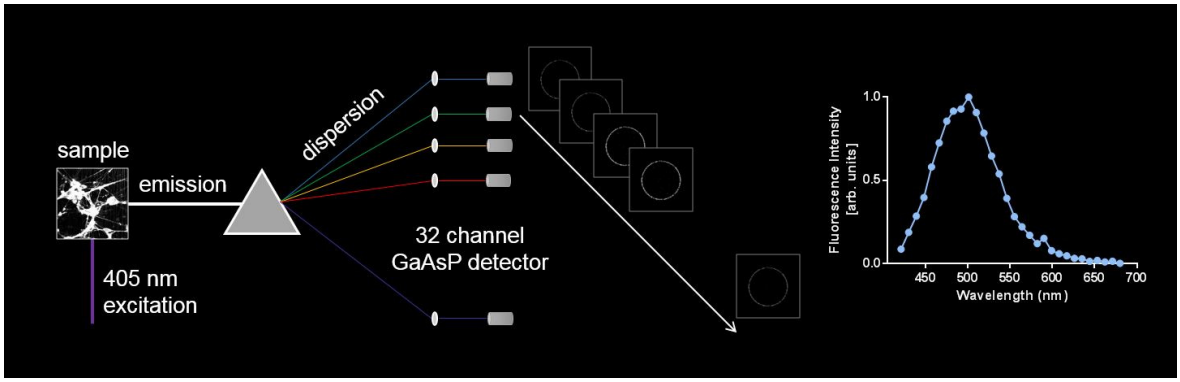


Figure 11 - Determination of GP maps from a given samples of cells or vesicles. First, the sample is illuminated using a 405 nm laser. Second, the collected fluorescent emission signal is dispersed into several parallel detectors of a 32-channel GaAsp detector. The intensities of the emission at 440 and 490 nm are then collected, averaged and used in conjunction with Equation 13 to determine the GP on a pixel-by-pixel basis. Finally, a typical emission spectrum for DOPC vesicles stained with c-Laurdan and excited with a 405 nm laser is shown. Adapted with permission from Sezgin et al.[182]

1.7 Thesis aims and objectives

The overall purpose of this thesis was to use giant unilamellar vesicles as cell models to isolate and quantify the effects of ultrasound and microbubble exposures on the properties phospholipid membranes and the dynamics of their intravesicular milieu. To achieve this, the following aims and objectives were set:

1. To design and manufacture a device able to produce model cells, thus enabling the isolation, characterisation, and quantification of key membrane and intracellular effects. This involves:
    (a) Designing a facile, cost-effective, and high-throughput rig that enables the production of defect-free and cell-sized lipid vesicles with tuneable membrane properties.
    (b) Establishing that the formed vesicles have comparable properties to those produced in state-of-the-art methods.
2. To design and characterise a device that allows the quantitative investigation of microbubble cavitation effects on biological and model membranes using fluorescence microscopy. This involves:
    (a) Designing and manufacturing a microscope-compatible device that allows high-magnification using oil-immersion objectives.
    (b) Optimising parameters to enable the generation of a uniform, reproducible, and tuneable ultrasound field.
    (c) Characterising the acoustic and thermal properties of the device such as the acoustic pressure, temperature of the piezoelectric chip, and compatibility with biological samples.

(d) Systematically investigating the device's applications, which include the study of ultrasound responsive agents, microbubble streaming patterns, and the interactions between microbubbles and cell models.

3. To determine the effect of microbubble-based ultrasound treatments on the molecular arrangement and permeability of model membranes containing cholesterol. This involves:

   (a) Characterising the properties of vesicles and microbubbles prior to the application of excitation.

   (b) Defining and applying therapeutically relevant exposure regimes.

   (c) Quantifying changes in vesicle membrane hydration using GP, as a result of exposure.

   (d) Determining the resulting changes in permeability of the vesicles by monitoring the uptake of a model drug using time-series single-vesicle fluorescent measurements.

4. To explore the effects of ultrasound in the intracellular milieu using giant vesicles as cell models. This involves:

   (a) Establishing a model for the analysis of intracellular streaming.

   (b) Visualising and quantifying the intracellular flows within giant unilamellar vesicles as a result of microbubble-based ultrasound treatments.

   (c) Establishing a method that can be used to extend the analysis to mammalian cells.

1.8 Thesis outline

Chapter I provides the context and motivation for the research, states the aims, and provides the background for the thesis. In Chapter II, a novel technique to produce giant unilamellar vesicles in a cost-effective, reproducible, and scalable manner is presented and characterised. Chapter III provides a detailed account of a novel acoustofluidic device for the optical and acoustic characterisation of cavitation activity, microstreaming flows, and ultrasound induced bioeffects. Chapter IV is composed of two parts. The first focuses on determining the changes in phospholipid membrane hydration and permeability as a result of various therapeutically relevant exposure conditions. The second examines the effect of pressure-driven laminar flow on the uptake of a normally impermeant fluorescent molecule. Chapter V focuses on the effect of therapeutically relevant exposures on the perturbations within the vesicle milieu, as a model for the movement of intracellular organelles. Chapter VI summarises the research findings, provides concluding remarks, and evaluates the limitations of this research.

II

Electroformation of Giant Unilamellar Vesicles on Stainless Steel Electrodes

This chapter provides the methodological framework for the production of biomimetic lipid membrane models employed throughout this thesis. It reports and validates a novel technique for the production of giant unilamellar vesicles using stainless steel electrodes. It also provides a review of the fabrication methods used to form giant unilamellar vesicles and outlines the associated costs, advantages, and disadvantages of each technique.

The assistance of Dr. Luca Baù in performing the NMR experiments and analysis is gratefully acknowledged.

The material discussed in this chapter has been presented in alternate form in:

Pereno, V. et al. Electroformation of Giant Unilamellar Vesicles on Stainless Steel Electrodes. **ACS Omega** 2, 994–1002 (2017)

2.0 Abstract

Giant unilamellar vesicles (GUVs) are well-established model systems for studying membrane structure and dynamics. Electroformation, also referred to as electroswelling, is one of the most prevalent methods for producing GUVs, as it enables modulation of the lipid hydration process to form relatively monodisperse, defect-free vesicles. Currently, however, it is expensive and time-consuming compared with other methods. In this study, it was demonstrated that 1,2-dioleoyl-sn-glycero-3-phosphatidylcholine GUVs can be prepared readily at a fraction of the cost on stainless steel electrodes, such as commercially available syringe needles, without any evidence of lipid oxidation or hydrolysis.

2.1. Introduction

Giant unilamellar vesicles (GUVs), often referred to as giant liposomes, are fluid-filled membranes that offer a useful basic model of a biological cell. GUVs have been widely used as models to study the fluid-fluid and gel-fluid phase coexistence of membrane lipids,[184–189] membrane transport phenomena,[190–195] the behaviour of native membranes,[196–199] the structure of early cells and protocells,[200] and more recently, cell biological activity.[193] In its simplest form a GUV consists of a single amphiphilic lipid bilayer that encloses an aqueous solution.

Among the multitude of production methods developed over several decades,[201–203] lipid film hydration,[204] electroformation,[205] lipid emulsification,[206,207] and microfluidic-based methods such as fluid jetting[208] and hydrodynamic flow focusing[209] are the most widely used. While the vesicle formation literature is rich with established formation protocols, each technique has its own inherent drawbacks and tradeoffs according to the application. The factors that affect the choice of a specific protocol include: technical expertise, the need for specialist equipment, and the degree to which vesicle characteristics need to be tuned. Of the methods cited above, electroformation is one of the most widespread.[201]

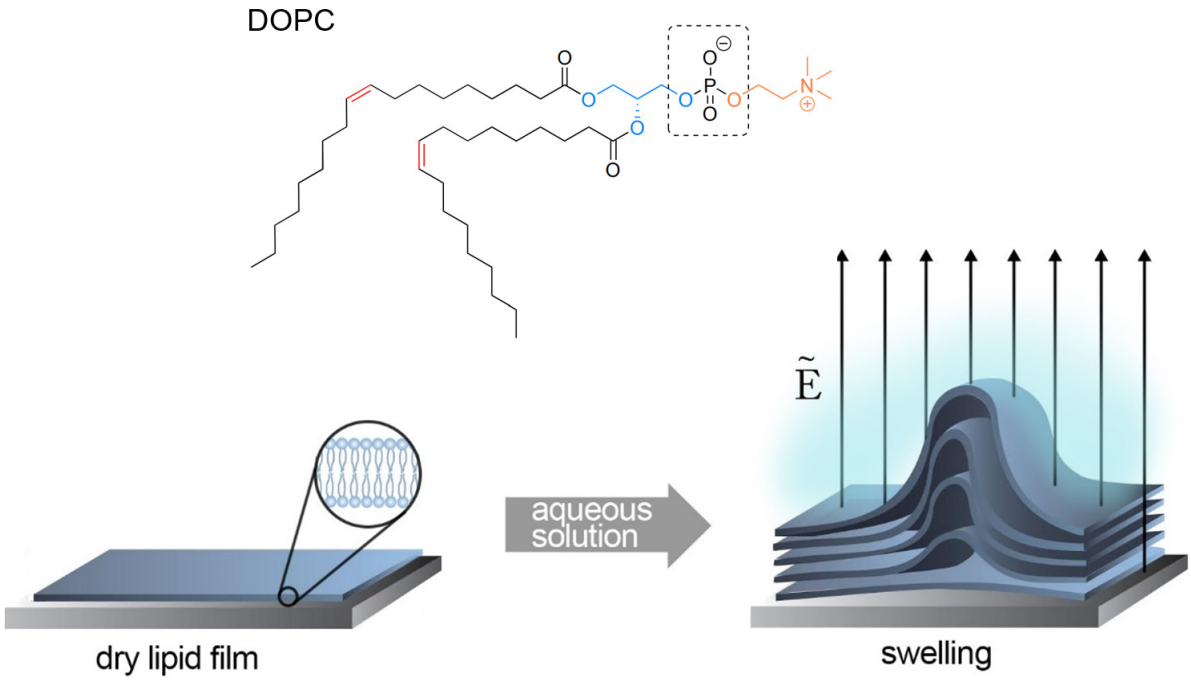


Figure 12 - Schematic of DOPC and vesicle electroformation from a dry lipid bilayer deposited on a substrate. Vesicles are formed upon hydration and application of an alternating electric field, $\tilde{E}$ (not to scale). The top panel shows some relevant moieties of 1,2-dioleoyl-sn-glycero-3-phosphatidylcholine (DOPC): double bonds (red), glycerol (blue), phosphate diester (dashed square) and choline (orange).

Electroformation of GUVs was pioneered by Angelova and Dimitrov in 1986[205]. It involves modulating the spontaneous swelling of lipids within an aqueous solution using an externally applied electric field (Figure 12). Typically, a solution of lipids dissolved in an organic solvent is deposited on two electrodes of indium tin oxide (ITO) coated glass or platinum. Following solvent evaporation, the electrodes are placed in contact with an aqueous solution. Subsequently, an alternating potential difference is applied across the electrodes, stimulating the swelling process of the hydrated lipid layer. However, the exact mechanism of electroformation remains unclear[210]. The mechanisms that contribute to the electroswelling process have been hypothesised to include: i. direct electrostatic interaction between the electrode and lipid headgroups, ii. electro-osmotic mechanical stress, iii. redistribution of double layer counter-ions between bilayers, and iv. decreased surface, membrane, and line tension[211–213]. All of these processes may play a role in the separation of the bilayer from the electrode and its hydration.

The main advantages of electroformation are that it requires comparatively little technical expertise to implement and that it yields spherical, relatively monodisperse, and unilamellar lipid vesicles. Set against this, however, is the cost of the electrodes, which limit the scalability of the technique.

In this chapter, a simple electrode modification in the standard electroformation protocol that reduces cost and chamber preparation time, while improving scalability, is presented and validated. 1,2-dioleoyl-*sn*-glycero-3-phosphatidylcholine (DOPC) was chosen as a representative unsaturated phospholipid, which is more prone to oxidation than saturated phospholipids such as 1,2-distearoyl-*sn*-glycero-3-phosphocholine (DSPC), 1,2-dipalmitoyl-*sn*-glycero-3-phosphocholine (DPPC) and 1,2-dimyristoyl-*sn*-glycero-3-phosphocholine (DMPC), to prove that stainless steel does not affect its structural integrity.
Stainless steel electrodes such as injection needles provide a significantly lower cost alternative to platinum and ITO electrodes, which are the established electrode materials reported in the electroformation literature. Other studies have also reported electroformation of vesicles on interdigitated and non-conductive substrates[214], albeit with limited adoption rates.

Stainless steel electrodes provide numerous advantages. Firstly, the rigidity of stainless steel compared to platinum reduces the risk of bending, improving control over electrode separation distance, thus leading to a more uniform electric field. In addition, disposable needles do not require cleaning in an ultrasound bath,[215] are readily available, and do not require the modification of current chambers.

The wide cost disparity between stainless steel and platinum enables two secondary modifications to the electroformation protocol: the use of longer electrodes and chamber parallelisation.[216] These lead, in turn, to an increase in overall vesicle production, concurrent electroformation and multi-parametric testing at high throughput.
While direct comparison between electroformation methods is complex, Table 1 provides an overview of the merits and drawbacks of different electrode materials used in the

electroformation of vesicles. To populate the table, the electrode surface area was fixed across all methods. The cost comparison was carried out on the face-value of the electrodes, without taking into account the cost of the purpose-built, polyoxymethylene electroformation chamber. A full cost breakdown of the electroformation chamber is provided in Section 2.2.2. It is worthy of note that, if the stainless steel electrodes were disposed of after every electroformation experiment, it would take approximately 292 experiments to match the cost of the platinum electrodes – ignoring overheads such as the time and cost of cleaning.

In the experiments reported here, these features are exploited using a purpose-built electroformation device, which consists of a polyoxymethylene base containing five electroformation chambers and a lid to hold the electrodes in position.

Table 5 - Summary of costs, advantages, and disadvantages of using stainless steel electrodes compared to platinum during electroformation. A detailed cost breakdown of the electroformation chamber is provided in Section 2.2.2. [a] Calculated for five pairs of 40 mm cylindrical electrodes with a diameter of 0.8 mm or an ITO surface of equivalent area (10 cm^2).

	Cost[a]	Disposable	Scalable	Machinable	Cleaning required	Consistent electrode separation
Platinum	~£584	Expensive	Expensive	Yes	Yes	Difficult
Stainless steel	~£2.00	Yes	Yes	Yes	Only if reused	Yes
ITO coated glass	~£27.00	Yes	Yes	No	Yes	Yes

To validate the proposed technique, vesicles were characterised in terms of their size distribution, lipid packing, and unilamellarity of the vesicles' membrane. In addition, the aqueous electroformation solution constituents were analysed using inductively coupled plasma optical emission spectroscopy (ICP-OES) to test whether any ions are released from the electrodes during electroformation. Lipid degradation was assessed by nuclear magnetic resonance (NMR).

2.2. Materials and methods

2.2.1. Electroformation chamber

The electroformation chamber (Figure 13a) is composed of two parts: the electroformation base and the chamber lid. The electroformation base (150 mm x 40 mm x 50 mm) was designed to accommodate five equidistant electroformation chambers with a length of 50 mm and diameter of 10 mm. The extremities of the chambers were tapered to increase vesicle concentration and facilitate collection of the GUVs after production. The electroformation lid (150 mm x 40 mm x 5 mm) consists of five pairs of through-holes (⌀ 1 mm) each aligned with an electroformation chamber and that are used to host the electrodes. On the side of the lid, 3 mm brass screws were positioned in correspondence to each electroformation chamber, in order to hold the electrodes in place once fully screwed. A copper bar (165 mm x 10 mm) ensures an electrical connection between corresponding electrodes. The chamber base and the lid were held together with four 4 mm screws at each corner of the device. The materials' cost of the electroformation device with five electroformation chambers was calculated to be ~£14.00.

A similar device (Figure 13b) was designed with the aim of visualising the vesicle electro-swelling process. The device was designed to be dimensionally compatible with a microscope stage and the working distance of a 40x objective. In this device, the electroformation electrodes were placed horizontally to allow the imaging of the entire electrode surface area. A 170 μm glass slide was coupled with the bottom of the chamber with silicone gel. The electrodes were connected using two sheets of stainless steel, in order to provide a common electrical connection.

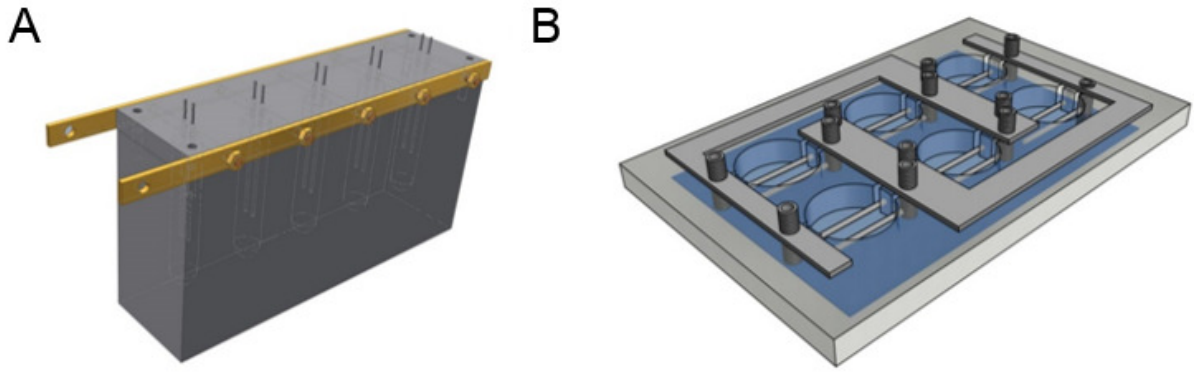


Figure 13- Vesicle electroformation devices for high-yield production and formation visualisation: A. scalable device with five electroformation chambers and needles held by brass screws, B. monitoring device with six chambers, brass screws and stainless steel sheets for electrical connection between common electrodes.

The electroformation chamber was cut from a solid piece of polyoxymethylene purchased from RS Components, UK, brass screws were also supplied by RS Components, UK, and 0.8 mm 21G 50 mm needles were purchased from Becton, Dickinson and Company, USA. 1,2-Dioleoyl-*sn*-glycero-3-phosphatidylcoline (DOPC) was sourced from Avanti Polar Lipids, Inc., USA. Cholesterol, sucrose, 2-[4-(2-hydroxyethyl)piperazin-1-yl]ethanesulfonic acid (HEPES) and bovine serum albumin (BSA) were purchased from Sigma Aldrich, USA. N-(7-Nitrobenz-2-oxa-1,3-diazol-4-yl)-1,2-dihexadecanoyl-*sn*-glycero-3-phosphoethanolamine, triethylammonium salt (NBD-PE) was purchased from ThermoFisher, UK. All reagents were used as received without further purification. The electrodes were connected to an Agilent 33220A signal generator, USA set to high impedance load. GUVs were imaged in a µ-Slide 8 well multi-well plate purchased from Ibidi GmbH, Germany. Ultra-pure water (MilliQ) from a Millipore filtration system (resistivity of >18.2 MΩ·cm) was used throughout all experiments.

2.2.2. Material cost

The cost of the Pt wires was calculated from the price of two 200 mm ⌀0.8mm electrodes from Goodfellow, UK obtained on 22 October 2014 (£292). The cost of the injection needles was calculated on 8* 21G 50mm ⌀0.8mm needles from Becton, Dickinson and Company, UK. The

price of ITO covered glass electrodes was calculated on an equivalent surface area of 8 needles, using the price of ITO square glass slides (~25 mm x 25 mm) from Sigma-Aldrich, UK.
The following table details the full cost breakdown of the custom-built electroformation chamber used in the experiments.

Table 6 - Cost breakdown details on the items, materials and costs of the components of the electroformation chamber. Prices were obtained 14/12/2016.

Item	Manufacturer	Price per item	Total price (£)
Delrin block	theplasticshop	9.75	9.75
Brass screws	RS Components	0.116	2.08
Brass nut	Westfield Fasteners	0.0058	1.04
Brass sheet	Macc Models	0.408	0.816
Total cost of electroformation chamber (£)			13.69

2.2.3. Electroformation protocol

The electroformation protocol consisted of preparing solutions of DOPC (1 mg/mL in chloroform) and cholesterol (10 mg/mL in chloroform) at a range of molar ratios between 1:0 and 1:3. The electrodes were rinsed in toluene and wiped using Kimwipes (Kimberly-Clark Professional, USA) to remove any traces of silicon lubricant. The lipid solution was then pipetted vertically onto the electrodes (50 µL per electrode pair) using a glass syringe, carefully coating the entire surface. After a drying phase of approximately 1 hr, the electroformation chamber was filled with sucrose solution (~3 mL, 200 mM sucrose in deionised water at room temperature), the electrodes were submerged, and the signal generator was connected via the brass screws on the sides of the chamber.

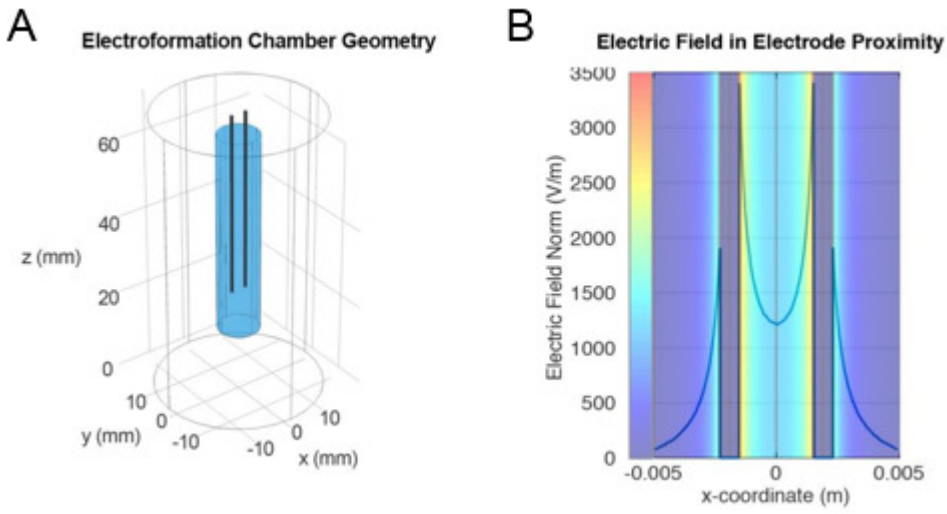


Figure 14 - Electroformation chamber characterisation A. shows the simulation geometry with emphasis on the sucrose-filled chamber (b) electric field along a cross section of the wires at z = 30mm. B. electric potential along a cross section of the wires at z = 30mm.

A 5 Vpp, 10 Hz sinusoidal excitation was applied for 2 hrs to induce repetitive stress on the hydrated lipid bilayer, leading to vesicle swelling. The effective voltage on the electroformation chamber was recorded using a high voltage probe and oscilloscope as 4.87 Vpp, indicating a 0.13 Vpp voltage difference due to an unmatched load of the signal generator. Subsequently, the frequency of the excitation was lowered to 5 Hz for 30 minutes to facilitate vesicle detachment. The electroformation parameters used in the protocol are summarised in Table 3. At the end of the electroformation process, the lid of the chamber was removed and the vesicles were slowly pipetted into a visualisation well using a 100-1000 µl pipette tip. To minimise the shear stress at the orifice, the end of pipette tip was cut by 2 mm using a pair of scissors. The same protocol was used for both SS304 and platinum electrodes.

Table 7 - Electroformation signal generator parameters for giant unilamellar vesicle formation

Electroformation Phase	**Parameters**		**Time (min)**
	Voltage (Vpp)	*Frequency (Hz)*	
I	5	10	120
II	5	5	30

2.2.4. GUV detection and sizing

The GUVs were imaged by phase-contrast microscopy using a Nikon ECLIPSE Ti inverted microscope (Nikon Corporation, Japan) and images were then processed using a purpose-built MATLAB® routine. The algorithm detects the GUVs based on the imfindcircles built-in MATLAB® function, calculates their diameter and plots a vesicle size histogram for all the vesicles detected.

In order to quantify the concentration of DOPC GUVs, a finite volume (100 µL) taken from the electroformation solution was placed in an 8-well imaging dish (Ibidi, UK) with 400 µL of PBS. The dish was coated with BSA by letting a 1 mg/mL BSA solution in DI water stand for two hours. The BSA solution was then rinsed gently with deionised water. After allowing the GUVs to sediment for a further two hours, the glass surface of the dish was imaged in order to cover the full area of the dish. A bounding grid that consisted of 39x45 tiles, with 10% overlap was used for stitching.

2.2.5. Lipid order measurements

The lateral organisation of the membrane lipids, also referred to as lipid packing, was quantified using a microscope-based spectral imaging technique.[217,218] For this purpose, an aliquot (100 µL) of GUV-rich solution was placed in an imaging well. The vesicles were then fluorescently labelled with a final concentration of 400 nM c-Laurdan, an environment-sensitive molecular probe. The solution was then diluted with 100 µL of PBS. In the case of the experiment relating lipid packing to electrode material, 400 µL of PBS was added to the solution.

The emission spectrum of c-Laurdan shifts as a function of the dipolar water relaxation, and thus the level of hydration within its surrounding microenvironment, which in turn is indicative of lipid packing in membranes. Generalised Polarisation (GP)[183] was employed as a relative measure of lipid packing on a scale of -1 to 1, where -1 represents the least packed and

1 represents the most packed membrane. Equation 13 describes the GP relative to the intensities at two specific wavelengths: 440 (I_{440}) and 490nm (I_{490}). Spectral imaging was performed using a Zeiss LSM780 confocal microscope equipped with a 32-channel GaAsP detector array. The vesicles were excited at 405nm and the spectral intensity of the signal was recorded in the 415 to 691nm range.

2.2.6. Inductively coupled plasma optical emission spectrometry

The concentration of metal ions in the electroformed samples was measured by ICP-OES with a Varian Vista MPX spectrometer, for both electrode materials.

2.2.7. Lipid extraction and NMR experiments

The samples for NMR analysis were prepared from nine simultaneous electroformation experiments. The content of each electroformation chamber (3 mL) was diluted with an equal volume of PBS in a 50 mL Falcon tube, which was then left to stand overnight at room temperature. GUV-enriched layers (500 µL each) were then withdrawn from the bottom of each Falcon tube, combined and freeze dried. The lipids were then extracted from the dried GUV samples with the Bligh and Dyer method[219]. Briefly, the sample was dispersed in water (0.8 mL), then methanol (2 mL) and chloroform (1 mL) were added with mixing after each addition. The sample was vortexed at 2500 rpm for 15 s and allowed to stand for 30 min. Chloroform (1 mL) and water (1 mL) were added, and the sample was centrifuged at 1000 g for 5 min to achieve complete phase separation. The bottom organic layer was withdrawn with a glass syringe, dried under a nitrogen stream and redissolved in $CDCl_3$ (600 µL) for analysis. Large Multilamellar Vesicles (LMVs) control samples with different lipid concentrations were prepared using the lipid hydration method. A solution of DOPC in chloroform was added to a glass vial and dried under a nitrogen stream. The lipid film was then hydrated by adding the same sucrose solution used for electroformation and vortexed for 2 min at 2500 rpm. After

adding an equal volume of PBS, the sample was left to stand at room temperature for 18 hrs. The lipids were then extracted with the same protocol used for the electroformed sample. ^{1}H-NMR spectra were acquired on a Bruker Ascend 400 spectrometer (at 400 MHz for ^{1}H and at 162 MHz for ^{31}P) with 30° pulses (Bruker zg30 sequence) and a 3s relaxation delay on a spectral width of 8000 Hz, while ^{31}P-NMR spectra were acquired with proton decoupling and a 3s relaxation delay on a spectral width of 64103 Hz. The spectra were apodised by multiplication with an exponential decay equivalent to 0.5 Hz line broadening and a Gaussian function equivalent to 1 Hz line broadening. ^{1}H-NMR spectra were referenced to residual non deuterated chloroform, while ^{31}P-NMR spectra were externally referenced to triphenylphosphine oxide.

2.2.8. Limit of detection of oxidised DOPC

The limit of detection of oxidized lipids was estimated as the ratio of the concentration of an oxidized DOPC reference in deuterated chloroform, $CDCl_3$, corresponding to a peak height of the aldehyde proton (9.75 ppm) equal to three times the baseline noise, and the concentration of DOPC in a typical analytical sample (340 μM). The concentrations were calculated using benzoic acid (Sigma Aldrich, UK) as an internal standard.
The oxidized reference was synthesized by photooxidation of 1 mL of a 10 mg/mL solution of DOPC in oxygen saturated CD_3OD in the presence of $[Ru(bpy)_3]^{2+}$ immobilized on a Dowex 50WX2 resin (50-100 mesh, 0.6 meq/mL, 4% $[Ru(bpy)_3]^{2+}$ loading) prepared according to a literature procedure.[220] A glass vial containing the resin and the DOPC solution was sealed and left to rotate on a rotator while illuminated with a fluorescent lamp (49315 FML27/65 GX10q-4, Eiko) from a distance of 10 cm. After 48 hours the solution was filtered and the resin was rinsed with methanol and chloroform. The solvent was removed with a nitrogen stream to afford a colorless oil that was dried under vacuum, redissolved in $CDCl_3$ and used without further purification. The ^{1}H-NMR spectrum shows the presence of secondary

oxidation products (including the aldehyde used to estimate the limit of detection), presumably from the decomposition of hydroperoxides, and hydrolysis products.

2.2.9. Vesicle unilamellarity

Vesicle unilamellarity was tested using a fluorescence quenching assay based on the measurement of the ratio of inner and outer layers of fluorescently labelled GUVs.[221,222] DOPC vesicles symmetrically labelled with the fluorescent lipid N-(7-nitrobenz-2-oxa-1,3-diazol-4-yl)-1,2-dihexadecanoyl-*sn*-glycero-3-phosphoethanolamine triethylammonium salt (NBD-PE) were electroformed and a time course of their fluorescence was measured in a plate reader. Sodium dithionite, a membrane impermeable quencher, was added to the sample in order to quench the fluorophores on the outer layer of the vesicles. The vesicles were then lysed by addition of Triton X-100, in order to expose all lipids to the quencher.
The protocol consisted in mixing 2.7 mL of fluorescent GUV suspension with 300 μL of a HEPES buffer at pH 7 (0.1 M HEPES and 1 M NaCl). Three wells of a 96 well plate were filled were filled with 200 μL of the buffered GUV suspension. Stable values of fluorescence intensity were measured at 520 nm emission on a FLUOstar Omega plate reader (BMG Labtech) before and after adding 4 μL of a freshly prepared solution of 1 M $Na_2S_2O_4$ in 1 M Tris buffer at pH 10, with excitation at 485 nm. Subsequently, 20 μL of a 10% v/v solution of Triton X-100 was added to the solution to cause vesicle lysis and expose all lipid structures to the quencher. A final stable value of fluorescence was recorded after the addition of the detergent. The unilamellarity index, defined as the fraction of leaflets that are not exposed to the solvent, was calculated as the ratio between the emission drop $I_{interior}$ caused by the addition of detergent and the total emission drop:

$$I_{total} = I_{interior} + I_{exterior} \qquad \textit{Equation 14}$$

2.2.10. Statistical analyses

Statistical testing was performed using one-way ANOVA for multiple comparison analysis while a Student's t-test was employed for direct comparison between two data sets. All data are expressed in terms of mean ± standard deviation and the number of independent replicates is expressed in the figure captions. The following conventions for statistical significance are used throughout the thesis: ns = $p > 0.05$, * = $p \leq 0.05$, ** = $p \leq 0.01$, *** = $p \leq 0.001$, **** = $p \leq 0.0001$.

2.3. Results and Discussion

2.3.1. Giant unilamellar vesicles production and imaging

Electroformation visualisation chambers have been used to monitor and verify the effective production of vesicles.[223] To assess the vesicle formation on stainless steel electrodes, swelling was visualised *in situ* (Figure 15a) using a second specially designed electroformation chamber with optical access using the protocol described in the Methods section. Vesicle formation was observed across most of the electrode surface, even prior to the application of the electric field (Figure 15a). Upon switching on the signal generator, the swelling was accelerated and vesicles reached moderate size (see Supplementary Video 1.1, Appendix B). DOPC vesicles swelling and detachment from an electrode were also observed (Figure 15b and Figure 15c).

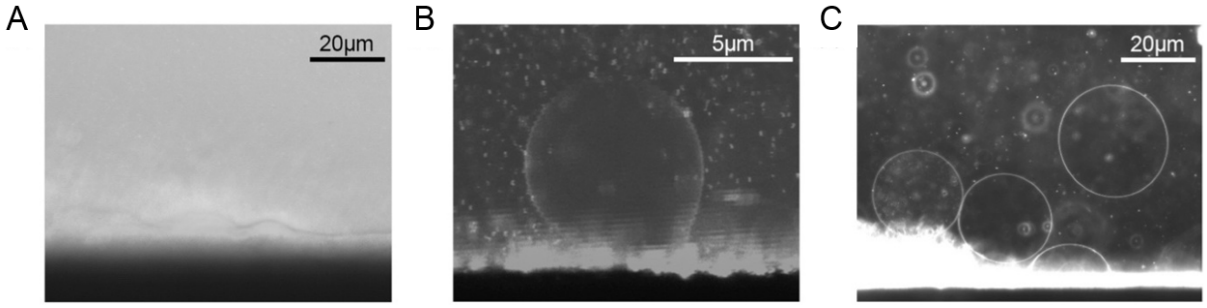


Figure 15 - Vesicles swelling from electroformation electrodes: A. hydrated lipid later commencing the swelling process, B. DiI labelled single vesicle swelling while attached to the electroformation electrodes and C. vesicles forming, swelling and detachment along the electrode.

Following the visualisation, vesicles were produced inside the device depicted in Figure 13 a using the electroformation protocol described in the Materials and methods section. The electrode material did not produce significant differences in the size distributions of the vesicles (Figure 16) and were within the ranges reported in existing literature (10-30 µm for DOPC vesicles).[224–226]

The yield of a single electroformation chamber was estimated by suspending 100 µL of GUV-rich solution in PBS and counting the number of vesicles at the bottom of a visualisation plate after allowing the vesicles to sediment. The vesicles were counted using a purpose-built

algorithm for both electrode materials. On average, the stainless steel electrode electroformation yielded 2256 vesicles (22560 vesicles/mL), against the 3114 (31140 vesicles/mL) yielded by the platinum wire electrodes. The difference however was not statistically significant.

It should be noted, however, that comparison between GUV studies is problematic due to differences in experimental parameters such as differences in osmotic pressure, electrode size and separation, electroformation solution, lipid species, electric field strength, focal plane, and vesicle manipulation technique.

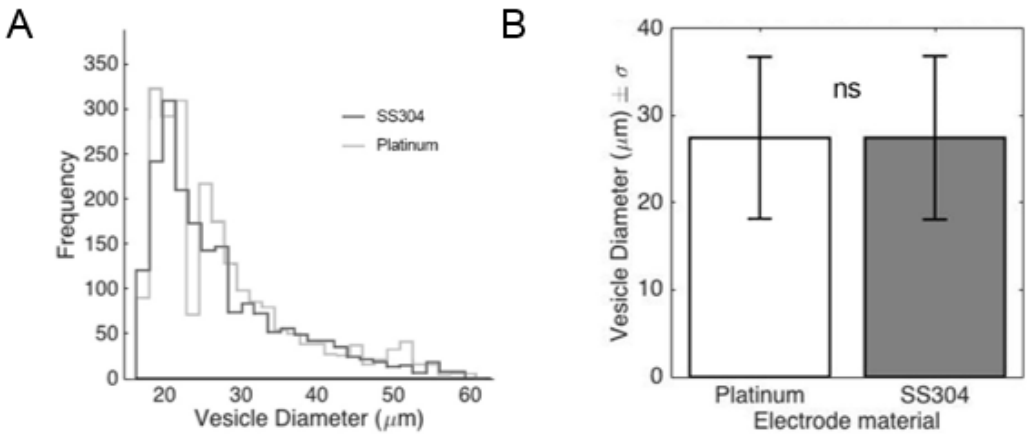


Figure 16 – A. DOPC vesicle size distribution as a function of electrode material. The white bars represent vesicles formed using platinum wires as electrodes, while the grey bars represent vesicles formed using stainless steel electrodes. B. Average vesicle diameter (± standard deviation) comparison for platinum and stainless steel electrodes. Three independent experiments were conducted and over 1500 vesicles were analysed for each electrode material.

2.3.2. Lipid order and size of vesicles composed of binary lipid mixtures

To test the parallelisation potential, vesicles with different compositions were produced simultaneously by varying the DOPC:cholesterol (DOPC:Chol) molar ratio in the multi chamber device.

The results depicted in Figure 17 were obtained by performing four concurrent electroformation experiments, coating the wires in each chamber with a different lipid composition. Figure 17a displays the average GPs and standard deviations of the vesicles for

each initial lipid composition. As the cholesterol volume fraction increases, the packing of the membrane also increases, as cholesterol intercalates between the DOPC lipids.[217,227,228] The electroformation cycle lasted for 2.5 hours, required limited set-up time, and was performed using 4 pairs of new injection needles (SS304), at a total electrode cost of approximately £2.00. The equivalent cost of Pt wire electrodes would have been approximately £584 and would have required electrode cleaning and straightening.

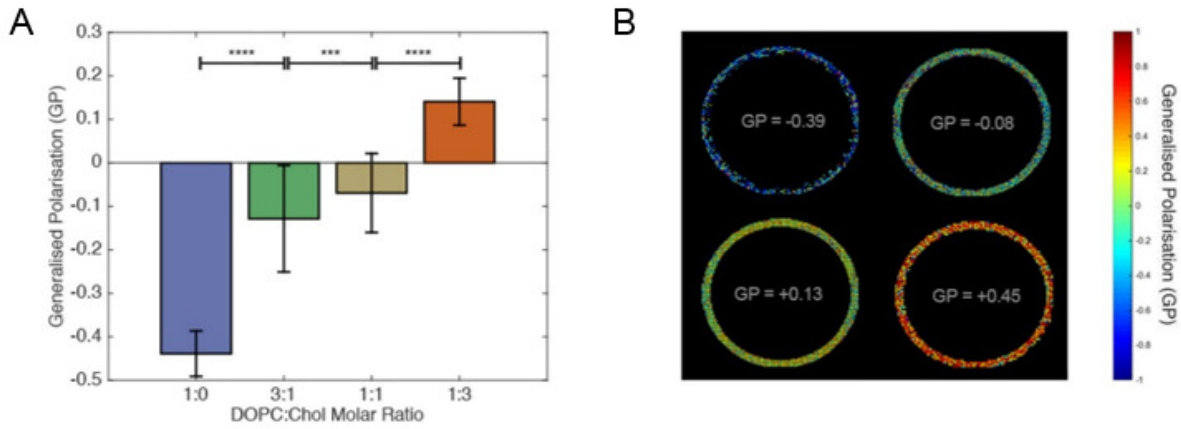


Figure 17 - Simultaneous electroformation of vesicles with dissimilar membrane properties: A. Generalised Polarisation of the vesicles as a function of initial lipid film formulation; B. Representative GP false-coloured images of four vesicles with different GP values.

The consistency in vesicle diameter was determined as a function of lipid composition. The vesicle size was not affected significantly by the molar fraction of cholesterol when compared to the 1:0 DOPC:Chol composition (Figure 18a). The electrode material did not have an effect on the lipid packing of GUV electrodes (Figure 18b). A higher osmolarity of the extravesicular environment yields vesicles with a higher membrane order, and thus a higher degree of lipid packing.[229]

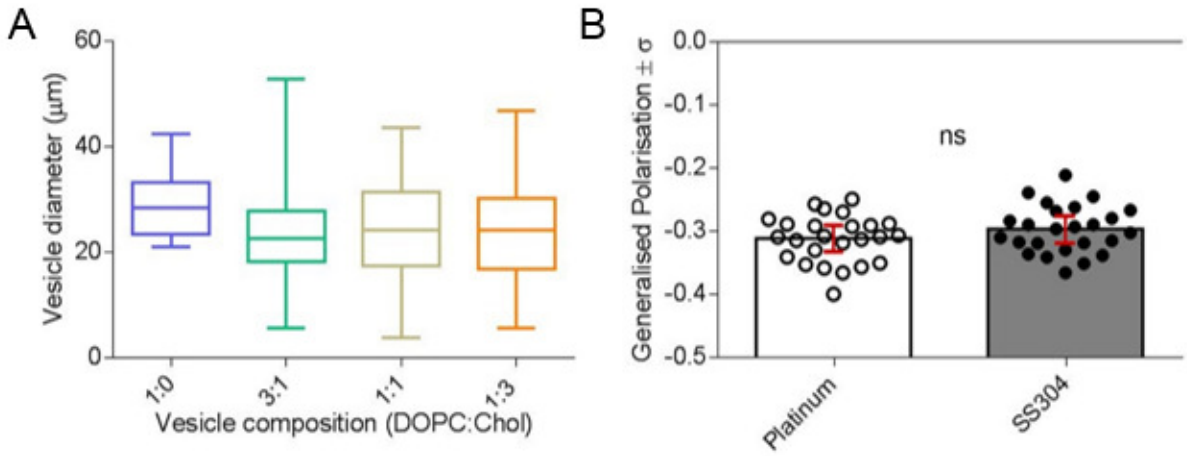


Figure 18 – A. Vesicle diameters as a function of lipid composition (b) Lipid packing of DOPC vesicles as a function of electrode material. GP values and vesicle sizes were obtained using a custom MATLAB script.

2.3.3. Leaching of metals from the electrodes

Leaching of transition metals from the electrodes can be a concern in electroformation of GUVs. Metal ions can bind to membranes[230] and alter their bilayer structure,[231] phase behavior[232] and stability against vesicle fusion.[233] Unwanted chemical reactions can also be catalyzed by trace metals: chromium, iron and nickel can initiate, and in some cases, propagate lipid peroxidation.[234]

The possibility of leaching of metals from the stainless steel electrodes under electroformation conditions was assessed by comparing the concentration of its constituents (Fe, Cr, Ni, and Mn) in GUV samples (Table 2) prepared with stainless steel electrodes and platinum electrodes. No increase in metal concentration compared to platinum electrodes was detected by inductively coupled plasma optical emission spectroscopy (ICP-OES). While no evidence of ion leaching was detected when the electroformation was carried out in 200 mM sucrose, this may not be the case in conductive electroformation solutions. On the contrary, platinum electrodes are routinely used to electroform vesicles in solutions of physiological ionic strength. A similar argument holds true for temperature, as electroformation of vesicles with higher transition temperatures require a heated chamber.

Table 8 - Concentrations of alloy constituents inside the electroformation chamber. The concentrations for both platinum and stainless steel electrodes are shown.

Element	% fraction in SS304	Concentration with Pt electrodes (ppm)	Concentration with SS304 electrodes (ppm)
Iron	65-71	1.3	1.2
Chromium	18-20	0.3	0.2
Nickel	8-12	0.1	0.1
Manganese	2	<0.1	<0.1

2.3.4. Lipid oxidation and hydrolysis

Products of lipid oxidation and hydrolysis, which can be generated at the electrode during the electroformation process,[235] are also known to affect the physical properties of phospholipid membranes. Even small amounts of degradation products can cause structural and dynamic changes, such as the formation of lipid rafts[235] or changes in permeability[236] and mechanical stability.[237] ^{1}H-NMR and ^{31}P-NMR spectroscopy are among the fastest and most informative analytical methods that have been used to characterize the chemical structure of phospholipids extracted from biological membranes and their degradation products.[238–241] The structural integrity of electroformed GUVs was assessed by comparing NMR spectra of the combined lipid extracts from nine electroformed GUV samples with a control obtained from large multilamellar vesicles (LMVs) prepared by lipid hydration. The ^{1}H-NMR spectra of lipids extracted from electroformed GUVs and from LMVs are compared in Figure 19. The spectra are identical, and both are consistent with pure DOPC. No degradation products were detected within a limit of detection of 1 mol%. Although trace impurities can be seen in the electroformed sample, the same impurities are found in the control. Their concentration remains constant as the concentration of DOPC in the control sample is increased from 0.34 mM to 3.4 mM, suggesting that they could be due to trace contamination rather than lipid degradation.

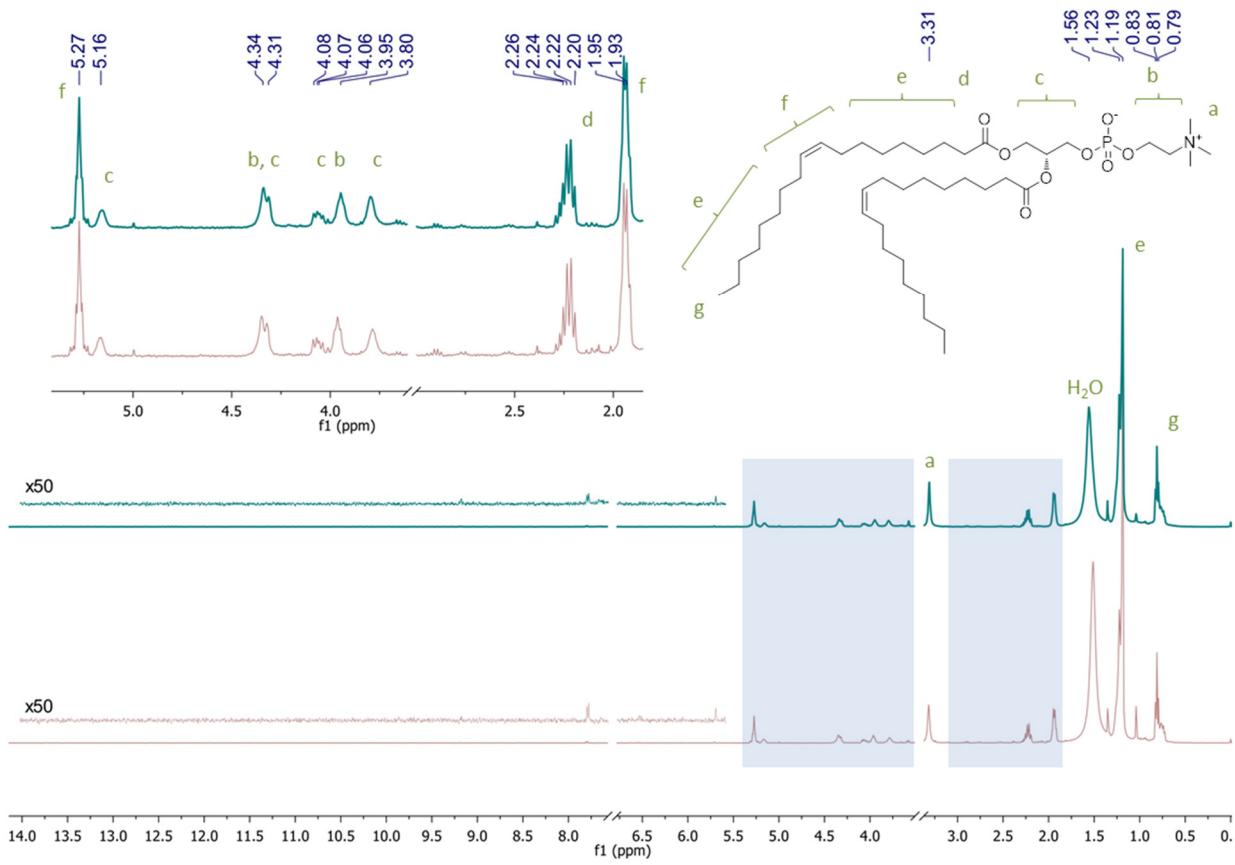


Figure 19 - ^{1}H-NMR spectrum of lipids extracted from electroformed GUVs (top trace) and LMVs (bottom trace). The residual solvent peaks of chloroform (7.26 ppm) and methanol (3.49 ppm) were removed for clarity. The inset shows a magnified view of the olefinic and head group protons.

The absence of hydrolysis products was confirmed by the ^{31}P-NMR spectrum, which shows only one signal in both samples. All isomers of lyso-PC would resonate downfield, where no signal was detected.

2.3.5. Unilamellarity of electroformed vesicles

Three independent suspensions of fluorescently labelled vesicles were prepared using the electroformation protocol outlined previously.

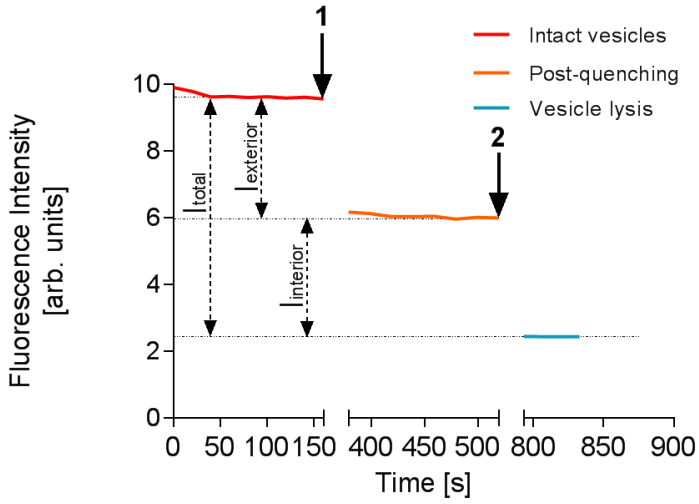


Figure 20 - Fluorescence intensity measurements of DOPC:NBD-PE vesicles. The fluorescence of intact vesicles is represented from time=0 to arrow 1. At arrow 1, the quencher is added to the suspension and the intensity is recorded until a stable value is reached. The emission drop is a measure of the number of fluorophores in outer leaflets only. At arrow 2, Triton X-100 is added to lyse the vesicles and fluorescence is recorded until a new stable value is reached. The corresponding emission drop is a measure of the number of fluorophores in inner leaflets. After each addition the plate was removed from the plate reader and shaken for several minutes (the time axis is correspondingly cut for clarity).

The ratio between the emission drop $I_{interior}$ caused by the addition of detergent and the total emission drop $I_{total} = I_{interior} + I_{exterior}$ is used as a measure of the fraction of leaflets that are not exposed to the solvent (unilamellarity index). A ratio of 51% ± 2.8%, which is consistent with unilamellarity, was measured (Figure 20). The measurements for all the three samples are summarised in Table 9.

Table 9 - Fluorescence measurements and calculations for fluorescence quenching assay.

Experiment	Pre-quenching	Quenched	Lysed	Unilamellarity
1	72.6	50.5	24.0	0.545
2	96.0	60.0	24.4	0.497
3	112	67.3	24.0	0.495

2.4. Conclusions

In this chapter, giant vesicle electroformation using an alternative electrode material been proposed and validated. It was demonstrated that electro-swelling of unilamellar vesicles occurs efficiently on stainless steel electrodes without any significant difference in vesicle size distribution, lipid degradation or leaching of metals in the electroformation chamber when compared to platinum electrodes. By using readily available stainless steel electrodes, it was shown that rapid, low-cost, and scalable electroformation can be achieved. This platform has potential application in biophysical investigations of lipid membranes, particularly in studies in which multiplexing is crucial, such as large-scale screening of bioactive compounds. The electroformation technique presented in this Chapter will be used in Chapters IV and IV to fabricate giant unilamellar vesicles used as cell models.

III

Layered acoustofluidic resonators for the simultaneous optical and acoustic characterisation of cavitation dynamics, microstreaming and biological effects

This chapter introduces the exposure methods used throughout the experiments presented in this thesis. A novel a microfluidic layered resonator that allows the simultaneous exposure to ultrasound, pressure-driven flow and microbubbles, alone and in combination, is presented. The device addresses the challenges associated with exposing, monitoring, and imaging biological samples and cavitation activity in conventional ultrasound exposure rigs.

The author gratefully acknowledges Dr. Dario Carugo for conceptualising the device, Mr. Miles Aron for performing the cavitation, emission monitoring, and sonoporation experiments, Mr. Oliver Vince for the layer thickness sensitivity analysis, Dr. Anjali Seth for producing nanodroplets, Dr. Marie de Saint Victor for the acoustic pressure calibrations, Dr. Christophoros Mannaris for experimental assistance, and Dr. Guillaume Lajoinie for performing high speed imaging. The author contributed by performing the 1D and 2D acoustic field simulations, temperature response characterisations, and impedance spectroscopy analysis.

The material discussed in this chapter has been presented in alternate form in:
Layered acoustofluidic resonators for the simultaneous optical and acoustic characterisation of cavitation dynamics, microstreaming and biological effects. **Biomicrofluidics** 12, 034109 (2018)

3.0 Abstract

The study of the effects of ultrasound-induced acoustic cavitation on biological structures is an active field in biomedical research. Of particular interest for therapeutic applications is the ability of oscillating microbubbles to promote both cellular and tissue membrane permeabilisation and to improve the distribution of therapeutic agents in tissue through extravasation and convective transport. The mechanisms that underpin the interaction between cavitating agents and tissues are, however, still poorly understood. One challenge is the practical difficulty involved in performing optical microscopy and acoustic emissions monitoring simultaneously in a biologically compatible environment. Here a microfluidic layered acoustic resonator (μLAR) developed for simultaneous ultrasound exposure, acoustic emissions monitoring and microscopy of biological samples is presented and characterised. The μLAR facilitates in vitro ultrasound experiments in which measurements of microbubble dynamics, microstreaming velocity fields, acoustic emissions and cell-microbubble interactions can be performed simultaneously. The device and analyses presented provide a means of performing mechanistic in vitro studies that may benefit the design of predictable and effective cavitation-based ultrasound treatments.

3.1. Introduction

3.1.1. Cavitation in ultrasound therapy

Over the past 3 decades, the potential of ultrasound (US) to increase the permeability of biological membranes to different classes of therapeutically active compounds has been widely demonstrated, paving the way for its use in the treatment of malignant and non-malignant diseases[242–244]. Cavitation, the creation and subsequent oscillation of gas and/or vapour bubbles, has been shown to play a key role in this process[245]. Consequently, a variety of different ultrasound-responsive agents (US-RAs), including coated gas microbubbles, phase-shift nanodroplets, and gas entrapping solid nanoparticles[39,246,247], have been developed to promote cavitation and thus enhance or localise the mechanical perturbation induced by US alone. The systemic distribution, circulation time and acoustic responsiveness of these agents strongly depend on the physical properties (i.e., size, compressibility, density) of the particles, and the chemical composition and charge of the surface coating. These properties can potentially be tailored for a desired application or therapeutic outcome. Moreover, agents can be functionalised with targeting species for efficient accumulation at a specific organ or tissue, upon application of external physical stimuli (i.e., magnetic fields[248]) or *via* bio-chemical interactions[249].

Performance optimisation and clinical translation of US-RAs, however, require a comprehensive understanding of the mechanisms of interaction with biological systems, from the sub-cellular level upwards. These mechanisms include a range of phenomena[11]: direct interaction between bubbles and cells through impingement,[119] disrupting the cell membrane or activating mechanosensitive ion channels; the production of microjets during bubble collapse[250] perforating the cell membrane; material transfer[251,252] altering the physical properties of the membrane; production of chemical species such as hydrogen peroxide[253]; shockwaves emitted by collapsing bubbles and cavitation induced microstreaming, which may facilitate drug delivery by increasing transport and mixing and/or by imposing high levels of

shear stress and spatial and/or temporal shear stress gradients[254,255,63]. The diversity of these mechanisms makes their study extremely challenging, as does the range of time and lengthscales over which they operate, from nanoseconds to hours and from sub-nanometre to mm, respectively. A detailed review of the techniques that have been applied and/or developed for this purpose may be found in the review by Lajoinie et al.[256]. The next section provides a brief overview.

3.1.2. Existing devices

Advanced analytical and optical instruments have been developed to probe the physical and chemical properties of biological cells and sub-cellular structures, at increasingly high spatial and temporal resolution[140,257–260]. The integration of commercial analytical and optical instrumentation with custom-built ultrasound stimulation rigs (i.e., water-tank based apparatus) however poses significant practical and technical challenges[256]. A typical experimental setup for ultrasound-mediated stimulation of biological samples consists of an acoustically and optically transparent chamber, such as an Opticell™ [140,261] (Thermo Fisher Scientific) or other custom-built devices[262]. These chambers are biologically compatible, and suitable for the generation of a well-defined and clinically relevant acoustic field. However, application of such chambers requires the use of a relatively large volume water tank, which limits the degree to which they can be integrated with optical microscopy systems. Moreover, parallel-plate chambers are often not designed for continuous-flow experimentation, and may suffer from high wall shear stress during priming or practical difficulties in removing exogenous air bubbles[262].

Alternative devices that do not require immersion in a water tank have been employed to investigate the physical and/or biological effects of cavitating agents. These include glass cuvettes, capillaries and cylindrical chambers that can be coupled to a piezoelectric element[263,264]. Given their material and dimensional properties, acoustic standing waves may compromise the uniformity of the acoustic pressure field, and devices are often not suitable for

high-resolution microscopy or for performing biological assays. Moreover, they are typically driven at relatively low ultrasound frequencies (i.e., 20-200 kHz) compared to the MHz range of frequencies used in therapeutic applications.

Microfluidic devices with integrated ultrasound sources (either bulk or surface waves) have also been reported, providing the advantage of physiologically relevant confinement and optical imaging at high spatial resolution[265–267]. They have been employed to investigate the behaviour of gas microbubbles under US excitation or to elicit membrane permeabilisation, but are often actuated at relatively high US frequencies (i.e., ≥ 2 MHz) corresponding to a resonance frequency of a composite structure and that are not therapeutically relevant. Moreover, the acoustic pressure in these systems is typically below the therapeutically relevant range, and strongly resonating structures may suffer from large acoustic pressure amplitude gradients in the internal fluid cavity. Such devices are also not typically reusable and their inner surfaces are difficult to treat or coat, if the constitutive layers are permanently bonded together (i.e. *via* treatment with oxygen plasma).

More conventional "acoustofluidic" devices utilise ultrasound standing wave (USW) fields within a fluid cavity in order to manipulate microparticles, biological cells or microorganisms towards specific regions of the ultrasound field[268,269]. These usually correspond to the pressure nodes of the USW, the positions of which can be tuned on-demand to achieve cell separation and sorting, sample filtration and concentration, or detection of target cells/organisms[100]. Notably, acoustofluidic devices have also been employed to investigate the enhanced mixing of chemical species associated with flow perturbations from cavitating microbubbles [270–275]. Acoustofluidic devices designed for acoustic manipulation normally comprise strong acoustic pressure and energy density gradients within their fluid cavities[276,277]. These gradients may result in relatively high acoustic streaming velocities, i.e. steady fluid motion induced by the USW field in the absence of cavitating agents[278]. Such devices are therefore not well suited to the study of cavitation induced bioeffects, since, for example, strongly resonating

acoustofluidic systems can themselves generate intracellular delivery of pharmaceutical compounds, due to the associated high streaming velocities[264].

3.1.3. Challenges

A combination of microscopy, high speed imaging, acoustic monitoring and chemical and biological assays is required in order to study the interactions between US-RAs and tissue. An ideal system should therefore:

(i) Provide a well-defined and spatially uniform acoustic pressure field to recreate consistent exposure conditions across a sample.

(ii) Minimise secondary acoustic effects, i.e., streaming and/or heating, to enable decoupling of the effects of US from those mediated by US-RAs.

(iii) Operate at US frequencies of therapeutic relevance, i.e. in the range 0.3 – 2 MHz.

(iv) Mimic the dimensional confinement typical of physiological microenvironments and physiologically-relevant flow conditions.

(v) Be compatible with small working-distance and/or high-magnification microscope objectives and high intensity illumination to facilitate high speed imaging of microbubble dynamics and/or fluorescence microscopy *in situ*.

(vi) Enable simultaneous monitoring of acoustic emissions.

(vii) Allow biological material to be maintained in a viable condition for sufficient time periods to study.

(viii) Enable convenient injection and extraction of material for analysis.

(ix) Be simple to operate, economical and reusable.

The aim of the work in this chapter was to build an acoustofluidic device that meets these requirements. The design is based on a thin-reflector resonator configuration[264,279], which has been adapted to achieve a uniform acoustic pressure field in the direction of US propagation,

at ultrasound frequencies suitable for transmission through both hard (0.5 MHz) and soft tissues (1 MHz).

In sections 3.2.4 and 3.3 the construction of the device, characterisation of the acoustic field and thermal properties are presented. In section 3.4.2, the utility of the device in characterising the behaviour of US-RAs both optically (using a high-magnification objective) and acoustically (using a polyvinylidene fluoride film), is demonstrated. A method for mapping the fluid velocity produced by cavitation microstreaming using particle streak velocimetry is described. Finally a demonstration of the device in observing bubble-cell interaction, quantifying the effects upon cell membrane integrity and determining the efficiency of microbubble-mediated cell sonoporation is presented.

3.2. Device design and fabrication

The microfluidic layered acoustic resonator (μLAR) devices used in this study consist of the following layers: i. a single piezoelectric element, ii. a ceramic carrier, iii. a fluid cavity, and iv. a glass reflector (Figure 21). Each μLAR is designed to be operated at the first thickness-mode resonant frequency of its layered structure, and has an acoustic pressure minimum located at the reflector-air boundary. This is in contrast to commonly employed half-wave and quarter-wave resonators, which typically have acoustic pressure nodes within their fluid cavities[280]. Thus, whilst half-wave resonators may trap particles at the midplane of the fluid cavity and quarter-wave resonators may manipulate particles nearby a boundary of the fluid cavity, in the μLAR configuration presented here the acoustic pressure gradient is minimised in the direction of ultrasound propagation across the fluid layer. The reflecting layer of the μLAR is much smaller than the wavelength of sound in the layered structure, thus potentially allowing for a more uniform field in the direction of ultrasound propagation at the cost of reflecting less acoustic energy into the fluid cavity. This trade-off nonetheless results in acoustic pressures and field gradients that are relevant for ultrasound mediated bioeffects. It should be noted that the terms 'reflector' and 'carrier', which will be retained for the sake of

consistency with the literature, do not strictly describe the function of these respective layers in the µLAR configurations presented herein. µLARs were thus designed as thin-reflector layered acoustic resonators, the advantages and disadvantages of which are discussed in the following sections.

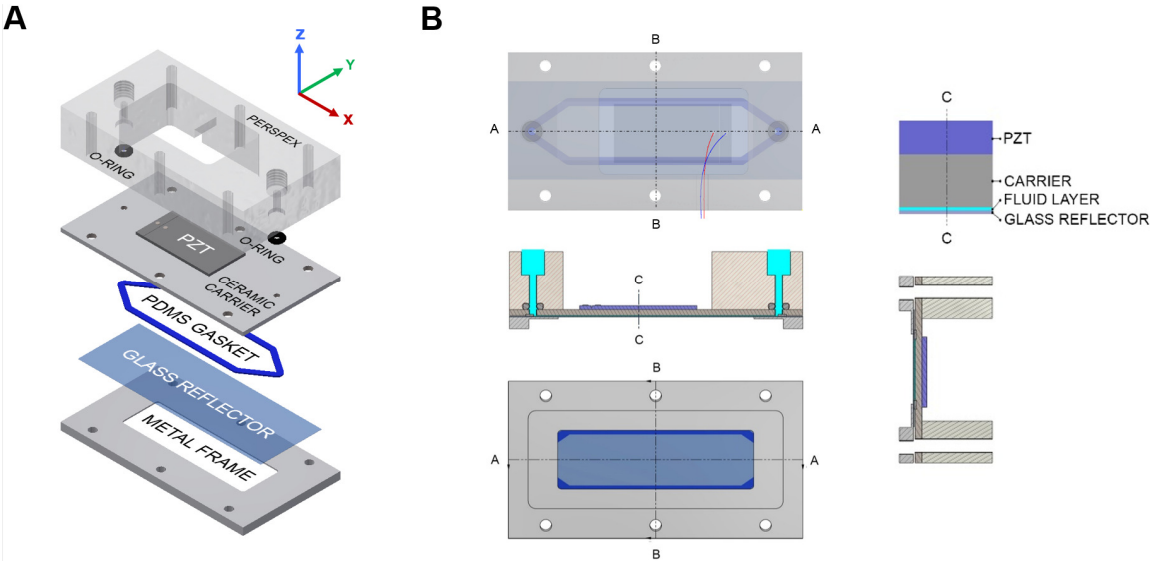


Figure 21 - Design of a µLAR device. A. Expanded view of the layered acoustic resonator including, top to bottom: i. Perspex® manifold, ii. o-rings iii. piezoceramic element coupled to the MACOR carrier layer, iv. PDMS gasket that forms the channel geometry, v. glass coverslip, and vi. aluminium frame. B. Schematic drawing of the assembled acoustofluidic device, showing relative layer thicknesses and cut-view in C-C and A-A planes.

3.2.1. The piezoelectric transducer

Two µLAR devices were designed to efficiently resonate at two therapeutically relevant ultrasound frequencies: 0.5 and 1 MHz. Commercially available 1 mm and 2 mm thick PZT-4 elements (Meggitt, UK) were employed to achieve the required thickness-mode resonances for the 1 MHz and 0.5 MHz µLAR designs, respectively. The adhesive used to permanently bond the piezoelectric transducer to the machinable ceramic carrier layer (Macor, Corning Inc.) was a two-part epoxy (RX771C/NC) chosen to provide efficient acoustic coupling and to prevent formation of air voids at the interface between the transducer and the carrier. The resin was cured at 30ºC for 24 hrs.

3.2.2. The carrier

Macor was selected as the carrier layer material because it provides excellent coupling and transmission of the ultrasound field with the fluid layer owing to its acoustic impedance (14 MRayl). It has a speed of sound (c) of 2520 m/s and density (ρ) of 5631 kg/m3, in comparison with PZT-4 (c = 4530 m/s, ρ = 7600 kg/m^3). Macor is preferable to other ceramics because it can be machined using ordinary metalworking tools to 13 μm tolerances, and can be inexpensively obtained at custom thicknesses and low quantities (in the present work, the Macor was from Ceramic Substrates and Components Ltd.). Moreover, it is a good thermal and electrical insulator and has a negligible thermal expansion coefficient, minimal outgassing and porosity (making it well suited to biological work), and is compatible with piezoelectric transducers, and for use with gas-filled agents.

The μLAR is fully compatible with fluorescence and reflection microscopy, which are sufficient for most biophysical investigations. One drawback of Macor is that it is optically opaque, rendering the μLAR incompatible with brightfield microscopy[268]. However, the Macor carrier can be sputter-coated with a nanoscopic layer of gold or aluminium to make it highly reflective. This approach was employed to enable imaging of microbubbles in the μLAR without fluorescence labelling, as is often necessary for high-speed imaging studies (described below) or for preserving fluorescence bandwidth.

3.2.3. The thin reflector

The thin-reflector design of the μLAR has several practical motivations. First and foremost, a thin reflecting layer allows for better optical accessibility. For both μLAR designs presented herein, a widely commercially-available glass coverslip was chosen as the reflector. Specifically, a #1.5 coverslip with 170 μm thickness was selected for compatibility with high-magnification microscopy and oil-immersion objectives. In addition to optimal optical characteristics, glass coverslips can be sterilized, provide a standard substrate for cellular adhesion and growth, are

inexpensive, do not need to be altered or machined for use in a μLAR device, are disposable and/or reusable, and have acceptable thickness variations across batches for use in μLARs (±10%).

Table 10 - Geometric and material properties of the constitutive layers for both the 0.5 MHz and the 1 MHz devices. The US wavelengths corresponding to 0.5 MHz and 1 MHz were calculated as 2.96 mm and 1.48 mm, respectively. The thicknesses refer to the layers shown in Figure 21.

	Layer	Material	Thickness (μm)	Thickness/λ	Density (kg/m^3)	Speed of sound (m/s)
1 MHz	*Transducer*	PZT-4	1000	0.676	7600	4530
	Glue layer	Epoxy	10	0.006	2156	2640
	Matching layer	Macor®	1200	0.811	5631	2520
	Fluid layer	Water	200	0.135	1000	1482
	Reflector	Glass	170	0.115	2200	5710
0.5 MHz	*Transducer*	PZT-4	2000	0.676	7600	4530
	Glue layer	Epoxy	10	0.003	2156	2640
	Matching layer	Macor®	700	0.236	5631	2520
	Fluid layer	Water	370	0.125	1000	1482
	Reflector	Glass	170	0.057	2200	5710

3.2.4. Construction

For the 1 MHz device, a 30 x 13 x 1 mm^3 piezoelectric element (PZT-4, Meggit PLC, UK) was acoustically coupled with a machinable ceramic layer using a thin film of epoxy resin (RX771C/NC, Robnor Resins Ltd, UK) cured at 30℃ for 24 h. To fabricate the 0.5 MHz device, a 30x13x2 mm^3 PZT-4 piezoceramic element (Meggit PLC, UK) was used. A fluid layer surrounded by a recess was milled in the ceramic layer. A polydimethylsiloxane (PDMS) gasket (Sylgard 184® Dow Corning Corporation, USA) was placed within the recess, and was formed by mixing previously degassed PDMS precursor and curing agent (10:1 w/w), followed by a 1 h curing step at 90℃. The reflector layer consists of a 75x25x0.17 mm^3 glass

slide (Logitech Ltd., Scotland). The layered device was held in place with a Perspex® block fitted with flat-bottom thread fluidic connectors (¼") to deliver fluid suspensions of US-RAs to the fluid layer of the device. An aluminium frame with optical access was used to secure the device layers simultaneously, allowing for microscopy. Table 10 summarises the geometric features and materials of the two devices. A schematic of the device is shown in Figure 21.

3.3. Device characterisation

3.3.1. Acoustic field

3.3.1.1. 1D mathematical model

In order to predict the approximate location of the pressure nodes, the normalised acoustic pressure across the constitutive layers of the devices was calculated using a one-dimensional mathematical model (implemented in MATLAB), previously developed by Hill et al. [281]. It comprises a transfer impedance model for the individual resonator layers, and a KLM model for the piezoelectric transducer[277]. This approach was previously employed by Glynne-Jones et al.[277] to maximise the performance of ultrasonic manipulation devices. It should be noted that a more comprehensive design approach was recently proposed by Hahn et al.[282], combining three-dimensional numerical simulations of the acoustic field with a multi-parametric optimisation routine.

The layer thicknesses of the carrier layer (Macor) and fluid layer (water) were determined in simulation by fixing the thicknesses of the piezoelectric transducer and the reflecting layer to those values determined by the rational and practical considerations described in the preceding sections. The remaining thicknesses of the carrier and fluid layers were tuned to minimize pressure gradients and avoid pressure nodes across the fluid layer, in the direction of US propagation. This was achieved by keeping the thickness-to-wavelength ratio of the fluid layer below 0.15. As a result, a relatively uniform acoustic pressure field in the direction of US propagation can be generated within the fluid layer of the device (Figure 22A and 22B). The

maximum pressure change within the fluid cavity is equal to 32% and 13% (of the maximum pressure), for the 0.5 MHz and 1 MHz devices, respectively. These values are much lower than those typically observed in half-wave[283] or quarter-wave[284] planar resonators specifically designed for particle/cell manipulation. Moreover, within the plane of interest for a particular experiment the pressure gradient will be even smaller. The exact dimensions will depend upon the nature of the investigation and the depth of field of the selected optics, but are likely to represent a small fraction of the total chamber depth.

When the 0.5 MHz μLAR is manufactured using layers with the nominal thicknesses, the resonant frequency of the device as calculated by the model is 0.525 MHz. The thickness of the matching layer was found to have very little influence on the operating frequency. The operating frequency varies between 0.50 MHz and 0.55 MHz if either the fluid layer or the reflecting layer have a thickness of ± 20 μm relative to their respective design thicknesses. This equates to a thickness change of 0.0042 and 0.0018 wavelengths in the fluid and reflecting layers, respectively. In the 1 MHz μLAR, the 1D simulation predicts that the device's resonant frequency is 1.18 MHz. This operating frequency is sensitive to the thickness of the fluid layer, decreasing from 1.36 MHz to 1.13 MHz as the layer thickness is varied ± 50% (± 100 μm, ± 0.047 wavelengths). The same change in matching layer thickness (± 100 μm, ± 0.080 wavelengths) causes the resonant frequency to decrease from 1.23 MHz to 1.13 MHz. A ± 20 μm (± 0.004 wavelengths) change in the thickness of the reflecting layer causes the resonant frequency to decrease from 1.185 MHz to 1.17 MHz. Further analysis of the μLAR operating frequency sensitivity can be found in the Appendix B.

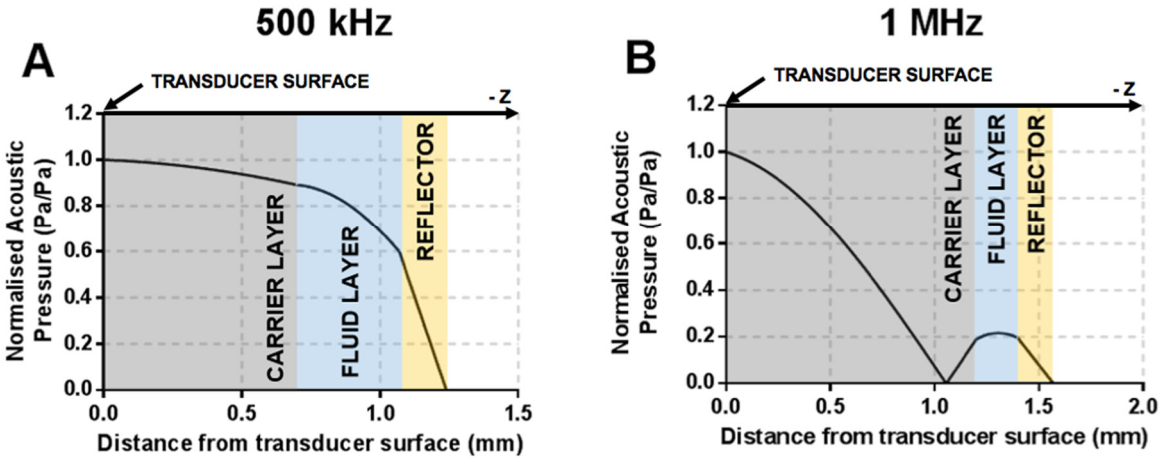


Figure 22 - Normalised acoustic pressure across the piezoelectric transducer, fluid and reflector layers of for the A. 0.5 MHz and B. 1 MHz μLAR devices respectively. Pressure was determined from 1D transfer impedance modelling.

3.3.1.2. 2D numerical model

The 1D model is an approximation that neglects lateral vibrations within the constitutive layers of the device, including surface waves or edge effects[277]. Therefore, the first-order acoustic fields within the devices were simulated in 2D using the Acoustic-Piezoelectric Interaction model in COMSOL Multiphysics®, which solves the harmonic, linearized acoustic problem as reported elsewhere[101]. The model geometry was discretised into finite elements, and further information on the triangular meshing scheme can be found in Figure 23 and Table 11.

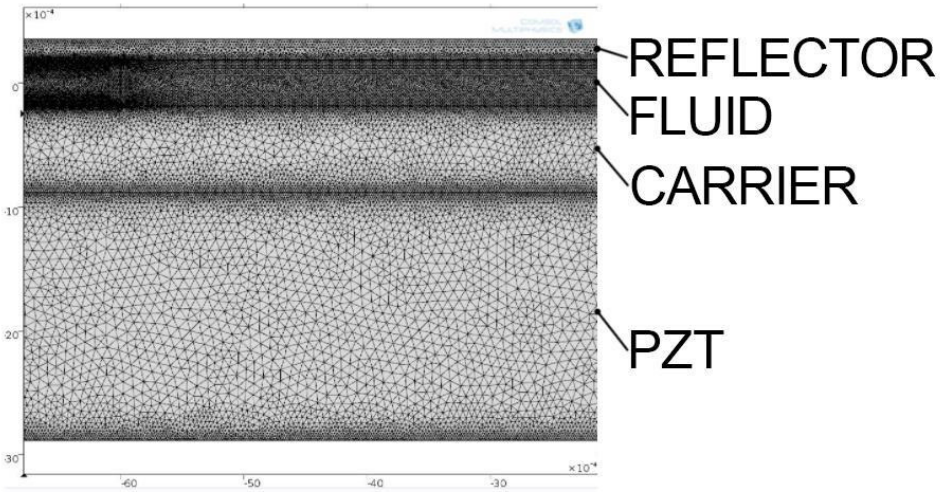


Figure 23 - Triangular mesh generation in the reflector, fluid, carriers, and transducer layers (top-down) performed in COMSOL Multiphysics® to model the acoustic pressure field within the fluid layer in the acoustofluidic devices.

Table 11 - Mesh parameters used in the COMSOL numerical model

Maximum element size [m]	$1x10^{-4}$
Minimum element size [m]	$1.2x10^{-5}$
Maximum element growth rate	1.3
Curvature factor	0.3
Resolution of narrow regions	1

Results show that, whilst the 1D modelling predicts a relatively uniform pressure field in the direction of US propagation, lateral gradients are present in the fluid layer and are particularly enhanced in the 1 MHz resonator (Figure 24A and 24B). These can be attributed to 'edge effects' or lateral modes of vibration of the thin glass reflector, at the higher US frequencies. Similar lateral gradients in the acoustic pressure field were discussed by Carugo et al. [280] in a thin-reflector resonator designed for acoustic manipulation of microorganisms at comparable US frequencies, and were addressed by introducing multiple lateral bars within the metal frame of the layered structure. This approach however may not be feasible in applications requiring integration with high magnification optics, and thus alternative strategies should be

implemented in an attempt to achieve a more uniform field. The mesh element size was adapted to the layer thickness (as shown in Figure 23), to ensure that the thinner features of the device had a sufficiently high mesh density.

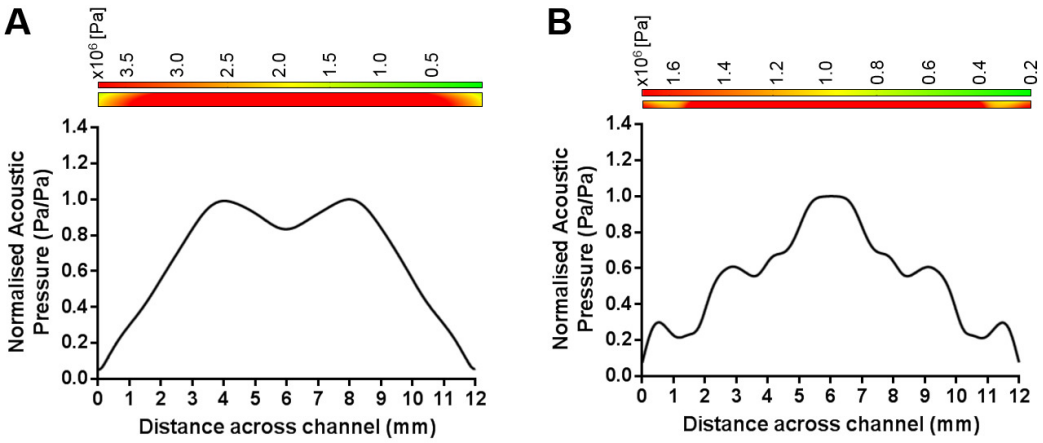


Figure 24 - Contours of normalised total acoustic pressure within the fluid layer (x-z plane) of both 0.5 and 1.0 MHz resonators. B. Corresponding acoustic pressure profiles along the width of the fluid layer. The pressures were quantified at z = 30 μm from the surface of the glass into the fluid layer.

3.3.1.3. Acoustic pressure

Therapeutically relevant pressures for sonoporation typically range from 0.15 to 0.5 MPa[285], with *in vitro* studies reporting membrane poration at acoustic pressures as low as 0.08 MPa[286]. Acoustic pressure also influences the lifetime of contrast agents both i*n vitro* and *in vivo*. Microbubbles can exist and oscillate up to 20,000 cycles at 1 MHz under low acoustic pressures (0.1 MPa), but their lifetime is significantly decreased at higher pressures (100 cycles at 0.4 MPa[287]) and/or lower frequencies. Experimental values of the acoustic pressure in the μLARs for different driving transducer voltages were determined by inserting a fibre-optic hydrophone into the fluid layer of the devices. Three independent measurements were performed in the 0-77 Vpp range to yield the input voltage-acoustic pressure curve shown in Figure 25A and 25B. The chamber was filled with deionised water, the fibre-optic tip was inserted through a 0.5 mm hole in the reflector layer, and a pressure ramp was measured at varying driving voltages. A positive correlation between the acoustic pressure and input voltage was observed, with acoustic pressure peaks of 0.25 MPa Peak Rarefactional Pressure

(PRFP) for the 1 MHz device, and 0.4 MPa for the 0.5 MHz device. It should be noted that other, less invasive methods for measuring acoustic pressure in microscale USW fields have been reported, such as the 'drop voltage' technique[103,264]. These methods, however, usually require efficient particle manipulation to the nodes of the USW, and therefore are not applicable to characterizing acoustofluidic devices with weak acoustic pressure gradients across their fluid cavities.

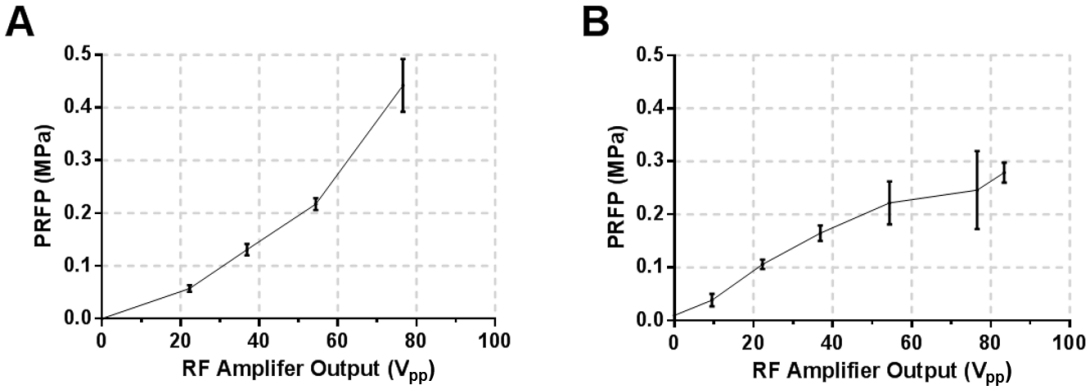


Figure 25 - Peak Rarefactional Pressure (PRFP) as a function of transducer driving voltage for the A. 0.5 MHz device and B. 1 MHz device. Pressure was determined experimentally using a fibre-optic hydrophone. Three repeats were performed for each data point, as indicated by the error bars.

3.3.2. Acoustic streaming

Although the μLAR is designed to minimize the standing wave pressure gradient in the direction of ultrasound propagation in the fluid layer, it is not entirely eliminated (particularly at continuous wave exposure conditions). Indeed, the microbubbles are expected to travel towards one of the boundary layers in the device under ultrasound exposure depending on their resonant frequencies[288]. For instance, in the 1 MHz μLAR device with SonoVue®, microbubbles that produced microstreaming were found at the carrier layer of the device and were the product of the coalescence of smaller microbubbles.

The Reynolds stresses that arise from acoustic energy gradients are responsible for acoustic streaming within the fluid layer of the devices[101]. In order to further minimise pressure gradients and hence acoustic streaming velocities, the thickness of the carrier layer was chosen

to be relatively large to prevent flexural modes. Moreover, the channel side walls were purposely fabricated in PDMS to take advantage of the more acoustically absorbent properties compared to MACOR[289]. The relatively uniform pressure field in the *z*-direction may also reduce the Rayleigh streaming within the fluid layer[280].

The acoustic streaming was quantified in the 1 MHz μLAR at the maximum acoustic pressures at which the devices are operated (77 Vpp driving voltage). Fluorescently-labelled 2 μm diameter latex beads (Sigma Aldrich, UK) were used as flow tracers (0.1% v/v) to allow flow magnitude quantification by particle streak velocimetry. The mean streaming velocity across three samples was 6.6 ± 5.8 μm/s. Note that the magnitude of the standard deviation here reflects the drop in velocity with distance from the centre of the streaming pattern. This is substantially lower than the streaming velocities generated by cavitation microstreaming, which may be of the order of 100 to >1000 μm/s (Fig. 4). Moreover, the streaming velocity in the μLAR is lower when compared with other acoustofluidic device configurations operated at comparable driving voltages. For instance, Lei et al.[103] reported a maximum in-plane streaming velocity of approximately 40 μm/s in an half-wave resonator operated at 30 Vpp (at 2.56 MHz), while Muller et al.[104] measured a maximum acoustophoretic velocity of 63 μm/s (for 0.5 μm diameter particles) in rectangular microchannels actuated at 1.62 Vpp and 1.94 MHz. The low streaming velocity makes μLAR devices suitable for discriminating the effects of acoustic streaming from those of US-RAs-induced microstreaming. A quantitative comparison with other acoustofluidic architectures is however difficult to perform, as the maximum streaming velocity depends on several factors including driving frequency, channel geometry, and the local acoustic pressure field.

3.3.3. Transducer temperature

Biological cells are typically very sensitive to variations in temperature and in a small fluid volume the heating produced by the ultrasound transducer cannot be ignored. The temperature response of the piezoelectric element was monitored during continuous excitation

using an infrared thermal imager (Monition Ltd, UK) at a room temperature of 23°C. The transducers were driven at 76.6 V for 15 minutes, and left to cool down for a further 15 minutes. Figure 26 shows the temperature over the transducer surface as a function of time, indicating a sharp increase in temperature (Δ1.5°C for the 500 kHz device, Δ1.0°C for the 1 MHz) in the first three minutes. This difference, however, is likely to have little influence on the temperature of the fluid layer, due to the thickness of the MACOR and glue layers. Furthermore, sonoporation studies do not typically involve long exposures (>10 min) to continuous wave ultrasound. This makes μLAR devices suitable for investigating the effects of ultrasound and US-RAs on target biological cells, by minimising secondary thermal effects caused by heating from the ultrasound source.

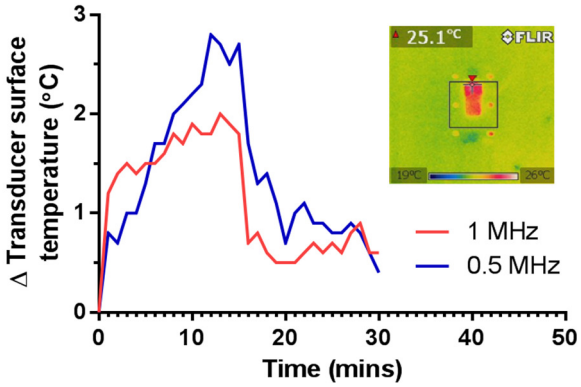


Figure 26 - Changes in transducer temperature during 15 minutes excitation followed by 15 minutes of cooling in both the 500 kHz and 1 MHz transducer. The transducers were both driven at 76.6 Vpp (n=1) . The inset shows a typical infrared image, which emphasises the heating piezoelectric element. The red arrow points to the maximum temperature within the area of interest (black frame), which is also reported in the top-left portion of the image.

3.3.4. Resonance frequency verification

The resonance frequencies of the devices were verified experimentally using an impedance spectral analyser (C60, Cypher Instruments LLC) and found to be 513 kHz and 908 kHz for the 0.5 MHz and 1 MHz devices, respectively. The impedance analysis was performed in both air- and water-filled conditions, in order to clearly identify the first thickness resonant frequency of the fluid-filled layered structure. The discrepancies between experimental measurements and 1D model predictions may be caused by fabrication tolerances, tightness of

the assembly, and lateral modes of vibration. The device was consistently operated at the experimentally determined resonant frequencies. Impedance spectra for both devices are shown in Figure 27.

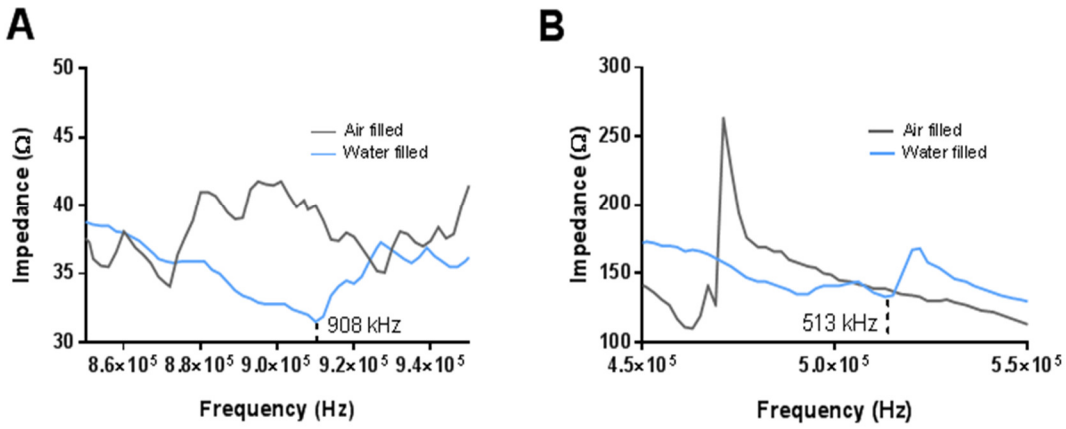


Figure 27 - Electrical impedance spectra for both 1.0 MHz (A) and 0.5 MHz (B) devices, and both air- and water-filled cavities. Resonant frequency of the devices is shown on each graph in correspondence with a through in impedance in the water-filled device that does not occur in the air-filled case.

3.3.5. Cell culture and sample preparation

A-549 cells, immortalized human alveolar adenocarcinoma cells, were grown in Dulbecco's Modified Eagle Medium (DMEM) with 10% fetal bovine serum (FBS) and 1% penicillin/streptomycin (P/S). MDCK cells, Madin-Darby canine kidney cells, were grown in DMEM with 10% FBS, 1% L-glutamine, 1% non-essential amino acids, and 1% P/S. Cells grown in T-75 flasks were passaged every three days at approximately 80% confluence. For experiments, approximately $1x10^6$ cells were seeded in 80 mm diameter petri dishes containing a single 75 mm 25 mm 0.17 mm glass coverslip (Logitech Ltd., Scotland) in 10 mL growth medium. Coverslips were sterilized in 70% ethanol for 30 min followed by washing with phosphate buffered saline (PBS) and 30 min UV exposure prior to seeding. Cells were grown in a temperature- and CO2-controlled incubator at 37°C and 5% CO_2. For experiments, the cells on glass coverslips were carefully transported to the μLAR device using sterile tweezers and washed twice with PBS by either pipetting directly into the inlet of the

device or by using a syringe pump with tubing connected to the inlet and outlet of the device. All materials were purchased from Thermo-Fisher unless stated otherwise.

3.3.6. Fluorescent labelling of cells and microbubbles

For Figure 31A, A-549 cell plasma membranes were labelled with a working concentration of 1X CellMask deep red in PBS, incubated for 10 min, and subsequently washed prior to imaging. Fluorescent microbubbles were produced according to the protocol described in Section 4.2.2.1 and labelled with the lipophilic dye, 1,1'-dioctadecyl-3,3,3',3'-tetramethylindocarbocyanine perchlorate (DiI) at 7:5000 from a stock solution containing 2.5 mg/mL DiI in dimethyl sulfoxide (DMSO, Sigma Aldrich, UK). In order to remove excess DiI from the formed MB suspension, the MB sample was centrifuged twice at 1000g for 10 min (400R Heraeus Labofuge), and MBs were re-suspended in PBS after each centrifugation cycle. prior to sonication and were subsequently washed 3x by centrifugation as described elsewhere[290]. For Figure 31B, A-549 cells were labelled with 200 nM C-Laurdan (Stratech Scientific ltd.) for 5 minutes prior to spectral imaging. For Figure 31C, MDCK cells were incubated with a PBS solution containing 1:1 DSPC-PEG 9:1 microbubbles (~1×10^8 microbubbles) and 1:20 propidium iodide (PI, red) and exposed to 0.140 MPa, 1 MHz, 60s continuous wave ultrasound. PI is cell-impermeable and fluoresces brightly upon binding DNA in membrane compromised or dead cells. Following ultrasound exposure, cells were labelled with 1 μM Calcein-AM 1:200 in PBS (green). Sonoporated cells are indicated by simultaneous propidium iodide and calcein-AM fluorescence. All materials were purchased from Thermo-Fisher unless stated otherwise.

3.3.7. Preparation of DSPC-PEG40s microbubbles

Therapeutically relevant phospholipid shelled microbubble production protocols were previously described by Carugo and colleagues[252]. 1,2-Distearoyl-sn-glycero-3-phosphocholine (DSPC, Avanti Polar Lipids, US) and polyoxyethylene (40) stearate (PEG40S, Sigma Aldrich,

UK) both dissolved in chloroform at 25 mg/mL and 10 mg/mL respectively, were mixed in a 15 mL glass vial at a 9:1 molar ratio. The solution was then heated on a hotplate set to 50°C for 12 h to allow the organic solvent to evaporate. The resulting dry lipid residue was suspended in 5 mL of phosphate buffered saline (PBS) solution for 1h on a hotplate set to 100°C. The lipids were then homogenised for 150 s at power rating 3 with a sonicator (XL 2000, probe diameter 3 mm, 20 W, 22.5 kHz, Misonix, USA) with the lipid completely immersed in the vial. Microbubbles were then formed by sonicating the the air-water interface for 30 s at power setting 14 while constantly blowing sulphur hexafluoride (The BOC Group plc, UK). The vial was capped and immediately placed in ice for approximately 5 minutes.

3.3.8. Preparation of magnetic perfluorocarbon droplets

A 1 mL of a solution of poly(ethylene glycol) methyl ether-*block*-poly(D,L-lactide)-*block*-decane in water (2.5 mg/mL) were added to 50 μL of perfluorohexane. The heterogeneous mixture was emulsified with an ultrasonic cell disruptor (Misonix Microson, 20 kHz, power setting 8, 20 seconds), diluted with 1 mL of water and washed three times by pelleting the droplets with a magnet and replacing the supernatant with PBS. The droplets were then further diluted by adding 3 ml of PBS and stored at 4°C.

3.3.9. Preparation of polymeric cups

Polymeric nanoparticles were synthesised using a technique[7] described by Kwan et al. in a previous publication[3]. A seed polymerisation technique was used to allow the entrapment and stabilisation of gas on the surface of polystyrene latex beads. In brief, the beads (2 mL at 10 wt%) were placed in a round bottom flask and diluted with filtered DI water until the final volume reached 36 mL. The flask was then deoxygenated using a nitrogen stream for at least 30 minutes. The flask was then transferred to a water bath which was preheated to 80°C. Methyl methacrylate (MMA), 2-hydroxyethyl methacrylate (HEMA) and divinyl benzene (80%, DVB) were then added to the mixture at a 10:1:6 v/v/v ratio, respectively. The solution

was then enriched with HEMA and DVB into a template particle mixture in a 10.1:1:6.4 9-anthracenylmethyl methracrylate (9ACM)-MMA/HEMA/DVB volume ratio. The reaction was then initiated with the addition of 1.7 mL potassium persulfate (KPS) at a 3.5 mg/mL concentration in water and was mixed vigorously for 5 hours. The solution was then washed suspended in DI water. Subsequently, the solution was air dried overnight to enable gas entrapment on the surface of the particles. The dry residue was then suspended in filtered DI water with 5% glucose and vigorously mixed to maximise dispersion.

3.4. Measurements

As indicated in the introduction, it is desirable to be able to perform simultaneous measurements of microbubble dynamics, fluid motion, acoustic emissions and cellular response within the same device in order to probe the mechanisms underlying bubble-cell interactions. The following sections describe how these measurements can be performed within the μLAR and present sample data for each.

3.4.1. Imaging of microbubble dynamics

Characterising the dynamic response of microbubbles to ultrasound excitation is essential in determining the mechanism(s) underpinning interactions between cells and US-RAs. Bubble oscillations may be highly non-linear, even at moderate ultrasound pressures, requiring extremely high imaging frame rates (>5MHz) and consequently specialised cameras and illumination sources.[292] To be compatible with these systems, the μLAR must provide sufficient optical access to the region of interest in terms of both the dimensions of the chamber and optical transparency of the upper layers. To confirm this, oscillations of SonoVue® (Bracco, Switzerland) microbubbles in the 500 kHz μLAR were recorded using the Brandaris 128 high-speed camera[256,293] in a series of 128 frame acquisitions recorded at 6 million frames per second (6 Mfps) at 10X magnification. The setup for Brandaris-128 experiments is shown in Figure 28A. To facilitate visualization of microbubble dynamics at

high frame rates in the μLAR, the Macor carrier layer was gold sputtered for 240 s at approximately 1 Angstrom/s, using a Cressington 108 sputter coater. The μLAR was positioned with the glass-reflector facing upwards toward the microscope objective of the Brandaris-128. Illumination was achieved using a CW LED source (KL2500 LED, Schott) and Xenon strobe flash.

A segment of the radius-time curve for an inertially-collapsing SonoVue® microbubble extracted from the camera footage can be seen in Figure 28B.

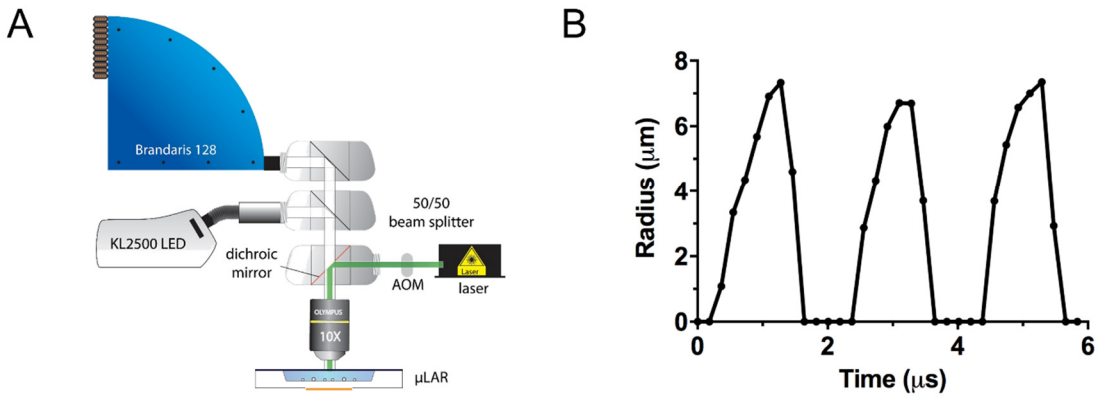


Figure 28 - Capturing microbubble dynamics in the μLAR with the Brandaris-128 high-speed camera. A. Schematic of the experimental setup. B. Radius-time curve from a single oscillating SonoVue® microbubble under 511 kHz ultrasound exposure as captured by the Brandaris-128 high speed camera at 6 million frames per second. Note that when the microbubble was too small to image, the radius was entered as 0 μm on the radius-time curve. The experiment was performed on one stationary microbubble.

3.4.2. Quantification of cavitation microstreaming velocities

Microstreaming has been hypothesized to play a major role in ultrasound-mediated drug delivery[273,294]. Shear stress and shear stress gradients have been associated with increased permeability[295,296], and may play a role in e.g. ultrasound-mediated blood-brain barrier opening[111,297] as well as in sonoporation[298]. It is therefore important to be able to visualise and quantify the flow field within the device so that correlation to cellular response can be investigated.

3.4.3. Particle streak velocimetry

There are multiple techniques for flow quantification, including particle image velocimetry (PIV), ultra-high-speed PTV[299] or astigmatism particle tracking velocimetry (APTV)[109,300]. For the purposes of illustration, the comparatively simple technique of PSV was used here but all of these methods can be employed with the μLAR. A suitable flow tracer, typically a suspension of fluorescent particles is injected into the region of interest. The motion of the tracer is then imaged over a series of frames. If the image exposure time is longer than the time required for a tracer particle to travel the physical pixel size of the images, a streak is produced in the image capturing the path of the particle. The average velocity of the tracer particle during the exposure time is the measured arc-length of the streak in the image divided by the exposure time. Thus with PSV, rapid changes in the flow field can be quantified from a single streak image.

3.4.4. Microstreaming from different US-RAs

Streak images were obtained by co-injection of a solution containing 2 μm diameter fluorescent beads used as flow tracers (Sigma Aldrich, used at 1:1000 dilution) with one of 3 different US-RAs: SonoVue® microbubbles, gas-trapping polymeric cups, and phase-shift droplets. Preparation of these cavitation agents is detailed in Sections 3.3.6-3.3.8. In the 1 MHz μLAR, SonoVue® microbubbles (Figure 29A and 26B), gas-trapping polymeric cups (Figure 29C and 4D), and phase-shift droplets (Figure 29E and 4F) all produced cavitation microstreaming flows under ultrasound exposure. At 1 MHz, a dipole microstreaming pattern with the microbubble located at the centre of the dipole was most commonly observed. Streaming patterns involving multiple microbubbles were also observed that were qualitatively similar to those described by Ooi et al. for larger bubbles [109]. The highest recorded microstreaming velocities, as determined by PSV, were on the order of 1000 μm/s and microstreaming patterns were found to produce velocities greater than 100 μm/s at a distance of more than 1 mm from the cavitating microbubble. This corresponds to an average wall

shear stress from microstreaming on the order of 1 mPa which agrees well with the study by Collis et al.[254] on shear stress from cavitation microstreaming.

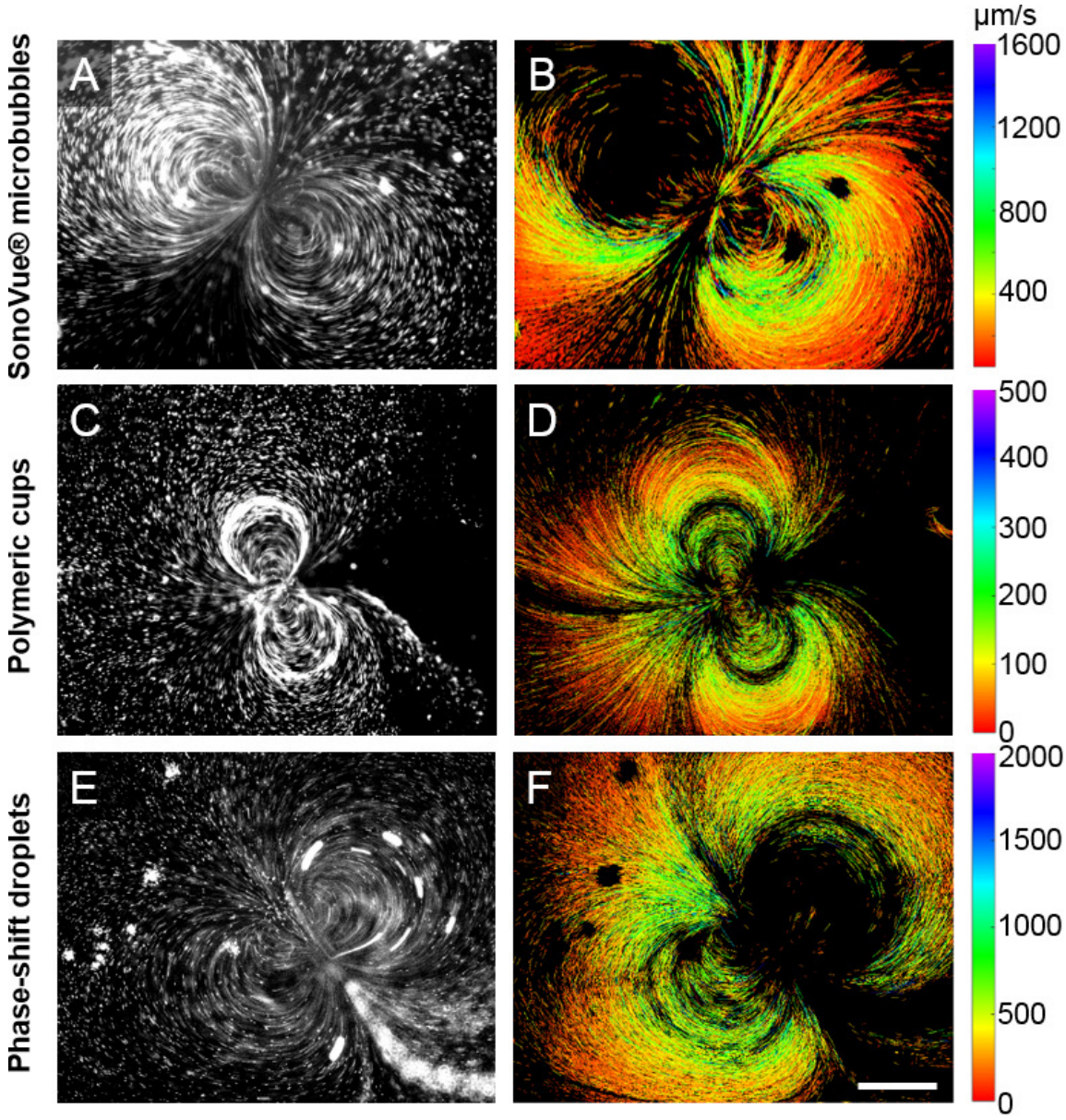


Figure 29 - Streak velocimetry performed on videos of fluorescent tracer beads moving in cavitation microstreaming flows induced by SonoVue® microbubbles (top), gas-trapping sub-micron polymeric cups (middle), and phase-shift droplets (bottom) under ultrasound exposure inside the µLAR. Figures show a brightness and contrast enhanced still from the videos analysed (left), and a pseudo-coloured composite of the headless velocity vectors for each streak analysed in the respective video (right). Colour bars are in µm/s. Scale bar = 350 µm. The USRAs were driven at 511 kHz, 0.146 MPa.

3.4.5. Monitoring of acoustic emissions

Acoustic emissions monitoring provides a means of classifying and quantifying cavitation activity non-invasively during ultrasound-mediated therapy with clinically-relevant spatial and temporal resolution [301,302]. It is thus of interest for any *in vitro* experiment investigating cavitation to simultaneously (passively) monitor acoustic emissions. Acoustic emissions from SonoVue® (Bracco, Switzerland) microbubbles, which give rise to both non-inertial and inertial cavitation activity, and gas-trapping polymeric cups, which only cavitate inertially, were monitored using a commercially-available electrically-insulated 28 μm thick polyvinylidene difluoride (PVDF) film sensor (SDT1-028K, Measurement Specialties) whilst exposed to ultrasound in the 500 kHz μLAR device. The sensor was externally coupled with ultrasound gel to the glass reflecting layer and held in place using the aluminium frame of the 500 kHz μLAR device. The voltage output from the PVDF sensor was amplified with 5X gain (SR445A, Stanford Research Systems) before being recorded with an oscilloscope (Waverunner 62 X*i*, Teledyne LeCroy).

It was found that the PVDF film sensor externally-coupled to the 500 kHz μLAR device was capable of detecting harmonic, ultra-harmonic, and broadband emissions from clinical ultrasound contrast agent SonoVue® microbubbles (Bracco, Switzerland) and polymeric nanocups (see Figure 30). The acoustic emissions results and fibre-optic hydrophone pressure measurements obtained from the acoustofluidic device are in good agreement with the acoustic emissions thresholds reported in the literature[63] for SonoVue® at 500 kHz and obtained using a conventional water-tank apparatus. Harmonic emissions at low ultrasound pressure, followed by widening of harmonic peaks and leakage of energy into ultra-harmonics as the ultrasound pressure increased, and finally broadband emissions at high ultrasound pressures were observed (Figure 30).

Acoustic emissions from gas-trapping polymeric cups are decidedly different. Notably, the acoustic emissions data from polymeric cups in the 500 kHz μLAR agree with the previously

described[39] broadband emissions threshold for these cavitation nuclei. Upon increasing the acoustic pressure, the polymeric cups exhibit a step-change from producing only modest acoustic emissions to producing substantial broadband noise. This threshold is hypothesised to be associated with the pressure required to elicit a bubble from the cup, which is coincident with the inertial cavitation threshold[303].

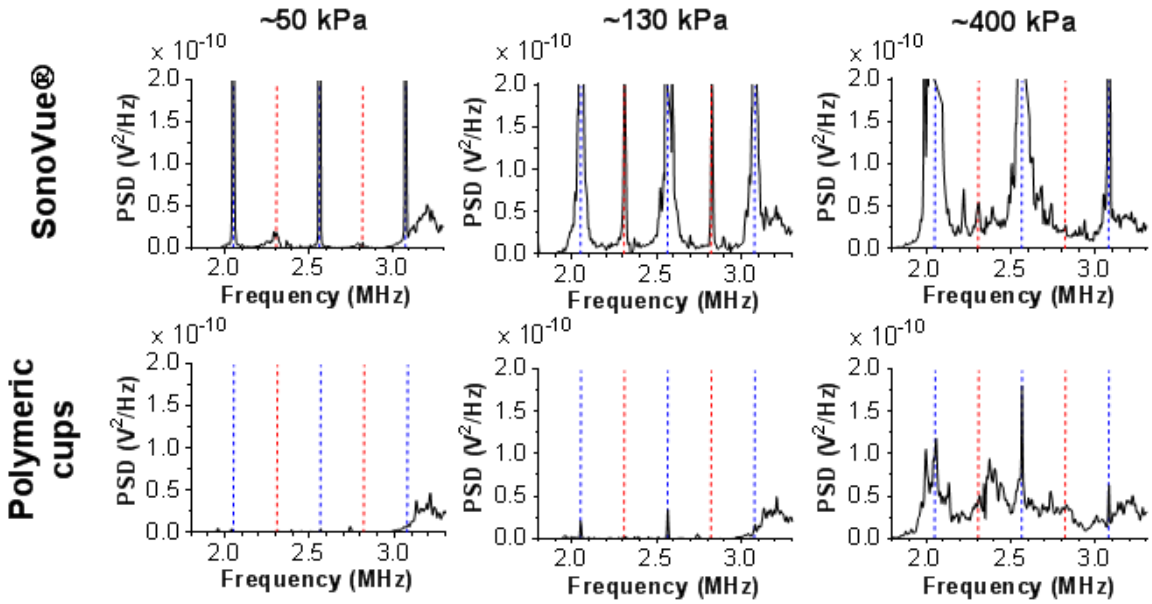


Figure 30 - Acoustic emissions of SonoVue® and polymeric cups exposed to 511 kHz ultrasound in a μLAR device, as detected by an externally-coupled PVDF film sensor. The power spectral density shown following background subtraction using the acoustic emissions of a control sample (no cavitation nuclei). The blue dashed lines indicate the harmonic frequencies. The red dashed lines indicate the ultra-harmonic frequencies. The acoustic pressure for each condition is indicated above.

3.4.6. Monitoring of biological effects

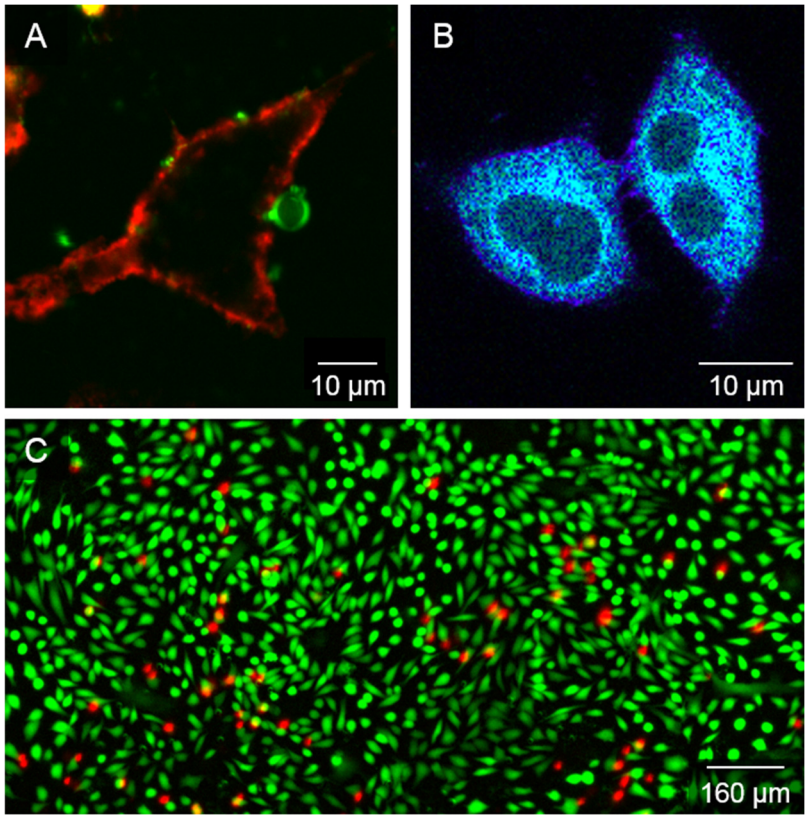


Figure 31 - Demonstration of microscopy with the µLAR device and biological cells. A. A-549 cell plasma membrane labelled with CellMask™ (red) and a fluorescent microbubble labelled with DiI (green) adhering to the cell membrane. B. A-549 cells labelled with polarity-sensitive dye c-Laurdan, used to determine membrane physical properties such as lipid packing. Image taken following ultrasound and microbubble exposure. Purple/blue regions indicate areas with higher/lower lipid bilayer hydration, while the dark areas within the cells indicate the cell nuclei. C. Sonoporation assay using cell-impermeant propidium iodide (red) to indicate permeability or cell death, and calcein (green) to indicate cell viability in MDCK cells exposed to ultrasound and microbubbles. Sonoporated cells are indicated by simultaneous propidium iodide and calcein fluorescence. The percentage of sonoporated cells was quantified using a purpose-built MATLAB script and determined to be 5.5% (872 cells stained with calcein and 52 stained with PI).

Fluorescence microscopy for visualising and quantifying interactions between US-RAs and cells remains an indispensable modality for understanding the interplay between such experimental parameters and the resultant biological effects. It has been used to quantify changes in intracellular calcium[304], reactive oxygen species generation[134], actin cytoskeleton integrity[305], membrane lipid ordering[252], and vesicular activity[253] among others[140,261]. The µLAR devices presented herein enable simultaneous control of ultrasound excitation and

fluorescence microscopy without the need for the more complex setups often employed to conduct such mechanistic investigations. In addition to compatibility with high magnification fluorescence microscopy, a key feature of the μLAR design is the ability to visualize during ultrasound exposure enabling the quantification of dynamic processes whether mechanical (e.g. microbubble oscillations, microstreaming flow fields, microbubble/cell membrane penetration), chemical (e.g. reactive oxygen species generation, lipid shedding/exchange), thermal (e.g. using thermo-sensitive dyes), or biological (e.g. subcellular response, drug uptake, vesicular transport). Protocols for using μLAR devices with living cells and fluorescence microscopy are detailed in Section 3.3.5. Examples of the utility of the μLAR for conducting *in vitro* experiments with cells and microbubbles are illustrated in Figure 31.

3.4.6.1. Bubble-cell interactions

Figure 31A shows the direct interaction between a fluorescent microbubble and a fluorescently-labelled cell plasma membrane following exposure to CW ultrasound at 1 MHz, 210 kPa for 60 s. This demonstrates the ability to visualize living cells and microbubbles *in situ* within the μLAR at high spatial resolution during and after ultrasound exposure.

3.4.6.2. Quantification of cell membrane properties

The μLAR also facilitates monitoring of cellular response to ultrasound exposure using appropriate fluorescent probes and quantitative microscopy techniques. Figure 31B shows cells labelled with a polarity-sensitive dye, c-Laurdan, used to determine membrane lipid packing as an indicator of permeability. The cells were imaged at 30 different emission wavelengths to quantify the spectral shift of c-Laurdan in response to ultrasound and microbubbles exposure. This technique was employed recently to quantify changes in the lipid packing of membranes resulting from the transfer of phospholipids from microbubbles shell to cell plasma membranes[252], in the 1 MHz μLAR.

3.4.6.3. Quantification of intracellular delivery

Targeted delivery of therapeutics is a key application area of biomedical ultrasound research. One way to achieve ultrasound and cavitation-enhanced delivery of therapeutics is by cavitation-mediated permeabilisation of the cell membrane, often referred to as sonoporation. In a third example experiment with the μLAR device, MDCK cells were sonoporated following ultrasound and microbubble exposure in the 500 kHz μLAR device. Figure 31A shows the results of a typical fluorescence sonoporation evaluation using cell-impermeant propidium iodide (red) to indicate permeability or cell death, Calcein (green) to indicate cell viability, and co-localized propidium iodide and Calcein fluorescence to indicate successful sonoporation. Figure 31B shows cells labelled with a polarity-sensitive dye, c-Laurdan, used to determine membrane lipid packing as an indicator of permeability. Panel C indicates the relative numbers of cells that are viable, dead, permeabilised or combinations thereof. The μLAR thus provides the opportunity for investigating sonoporation efficiency as function of a wide range of experimental parameters (e.g. driving frequency, pulse repetition frequency (PRF), pulse length, total exposure time, dissolved gas concentration, cavitation agent). Such an optimization for the cell line of interest is ideal before conducting *in vitro* and *in vivo* investigations involving sonoporation on drug delivery or bio-effects. The μLAR serves to ease the experimental burden of this often expensive and time-consuming endeavour[128,306,307].

3.5. Limitations and future perspectives

In its current configuration, the μLAR utilises a rigid glass surface as a substrate for biological cells. The mechanical properties of physical boundaries can impact on microbubble cavitation dynamics and the associated microstreaming patterns; but they will also have an effect on the behaviour of cells either in the presence or absence of mechanical stimuli. Future work will investigate how these properties may influence ultrasound-mediated bioeffects. Reflector layers with different mechanical properties could be employed to mimic different soft and hard target tissues. For instance, Glynne-Jones et al. [279] reported on a thin-reflector resonator comprising a cellulose acetate reflector layer, designed for manipulation of microparticles towards a surface. In order to mimic a softer substrate (which is relevant to many *in-vivo* conditions), the glass surface could also be coated using an acoustically- and optically-transparent hydrogel. For instance, the acoustical properties of biocompatible materials - including hydrogels - with different stiffness have been systematically investigated in a recent study by Cafarelli et al.[308]. Cells could be potentially seeded within the hydrogel layer to also generate a three-dimensional microenvironment, as opposed to a two-dimensional monolayer of cells as reported in the present study.

In this study, acoustic pressures in the range 0-0.4 and 0-0.3 MPa for the 0.5 and the 1 MHz resonators, respectively were reproduced. It may however be desirable to generate a wider range of acoustic pressures, to replicate different acoustic stimulation regimes and therapeutic applications of ultrasound. In order to minimise undesired increase in transducer temperature at the higher driving voltages, the use of pulsed wave may be preferable. A temperature controlled system (based on Peltier elements) could also be integrated with the device, as reported by Ohlin et al.[276] for an acoustofluidic device intended for cell levitation and manipulation at 1 MPa acoustic pressure.

Again, in the experiments reported here, flow was only utilised to enable changes of medium and for injection of tracer particles and fluorescent dyes. It should be noted, however, that

μLAR could also act as a flow cell, for exposure of biological cells to physiologically relevant fluid shear stress levels. The aspect ratio of the fluid layer and its tapered inlet/outlet sections are designed to generate a relatively uniform shear stress field over the reflector surface. Flow perfusion may also be beneficial if medium replenishment is needed, for long-term acoustic stimulation experiments. In addition, particle trapping and size-selective sorting of micro-scale particles has been achieved by manipulating cavitation microstreaming patterns in the presence of a pressure-driven background flow[309]. The μLAR device concept could be employed to further develop and characterize this technique.

3.6. Conclusions

Ultrasound, in particular in combination with US-RAs, has shown potential for inducing therapeutically relevant effects on cells and tissues, with application in the treatment of malignant and non-malignant diseases. A more comprehensive understanding of their interaction with biological systems however, requires the ability to generate acoustic fields within physical domains that are accessible by high-resolution analytical and optical instruments. This is difficult to achieve using water-tank based equipment that is commonly employed in biomedical ultrasound laboratories.

In order to overcome this limitation, the design, fabrication and experimental characterisation of acoustofluidic resonators (μLARs) suitable for investigating the acoustic behaviour of US-RAs and their interaction with biological cells were presented. The devices are based on a thin-reflector resonator configuration, adapted to minimise pressure gradients in the direction of ultrasound propagation; as well as thermal and other secondary effects of ultrasound, e.g. acoustic streaming, allowing for the discrimination of the effects of US alone from those of US-RAs.

In this chapter, the generation of ultrasound fields at therapeutically relevant acoustic pressures and frequencies; compatibility of the devices with ultra-high speed imaging for monitoring microbubble dynamics; the integration of transducers for simultaneously recording acoustic emissions; quantification of the microstreaming flows produced by different US-RAs using particle streak velocimetry; and observation and quantification of ultrasound/cavitation mediated changes in cell membrane permeability and intracellular delivery using fluorescence microscopy were demonstrated. The device presented in this chapter was used throughout Chapters IV and V to expose vesicles to therapeutically relevant stimuli.

IV

Investigating the role of membrane hydration as a mediator of permeability in microbubble mediated drug delivery

This chapter builds upon the work presented in Chapters I and II and explores the effect of different exposure regimes on the membrane hydration and permeability of giant unilamellar vesicles. The effect of exposing vesicles to clinically relevant pressure-driven flow, ultrasound, microbubbles, PEG40s, and lipid debris, alone and in combination, were investigated.

The author gratefully acknowledges the assistance of Dr. Luca Baù in the analysis of fluorescence uptake inside giant vesicles. The author also acknowledges Dr. Joshua Owen for the production of microbubble suspensions.

4.0 Abstract

Whilst ultrasound responsive microbubble agents hold much promise for targeted delivery of therapeutic compounds, the biophysical mechanisms that underpin the interactions between microbubbles and cells are still poorly understood. To investigate these mechanisms, Giant Unilamellar Vesicles (GUVs) made with 1,2-dioleoyl-*sn*-glycero-3-phosphocholine and cholesterol were employed as cell models to quantify changes in membrane properties as a result of exposure to ultrasound (1 MHz, 188 kPa, 60 s continuous-wave) and phospholipid-shelled microbubbles both separately and in combination. Quantification of membrane lipid order in vesicles was performed by spectral imaging of a polarity-sensitive dye, c-Laurdan, and subsequent determination of the Generalised Polarisation (GP). In parallel, the permeation of a model drug (fluorescein sodium salt) through the lipid bilayer was analysed optically by confocal microscopy. There was found to be a positive correlation between fluorescein uptake and the reduction in lipid packing produced by ultrasound exposure. This was similar to the effect of pressure-driven flow in the surrounding medium and therefore attributed to the shear stress produced by acoustic streaming. The addition of microbubbles, both with and without ultrasound, led to a high spatial variability in vesicle membrane packing. Confocal imaging indicated that this was the result of material transfer between the microbubble shell and vesicles. An increase in fluorescein uptake followed, and was attributed to the creation of local regions of high membrane permeability at the fluid-gel phase boundaries. The results thus indicate that a combination of physical and chemical effects are involved in the interactions between microbubbles and lipid bilayers, potentially benefiting the design of microbubble agents for therapeutic delivery.

4.1. Introduction

The biological effects caused by ultrasound and microbubbles are dependent on the ultrasound frequency, intensity, and time of exposure, as well as the nature of the tissue involved[310]. At therapeutic frequencies (0.25-1.6 MHz), and relatively low acoustic pressures (<500 kPa), the rapid volumetric changes that microbubbles undergo when subjected to an oscillatory pressure field can cause various biological effects. The repetitive radial expansions and contractions impart mechanical stresses on cell membranes on wide-ranging time and length scales.[119]

The streaming flows resulting from microbubble oscillation can also impose significant fluid shear stress on the surrounding biological tissue up to several hundreds of micrometres away from the cavitation source. This effect has been shown to enhance drug transport and delivery of conventional systemic therapies in tissue and across the cellular membrane[135]. These effects are intensified by primary and secondary acoustic radiation forces that displace the microbubbles towards nearby surfaces, such as other microbubbles and vessel walls.

Several studies have demonstrated that the use of microbubbles and ultrasound in combination may lead to transient membrane pore formation, accelerate clot lysis, and breach the blood brain barrier (BBB). This enables the intracellular transport of normally membrane-impermeable macromolecules such as genetic drugs, peptides, and proteins[11] across the cell membrane – considerably extending the available therapeutic options compared to traditional systemic administration of free chemotherapeutics.

Chemical interactions may also play an important role in sonoporation. *In vitro* studies have reported that contact between the microbubble shell and the cell membrane causes material deposition or transfer from the microbubble shell to the cell membrane[139,140]; altering the cell membrane's properties and potentially acting as a delivery vehicle. The generation of Reactive Oxygen Species (ROS) has also been reported as a potential mechanism for sonoporation. In fact, ROS modulate the intracellular Ca^{2+} balance and trigger membrane lipid peroxidation[73],

which in turn leads to membrane disruption and poration[143], permeabilisation[143], and the formation of raft-like structures[134].

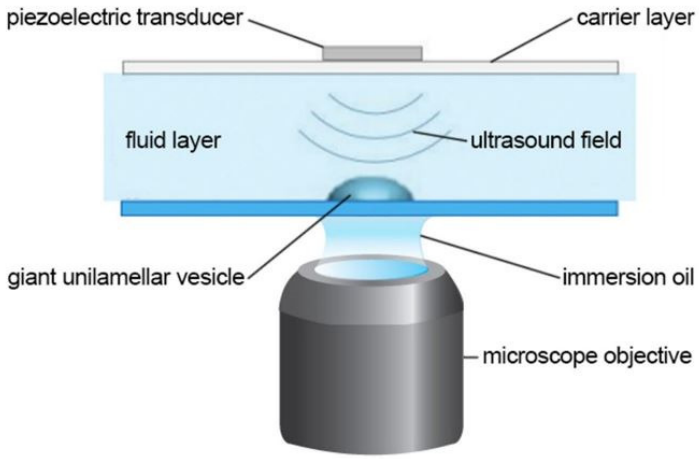


Figure 32 - Experimental setup showing a fixated vesicles subject to ultrasound exposure in the presence of microbubbles. The cross-sectional diagram is not to scale.

Previous work[252] has provided preliminary evidence of the ability of microbubbles to alter the plasma membrane properties of A549 and CHO-K1 cells, with and without ultrasound exposure, in a manner that was dependent upon the microbubble formulation. In addition, it was found that polyethylene glycol stearate (40) had a fluidising effect on cell membranes, which diminished when the microbubble solution was washed by centrifugation. Results using vesicles in suspension also suggested that exposure to microbubbles affected their lipid membrane order. Ultrasound alone, however, had no or very limited effect on the lipid order of either cellular or artificial membranes.

The present study investigates further the effect of different exposure conditions on the lipid order of artificial bilayers and whether or not these are related to changes in membrane permeability. GUVs provide a tuneable biomimetic membrane model that allows the study of fundamental effects on lipid membranes. Lipid membranes play an important role in the cell's physical organisation, protein function, active and passive transport, and signalling[311]. By selectively probing lipid membrane properties, the individual linkages with each of these

functions can be made more readily. Furthermore, the tuneable size and composition, coupled with the invariant quasi-spherical shape of GUVs, enables facile quantification of membrane and intra-vesicle fluorescence over extended periods of time when compared to cells.

Building on this previous work, lipid packing was quantified as a measure of membrane response as it is an important determinant of membrane permeability[312] and affects numerous cellular functions and properties. These include the mobility of proteins and membrane rafts[146,313,314], the opening and closing of ion channels[315] and cellular proliferation and death.[316–318] Moreover, single-vesicle measurements to quantify the uptake of fluorescein sodium salt (fluorescein) as a model drug, were performed. Fluorescein is a water-soluble fluorescent molecule that has been widely used to study the permeability of lipid membranes, cells, and vessels. It is normally impermeable to lipid membranes and its size and partition coefficient are comparable to common chemotherapy drugs such as Fluorouracil (5FU).

Quantifying the physico-chemical effects of microbubble-membrane interactions that underpin ultrasound and microbubble mediated drug delivery is important to enable the design of effective, repeatable, and predictable treatments. In this study, evidence of how ultrasound and phospholipid-shelled microbubbles, alone and in combination, can alter the hydration levels and permeability of cholesterol-doped GUVs was provided. The effect of microbubble constituents, such as lipids and PEG40s, on the properties of lipid membranes was also examined by providing microscopic evidence and quantitative data on membrane hydration and fluorescence uptake.

4.2. Materials and methods

4.2.1. Giant unilamellar vesicle characterisation

4.2.1.1. GUV formation protocol

Vesicles were electroformed on stainless steel needles following a previously described protocol developed in-house.[319] In brief, solutions of 1,2-distearoyl-sn-glycero-3-phosphocholine (DOPC) (25 mg/mL in chloroform) and cholesterol (Chol) (10 mg/mL in chloroform) were mixed at varying molar fractions (1:0, 3:1, 1:1, and 3:1). 1,2-dipalmitoyl-sn-glycero-3-phosphoethanolamine-N-(cap-biotinyl) sodium salt (DPPE-biotin) was then added to the solution at 1 mol% to functionalise the lipids and allow for vesicle fixation. The resulting solution was then pipetted vertically onto a pair of stainless steel electrodes (50 µl per pair) using a 100 µl glass syringe. After drying, the electroformation chamber was filled with sucrose solution (~3 mL, 200 mM sucrose in MilliQ deionised water at 23°C), the electrodes were submerged, and the signal generator (Agilent 33220A) was connected using brass rods on the chamber sides. A 10 Hz, 5-volt peak-to-peak voltage (Vpp) sinusoidal excitation was then applied for 2 hours, followed by 30 minutes at a lower frequency of 5 Hz to facilitate vesicle detachment. 400 µl of the resulting vesicle suspension was pipetted into a 2 mL Eppendorf tube containing 100 µl of phosphate buffered saline (PBS) solution, ready for injection into the acoustofluidic device.

4.2.1.2. Glass functionalisation and vesicle fixation

To avoid vesicle motion between and during image acquisitions, and to provide more accurate modelling of the vessel's endothelial layer, the vesicles were fixed to the chamber's glass slide using an avidin-biotin linkage.[320] The glass was primed by injecting 600 µl of a solution containing biotin labelled bovine albumin (bBSA) (10 mg/mL in PBS) which was incubated in the device for two hours at room temperature. After washing with deionised water, an avidin solution (1 mg/mL in PBS) was injected into the device and incubated for an

additional four hours. After repeating the washing step, a 500 µl vesicle suspension was injected and the vesicles were allowed to sediment for 30 minutes.

4.2.1.3. Vesicle-glass binding strength

To determine the wall shear stress that the vesicles would be able to withstand without detachment, GUVs were fixed to the glass and subjected to flow rates in the range of 0-6000 µL/min (corresponding to a wall shear stress in the range of 0-12.5 Pa). The flow was generated by a syringe pump (New Era Pump Systems Inc., USA) connected to the inlet of the device. Flow exposure protocols comprised the following steps: (i) the vesicles were exposed for one minute, (ii) the flow was paused, (iii) the vesicles were counted, and (iv) the flow rate was increased further. Vesicles were counted manually using ImageJ® Cell Counter, and a percentage was computed based on the ratio of vesicles still attached to the glass after flow, compared to their initial number.

4.2.2. Preparation of microbubble solutions

4.2.2.1. DSPC-PEG40s microbubbles

The microbubble suspensions were formed using the protocol described in Section 3.3.7. In brief, 1,2-Distearoyl-sn-glycero-3-phosphocholine (DSPC) and polyoxyethylene (40) stearate (PEG40s) were dissolved in chloroform, at a 9:1 DSPC: PEG40s molar ratio. The resulting solution was then placed in a 15 mL glass vial and chloroform was evaporated overnight using a hotplate set to 50˚C. The vial was then filled with 5 mL PBS and stirred for 30 min on a hotplate set to 100˚C. The solution was then sonicated with a fully submerged tip for 150 s, followed by a second sonication for 20 s while blowing Sulphur Hexafluoride (SF_6) at the gas-liquid interface. The vial was then placed in ice for approximately 15 minutes and the suspension was washed three times by centrifugation (300 RCF, 10 min) and diluted in PBS to reach a final concentration of ~$1x10^6$ microbubbles/mL. Bright field microscope images of microbubbles were acquired within a Neubauer haemocytometer. Microbubbles were then

counted and sized using a purpose-built algorithm previously developed by Sennoga and colleagues[321].

4.2.2.2. DSPE-PEG2000-Rhodamine microbubbles

The microbubble suspensions were formed by dissolving 1,2-Distearoyl-sn-glycero-3-phosphocholine (DSPC), 1,2-distearoyl-sn-glycero-3-phosphoethanolamine-N-[(methoxypolyethylene glycol)-2000] (ammonium salt) DSPE-PEG(2000) and 1,2-dipalmitoyl-sn-glycero-3-phosphoethanolamine-N-(lissamine rhodamine B sulfonyl) (ammonium salt) at an 89:10.7:0.3 molar ratio. The resulting solution was then placed in a 15 mL glass vial and chloroform was evaporated overnight using a hotplate set to 50°C. The same protocol used for the DSPC-PEG40s microbubbles described in section 2.2.1 was followed hereafter.

4.2.3. Generalised polarisation measurements

Membrane hydration has been used in the past as a proxy to quantify the degree of lipid packing in membrane bilayers[322]. The emission spectrum of c-Laurdan, a lipophilic environment-sensitive fluorescent probe, varies as a function of the dipolar relaxation of water, which is related to the level of hydration and order of its surrounding microenvironment. Generalised Polarisation (GP)[182] was employed as a relative measure to quantify lipid packing. Its value ranges from -1 to +1, where -1 and +1 represent the lowest and highest levels of packing, respectively. Equation 13 expresses the GP relative to the emission intensity of c-Laurdan (Figure 3e) at two specific wavelengths, 440 and 490 nm. The microbubbles and vesicles were fluorescently labelled with c-Laurdan at a concentration of 400 nM incubated for approximately 30 minutes, excited using a 405 nm laser, and imaged using a Zeiss 780 confocal microscope equipped with a 63x Plan-Apochromat 63x/1.40 Oil DIC M27 objective and 32-channel GaAsP detector array. The image stacks were processed using a previously

developed[171] MATLAB® routine to obtain vesicle GP values, contours and histograms for different GUV populations.

4.2.3.1. Effect of photobleaching on generalised polarisation

Control experiments were performed to determine whether imaging a single GUV multiple times would affect the membrane GP. Single vesicles with varying cholesterol content were imaged consecutively four times with a Zeiss 63x Plan-Apochromat objective at 2 % laser power, with pinhole set to one Airy Unit and frame size of 512x512 pixels. The mean membrane GP values of the control and the mean GP after four acquisitions were compared for varying amounts of cholesterol.

4.2.4. Acoustofluidic device

A purpose-built thin-reflector acoustofluidic chamber described in Chapter III was used throughout the experiments presented in this chapter. The device was driven at a clinically relevant frequency of 1 MHz with acoustic pressures up to 400 kPa and used as a flow cell to expose vesicles to ultrasound, steady flow, and microbubbles.

4.2.4.1. Frequency and pressure field characterisation

The layer thicknesses were designed to minimise the acoustic pressure gradient across the fluid channel, thereby creating a spatially uniform pressure field. By performing a frequency sweep using an impedance spectrum analyser (Cypher Instruments, UK), a driving frequency of 1.014 MHz was selected as the resonant frequency of the multi-layered structure. A 70 mVpp sinusoidal waveform was generated using an Agilent 33220A function generator, amplified 55dB using a RF power amplifier (Aquitek, France) and fed to the piezoelectric element. To characterise the acoustic pressure in the fluid layer, a fibre-optic hydrophone (Precision Acoustics ltd, UK) was inserted within the fluid channel through a 0.5 mm hole in the glass

slide. Figure 34c shows the acoustic pressure inside the fluid layer as a function of the signal generator output voltage.

4.2.4.2. Acoustic streaming

The acoustic streaming set up during ultrasound exposure was quantified optically using Particle Tracking Velocimetry (PTV). A solution of 1 μm diameter fluorescent latex beads (1% v/v) in deionised water was injected into the device. The solution was then exposed to ultrasound at varying acoustic pressures, each for one minute. The flow tracers were then tracked using the TrackMate® ImageJ® plugin from microscope images acquired using a Nikon ECLIPSE Ti inverted microscope (Nikon Corporation, Japan). Bead velocities in a plane corresponding approximately to the GUV mid-plane were then computed and averaged as a function of acoustic pressure.

4.2.4.3. Temperature changes as a result of US exposure

The temperature changes on the surface of the piezoelectric element were monitored using a FLIR infrared thermal camera (Monition, UK). The piezoelectric chip was driven at 76.6 Vpp (the maximum driving voltage used to minimise heating) for 15 minutes and left to cool for a further 15 minutes. The temperature was recorded every minute throughout the experiment.

4.2.5. Vesicle excitation modes and protocols for GP quantification

Changes in vesicle membrane lipid packing were quantified as a result of four modes of excitation, as reported below in paragraphs 2.5.1-2.5.5. In each case, control GP values were acquired, stimulation was applied for one minute, and post-excitation values were obtained. GUVs were examined at the ambient temperature of ~23°C.

4.2.5.1. Shear flow only

Phosphate-buffered Saline (PBS) was flowed into the device using a syringe pump to achieve an average wall shear stress of 1.25 Pa. The average wall shear stress was calculated from:[323]

$$\tau_w = \frac{6Q\mu}{h^2 w} \quad \textit{Equation 15}$$

where Q is the volumetric flow rate, μ is the dynamic viscosity of the perfusate, and h and w are the cross-sectional dimensions of the flow channel. Physiological flow velocities range from ~30 μm/s in capillaries, 15 mm/s in the vena cava, and 40 cm/s in the aorta. Physiological shear stress levels range from 0.1 to 6 Pa in the venous system with peaks of 7 Pa in the arteries[324]. The flow rate was chosen as an approximate value of the cavitation microstreaming flows (in the order of a few mm/s) recorded in the same device previously by the authors.

4.2.5.2. Ultrasound only

The piezoelectric transducer was driven continuously with a sinusoidal waveform at 39.4 Vpp and 1.014 MHz, to achieve an acoustic peak negative pressure of 188 kPa. The ultrasound was delivered continuously to deliver a higher ultrasound dose and enhance bioeffects. An optimisation of exposure parameters is however required to maximise treatment efficiency. Nonetheless, the acoustic pressure employed lies within the low-end range of pressures known to produce bioeffects reported previously in sonoporation studies. These include, but are not limited to, pore formation (peak-to-peak pressure = 190 kPa, PRF = 10kHz, 20 cycle burst, 40 s)[325], membrane hyperpolarisation (peak-to-peak pressure = 500 kPa, PRF = 20 Hz, duty cycle = 0.2%, duration = 40 s)[121], and uptake of fluorescently labelled dextrans (peak-negative pressure = 220 kPa, 6.2% duty cycle, 20 Hz PRF, duration = 30 s).[129]

4.2.5.3. Microbubbles only

A 500 µl microbubble suspension was gradually injected into the chamber using a micropipette and incubated for one minute. The chamber was then washed gently by injecting 1 mL of PBS.

4.2.5.4. Ultrasound and microbubbles combined

Immediately following microbubble injection, the vesicles were exposed to an ultrasound field with the same conditions outlined in Section 4.2.3.3. The vesicles were then washed with 1 mL of PBS.

4.2.5.5. Free PEG40s

The effect of free PEG40s on the lipid packing of GUVs containing varying amounts of cholesterol, was investigated. For each lipid formulation, a 250 µL GUV solution was diluted with either an equal volume of PBS or a PBS solution containing free PEG40s (0.5 mg/mL). This concentration was chosen by calculating the theoretical maximum concentration of PEG40s in a microbubble suspension prior to injection. The membrane GP in the presence and absence of PEG40s was determined for each formulation.

4.2.6. Visualisation of microbubble shell material deposition

To observe and quantify microbubble lipid colocalisation in the vesicle membrane, GUVs were stained using the lipophilic dye (1% w/v) CellMask™ Deep Red (excitation peak: 650 nm, emission peak: 670 nm), while microbubble lipids were tagged with Rhodamine B (excitation peak: 550 nm, emission peak: 580 nm). To avoid spectral bleed-through, the two fluorophores were selected for having distinct excitation and emission characteristics. The microscope acquisition settings were also tuned to ensure no overlap in emission. To quantify colocalisation of microbubble lipids with the vesicle lipids, the signal overlap between microbubble shell fragments and GUVs was determined using Costes' mask following

thresholding. The size of the lipid fragments (> 4 pixels, ~500 nm) was determined using the Zeiss Zen Black® native microscope suite. GUVs were examined at the ambient temperature of ~ 23°C.

4.2.7. Modulation of the uptake of a model drug during treatment

To relate the changes in membrane GP to changes in permeability, fluorescein sodium salt was used to quantify uptake as a result of exposure to different treatments. An aliquot of 3:1 DOPC:Chol vesicles was mixed in equal volumes with a 60 μM fluorescein solution in PBS. The resulting solution was then pipetted inside the acoustofluidic device and similar excitation protocols to those described in Section 4.2.3 were applied. The vesicles were imaged during the course of 30 minutes using a Zeiss LSM 780 confocal microscope, while the fluorescence signal inside the vesicles was analysed using a custom-built Matlab® routine. The data were then normalised to the initial fluorescence value and to the background signal of the fluorescein. Figure 33 shows a representative image of the vesicles, outlining the analysis steps performed by the routine.

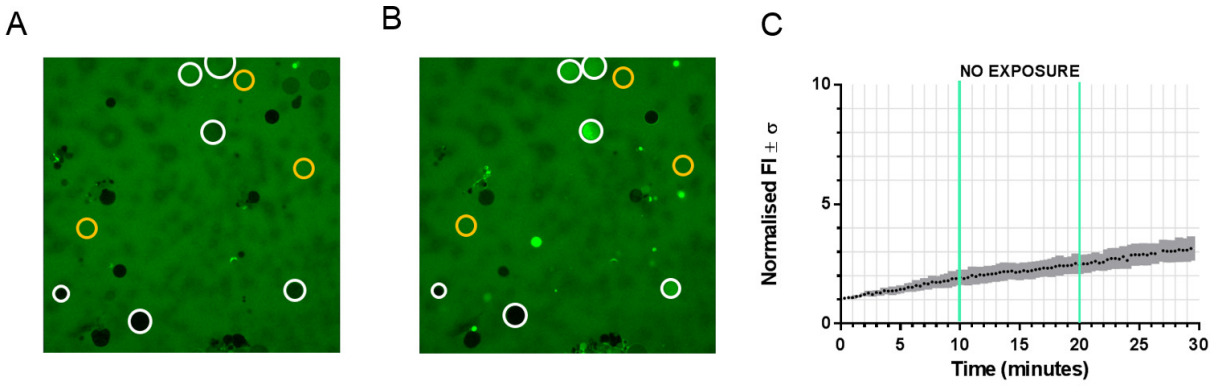


Figure 33 - Algorithm to obtain vesicle fluorescence uptake profiles. A. Representative fluorescence confocal image of GUVs adhering to the glass slide. White circles show vesicle detection, while yellow circles show background sampling. Initially impermeable vesicles are represented by black circles, while the green signal is emitted by the PBS-fluorescein sodium salt solution. B. Representative fluorescence confocal image of GUVs adhering to the glass slide after excitation. C. Representative intra-vesicle fluorescence curve. Fluorescence is normalised to background and initial value. The grey shaded area represents the population variability in fluorescence signal within the vesicles' milieu at a given time point.

4.2.8. Excitation protocols for the quantification of fluorescein uptake

4.2.8.1. No exposure

The vesicles-fluorescein solution was immediately pipetted into the acoustofluidic device after mixing. Within a few minutes, black circles were visible in proximity to the glass slide as the vesicles containing no fluorescein sedimented. The vesicles were imaged continuously for 30 minutes, at an approximate acquisition rate of 3 frames/minute.

4.2.8.2. Blank injection

In order to examine the effect of injection on the vesicles' permeability, a 60 μM fluorescein solution in PBS was injected in the chamber containing vesicles surrounded by the same solution. The injection was performed after 10 minutes of microscope acquisition and the uptake was monitored for the remaining 20 minutes.

4.2.8.3. Ultrasound only

After the vesicles sedimented, they were imaged for 10 minutes in order to obtain a baseline uptake. Then, the vesicles were subjected to continuous ultrasound excitation (~190 kPa, 1 MHz) for 10 minutes. To examine the recovery dynamics of the membrane, the vesicles were imaged for a further 10 minutes without any excitation.

4.2.8.4. Pressure-driven flow

Following sedimentation, vesicles were imaged for 10 minutes to obtain a baseline uptake measurement. Vesicles were then exposed to shear flow (600 μL/min, 1.25 Pa shear at the glass surface) for 10 minutes, and for a further 10 minutes without any excitation.

4.2.8.5. Microbubbles only

After obtaining a baseline uptake measurement for 10 minutes, a 500 μL fluorescent (rhodamine-tagged lipids in fluorescein) microbubble solution (DSPC:PEG 9:1) was injected into the acoustofluidic device. Vesicles were then imaged continuously for 20 minutes.

4.2.8.6. Ultrasound and microbubbles combined

Following the acquisition of a baseline uptake, a 500 µL aliquot of microbubbles was injected into the device and exposed to ultrasound for 20 minutes after 10 minutes of acquisition with no exposure. The vesicles were then imaged continuously for the following 20 minutes.

4.2.8.7. Free PEG40s

The fluorescence uptake of the vesicles in the presence of free PEG40s (0.5 mg/mL) was performed continuously over 30 minutes. Free PEG40s was added to the fluorescent-vesicle solution prior to the injection in the microfluidic device. A control experiment was performed in the absence of any PEG40s in order to compare the two uptake curves.

4.2.8.8. Microbubble shell debris

To quantify potential changes vesicle permeability due to in the presence of DSPC debris on the lipid bilayer, vesicles were first injected into the device to sediment and bind to the glass surface. Second, a 500 µL microbubble solution was injected into the device and incubated for 1 minute. The device was then flushed with 60 µM PBS-fluorescein solution. Vesicles were then imaged continuously for 30 minutes.

4.2.8.9. Temperature

The effect of temperature on the vesicles' uptake profile was determined using a thermostatic chamber. Vesicles were first imaged for 10 minutes, following a heating phase for 10 minutes, and a recovery phase for the final 10 minutes. The temperature rise was set based upon the maximum temperature that the piezoelectric chip reaches during a 10-minute US exposure ($\Delta T = 1.6^{o}C$). This was determined previously using an infrared camera (FLIR Systems, USA). The temperature inside the thermostatic chamber was monitored using a thermocouple and recorded for 10 minutes, a final recording was performed at the end of the experiment. Figure 47 shows the temperature of the chamber and vesicle uptake throughout the experiment.

A model for transient conduction was used to estimate the temperature change at the vesicle-glass boundary as a result of heating in the thermostatic chamber.

Equation 16 was used, coupled with a semi-infinite approximation and constant temperature, to estimate the time it would take for the side of the glass in contact with the vesicles to reach the temperature inside the chamber.

$$\frac{T(x,t) - T_{\text{surface}}}{T_i - T_{\text{surface}}} = \text{erf}\left(\frac{x}{2\sqrt{\alpha t}}\right) \quad \textit{Equation 16}$$

T(x,t) represents the temperature at a distance *x* in a semi-infinite wall at time *t*. $T_{surface}$ is the constant temperature, T_i is the initial temperature of the glass slide, and α is the thermal diffusivity of the glass slide (7×10^{-7} m^2/s)[37]. Figure 47 shows the temperature at the extremity of the glass slide in contact with the fluid layer. Within ~100 s, the temperature at the inner surface of the glass slide (where vesicles are located) is equal to the temperature at the outer surface of the glass slide (the one directly exposed to the thermostatic chamber).

4.2.9. Data and statistical analyses

Statistical testing was performed using one-way ANOVA for multiple comparison analysis, while t-tests were employed for direct comparison between two data sets. All data are expressed in terms of mean ± standard deviation and the number of independent replicates is reported in the figure captions. The following conventions for statistical significance are used throughout the paper: ns = $p > 0.05$, * = $p \leq 0.05$.

4.3. Results and discussion

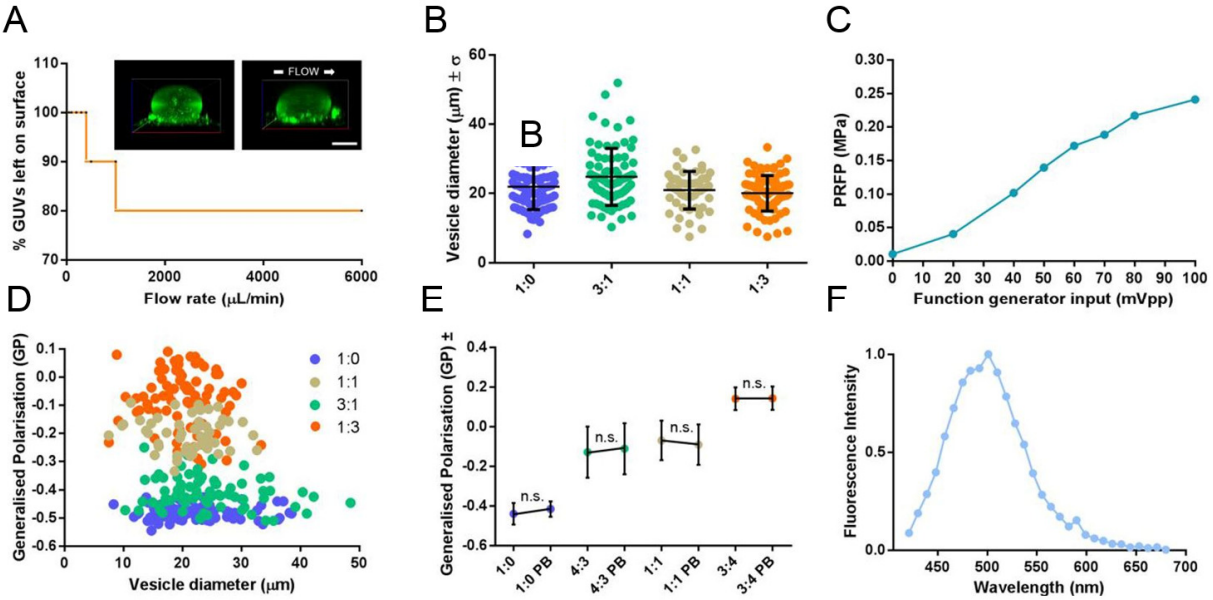


Figure 34 - A. Characterisation of avidin-biotin binding strength. Scale bar = 15 µm. B. Vesicle diameter as a function of DOPC:Chol molar ratio. C. Acoustic Pressure inside the fluid layer of the acoustofluidic device at varying function generator driving voltages. D. Generalised Polarisation as a function of vesicle diameter. Statistical significance was determined by performing a one-way ANOVA on all groups. E. Effect of photo-bleaching on GP of lipid membranes. Unpaired t-tests were performed on samples with the same composition. F. Emission spectrum of c-Laurdan when incorporated into DOPC GUVs. The sudden increase in signal at 590 nm is an artefact due to light leakage through the Acosto Optical Tunable Filter (AOTF) at 594 nm.

4.3.1. Setup characterisation

Electroformation parameters were tuned to yield biologically relevant vesicle sizes compared to cells (~10-30 µm) (Figure 34b-d). The mean vesicle diameter did not vary significantly with cholesterol content (Figure 34b) and was, 22.98 µm ± 9.35 µm. The molar fraction of cholesterol was varied to obtain vesicles of different membrane lipid packing, without the need to change the lipid species. Cholesterol is an abundant and fundamental constituent of the plasma membrane of eukaryotic cells, making up approximately 17% of the total plasma membrane lipids by weight[326]. When incorporated in liquid disordered phase membranes, its inflexible and planar steroid ring lies between the lipids' fatty acid tails, leading to a higher degree of condensation and packing[327]. Control populations were generated in order to assess

the degree of variability and reproducibility of the vesicles' lipid order. In the pure lipid case, the GP was GP(1:0) = -0.48 ± 0.04. As the molar fraction of cholesterol was increased, the GP of the vesicles increased accordingly: GP(3:1) = -0.42 ± 0.03, GP(1:1) = -0.18 ± 0.07, and GP(1:3) = -0.02 ± 0.05. The values in brackets denote the molar fraction of the lipid solution deposited on the electroformation electrodes. As expected, no correlation between GP and vesicle diameter was found (Figure 34d).

4.3.1.1. Microbubble properties

The diameter of the microbubbles in suspension was determined using an image analysis tool[171]. Approximately 6000 bubbles were counted and sized, yielding a mean diameter of 1.47 ± 0.89 μm. The microbubble shell images were also segmented and their GP was calculated to be GP(DSPC:PEG 9:1 MBs) = 0.479 ± 0.048. Figure 35a shows a confocal image of an aliquot of microbubbles stained with c-Laurdan.

4.3.1.2. Acoustic pressure measurements

The average acoustic pressure inside the fluid layer of the acoustofluidic device was determined by averaging three independent readings, yielding 188 ± 37 kPa for a 39.4 Vpp voltage input on the piezoelectric transducer (Figure 34c). It is worth noting that this value is an estimate, given the practical challenges in measuring experimental values of acoustic pressure in micrometre-scale devices using a fibre optic hydrophone. In addition, a 15% error due to the calibration uncertainty of hydrophones must be taken into consideration.

4.3.1.3. Avidin-biotin assay binding strength

No detachment or size changes were recorded at a shear stress magnitude of 1.25 Pa. At 12.5 Pa, 80% of the vesicles were still intact on the glass slide (Figure 34a). For the other 20% of the vesicles, a circular fluorescent area was found in the area corresponding to the original vesicle position. This may suggest that, while shear flow was not sufficient to detach the

vesicle lipid bilayer from the bBSA-avidin layer, the tension in the lipid bilayer caused rupture, rather than detachment, of the more fragile vesicles.

4.3.1.4. Temperature changes as a result of ultrasound exposure

To investigate potential temperature-induced effects on the vesicle membranes, the temperature of the piezoelectric surface was monitored over 15 minute of operation at 76.6 Vpp followed by a 15-minute cooling phase. The temperature change of the piezoelectric surface did not exceed 1°C during the first minute of exposure (Figure 47). Due to the good insulating performance of both the epoxy resin and the ceramic MACOR© carrier layer, the lower driving voltage used in the experiments to minimise heating, and the heat convection in the 200 μm fluid layer, it is assumed that the temperature rise at the glass surface will be no more than a fraction of a degree. Moreover, previous studies[181,328] have shown that changes in Laurdan GP of multicomponent vesicles as a result of a 1°C temperature rise are small (ΔGP = <0.01), particularly when the lipids are far from their transition temperature.

4.3.1.5. Effect of photobleaching on generalised polarisation

The effect of fluorescence bleaching on GP values was determined to be not statistically (paired t-test) significant at the laser powers and acquisition settings used throughout the experiments presented in this study, as shown in Figure 34e.

4.3.1.6. Acoustic streaming

The acoustic streaming that arises from acoustic energy gradients was characterised using Particle Tracking Velocimetry (PTV). At the highest acoustic pressure, the average acoustic streaming velocity in the active area under the piezoelectric element was measured as 15.13 ± 3.50 μm/s. Previous studies have reported in-plane streaming velocities below 100 μm/s in half-wave resonators and rectangular microchannels operated at 1.94-2.56 MHz and actuated at voltages up to 30 Vpp. The streaming velocities recorded were below those reported in the

literature, and significantly lower than the fluid velocities generated by cavitation microstreaming (100 to 1000 mm/s) (Figure 35c).

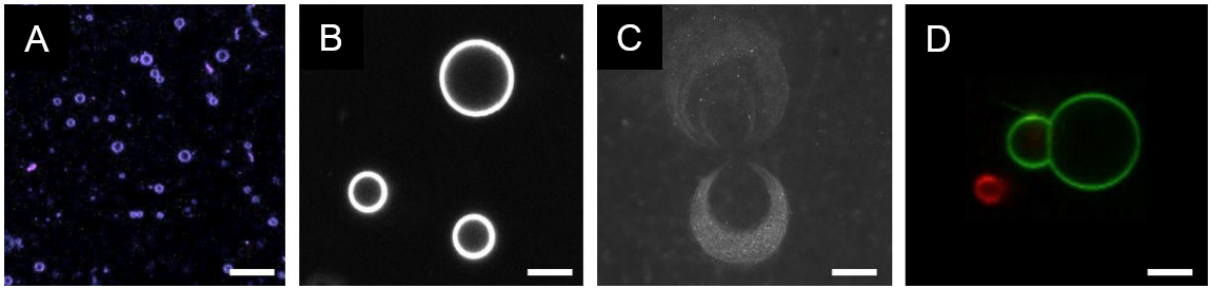


Figure 35 – A. Confocal image of microbubbles stained with c-Laurdan. Scale bar = 30 μm. B. Confocal image of three GUVs of different sizes. Scale bar = 10 μm. C. Cavitation microstreaming vortexes, traced by 1 μm fluorescent beads, as a result of the volumetric expansions and contraction of SonoVue® microbubbles at ~50 kPa. Scale bar = 100 μm. D. Two adjacent-fused GUV (green) adjacent to a microbubble (red). Scale bar = 15 μm.

4.3.2. Changes in membrane lipid order as a result of varying exposure regimes

Vesicles with various levels of cholesterol were formed to determine how different lipid packing characteristics affect the response of the membrane. Generalised Polarisation (GP) was employed as a metric to quantify the changes in membrane lipid packing, where a positive change in GP indicates an increase in lipid packing, and *vice versa* for negative GP changes.

4.3.2.1. Ultrasound only

In all four vesicle formulations, exposure to ultrasound alone caused a decrease in membrane packing, with significant differences ($p < 0.05$) in all formulations but the 1:0 DOPC case. The decrease (Figure 36a, $\Delta GP = -0.03 \pm 0.04$) in lipid packing of the pure DOPC vesicles was smaller, potentially because the highly liquid and disordered mobile nature of their unperturbed membrane lipids (which lie at the negative extremity of the GP range) prevents further fluidisation and disordering. Similar considerations may explain the results seen with vesicles exposed to pressure-driven flow, where the 1:0 DOPC vesicles' membranes exhibited a non-statistically significant decrease (Figure 36, $\Delta GP = -0.04 \pm 0.04$) in lipid order. Ultrasound did have an effect on the 3:1, 1:1, and 1:3 DOPC:Chol vesicles, where the changes recorded were -0.06 ± 0.02, -0.08 ± 0.08, and -0.07 ± 0.05.

Upon exposure to ultrasound, the mechanical wave-matter interactions provoked by the ultrasound wave have been shown to induce oscillatory motion, increase bilayer displacement and tension, and increase the membrane's area per lipid molecule[329], all of which have been linked to decreases in lipid packing. A study by Mendelson et al. found that ultrasound disrupts the hydrophobic moieties of the lipid membrane[330], while Lawaczeck et al.[331] linked US exposure to the formation of structural defects in the lipid membrane. In addition, acoustic radiation force and acoustic streaming compress the vesicle against the glass slide, causing an increase in tension and curvature in the membrane at the equatorial plane. Both effects have been linked in the past with an increase in membrane hydration.[316]

In addition, the generation of mild streaming velocities upon exposure to ultrasound (~15 μm/s mean velocity) may also affect the lipid organisation in the vesicle membrane. While the streaming velocities measured in the devices were small in comparison to those seen in acoustofluidic devices previously described in the literature[95,279], fluid shear stress would still be expected to induce some membrane deformation, membrane lipid diffusion and streaming within the vesicle's milieu[332], as reported in previous studies[333–335]. For instance, Sebastian et al.[163] investigated the intra-vesicle streaming velocities as a function of externally applied flow up to 2500 μm/s; Honerkamp-Smith et al.[333] used a similar method to determine the viscosity of vesicles' lipid bilayers (~10-100 μm/s); and Yamada et al. studied the velocity of membrane domains as a result of externally applied shear-driven flow (0-2000 μm/s) in microfluidic wells. The shear stress caused by acoustic streaming may also facilitate the formation of partitions at the phospholipid head group level that permit penetration of water within the lipid bilayer[336].

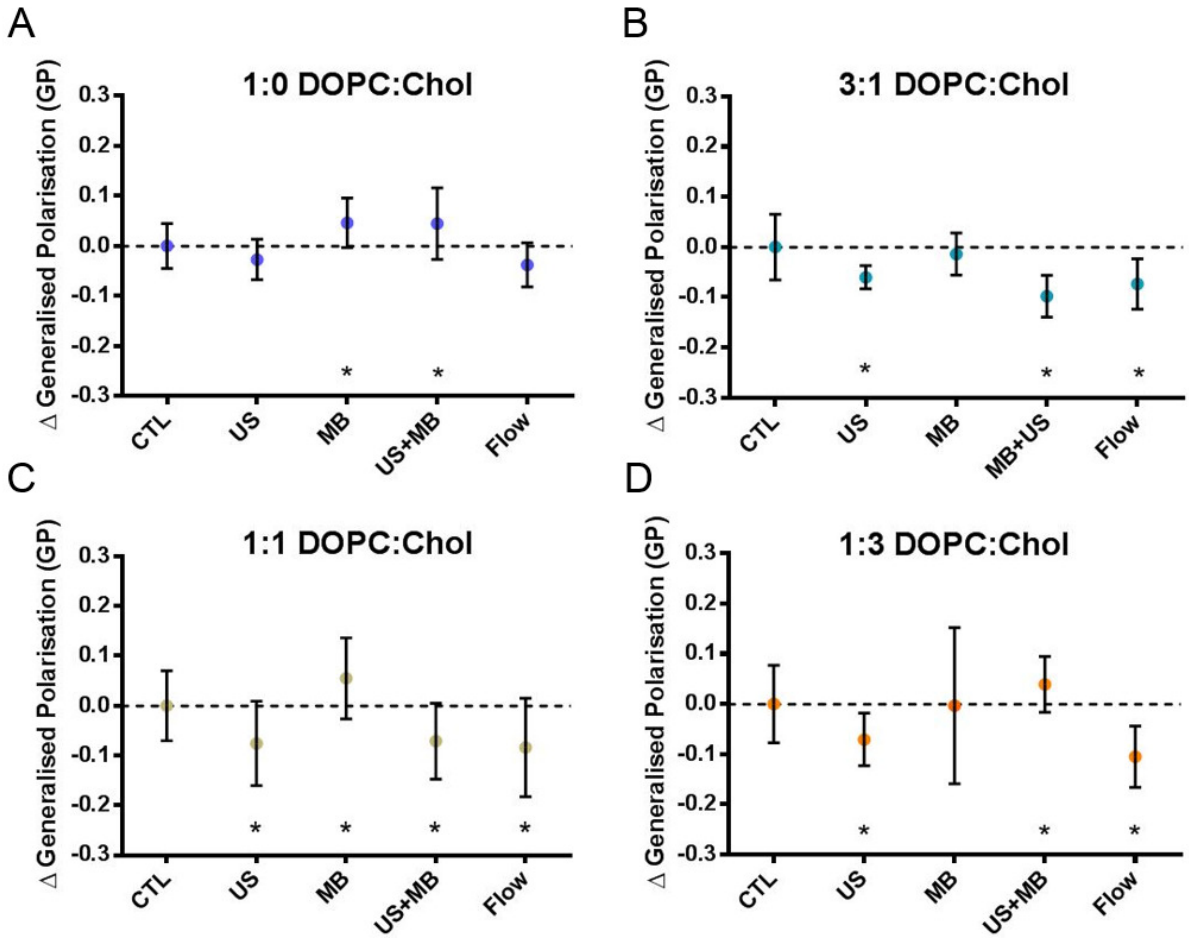


Figure 36 - Changes in lipid order upon exposure to different excitation regimes. a. Effects on 1:0 GUVs. b. Effects on 3:1 GUVs. c. Effects on 1:1 GUVs. d. Effects on 1:3 GUVs. A total of 411 vesicles were analysed with an average of 21 vesicles for each condition (n = 3). Statistical significance inferred by first performing a one-way ANOVA followed by Tukey's multiple comparisons test between each condition and control. The error bars represent the variability in changes in GP between repeats for each exposure condition.

4.3.2.2. Pressure-driven flow

While acoustic streaming cannot be decoupled from other effects of ultrasound in continuous-wave mode, the effect of shear flow was also assessed separately in order to determine its contribution to any change in the vesicles' GP.

A statistically significant decrease in lipid packing as a result of exposure to flow was observed for all lipid formulations that contained cholesterol. The changes recorded were in the range of -0.03 ± 0.04 to -0.10 ± 0.06 (Figure 36) indicating hydration of the vesicle membrane. Upon exposure to shear flow, the highly dynamic, loosely packed, phospholipids undergo

rapid lateral diffusion confined by vesicle contours. Shear stress results in momentum transfer from the surrounding fluid to the membrane, causing the lipids to effectively flow in circulation patterns constricted by the shape of the vesicle (Figure 37). As a result, the lipid head groups on the vesicle membrane become less packed, and the tails more disordered.[315] This effect has been reported previously in lipid vesicles[337] and red blood cells[338,339] and is modulated by the properties of the membrane[340]. Another, previously reported,[341] effect observed was the occurrence of lipid tubules in proximity of the vesicles after applying flow, which may also contribute in decreasing the lipid packing by the shedding of lipid material. (Figure 38c).

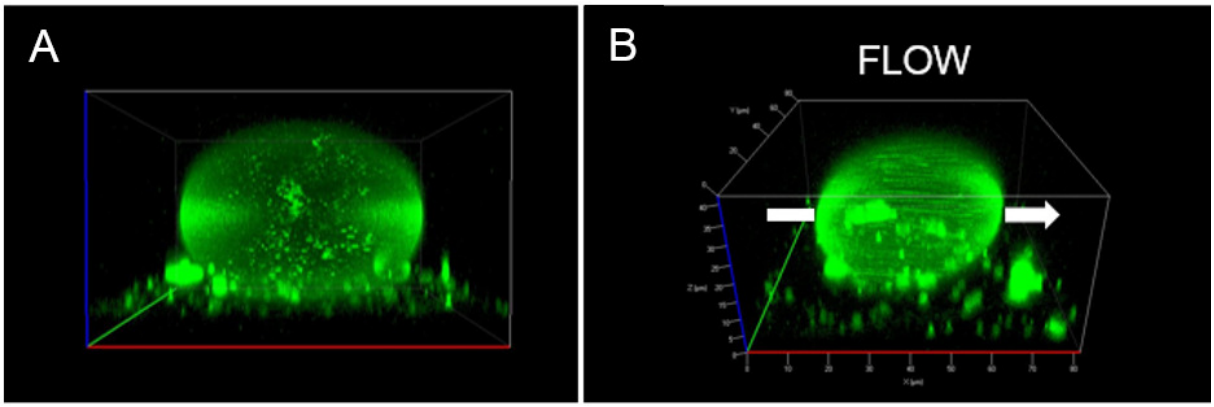


Figure 37 - A. 3D image of a DOPC GUV fixated to the glass slide of the acoustofluidic device. B. 3D image of a fixated DOPC GUV deformed in flow conditions (600µL/min, 0.125 Pa). The white arrow represents the direction of flow.

The increase in local hydration of the membrane becomes more pronounced with increasing cholesterol fraction, suggesting that the ease with which water enters and leaves the membrane is dependent upon lipid order ($p = 0.014$, one-way ANOVA). While a higher cholesterol fraction is known to stabilise membranes, the non-equilibrium dynamic behaviour of lipids and cholesterol in external flows remains largely unknown. Previous studies have characterised the flow patterns on the vesicle membrane, reporting orbiting patterns and gradual migration of lipid-ordered phases towards the two vortexes on either side of the vesicle midline.[340] Whether the dynamic behaviour of the membrane layer leads to the partition and heterogeneous distribution of cholesterol on the membrane itself requires

further study. Limited research has been conducted on the changes in physical properties (such as lipid order, fluidity and cholesterol content) of lipid vesicles in dynamic conditions.

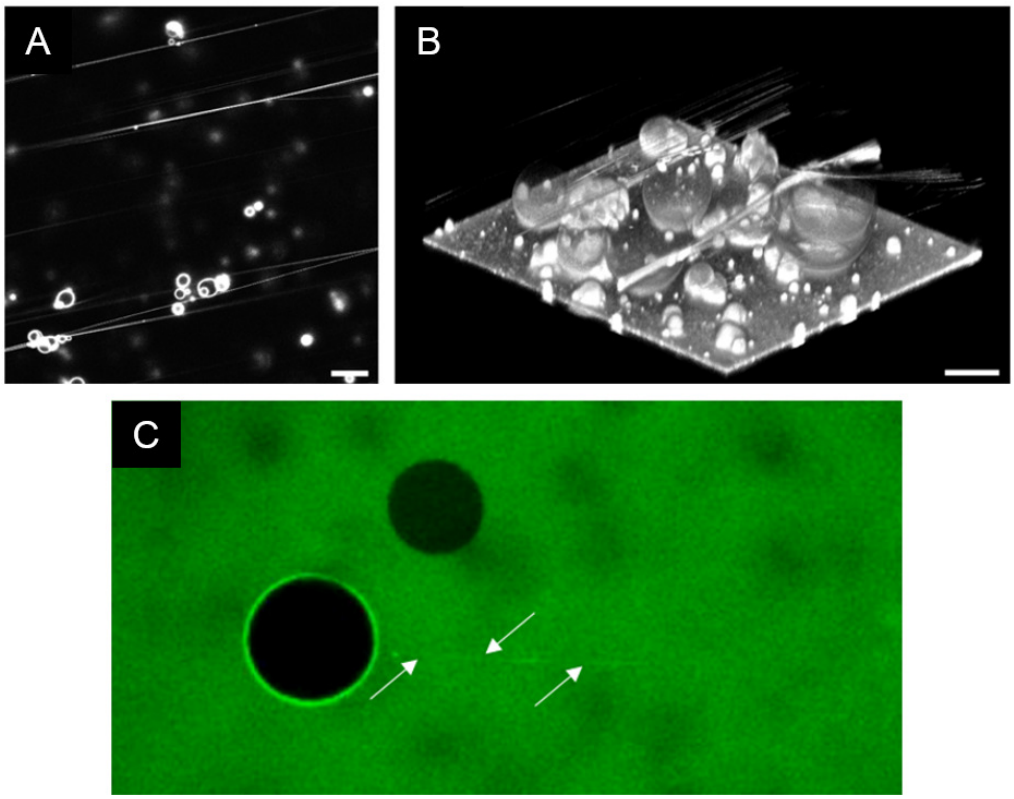


Figure 38 - A. Fluorescent lipid tubules stemming off a multilamellar vesicle during pressure-driven shear flow. B. 3D confocal image of GUVs surrounded by lipid tubules resulting from shear flow. C. Fluorescent image of GUVs and microtubules in the presence of fluorescein sodium salt.

Reversible shape deformations of the vesicles were also observed upon application of the shear flow. A video of a GUV undergoing significant shape deformation and intra-vesicle streaming under shear flow is included in the Supplementary Video 3.1, Appendix B. In a study on DOPC liposomes, it was found that lateral stretching of the bilayers leads to a decrease in the thickness of the bilayer, due to weak coupling between area and volume, which typically results in lower membrane hydration[316]. However, other theoretical studies have suggested that bilayer tension and membrane bending cause a reduction in lipid packing and disordering of the lipid tails.[315] Reduction in the lipid order of POPC vesicles under shear flow has also been reported previously[179], providing further evidence that fluid flows achieved by acoustic and cavitation microstreaming (generated by ultrasound alone or in combination with microbubbles

respectively) can alter the properties of model lipid membranes. However, the extent to which this occurs, depends on the characteristics of the flow such as magnitude, vorticity, and turbulence. These are in turn determined by the US characteristics that lead to acoustic streaming and positioning of the vesicle relative to microstreaming vortexes.

Only a limited number of studies focus on the dynamics of membrane hydration as a result of varying exposure conditions. Notably, Yamamoto et al.[179] obtained a Laurdan-GP time series of DPPC:DOPC:Chol 2:2:1 GUVs and human pulmonary artery endothelial cells as a result of flow-driven shear stress. The results in cells showed that the lipid packing was partially restored upon stopping the flow, while this did not occur in GUVs. Further investigation on the changes in GP during and after exposure must be performed to fully characterise the temporal dynamics of lipid packing.

4.3.2.3. Microbubbles only

Positive changes in lipid order of giant unilamellar vesicles were observed as a result of exposure to clinically relevant contrast agent formulations (Figure 35a). Microbubbles caused significant GP increases in the most fluid (1:0) and the (1:1) vesicle formulations (ΔGP = +0.05 ± 0.05, +0.06 ± 0.08 respectively); and a statistically insignificant decrease (ΔGP = -0.01 ± 0.04) in the 3:1 DOPC:Chol vesicles.

The presence of regions in the membrane with distinctively higher GP suggests the occurrence of chemical interactions between the microbubbles' DSPC and the vesicle DOPC lipids, providing preliminary evidence for DSPC lipid deposition onto the DOPC vesicle surface. This is shown in Figure 39, where the GP maps of a 3:1 DOPC:Chol GUV pre- and post- US+MB treatment are depicted. Figure 39c clearly shows high-GP regions when compared to the control case (Figure 39). A λ-stack image from the microscope's field of view was also included, to highlight the Laurdan spectral shift in the high-GP regions (Figure 39).

The changes in lipid order can be attributed to both microbubble-membrane interactions, and compositional changes resulting from chemical interactions of the lipid bilayer with the microbubble suspension medium. For example, both DSPC and PEG40s may interact with the lipid bilayer, altering its membrane properties.

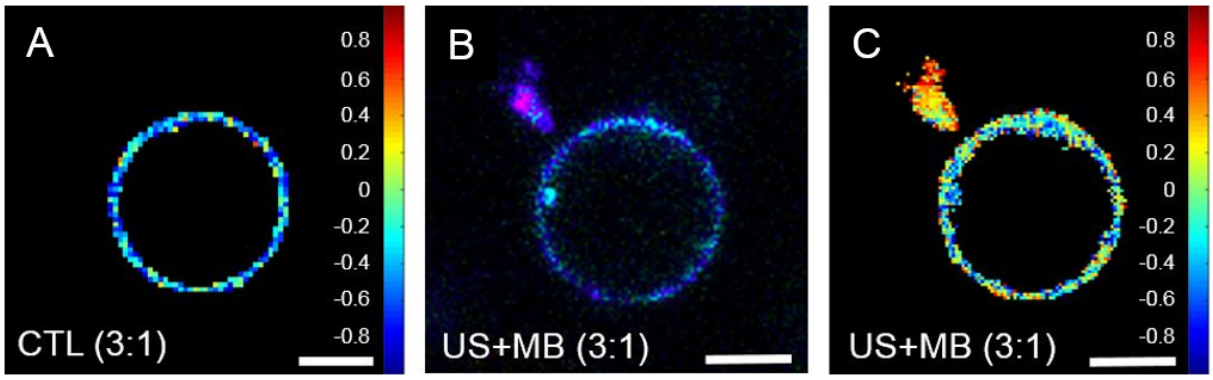


Figure 39 - A. Representative GP map of a 3:1 DOPC:Chol GUV in the absence of US or MB (GP = -0.39 ± 0.28). B. Confocal lambda image showing coexistent DOPC (blue) and DSPC lipids (purple) as a result of US+MB exposure. C. GP map for the vesicle shown in b, with areas of markedly higher GP (average GP = -0.17 ± 0.1). The structure in the top left hand is likely DSPC lipid debris.

4.3.2.4. Ultrasound and microbubbles combined

Exposure to US+MB yielded contrasting effects on the lipid order of the vesicle membranes. In 1:0 and 1:3 DOPC:Chol vesicles, MB+US increased the membrane lipid packing compared to the control ($\Delta GP = 0.04 \pm 0.07$ and $\Delta GP = +0.04 \pm 0.05$, respectively). Membrane packing decreased, however, in the case of the 3:1 and 1:1 vesicles ($\Delta GP = -0.09 \pm 0.04$ and $\Delta GP = -0.07 \pm 0.07$, respectively). These results are likely due to the multiple competing factors determining membrane order. For example, increased order may be associated with DSPC lipid incorporation, surfactant interactions, or membrane peroxidation; while disordering may be attributed to the effects of ultrasound exposure and shear stress caused by cavitation microstreaming.

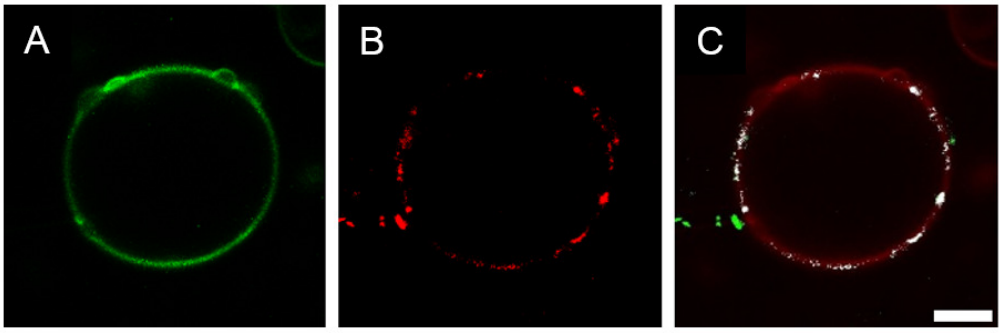


Figure 40 - GUV mid-plane Maximum Intensity Projection (MIP) performed with modified histogram reveal DSPC lipid diffusion across the membrane and the formation of vesicle-like structure within the GUV lumen. A. DOPC:Chol 3:1 GUV stained with CellMask Deep Red. B. MIP summation reveal DSPC lipid dynamics on DOPC GUV. C. Overlaid image of the vesicle with the DSPC microbubble lipids. White areas represent Costes' colocalisation mask. Scale bar = 10µm.

Compositional changes resulting from lipid incorporation may result from direct contact with both stationary and cavitating microbubbles, or indirectly from lipid debris present in the microbubble solution. Lipids may be released in the solution during microbubble production (particularly during the sonication step) and/or shed during cavitation[342]. While no study specifically considers the effect of lipid debris in microbubble solutions on artificial membranes, Der Loughian et al.[343] observed lipid deposition from microbubbles on a single bilayer when exposed to ultrasound, while De Cock and colleagues[331] have shown that nanoparticle-loaded microbubbles deposit shell material on the plasma membrane after ultrasound-triggered detachment. Given the lower hydration levels of highly saturated DSPC lipid aggregates, any lipid transfer from the microbubble surface (as shown in Figure 39) is likely to result in an increased GP of the vesicle membrane.

4.3.2.5. Exposure to PEG40s

Polyethylene glycol (40) stearate is an essential component of the microbubble's shell monolayer, aiding the formation and stability of microbubble suspensions. PEG40s can interact with the vesicles by either being transferred upon contact between the microbubbles and the vesicles, or can interact passively due to its presence in the microbubble suspension. Previous studies have suggested that PEG40s emulsifier is 'squeezed-out' from the

microbubble shell into the solution during the microbubble formation process when the surface tension of the microbubble coating exceeds 35 mN/m.[83]

Figure 36a shows that an increase in membrane lipid order was observed for pure DOPC vesicles, with a greater increase for formulations containing cholesterol up to 50 mol %. For membranes containing 75 mol % cholesterol, while an ordering effect was recorded, an unpaired t-test indicated that the outcome was statistically insignificant. This may be due to the membrane being so highly packed as to hinder the incorporation of exogenous molecules and therefore limiting the ordering effect of PEG40s. For all formulations, no domain formation was resolved optically and no significant changes in vesicle diameter were recorded in the presence of PEG40s, as shown in Figure 41b.

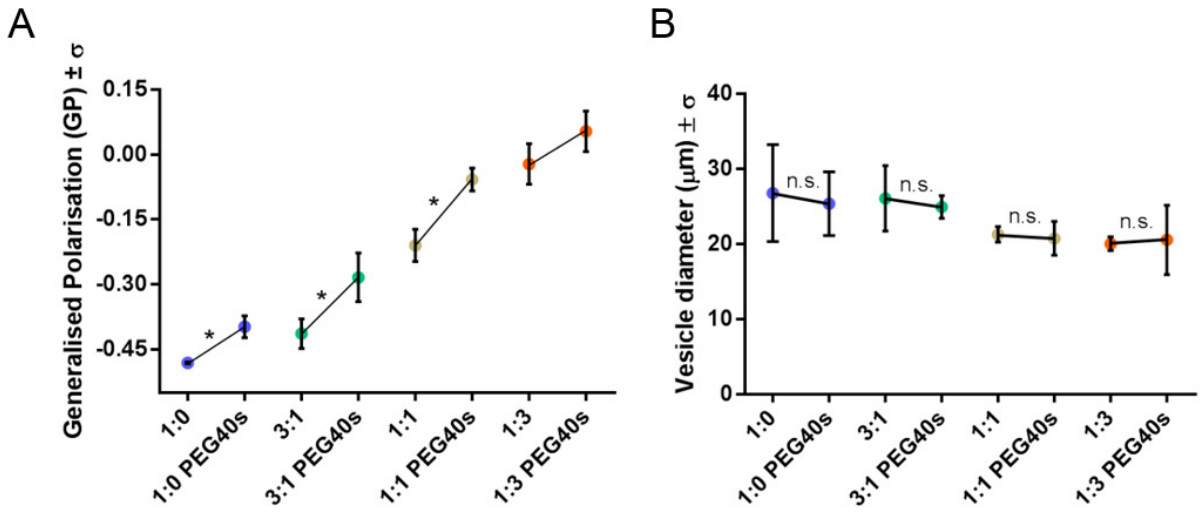


Figure 41 - A. Effect of free PEG40s on the lipid order of DOPC:Chol vesicles. Results are depicted in the presence and absence of free PEG40s and connecting dots represent changes in the lipid order for each formulation. B. Effect of PEG40s on vesicle size for four vesicle formulations. Statistical significance testing was performed on three independent experiments, for a total of 518 vesicles with at least 54 vesicles per formulation.

Despite a large number of studies addressing the effect of PEG on the hydration levels and lipid packing of liposomes, relatively few studies have investigated the effect of PEG conjugated with hydrophobic molecules such as stearic acid. The mechanisms by which PEG interacts with membranes remains a controversial matter.[344] A wide parameter space that

spans exposure time-scales, pH, concentrations, chain lengths, and surfactant and lipid structures, makes molecular interpretations challenging.

At low concentrations, free PEG has been shown to cause dehydration of the membrane with a consequent increase of the lipid packing of DOPC, DPPC, EPC and POPC vesicles. It was shown that the chain length of the PEG also affects the degree of dehydration of the membrane. In contradiction to these findings, however, Holmsen et al.[345] reported that membrane destabilisation as a result of PEG is a function of the initial surface pressure of the membrane. The characteristics of the hydrophobic moiety of the surfactant[346–348] and the PEG chain length[347] also affect the extent membrane hydration is influenced.

Garbuzenko et al.[348] studied the effect of DSPE-PEG, which has the same hydrophobic moiety structure as the steric acid in PEG40s, in the presence and absence of 40 mol% cholesterol on the lateral packing of EPC liposomes, showing evidence for an increase in lipid packing with and without cholesterol. This observation is consistent with the findings presented here, as PEG40s increased the lipid packing of the vesicles, independently of molar fraction. PEG lipids in phospholipid vesicles have also been shown to reduce leakage of encapsulated hydrophilic substances[346], indicating that dehydration and an increased lateral density of the lipid molecules causes a decrease in permeability of the vesicles.

In the experiments presented here, the most likely explanation is that the PEG chains and the stearic acid of the PEG40s surfactant molecule interact with the vesicle's membrane in two separate ways. When in micellar form, the PEG40s exposes its PEG chain to the surrounding environment and, when in contact with a vesicle, it dehydrates the membrane due to its water binding characteristics. Alternatively, the hydrophobic stearic acid may be incorporated within the lipid bilayer, further increasing the packing of the lipids.

4.3.2.6. Effect of cholesterol molar fraction

Cholesterol plays an important role in modulating membrane fluidity and is abundant in the cell's plasma membrane, particularly in membrane domains such as rafts and caveolae. The molar fraction of cholesterol was a significant factor in determining the changes in GP for the exposures involving pressure-driven shear flow and those involving microbubble exposure. However, the membrane's cholesterol content did not appear to influence the effect of ultrasound on the lipid packing of membranes. Notably, in the case of pressure driven shear flow, the increase in cholesterol coincided with more significant decrease in lipid packing. Exposure to PEG40s increased the lipid packing of the majority of the vesicle formulations, without affecting the vesicle size (Figure 41b).

Correlations were less evident in the cases where microbubble exposure occurred. For the MB-only case, significant changes in lipid packing were recorded in the 1:0 and the 1:1 DOPC:Chol formulations. When microbubbles were exposed to ultrasound, positive changes in lipid packing were recorded for the 1:0 and 1:3 formulations, while a decrease in packing occurred for the 3:1 and the 1:1 formulations. The contrasting results in bulk vesicle GP changes may be partially attributed to the behaviour of the DSPC when internalised within the DOPC membrane. Zhao et al.[349] studied the vesicle phase separation in DOPC:DSPC:Chol ternary mixtures, providing a phase diagram showing how the lipids can either arrange themselves uniformly, in distinct circular phases, or in a combination of linear and round features. However, the study focused on vesicles formed with a known initial lipid ratio, and no study has been conducted on the phase-behaviour of DOPC-Chol vesicles with exogenous addition of DSPC.

As mentioned above, the interaction between vesicles and cavitating microbubbles is a multifactorial process that involves mechanical and chemical effects. These are characterised by their multiscale nature: changes in vesicle properties occur at the molecular scale, vesicle deformations take place microscopically, while fluid transport affects a large number of

vesicles simultaneously. Timescales also vary considerably, ranging from microseconds in microbubble oscillations to several milliseconds in acoustic streaming.

The contrasting results obtained when exposing the vesicles to US+MB highlight the stochastic nature of cavitation and its interaction with model membranes. The initial properties of the membranes, the amount of deposited lipid on the membrane surface, and the cavitation activity within the acoustofluidic chamber are all parameters, that are difficult to control, and each may contribute differently to the measured net GP change. Future studies may be required in order to provide a direct correlation between local physical phenomena (i.e., streaming velocity or cavitation activity) and changes in lipid order. For instance, simultaneous spectral imaging and acoustic emission monitoring from microbubbles (i.e., using a custom-built polyvinylidene fluoride film[350]) will be performed in the future.

4.3.3. Microbubble-shell lipid deposition on DOPC vesicles

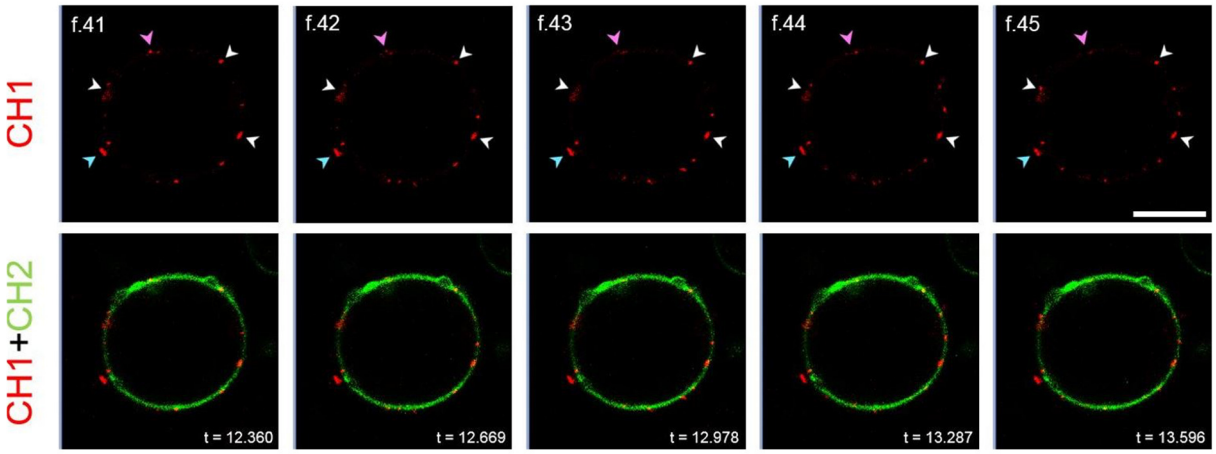


Figure 42 - GUV mid-plane time-series for a DOPC:Chol 3:1 GUV. CH1 (red) reveals the fluorescently tagged DSPC lipid movement. CH2 (green) shows the GUV membrane. The timestamps for the frames are displayed in the bottom right. A full video is included in the Supplementary Information (Appendix B). Scale bar = 10 μm. Magenta arrows point to lipid structures that are mobile but constrained to the membrane, white arrows point immobile structures, and the cyan arrow points to a lipid structure that is linked, but not incorporated, in the GUV membrane.

The interaction between vesicles and debris from microbubble shells was studied by labelling the microbubbles with DSPE-PEG2000-Rhodamine and the vesicles with a fluorescent lipid analogue (CellMask™), and visualising them as separate tracks in a dual channel image. Figure 42 shows an example of a GUV with fluorescently-tagged DSPE-PEG2000 lipids on the bilayer membrane, imaged after US+MB exposure. The time-series displays the dynamic nature of the lipid interactions on the vesicle surface, highlighting four modes of interaction: i. diffusion of fused lipids, ii. immobile domains; iii. mobile domains, and iv. anchored structures. In one case, an omega-shaped vesicle-like structure composed for the larger part of DSPC was formed within the GUV. To emphasise the colocalisation on the vesicle membrane, 40B has been displayed as a Maximum Intensity Projection summed over 60 frames, showing clearly the DSPC is constrained to the vesicle's membrane. This was also confirmed by Costes'[351] mask, where white pixels highlight the colocalised signal in Figure 40. A video (Supplementary Video 3.2, Appendix B) for the time-series are both included in the Supporting Information.

Lipid shedding as a result of shear stress, rapid expansions and contractions, fusion of free lipids and micelles in the solution, as well as direct contact, are all mechanisms that could induce chemical interactions in ultrasound and microbubble mediated drug delivery. In the absence of ultrasound, interactions between the microbubble shell lipids and the vesicles are facilitated by contact upon injection of the microbubbles, during the standing phase, and during washing. Upon exposure to ultrasound, the microbubbles are directed towards the GUV layer, promoting closer contact and lipid exchange. Microbubble coalescence and dissolution may also cause lipids to be released into the solution that may interact with the vesicles. Furthermore, acoustic streaming and cavitation activity associated with ultrasound exposure will aid transport of micelles and lipid fragments present in the microbubble batch.

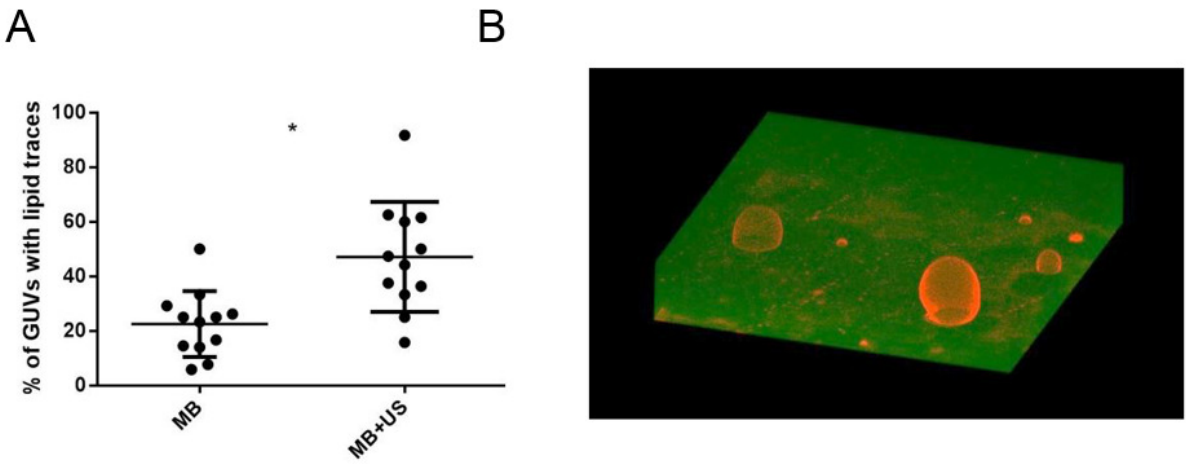


Figure 43 - A. Fraction of GUVs with lipid traces in the case of microbubble injection only and microbubble injection with ultrasound exposure. Statistical testing was performed on three independent experiments each with >100 3:1 DOPC:Chol GUVs. Each point represents the % calculated for a single 512x512 pixel microscope image. The results were shown to be statistically significant by an unpaired, non-parametric, t-test (Mann-Whitney). B. 3D-stack image of DOPC:Chol 3:1 vesicles completely covered with DSPC debris (red) and surrounded by a fluorescein solution (green). The size of the slice is 212 μm x 212 μm x 37 μm.

The fraction of GUVs that presented traces of fluorescently tagged lipids was compared to the number of GUVs with no traces of exogenous fluorescence. It was found that the fraction of GUVs with fluorescent DSPC lipids following MB exposure was 22.57% ± 12.10 and was lower than the US+MB case, where the percentage of vesicles with DSPC lipids was 47.11% ± 20.18, as shown in Figure 43. An increase in measurement deviation was also observed, indicative of an effect variation due to the transport of lipid debris in the fluid channel by acoustic and cavitation microstreaming. These findings are interesting because the modes in which microbubble lipids are deposited, incorporated, and transported on the cell's membrane may affect the effectiveness of therapies that involve drug-loaded microbubbles. Whether the lipids are stationary, mobile, or are simply anchored to the membrane, may affect the capacity to control and sustain the release of the therapeutic agent, as well as affecting its intracellular kinetics.

4.3.4. Vesicle permeabilisation

Having demonstrated that vesicle membrane properties can be modulated through exposure to ultrasound, pressure-driven flow, and microbubbles, alone and in combination, the effects of the same exposure conditions on the uptake of fluorescent molecules were evaluated. The fluorescence uptake of single, cell-sized vesicles was quantified from microscope images. Cholesterol-doped DOPC vesicles (3:1 DOPC:Chol) were used as biomimetic models for the cholesterol-rich, fluid domains of mammalian cells. The vesicles were also normally impermeable to fluorescein, providing a low baseline for the permeation study.

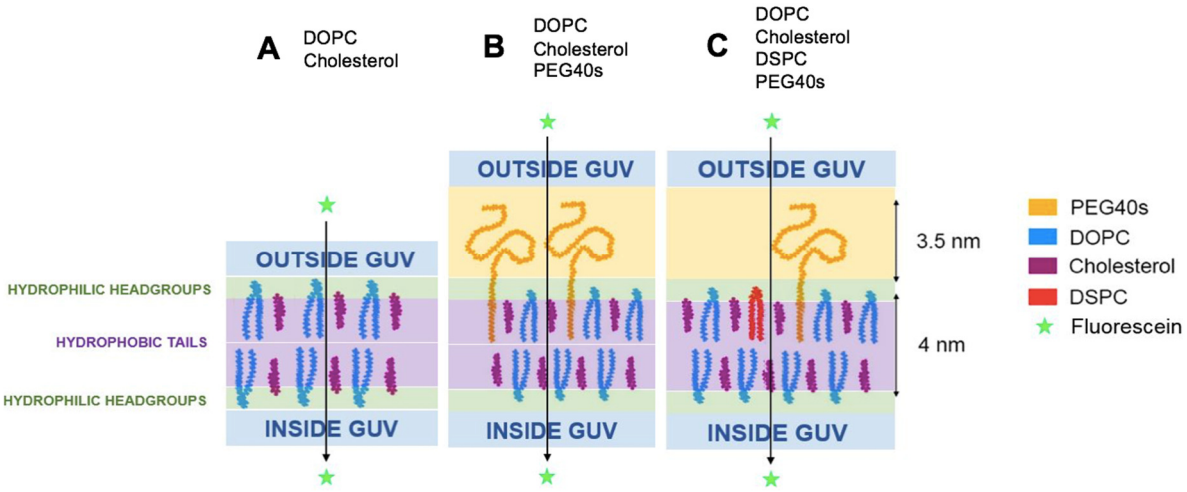


Figure 44 – Schematic diagram of fluorescein molecules penetrating the GUV membrane in different scenarios. A. DOPC:Chol membrane B. DOPC:Chol membrane with stearic moiety of PEG40s anchored within the DOPC:Chol bilayer. C. DOPC:Chol membrane with DSPC and PEG40s following exposure to microbubbles.

4.3.5. Fluorescence uptake

4.3.5.1. No exposure

First, the vesicles were imaged continuously for 30 minutes without applying any excitation. The fluorescence intensity of the signal within the mid-plane of the vesicle lumen shows a small, linear and sustained increase throughout the acquisition. This case constitutes a control baseline for the following exposure experiments (Figure 46a-d). In some cases, vesicles exhibited high intravesicle fluorescence prior to imaging. This may be due to shear stress

acting on the GUV membrane during pipetting or transfer through the device's orifices. In a limited number of cases, the intravesicle fluorescence appeared to be higher than the background. This suggests a proton exchange across the vesicle membrane, leading to a pH gradient driven increase in fluorescence above the background signal. For all experiments, however, only vesicles that exhibited initial fluorescence values within the noise floor were analysed. The standard deviation corresponds to the intervesicle variability in intravesicle fluorescence at a given time point.

4.3.5.2. Blank injection control

This was performed in order to isolate the shear effect caused by injecting media into the acoustofluidic device. The fluorescence levels inside the vesicles did not show any sudden change and the uptake rate was unaffected throughout the acquisition time. The standard deviation was comparable to that registered for the control case (Figure 45).

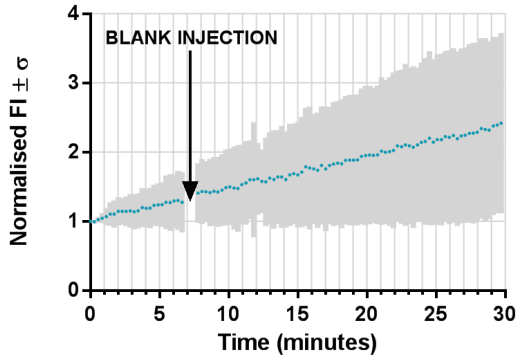


Figure 45 - Fluorescence signal as a function of time. Effect of blank injection on the uptake profile of the vesicles. Lack of data during injection due to lifting of microscope arm during injection.

4.3.5.3. Exposure to ultrasound only

The fluorescence signal of the vesicles increased consistently with the controls in the first 10 minutes. Upon application of the ultrasound field, the uptake rate increased accordingly, until the exposure was terminated. The fluorescence increase continued after the exposure, but at a slower rate in the last 5 minutes of acquisition (Figure 46a). The spikes in fluorescence

correspond to the triggering of the ultrasound field, caused by the movement of the glass slide as a result of ultrasound radiation force.

The findings are consistent with those previously reported by Small et al.[352], showing that the transport of molecules through cholesterol-doped bilayers (Figure 44a) is facilitated through more loosely packed, liquid disordered membranes. This was in-line with the GP results obtained for 3:1 vesicles, where GUVs exposed to ultrasound exhibited a lower GP when compared to control (ΔGP = -0.13). However, while the exact mechanism remains elusive, changes in the fluorescence uptake due to ultrasound alone have been previously related to molecular vibrations, membrane poration, hydrophobic lipid tail disruption[330], shape changes[329], and induction of structural defects.[353]

4.3.5.4. Exposure to pressure-driven flow

The fluorescence uptake during the acquisition of the baseline was consistent with the data acquired for exposure to ultrasound and controls. Upon activating the syringe pump, the fluorescence uptake increased throughout the exposure. The rate of increase was then restrained upon ceasing the flow around the vesicles.

Analogously to ultrasound exposure, the increase in uptake upon activation of the pressure-driven flow is in line with the findings on the changes in lipid packing of the vesicle (ΔGP(flow) = -0.07). As the flow surrounding the vesicle decreases the membrane's lipid packing, this in turn causes an increase in permeation, leading to an increase in fluorescent signal within the vesicle's milieu. While the leading hypothesis for trans-membrane permeation is pore formation[352], no pores within the optical resolution of the system (240 nm) were observed. However, this does not exclude their occurrence.

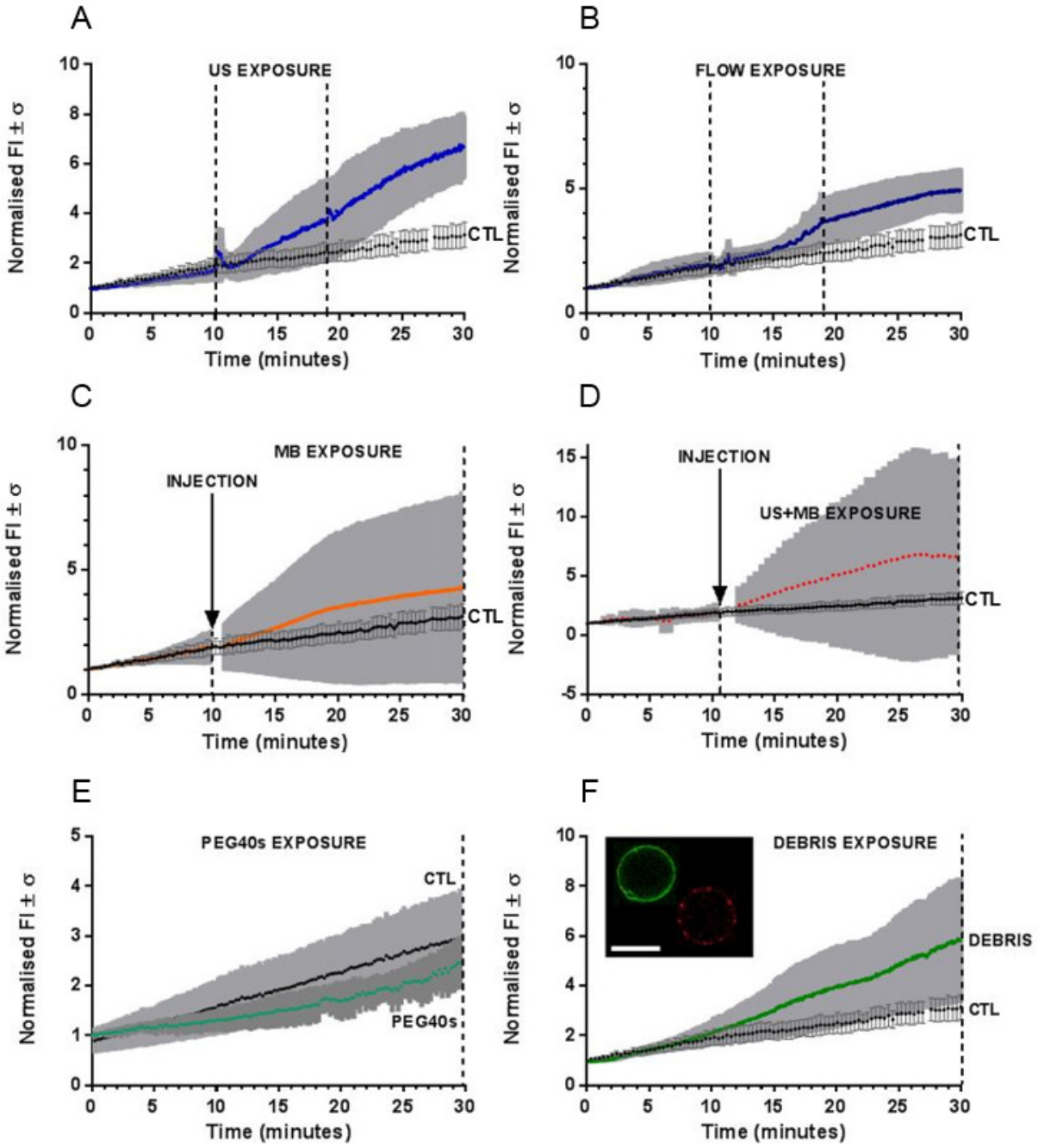


Figure 46 - Average fluorescence uptake as a result of different exposure regimes A. ultrasound exposure. Time point at t=27.27 s was removed due to artefact in image series. B. flow exposure C. microbubble exposure D. ultrasound and microbubble exposure E. free PEG40s exposure. F. DSPC debris exposure. The inset shows a GUV stained with CellMask™ and the debris on its surface. Scale bar = 20 μm. In all images, dotted lines show the period of exposure, while arrows show the time point at which injection was performed. For each condition, three independent experiments were performed for a total of 251 vesicles. The grey shaded regions correspond to the variability in intravesicle fluorescence in the vesicle population at a given time point. The black dotted lines represent the control for each condition.

4.3.5.5. Exposure to microbubbles

Prior to the microbubble injection, the fluorescence inside the vesicle lumen increased in accordance to the data acquired in control conditions (Figure 46c). Following injection, the rate at which the signal inside the vesicle increased until t = 20 minutes and decreased slightly thereafter. The gap in the data corresponds to the time the microscope's arm was lifted in order to allow easier access to the acoustofluidic device for microbubble injection. The increase in uptake may be linked to the coexistence of distinct lipid phases resulting from microbubble lipid deposition on the vesicle membrane (as shown in the inset of Figure 46f and in the schematic in Figure 44c. This is consistent with the findings shown in Figure 43, where >22% of the vesicles imaged presented lipid traces following microbubble exposure. Previous studies[352,354] have investigated the effect of phase transition and coexistence[352,354,355] on the permeation of molecules though lipid membranes, indicating higher permeation in the presence of fluid-gel phase boundary.

4.3.5.6. Exposure to ultrasound and microbubbles

While the presence of DSPC debris leads to an increase in membrane GP and ultrasound/flow generally decrease it, exposure to US+MB increased the uptake of fluorescein in all cases (Figure 46d). This shows that, while the average GP of a vesicle may increase due to debris deposition on the membrane surface, this does not necessarily indicate a lower permeability. As mentioned in section 4.3.6.5, phase coexistence between liquid-ordered and disordered phases may lead to an increase in permeability at the point of contact between liquid and gel phases of the membrane. Exposure to ultrasound, coupled with acoustic and cavitation microstreaming, increases the probability of the interaction between microbubble lipids and DOPC vesicles, as well as decreasing the diffusion time of DSPC fragments within the GUVs (Figure 44c). This is consistent with the data presented in Figure 42, where exposure US+MB increased the GUVs with lipid traces. This is also reflected by the higher standard deviation of the US+MB uptake curve.

4.3.5.7. Exposure to microbubble shell debris

To explore the effect of lipid debris on fluorescein uptake, the intravesicle fluorescent signal of vesicles with debris on their surface was monitored for 30 minutes. Compared to the control case, the vesicles with DSPC debris on their surface showed a sustained increase in mid-plane fluorescence (Figure 46f). The standard deviation compared to the control was also considerably higher, which reflects different uptake behaviour in the vesicles. While the microbubble debris is expected to increase the GP of the vesicles (as quantified and shown in Figure 39), and therefore decrease the permeation across the bilayer, here the permeability of the bilayer increased upon exposure to microbubble debris. Similarly to MB and MB+US exposure, these results are in agreement with those reported previously in ternary lipid mixtures, where an increase fluorescence release was linked to the coexistence of fluid/gel phases on the vesicle membrane.[352]

4.3.5.8. Exposure to PEG40s

Vesicles exposed to free PEG40s in solution did not exhibit a statistically significant difference in fluorescence uptake compared to the control (Figure 46e). However, it is expected that, as the lipid molecules are more tightly packed in the presence of PEG40s (Figure 41), the fluorescein molecules' ability to penetrate the membrane decreases. Moreover, it is hypothesised that the PEG brush layer attached to the external leaflet of the vesicle membrane adds a further barrier, further hindering the penetration of fluorescein molecule (Figure 44b).

4.3.5.9. Exposure to heat

Vesicles in fluorescein solution were exposed to heat in the microscope's thermostatic chamber (Figure 47a), according to the heating curve acquired using an infrared camera (Figure 47).

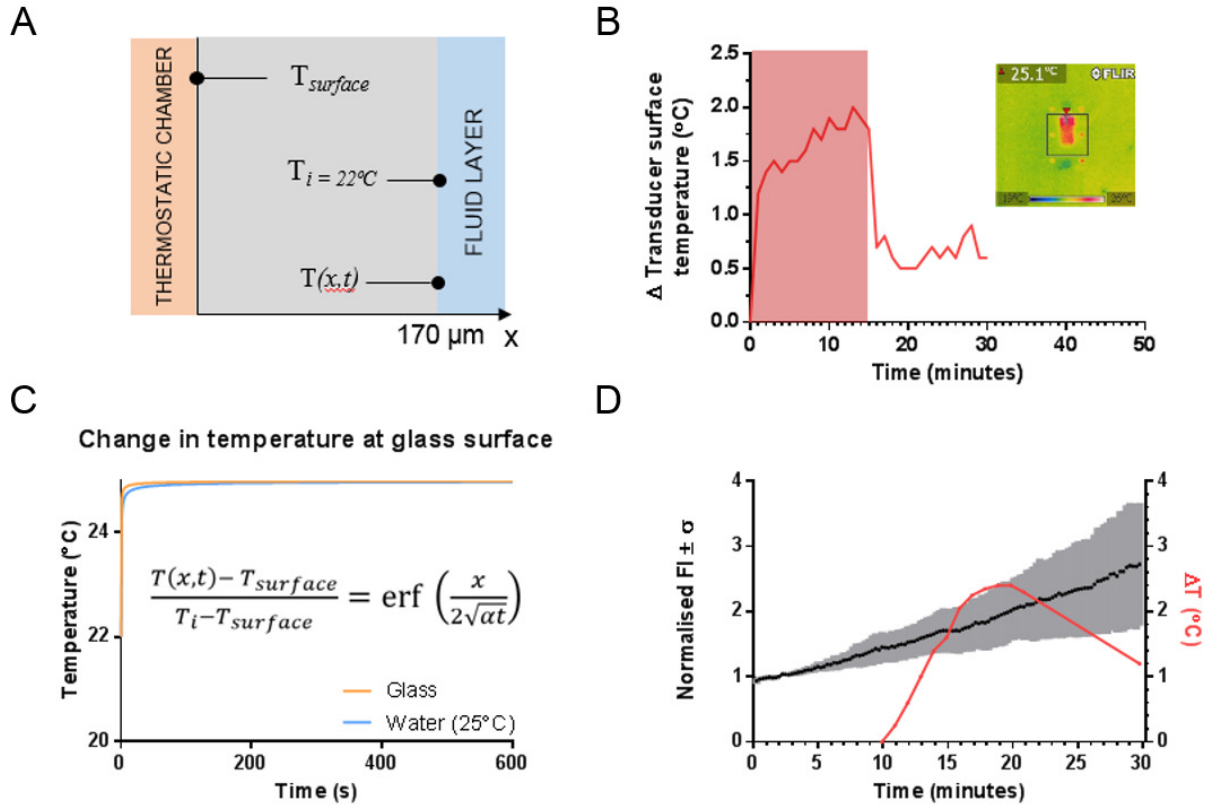


Figure 47 – A. Diagram of glass slide to illustrate heating by thermostatic chamber B. Heating of piezoelectric element as a result of ultrasound exposure. The chip was heated for 15 minutes continuously and left to cool for a subsequent 15 minutes. The insert shows a typical image acquired with the infrared camera. C. Heating of the inner surface of the glass slide. T surface represents the side in contact with the air in the thermostatic chamber while Ti represents the initial temperature of the inner surface of the glass. D. Normalised intra-vesicle fluorescence intensity as a result of heat exposure.

Heat was rapidly conducted through the glass later, reaching the GUVs after only a few seconds (Figure 47c). When the vesicles were exposed to the heat, no significant difference was detected on the uptake curve compared to control (Figure 47d).

4.3.6. Relationship between lipid packing changes and permeability

The order of lipid bilayers has been previously shown to correlate with membrane compressibility, area per lipid, surface pressure, and permeability.[356,357] It is therefore conceivable that the permeability of vesicles to small molecules can be modulated by altering the lipid packing of their membrane. Based on the literature, a decrease in lipid packing would be expected to correspond to an increase in membrane permeability, and *vice versa* for

an increase in packing[356]. This was found to be the case for exposures that did not involve microbubbles or shell debris (ultrasound, flow and PEG40s). In contrast, when the vesicles were exposed to microbubbles, the vesicle membranes were no longer in a single phase, as microbubble shell material was incorporated within the DOPC lipid bilayer. In many cases, two distinct phases were seen to coexist on the vesicle membrane, resulting in an increase in *average* lipid packing. This, however, did not reduce the uptake of fluorescein. Rather, average uptake was also seen to increase, with a high variability between individual vesicles. This is consistent with previous studies in which the coexistence of distinct lipid phases has been shown to facilitate the transport of small molecules across phase boundaries[352,354,355]. In the case of exposure to US+MB, the increase in uptake may be jointly attributed to local decreases in packing caused by phase separation and the effects of cavitation microstreaming flows.

4.3.7. Relevance to cells

DOPC is commonly employed as a non-raft mimetic lipid in membrane studies, and is known to assemble in an extremely disordered state. When mixed with cholesterol, DOPC membranes become more ordered (Figure 34 d-e), while maintaining a single liquid phase. In comparison, natural lipid mixtures such as Porcine Brain PC and Bovine Liver PC form slightly more ordered vesicles compared to pure DOPC[164] (Pure DOPC: = ~-0.3; Porcine Brain PC: ~0.27; Bovine Liver PC = ~-0.25). In plasma membranes, the c-Laurdan generalised polarisation varies greatly with cell type: the membrane generalised polarisation of Rat Basophilic Leukaemia cells (RBL), human lung carcinoma (A549), and human colon adenocarcinoma (DLD-1), for example, were reported as -0.15[358], +0.13, and +0.18[252] respectively.

The changes in lipid packing reported throughout this study were consistent with those published previously for plasma membranes. However, while Carugo et al.[252] reported no changes in lipid packing as a result of ultrasound exposure in cells, the vesicle membranes did exhibit a decrease in lipid order when exposed to ultrasound in the experiments presented

here. This may be explained by the fact that, despite being subjected to analogous forces, the membrane integrity provided by the cytoskeleton and membrane proteins, coupled with a heterogeneous lipid composition and a lower baseline membrane hydration, may play an important role in preserving lipid order in cell membranes.

Contrasting results between vesicles and cells were also observed upon exposure to PEG40s. While exposure to free PEG40s increased the GP for every GUV formulation in this study, an opposite effect was observed previously[252] in cells. These changes can be attributed to PEG40s-led conformational changes in membrane proteins, interactions with membrane carbohydrates, disruption of ion channel function, incorporation, and disruption of cholesterol-mediated lipid order regulation. Moreover, the relationship between PEG and membrane packing has shown to be non-linear and is dependent on the lipid composition of the membrane[359].

The fluidising effects of pressure-driven flow, acoustic streaming and cavitation streaming are directly translatable to cells. Consistent with the results presented here on vesicles, many *in vitro* studies[336,337,360] have reported disordering effects on the endothelial cells as a result of shear flow. Moreover, the formation of oxidisers during cavitation have been shown to increase the permeability of the endothelial layer at acoustic pressures and frequencies comparable to those used in this study.

Altering the lipid packing and composition of cellular plasma membranes may have disparate physiological implications. Previous studies have related the state of the plasma membrane to various cellular functions, such as the endocytic process[11], ion channel function[315], cellular signalling[316–318,361], behaviour of membrane proteins[146,313,314], and enzymatic activity[362]. While material deposition from microbubble shells routinely used in ultrasonography onto the endothelial layer has been reported previously[252,331,343], the long term effects on cell viability remain unclear.

4.3.8. Limitations

Although acoustofluidic devices have considerable practical advantages in combining ultrasound exposure and microscopy in comparison to traditional water tank setups, the experimental apparatus used in the present study also presents limitations. First, the acoustofluidic device in its current form can only support monolayers of GUVs and cells, and therefore fails to capture the complexity of 3D tissue structures. Secondly, while the thin-glass reflector layer at the water-air interface is necessary for creating a standing wave within the fluid layer, a rigid boundary is not representative of *in vivo* conditions[113,115,363,364].

While confocal imaging is necessary to isolate the equatorial section of a spherical vesicle to limit photo-selection effects[365], the computed GP and the lipid debris quantification only relate to the GUV mid-plane and not the entire vesicle, possibly introducing bias in the results. Vesicles that underwent permanent deformations, presented membrane defects, or were fused with other vesicles, were discarded prior to the analysis.

In some cases, during microbubble exposure to ultrasound, large areas with lysed vesicles were identified. This may introduce bias in the quantification of GP, as the vesicles that have been subjected to the highest shear stress could not be included in the results. It is hypothesised that these areas correspond to the location of microstreaming vortex dipoles, and that the vigorous shear flow causes the vesicle membrane to rupture. However, this could not be verified directly as streaming fields and lipid packing were not monitored simultaneously.

Single-vesicle imaging poses advantages compared to bulk measurements associated with spectroscopic techniques, as single vesicles can be visualised and analysed independently and errors can be accounted for. However, the amount of data that can be obtained is significantly lower compared to samples analysed in a cuvette. In bulk measurements, while millions of GUVs can be analysed simultaneously, an intrinsic averaging effect gives rise to loss of information such as vesicle lysis and background quantification. Moreover, while high magnification (63x) confocal microscopy does provide substantial information about the

vesicle morphology, it may not be able to resolve pores if they are smaller than the optical resolution of the microscope.

While GUVs offer a versatile and useful model to understand the basic interactions between microbubbles and cells, they fall short in capturing the complexity of the cell's plasma membrane. While proteins, ion channels, cytoskeletal binding sites and a complex lipid mosaic all affect the structure and packing of the cell membrane, the present study takes a bottom-up approach in providing fundamental evidence of the physical and chemical interactions involving lipid vesicles and clinically relevant microbubbles. As indicated in the previous section, the results may not translate directly to other lipid and microbubble formulations, and further study is needed to elucidate and generalise the physico-chemical mechanisms involved. *In vivo* translation will depend on microbubble concentration and composition, exposure conditions, duration of contact, flow conditions within vessels, and interactions with plasma and red blood cells.

4.4. Conclusions

The findings presented in this study provide quantitative evidence that a combination of mechanical and chemical effects induced by US+MBs produce changes in the properties of synthetic lipid vesicles; and that these changes in turn lead to increased permeation through their lipid bilayers.

Exposure to ultrasound was found to decrease the lipid packing of the phospholipid vesicles. Similar disordering effects were observed in the presence of US+MBs, as well as in the case of pressure-driven flow. This suggests that the cholesterol-doped DOPC lipid bilayers are sensitive to shear stress, irrespective of whether it is caused by flow, acoustic or cavitation induced streaming.

In contrast, the average lipid order of the vesicles increased only in the presence of microbubbles. Two mechanisms to explain this effect were proposed. The first involves the

incorporation of highly saturated microbubble-shell DSPC lipids to form a two phase system containing more tightly packed regions of DSPC within the more fluid DOPC membrane leading to an overall increase in the measured packing. Evidence of the exchange was substantiated by the microscope images that clearly show fluorescent DSPE-PEG2000-Rhodamine attached to the microbubble shell. The second mechanism is related to the dehydrating effect of a second microbubble constituent, PEG40s. When free PEG40s was added to the vesicle suspension alone, an increase in average GP was also observed.

An increase in uptake of fluorescein sodium salt was recorded under all exposure conditions except free PEG40s. The increase in uptake associated with ultrasound exposure and pressure-driven flow was accompanied by a decrease in lipid packing as expected from previous studies. The effect of microbubbles both with and without ultrasound exposure was found to be more complex, with an increase in fluorescein sodium salt observed despite an increase in mean GP. This is most likely to have been due to the transfer of material from the microbubbles creating regions of increased local permeability in the vesicle membrane that facilitated fluorescein uptake but were not reflected in the mean GP measurement. The large standard deviation in the measured uptake for vesicles exposed to microbubbles also demonstrate the importance of physical proximity between them.

In summary, this study provides evidence of the ability of microbubbles to modulate hydration and permeability of lipid vesicles. Membrane property changes occur as a result of mechanical stimulation such as ultrasound and shear stress exposure, as well as through chemical effects associated with the incorporation of microbubble constituents, such as lipids and PEG40s, in the vesicle membrane.

V

Ultrasound and microbubble-mediated luminal movement

Following the investigation of ultrasound-mediated membrane effects addressed in Chapter IV, the aim of this chapter is to investigate a relatively unexplored field in sonoporation: the dynamics of the intracellular environment. Giant vesicles were used as cell models and the fluctuations of encapsulated flow tracers were monitored during the exposure to various excitation regimes. A preliminary study on the dynamics of intracellular vesicles is also presented.

5.0 Abstract

Studies on the bioeffects of ultrasound and microbubbles have focused mainly on transport in bulk tissue, drug uptake by individual cells, and disruption of biological membranes. Relatively little is known about the physical perturbations and fluid dynamics of the intracellular environment as a result of ultrasound exposure. Actuating the motion of cytoplasmic constituents may induce a broad range of underexplored and therapeutically relevant downstream bioeffects, potentially benefiting the design of microbubble-based treatments.

To investigate the intracellular effects of ultrasound, a custom acoustofluidic chamber was employed to enable simultaneous ultrasound exposure and *in situ* microscopy. The motion of fluorescent tracer beads within the lumen of giant unilamellar vesicles was tracked before and during exposure to ultrasound and microbubbles, alone and in combination.
Experimental observations reveal the onset of streaming within the lumen of the vesicles (referred to as intraluminal streaming) upon exposure to pressure-driven flow, ultrasound (1 MHz, 150 kPa, 60 s CW standing and travelling wave), and microbubbles (1,2-Distearoyl-sn-glycero-3-phosphocholine-PEG40s (DSPC-PEG40s); alone and in combination. The results show the formation of streaming patterns within the lumen of the vesicles upon exposure to flow, ultrasound, and ultrasound and microbubbles combined. It was shown that the velocity of the flows were correlated with applied flow velocity and acoustic pressure. Furthermore, the presence of microbubbles led to an increase in luminal flow velocities. Further research on intracellular forces, the occurrence of intracellular streaming, and the associated biological implications on mammalian cells is required to fully determine the implications for microbubble-based therapy.

5.1. Introduction

Gas-filled microbubbles stabilised by lipids, denaturated proteins, or polymer shells have been used in medical imaging as ultrasound contrast agents due to their high echogenicity. More recently, their therapeutic potential has been investigated in the context of targeted drug delivery, with particular emphasis on transient permeabilisation of the cell membrane, a mechanism frequently referred to as sonoporation.

When exposed to an ultrasound (US) field, microbubbles expand and contract at a frequency and amplitude determined by the US wave[23]. When these volumetric oscillations occur proximal to the cell plasma membrane, the resulting tensile, compressive, and shear forces associated with microbubble cavitation and collapse lead to a variety of bioeffects[11], which include activation of mechanosensitive channels[366], and reversible poration[305,367] or irreversible rupture[368] of the cell membrane. Transient formation of membrane pores has been observed *in vitro*, and has been shown to promote uptake of therapeutic molecules in a targeted manner[119]. However, it remains unclear whether physical alterations of the cell membrane are induced directly by the dynamic behaviour of cavitating microbubbles, or as a result of the shear stress caused by cavitation microstreaming flow.

Cavitation microstreaming occurs due to viscous attenuation of the irradiated ultrasound wave from radially vibrating microbubbles[369]. Particle velocimetry experiments have shown that orbital microstreaming flows near oscillating microbubbles can reach velocities of a few millimetres per second[366], thus imparting wall shear stresses up to a few Pa to vessel walls and neighboring cells[350,366,370] and causing tension on the cell membrane[371]. The resulting membrane strain potentially causes temporary permeabilisation[116], allowing for enhanced intracellular delivery of therapeutic compounds.[372]

Membrane effects have therefore received significant attention in ultrasound-mediated drug delivery; for instance, several studies have reported on plasma membrane poration[305,373,374] and fluidisation[360,375,376], analysed the cell plasma membrane surface divergence[366], and quantified

changes in the molecular arrangement of membrane's constituents[252]. However, only a limited body of work has been dedicated to shear force transmission from the extracellular to the intracellular compartments.

Work done by Zhong et al.[305] has shown that the effects of cavitation are not restricted to the cell membrane, but extend to the intracellular milieu by disrupting the interconnected network of subcellular cytoskeletal filaments. In the context of microbubble-mediated ultrasound drug delivery, intracellular reorganization and the enhancement or inhibition of intracellular transport may potentially have important implications for drug bioavailability, efficacy, and toxicity. More broadly, movement of intracellular fluid and organelles play an important role in cellular functions such as endocytosis[377], and may influence processes that rely on intracellular transport and balance of ions. For example, the membrane repair process involved in transient sonoporation has been hypothesised to rely on the recruitment and exocytosis of lipid vesicles that fuse with the plasma membrane to reseal the pores at the rupture site[378]. Modification or interruption of intracellular traffic by exposure to ultrasound may have significant safety implications, as the impairment of vesicular transport is implicated in various diseases including cancer[379], diabetes[380], heart disease[381], and also in immunological[382], neurological[383], and developmental disorders.[384]

The intracellular effects of ultrasound exposure have disproportionately focused on plant cells. Although the structure and function of plant cells differ greatly from mammalian cells, they serve as a useful model to elucidate the physical mechanisms that underpin the dynamics of intracellular structures under ultrasound exposure. Previous studies have described "churning" of intracellular organelles at various acoustic pressures and frequencies, and have reported on chromosomal abnormalities[385], reversible suppression of DNA and RNA[386], reduction in mitotic index[386], as well as changes in the internal structure of mitochondria[387]. At low acoustic pressures, the effects were largely reversible and mainly involved accumulation and movement of organelles in a slow, centrifugal motion.[388] At the frequencies used in this

chapter (1 MHz), a wide range of bioeffects have been observed. Dyer et al.[389] exposed algae hydrodictyon to ultrasound at a frequency of 1 MHz, and observed acoustic radiation force mediated accumulation of organelles at equally spaced intervals coinciding with the pressure nodes of the ultrasound wave. Other studies have reported on the disturbance and disorganisation of the contents of the vacuole, along with acoustic microstreaming within the cytoplasm. Gershoy et al.[390] associated the flow within the cell with the presence of gas filled intercellular cavities that pulsate in the presence of an ultrasound field, similarly to microbubbles attached to a cell membrane. This was confirmed by Johnsson and Lindval[391], who reported churning of intracellular contents in a "low speed centrifuge", at ultrasound frequencies of 1 MHz. To the best of the author's knowledge, no study has investigated intracellular movements as a result of exposure to therapeutically relevant ultrasound conditions and microbubbles.

To investigate the mechanisms involved in ultrasound mediated intracellular streaming, phospholipid vesicles formed using a mixture of 1,2-dioleoyl-sn-glycero-3-phosphocholine (DOPC) and cholesterol, a natural constituent of plasma membranes, were exposed to pressure-driven flow, ultrasound, and microbubbles, alone and in combination. Previous studies[71,392,393] have investigated shear transmission in lipid vesicles with a similar composition to those employed in this study as an investigational model for mechanotransduction. Membrane deformation and intracellular flow were observed in these earlier studies, including luminal flow within the vesicles.

5.2. Materials and Methods

A custom-built acoustofluidic chamber (Figure 48) was employed to expose lipid vesicle to pressure-driven flow, ultrasound, and microbubbles, as described in Chapter III. The device was driven at the thickness resonance frequency of the assembly, which was determined as 1.014 MHz.

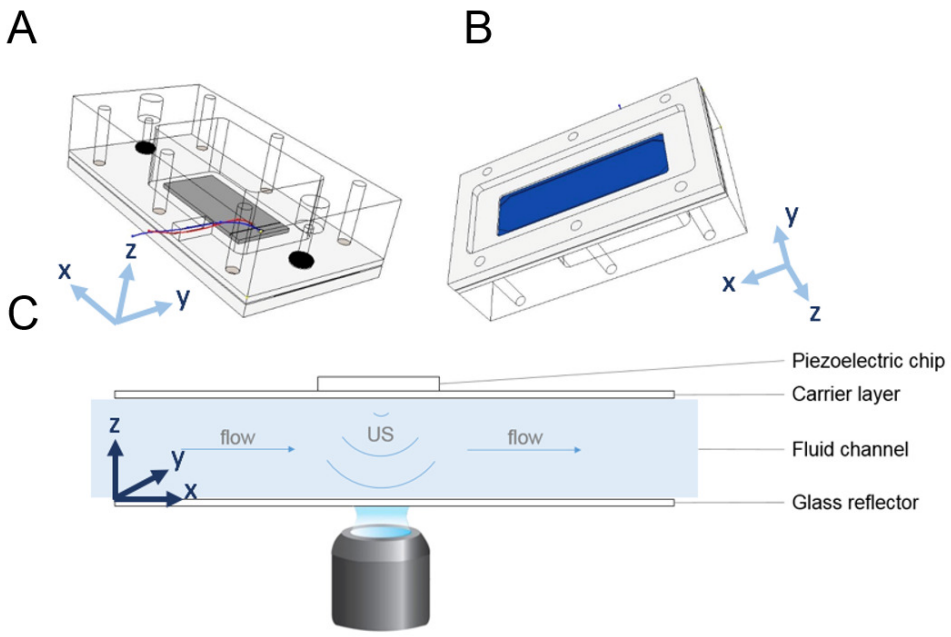


Figure 48 - A. Top view of the device, showing the grey piezoelectric chip with electrical wires. B. Bottom view of the device showing the glass slide that encloses the fluid channel. C. Side view of the channel, showing the device geometry and the constitutive layers. Not to scale.

5.2.1. Production of giant vesicles and encapsulation of flow tracers

Giant vesicles were produced on stainless steel using the electroformation protocol described in Chapter II with a solution of water and sucrose (200 mM) containing monodisperse 500 nm carboxylated fluorescent latex beads.[319] The size of the monodisperse beads was chosen to be significantly smaller than the dynamic length scale of the channel, i.e. the channel height, in order to obtain a good compromise between visibility and flow fidelity.[394] The ratio between the fluid and particle density, and kinematic viscosity, resulted in a particle response time orders of magnitudes smaller than the smallest time scales of the flow (μm/s). In addition, the

acoustic radiation force on sub-micrometric particles are small, as the radiation force scales with the particle's volume. The average diameter of the vesicles that were analysed was measured to be 31 ± 17 μm.

A sinusoidal voltage with a peak-to-peak amplitude of 4.86 Vpp and a frequency of 10 Hz was then applied to the electrodes for two hours. The frequency was then lowered to 5 Hz to stimulate vesicle detachment from the electrode surface. The needles were removed, and an aliquot of the resulting solution rich in vesicles containing fluorescent tracers was mixed with an equal amount of PBS, to dilute the extravesicular solution and thus promote vesicle sedimentation upon injection into the device. The average size of the vesicles was determined optically using the proprietary Zeiss Zen Black software. Figure 49b shows a colourised confocal image of three vesicles containing fluorescent beads.

5.2.2. Vesicle fixation to the glass slide

To provide a more realistic resemblance of a cell monolayer, vesicles were bound to a glass slide (reflector layer) using an avidin-biotin linkage. This was achieved by doping the vesicles with biotinylated lipids prior to the formation process (as described above), and by coating the glass slide with biotinylated serum albumin (bBSA) and avidin from egg white, following a protocol described previously by Kuhn et al.[320] Upon priming the chamber with the vesicle-rich solution, the vesicles sediment due to the density difference between sucrose and PBS (1.02 and 1.00394[395] g/cm^3 respectively) and, coming into contact with the glass slide, bind with the avidin layer. After an incubation phase of approximately 10 minutes, the device was flushed to remove excess latex beads. Figure 49A shows bound vesicles stained with c-Laurdan.

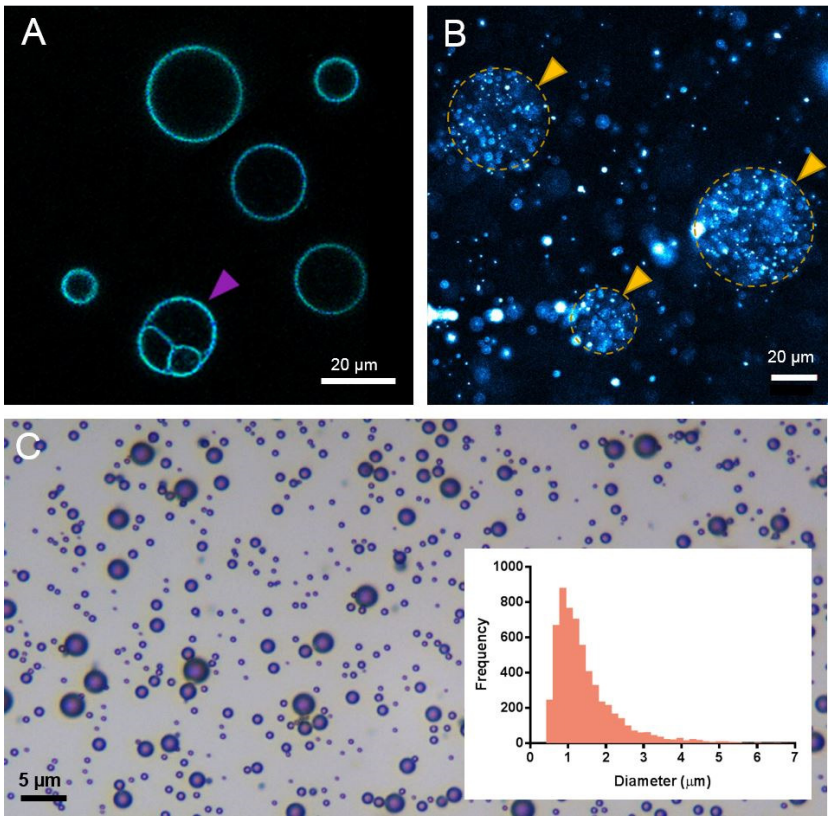


Figure 49 - A. Spectral image of DOPC GUVs stained with c-Laurdan. The purple arrow indicates a representative multilamellar GUV that is excluded from the analysis. B. – Confocal microscope image of three GUVs of different sizes with encapsulated fluorescent latex beads (500 nm) within their lumen bound to the glass surface. The image was acquired using a Zeiss LSM 780 confocal microscope equipped with a 63x plan-Apochromat oil-immersion objective. C. Suspension of DSPC: PEG40s 9:1 microbubbles imaged in a Neubauer haemocytometer for microbubble counting and sizing. Inset indicates microbubble size distribution of a representative microbubble sample. Mean size = 1.47 µm ± 0.89 µm.

5.2.3. Production and characterisation of microbubbles

Lipid-shelled microbubble suspensions were prepared as described in Section 4.2.2.1.

5.2.4. Exposure conditions

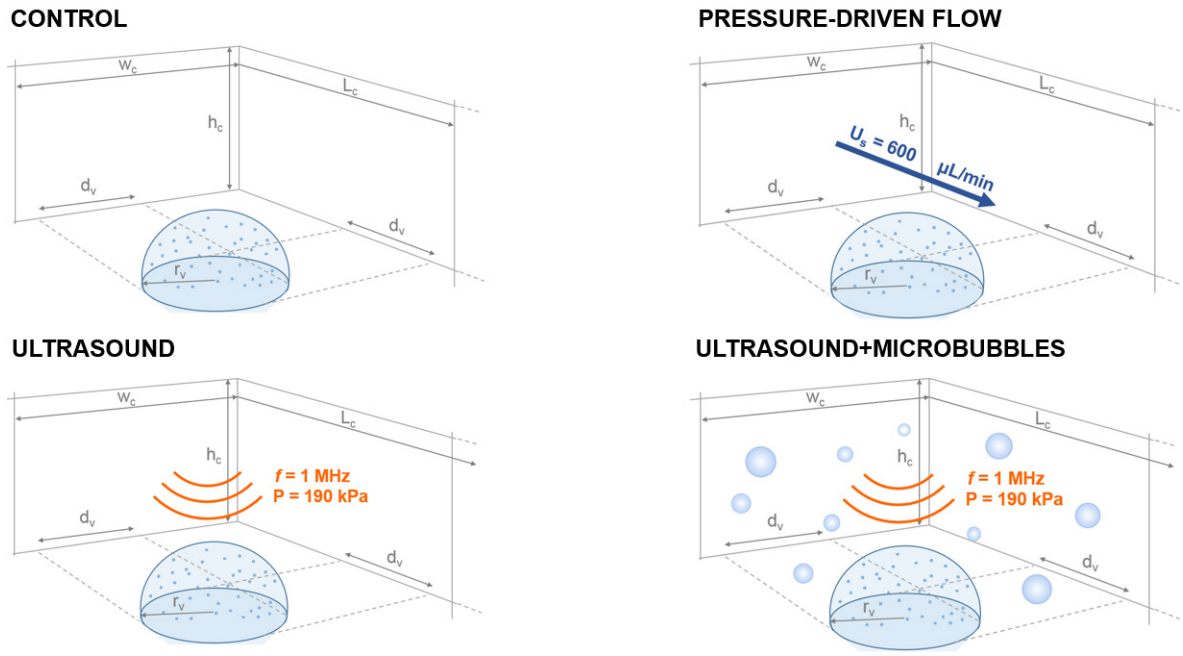


Figure 50 - Vesicle exposure conditions. In the control case (top left) the vesicles were left to stand for one minute while being imaged with no excitation applied. In the pressure-driven flow case (top right image), the vesicles were subject to a steady flow indicated by the arrow. In the case of ultrasound exposure (bottom left), the vesicles were exposed to a sinusoidal acoustic pressure wave with 190 kPa peak-negative pressure, at 1 MHz frequency (continuous wave). In the presence of microbubbles and ultrasound (bottom right), DSPC:PEG 9:1 microbubbles were injected to achieve a final concentration of $1x10^6$ MBs/mL and were immediately exposed to ultrasound in the same conditions as those used in the ultrasound-only case. In every condition, the vesicles were stimulated for one minute. d_v represents the diameter of the vesicle, w_c represents the width of the chamber (12 mm), L_c represents the length of the chamber (60 mm).

5.2.4.1. Imaging and controls

Vesicles were imaged using an inverted Nikon Ti Eclipse® microscope equipped with a cool-LED excitation system, an automated stage, CCD camera, and low numerical aperture (NA) objective (40x magnification). The vesicles containing beads were imaged in fluorescence mode (excitation: 575 nm, emission: 610 nm), at 5 frames per second with an exposure time

of 200 ms and 2x digital gain. To record a baseline bead velocity, vesicles were imaged continuously for one minute with no excitation. Figure 50 shows a schematic of the exposure conditions used in this study. Vesicles were selected for imaging according to whether they contained a sufficient number of beads and the absence of a multilamellar membrane. All experiments were performed at room temperature.

5.2.4.2. Pressure-driven shear flow

A laminar Poiseuille flow was established in the fluid channel of the device using a syringe pump (Cole Palmer, UK) and a 20 mL plastic syringe (Becton Dickinson, UK), to achieve an average channel wall shear stress of 1.25 Pa. The wall shear stress (WSS) was calculated from Equation 15.

5.2.4.3. Ultrasound exposure

The piezoelectric chip was driven with a 39.4 Vpp, 1.014 MHz sinusoidal input generated using an Agilent 33220A arbitrary waveform generator subjected to a 55 dB amplification using a RF amplifier (E&I, USA). The resulting peak negative acoustic pressure in the fluid channel was quantified by inserting a fibre-optic hydrophone within the fluid, and was determined to be 188 kPa, which is within the therapeutic range used in microbubble-based ultrasound mediated therapy[121,129,325]. Vesicles were exposed to ultrasound for one minute continuously.

5.2.4.4. Ultrasound and microbubble exposure

Vesicles were exposed to ultrasound in the presence of microbubbles for one minute. This was achieved by injecting microbubbles at a final concentration of $1x10^6$ MB/mL, and immediately activating the ultrasound field with the same parameters described in Section 4.2.3.

5.2.5. Bead velocity analysis

Tracking of single fluorescent beads was performed using the native ImageJ® TrackMate® plugin. The dynamics of single beads were monitored on a frame-by-frame basis to reveal individual particle trajectories and velocities. First, a region of interest was determined and cropped in order to separate the area covered by a single GUV and the background. Secondly, the beads were detected automatically using the built-in detection algorithm and were individually identified on each frame pair. Thirdly, the average velocity of the beads was determined by averaging the velocities in each frame pair for all the bead trajectories detected. The individual trajectories were checked manually to avoid detection errors that arise when two beads in two separate tracks merge. Figure 51 (right) shows the automatically detected trajectories of beads used in the bead velocity analysis. The illustrative average flows in Figure 51 (centre) were extrapolated using a time-resolved particle image velocimetry tool (PIVLab®) to obtain a higher vector flow density. Particle velocities were quantified bi-dimensionally in the *x*-*y* plane (as shown in Figure 51), given the depth of field of the microscope (~55 μm). The images were pre-processed to exclude stationary features in the field of view, subjected to a high pass filter with a 15x15 pixel area to improve particle detection, and calibrated using the width of the frame. The interrogation area was set in order to resolve the particle movement in the vesicle area. A further processing step was carried out to retain particles with velocities within three standard deviations of the mean.

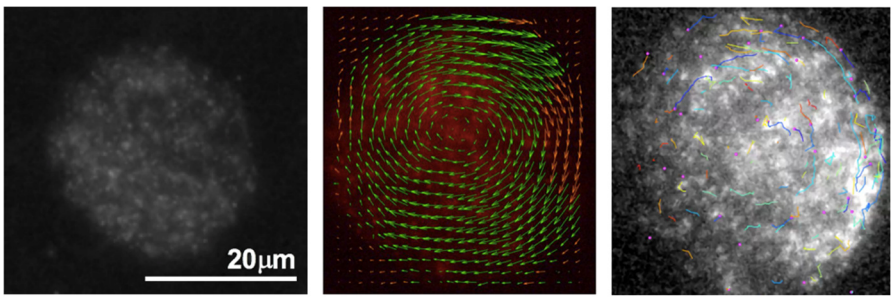


Figure 51 – (left) Fluorescence image of a GUV frame containing flow-tracer beads (centre) Example average flow map obtained with PIVLab® (right) fluorescent image of the same GUV with superimposed detected and validated bead tracks.

5.2.6. Statistical analysis

Statistical significance was determined by first performing a one-way ANOVA on all exposure conditions followed by Tukey's multiple comparisons test between each condition and the respective control.

5.3. Results and Discussion

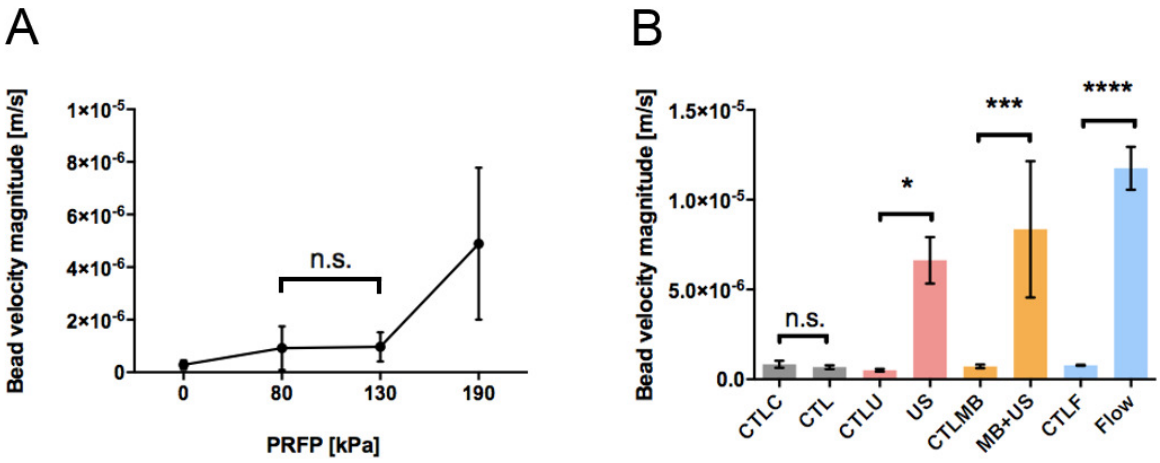


Figure 52 – A. Bead velocity during ultrasound exposure at varying ultrasound acoustic pressures (n = 3). B. Average bead velocity magnitude within the vesicle lumen as a result of varying exposure conditions. Error bars represent standard deviation for different vesicles exposed to the same conditions. Statistical significance was first tested using a one-way ANOVA on the bead velocities during exposure ($p<0.01$) and a Tukey-Cramer post-hoc was used to compare exposure conditions to their respective controls (n = 4).

5.3.1. No exposure

When no excitation was applied, vesicles maintained their shape and exhibited minimal fluctuations of the lipid membrane, known as flickering, as previously reported.[396–398] While most latex beads appeared as individual particles, some clustering was observed. Beads moved within the vesicles' lumen in a random fashion, typical of Brownian motion, and no mean displacement was measured. The average bead velocity was measured as 0.8 ± 0.2 μm/s (as shown in Figure 52(right).

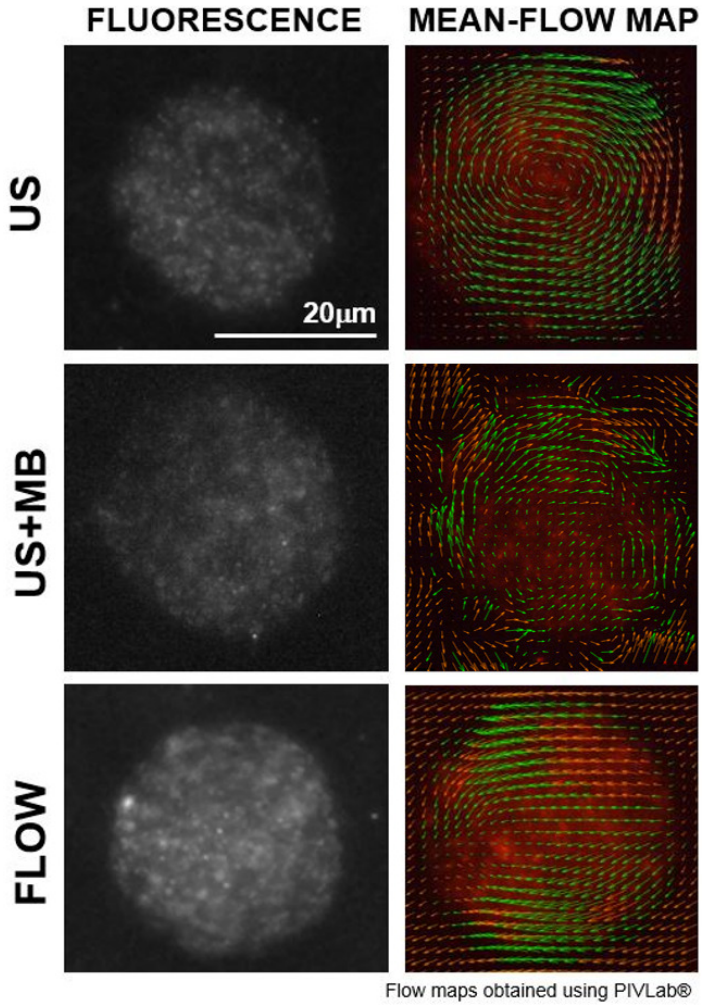


Figure 53 - (left) Fluorescence image frames of vesicles with encapsulated beads during varying exposure conditions. Corresponding averaged flow fields generated using PIVLab®. The averaging was applied across all frames acquired during exposure. Interpolated vectors are labelled orange. Vectors calculated throughout all the frames with at least six particle pairs have been labelled green.

5.3.2. Pressure-driven flow

A fully developed Poiseuille flow was formed within the channel seconds after activation of the syringe pump, as predicted by the low Reynolds number in the channel. As shown in Figure 37, the GUV tilts towards the direction of flow immediately after activation, and the deformed shape is maintained for the whole duration of the exposure.

As a result of pressure-driven shear flow, fluorescent beads immediately started to move in two circulation patterns inside the vesicle (Figure 53). The double vortex flows are a result of the symmetrical forces imparted by the flow on the vesicle membrane. When exposed to shear

stress, the vesicle membrane lipids effectively flow along the contours of the vesicle, which results in areas of membrane tension and compression.

The average fluid velocity was determined to be 12 ± 0.12 μm/s, as shown in Figure 52(right), with minimal variation over time. The average fluid velocity did not show any correlation with the vesicle's diameter (data not shown), as previously observed by Sebastien et al.[163] in lipid vesicles with diameters up to 23 μm and velocities up to 2500 μm/s.

The movement of fluorescent beads is determined by the transfer of momentum from the extra-vesicular fluid to the intra-vesicular fluid, via the vesicle membrane. The fluid state of DOPC:Chol membranes allows lipids to rearrange themselves along the vesicle contours, causing an average flow of membrane lipids upon application of an external stress.

As the velocity profile in a rectangular duct follows a quadratic relation relative to the *y* position in the channel, the streamlines across the vesicle will be symmetrical at the centre of the channel (as shown in Figure 53, bottom), and increasingly asymmetric closer to the channel walls. This was also reported by Sebastien et al.[163], showing that at the centre of the channel the intravesicular flow exhibited symmetric vortex dipoles, while at the extremities the circulation patterns were quasi-circular, with a size reduction of the vortex closer to the sidewall of the flow channel.

The results presented here are consistent with those reported in previous studies on phospholipid vesicles subjected to flow. Membrane translation has been observed and quantified by Yamada et al.[399], while intravesicle particle movement was first reported by Keller et al.[400]. Other studies have related the intravesicle flow velocity to the membrane properties of the vesicle's phospholipid membrane[401].

5.3.3. Ultrasound exposure

Upon exposure to ultrasound, fluorescent tracers exhibited movement perpendicular to the direction of ultrasound propagation. A wide range of circulation patterns were set up within

the vesicle lumen, which differed from the vortex dipoles observed in the case of steady shear flow. The average velocity was of 6.5 ± 1.3 μm/s, and the variance in the velocity values depended on the location of the vesicle within the fluid channel, as this determines the characteristics of the ultrasound field as well as the magnitude of the acoustic streaming at a particular location. Figure 54 shows a representative image of the tracks generated by the PTV algorithm and the movement of an arbitrary particle translating within the vesicle lumen as a result of ultrasound exposure. In vesicles located near the edges of the flow chamber (± y direction), particle accumulation was observed. This is likely due to lateral gradients in the acoustic pressure field, coupled with secondary radiation forces within the fluid channel, which cause particles to accumulation and clustering.

Acoustic streaming flow patterns in the vesicle plane were observed and quantified in three separate fields of view. The average velocity immediately above the reflector surface in the plane of the transducer after one minute of stimulation was determined using particle tracking velocimetry to be 15.1 ± 3.5 μm. Eckart streaming was assumed to be negligible in water over the small distances considered in this study. Moreover, it was found that the intravesicle bead velocity was correlated with acoustic pressure within the fluid channel (Figure 52, left). With increasing acoustic pressure, the bead velocity increased accordingly.

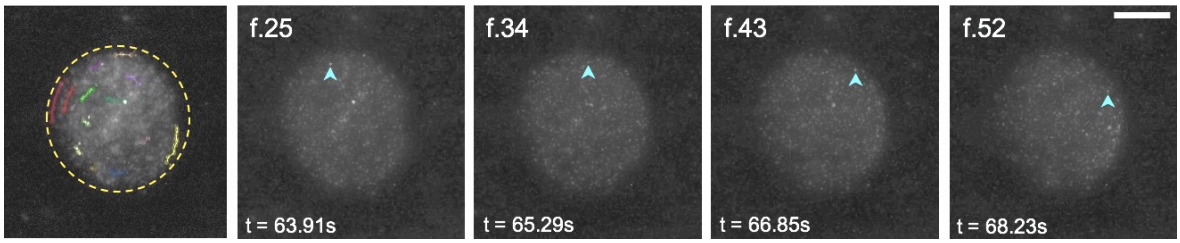


Figure 54 - Latex beads streaming within the lumen of a GUV. Cyan chevron indicates the position of a single bead in successive frames when exposed to 1 MHz, 188 kPa ultrasound in continuous wave. Scale bar = 10 μm.

5.3.4. Ultrasound and microbubbles

When exposed to microbubbles and ultrasound, vesicles exhibited higher intraluminal fluid velocity when compared to exposure to ultrasound alone (Figure 52). The increase in flow

velocity was not instantaneous as observed during pressure-driven flow, but erratic and discontinuous, as shown in Supplementary Video 4.3 (Appendix B). This behaviour is likely the result of concurrent superposition of the effects of ultrasound and microbubbles, such as primary and secondary radiation forces between microbubbles, as well as acoustic and cavitation microstreaming. This is also reflected in the higher standard deviation of the average bead velocity, compared to the other exposure conditions. The average bead velocity during exposure to ultrasound and microbubbles was recorded as 8.5 ± 3.8 μm/s (Figure 52, right).

Fluid velocities induced by stable cavitation of microbubbles are higher in magnitude when compared to acoustic streaming velocities, and affect the vesicles heterogeneously depending on the relative position of the cavitating microbubble. In a similar fashion to pressure-driven flow, the forces on the lipid membrane cause the membrane lipids to flow constrained by the vesicle contours. Non-uniform flows in proximity to the exterior of a vesicle in turn lead to asymmetric flows in the vesicle, confirmed by the flow patterns generated by particle image velocimetry (Figure 53). Asymmetric flows within a vesicle cause positive and negative divergence and a heterogeneous stress profile on the vesicle surface that may lead to rupture of the membrane. However, while other studies have reported pore formation in lipid vesicles as a result of transmembrane osmotic differentials[402], no pores were observed within the time and optical resolution of the imaging system in this study.

In many cases, vesicles lysed upon activation of the ultrasound field in the presence of microbubbles. Porter et al. reported lysis tensions for cholesterol-doped DOPC vesicles (5:1 molar ratio) as 1.89 mN/m[403]. The incorporation of microbubble lipid debris onto the GUV surface, previously reported by the authors, may also potentially affect lysis tension of the membrane.[404]

5.3.5. Biological implications

The healthy functioning of mammalian cells relies on the movement of cargos between cellular compartments in a three dimensional space through distances multiple times their size. The movement is systematic and is mediated by motor proteins that carry vesicles along tubules within the cell's cytoskeletal network. Previous studies have reported intracellular vesicle transport velocities in the order of 0-3 μm/s[377,405,406], which is well within the range of bead velocities reported in this study (0.8 ± 0.2 μm/s for no exposure, 12 ± 0.12 μm/s for pressure-driven flow, 6.5 ± 1.3 μm/s for ultrasound, 8.5 ± 3.8 μm/s for ultrasound and microbubbles). The streaming velocities are of sufficient magnitude to affect ion balance, protein trafficking, and cargo transport, potentially leading to altered cellular functions and pathogenesis. [407] However, mammalian cells have a developed cytoskeletal structure, are packed with organelles, and have a denser plasma membrane compared to giant vesicles. The magnitude of intracellular effects would also depend on the cell type; for example, metastatic tumour cells have been shown to be more pliable with lower cytoskeletal densities, and exhibit faster intracellular dynamics than their healthy counterparts.[408] The remaining sections of this Chapter will focus on determining whether similar effects observed in giant vesicles also occur in mammalian cells. A preliminary set of experiments to quantify the changes in intracellular vesicles trafficking as a result of steady flow, ultrasound, and microbubbles are described.

5.4. Intracellular trafficking

Tracking small (<250 nm) particles within cells is an arduous task due to light diffraction-limited spatial resolution, particle uptake mechanisms, and specificity in fluorophore tagging. For these reasons, in the following experiments, the movement of intracellular lipid vesicles was monitored, due to their size and the low selectivity of lipid membrane stains, which allow the simultaneous staining of intracellular vesicles and the plasma membrane. The movement of lipid vesicles in alveolar basal epithelial cells, used as cell models, was tracked and quantified using confocal microscopy coupled with particle tracking velocimetry. Figure 55 is a representation of the comparison between the latex spheres encapsulated in GUVs and the intracellular lipid vesicles tracked in this part of the study.

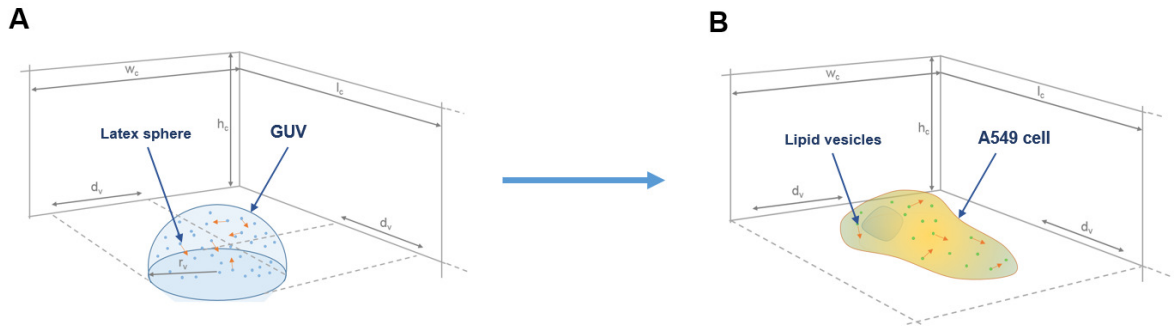


Figure 55 - Comparison between intracellular tracking in GUVs and cells A. Representative giant unilamellar vesicle encapsulating latex spheres within the acoustofluidic device. B. Illustration of a A549 cell with stained lipid vesicles in the acoustofluidic device.

5.4.1. Materials and Methods

Cells were exposed to pressure-driven flow, ultrasound, and targeted microbubbles, alone and in combination, according to the protocols described in Section 5.2.6. Cells were imaged on a Zeiss 780 LSM confocal microscope equipped with a Zeiss Apochromat 63x objective. The pinhole was adjusted to maximise the fluorescence signal while maintaining a ~10 µm imaging slice. Cells were individually imaged with a bidirectional scan to minimise the frame

size and obtain the highest achievable frame rate. Depending on the size of the frame, the acquisition rate varied from 8 to 12 frames per second.

5.4.1.1. Cell culture

A549 adenocarcinoma human alveolar basal epithelial cells (ATCC, USA) were cultured in DMEM (Life Technologies, UK) supplemented with 10% Fetal Bovine Serum (Life Technologies) and 1% Penicillin/Streptomycin (Life Technologies, UK). Two days before experiments, cells were passaged with 0.05% Trypsin/EDTA solution, and seeded on 75 x 25 mm #1.5 glass coverslips (Logitech, UK) at a density of 5000 cells/cm^2, and cultured until use in the same media. On the day of experiments, coverslips were mounted onto the ultrasound device and stained using Fluorobrite DMEM:CellMask™ (ThermoFisher Scientific, UK) solution at a 1:1000 v/v concentration and incubated for 45 minutes. For Figure 58, 500 nM MitoTracker Red™ (Life Technologies, UK) was added to the solution to stain mitochondria.

Following incubation, cells were washed and kept in Fluorobrite DMEM (enhanced basal media for imaging) during experimentation. For experiments with microbubbles, a solution of charged microbubbles (DSPC:DSEPC:PEG40s) with a concentration of ~$1x10^6$ microbubbles/mL was injected into the device, left to stand for 10 minutes to facilitate the attachment of the microbubbles to the cell membrane, and then flushed with a fresh 1 mL aliquot of Fluorobrite DMEM. The exposure conditions followed those reported in Section 5.2.6. The controls for each condition were obtained in the absence of any excitation for one minute, followed by one minute of exposure. Figure 56 shows a schematic representation of the stimuli applied.

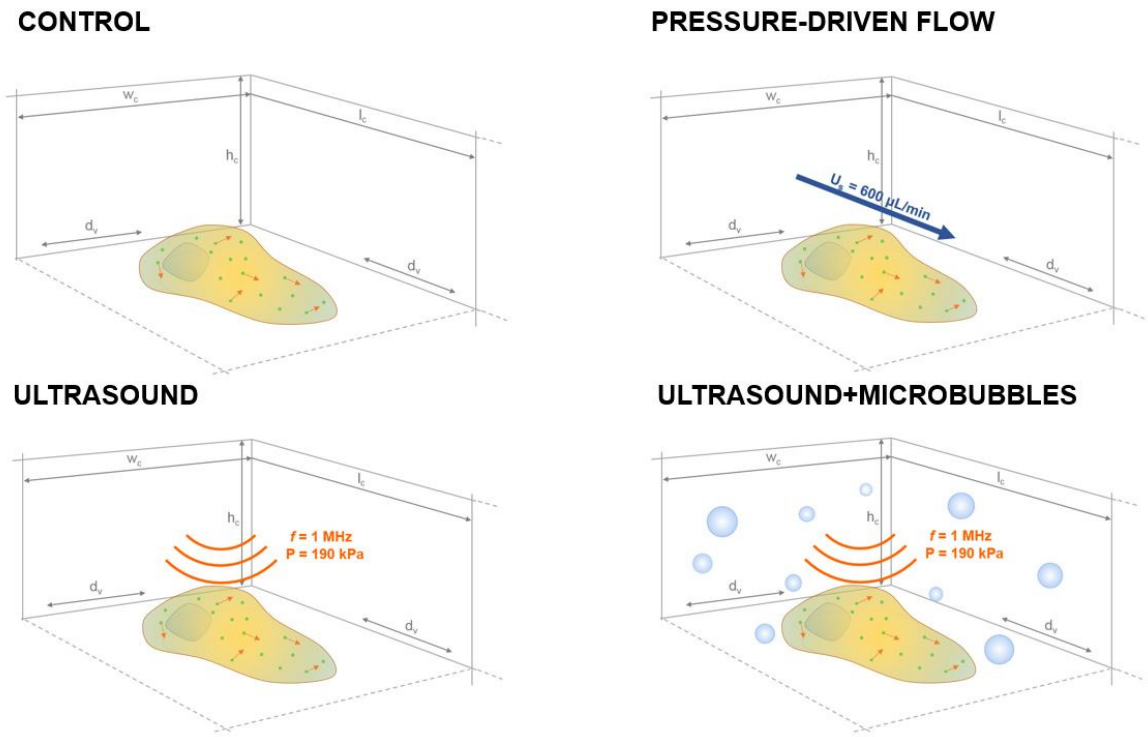


Figure 56 - Illustration of the conditions cells were exposed to. Control: cells were left to stand and imaged for two minutes. Pressure driven flow: cells were imaged for one minute and then exposed for a subsequent minute to flow. Ultrasound: cells were imaged for one minute and then exposed to ultrasound (1 MHz, 190 kPa, CW) for a subsequent minute. Ultrasound and microbubbles: cells were imaged for one minute in a suspension of charged microbubbles and then exposed to ultrasound (1 MHz, 190 kPa, CW) for a subsequent minute.

5.4.1.2. Image analysis

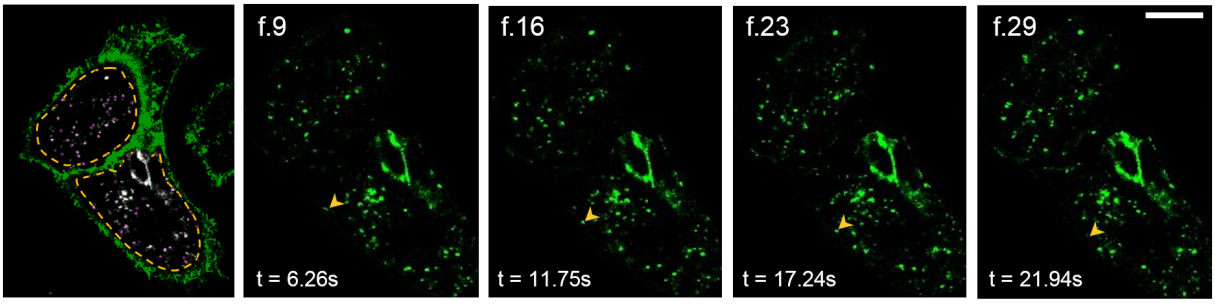


Figure 57 - Particle tracking of lipid vesicles within regions of interest in the cellular lumen. Scale bar = 15 µm. The yellow chevron indicates a fluorescent lipid structure that is translating within the cell.

The confocal videos of the intracellular dynamics were exported from Zeiss Zen Black Edition to a series of successive frames. The stack was then opened in ImageJ® for further analysis. The intracellular milieu was then segmented manually and cropped from the image stack. The

brightness and contrast of the image was then enhanced to improve the signal to noise ratio of the image. The ImageJ® plugin TrackMate® was then used to detect the vesicles on a frame-by-frame basis (Figure 57, frame 1). To achieve this, particle size and intensity were set using the plugin user interface to allow particle tracking between frame pairs. After the detection stage, the tracks were thresholded according to length, to exclude particles that were observed for less than five frames. After the detection and analysis stage, the tracks were manually verified to eliminate errors associated with particle splitting and defocusing. The vesicles detected at the start of the exposure were analysed independently from their dynamics during exposure. The average velocity of the vesicles corresponds to the average velocity of the beads within all the successive frame pairs analysed. Figure 57 shows the steps involved in segmentation and detection (frame 1) and the representative tracking of a vesicle across video frames (frames 9-29).

5.4.1.3. Statistical analyses

A one-way ANOVA was used for multiple comparison tests, while t-tests were employed for the comparison of two data sets. All data are expressed in terms of mean ± standard deviation and the number of independent replicates is reported in the figure captions. The following conventions for statistical significance are used throughout the paper: ns = $p > 0.05$, * = $p \leq 0.05$.

5.4.2. Results

While the experimental observations in GUVs showed an increased movement of beads when exposed to pressure-driven flow, ultrasound, and microbubbles, alone and in combination, no statistically significant changes (one-way ANOVA between exposures) in the lipid vesicle trafficking (as shown in Figure 58) were detected. The average velocity of the beads did not exceed 200 nm/s, and t-tests did not reveal any differences between the controls and their respective exposures.

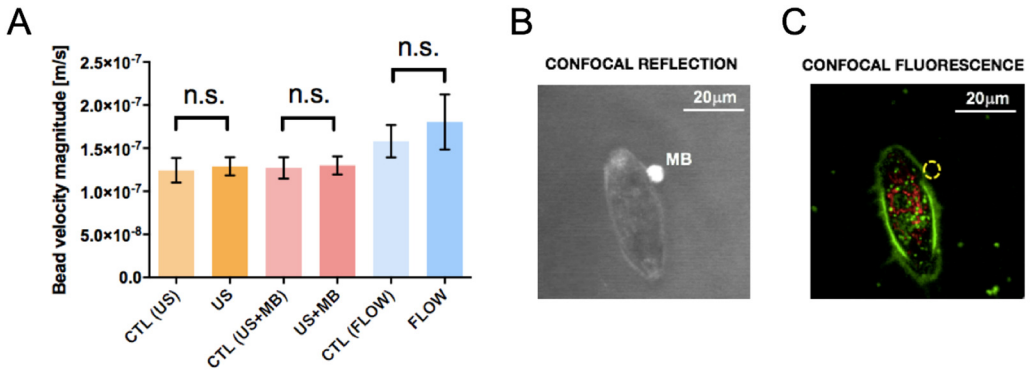


Figure 58 - A. Vesicle velocity magnitude as a result of varying exposure conditions. Statistical testing revealed no statistical difference between conditions (ANOVA). Three independent replicates were analysed. B. Confocal reflection microscopy of a cell with microbubble attached to its surface C. Fluorescence image of the cell shown in (B) with tagged lipids (CellMask™) and Mitotracker™. The corresponding location of the microbubble is shown by the dotted yellow circle.

The absence of velocity changes in the vesicular trafficking upon exposure to exogenous stimulation may be attributed to a number of reasons. The first is that the forces that drag the vesicles across cytoskeletal fibres are greater than those imparted by the stimuli. The second relates to the higher cytoplasmic consistency and viscosity of intact mammalian cells compared to the lumen of a GUVs, which may prevent any form of intracellular streaming, as hypothesised by Williams[409].

The method of analysis may also be a contributing factor in the recording of low intracellular vesicle velocities. To avoid measurement bias, the velocity analysis was performed on all vesicles detected in the first frame, independently from whether they moved or remained stationary while stimulated. However, the large majority of vesicles either remained stationary or exhibited a "saltatory" (stationary with occasional fast displacement[410]) motion across the vesicle, skewing the results toward lower vesicle speeds.

A further challenge is the movement of cells during the exposure. As the cells adapt and move, they change aspect during the imaging process. However, due to the wrapping of the frame around the entire area of the cell during imaging, coupled with the confocal configuration of the microscope, tracking these changes in three dimensions is an arduous task.

To address this challenges, the analysis could be modified to include stationary structures within the cell as fiducials, thus allowing image registration on the particle trajectories. Future work may include tagging other organelles within the cells, such as mitochondria (as shown in red in Figure 58) and explore whether targeted microbubbles (Figure 58C and Figure 58D) cause localised intracellular movement in their vicinity, as shown by Dyer and Nyborg in Elodea cells[411]. In addition, novel techniques such as defocusing microscopy[163] may be implemented to obtain 3D movement maps of the vesicles.

5.5. Conclusions

DOPC giant unilamellar vesicles doped with cholesterol were exposed to pressure-driven flow, ultrasound, and ultrasound in combination with microbubbles. The resulting flows within their lumen were observed and quantified using particle tracking velocimetry. In the control cases, no average particle movement was observed other than Brownian motion; however, all other exposure conditions caused particles within the vesicle lumen to move.

In the case of pressure-driven flow, two vortexes were established inside the vesicles, confirming results previously reported in the literature[163,412,413]. This effect is related to the membrane dynamics under shear flow, which effectively acts as a fluid layer, resulting in intravesicular movement. Upon exposure to ultrasound, beads also exhibited an average bead movement of 6.5 ± 1.3 μm/s. Upon exposure to microbubbles, the superposition of flow-mediated, and ultrasound-mediated effects occurs. Vesicles are subject to an ultrasound field that has been shown to cause intravesicular flow on its own. Secondly, the fluid flows created by cavitating microbubbles also affect the movement of beads within the lumen of the vesicles. The shear stress applied on the vesicle membrane during exposure to ultrasound and microbubbles varies significantly in magnitude, direction, and time and length scales. Erratic changes in bead velocity and intravesicle flow patterns during ultrasound and microbubbles exposure suggest rapid changes in the flow velocity of the membrane and surface divergence.

This is reflected by the average standard deviation of the bead velocity, which was found to be 8.5 ± 3.8 μm/s.

Future work may focus on the numerical modelling of the intravesicle perturbations and solving attenuation-driven and boundary streaming equations within a fluid hemisphere cavity in a channel, in order to aid the decoupling of ultrasound and shear effects on the movement of the vesicle contents.

A preliminary study was presented to quantify the movement of intracellular vesicles to various exposure regimes. It was shown that intracellular vesicles could be readily tracked, microbubbles could be functionalised to adhere to the cell surface, and the movement of mitochondria was readily imaged. No significant differences were recorded in the movement of intracellular vesicle as a result of pressure-driven flow, ultrasound, and microbubbles. However, the lack of observable effects may have been due to the low acoustic pressures used, vesicle attachment to the cytoskeleton, and the high density of the cytoplasm. Future work may include the use of a wide-field microscope to limit organelle defocusing, implementation of image registration algorithms to account for cellular displacement, and the use of more relevant endothelial cell models. In addition, higher acoustic pressure amplitudes could be investigated.

The effects of ultrasound and microbubbles on the perturbation of the intracellular content of human cells are significant for various cellular functions and pathogenesis, but remain under investigated. The motivation, results and observations presented in this study lay the groundwork for further investigations to study the intracellular movement as a result of pressure-driven flow and ultrasound exposure, alone and combined with microbubbles.

VI

Conclusions and Future Work

In this chapter the overall conclusions of the thesis are compiled and compared to the aims outlined in Chapter I. The limitations of the work and aspects that warrant future investigation are discussed.

1.0 Overview

Sonopermeabilisation represents a promising drug delivery strategy that may strengthen the arsenal of therapies against cancer. A growing literature,[11,256] that includes numerical modelling[414], *in vitro*[292] and *in vivo*[415] studies, confirms its potential as an adjuvant to existing drug treatments for numerous diseases. Earlier in this thesis the knowledge gaps that are slowing its translation were discussed and the overall objective of this work was to provide new tools for investigating the mechanisms involved in ultrasound-mediated therapy. Visualising and quantifying the interdependencies and correlations between microbubble dynamics and their effects on cells is imperative to enable the design of effective, repeatable and predictable treatments.

Section 1.5 outlined the research challenges, which included: the difficulty involved in isolating cellular parameters such as the lipid membrane and the intracellular milieu, the need for non-invasive visualisation and quantification of biological features at the molecular scale, and the creation of a predictable and repeatable ultrasound field under therapeutically relevant conditions.

To address these challenges, the thesis set four aims. The first involved designing and manufacturing a rapid and cost-effective method for creating cellular membrane models in a reproducible manner; thus enabling the isolation, characterisation, and quantification of intravesicular parameters involved in microbubble-mediated ultrasound treatment. The second involved designing and characterising a device that would enable the exposure of biological samples to a known ultrasound field in the presence of cavitation agents, simultaneous with non-invasive optical and acoustic monitoring. The third aim was to investigate the effects upon the molecular arrangement of giant phospholipid vesicles of therapeutically relevant exposure conditions, using quantitative fluorescence microscopy. The final aim was to make a preliminary study of intracellular fluid flow induced by exposure to ultrasound and cavitation.

Chapter I described the research context and motivation, the aims and objectives, and provided an outline of the thesis structure. Chapter II presented a novel technique to fabricate phospholipid vesicles suitable for use as cell models. Chapter III described the design, construction and characterisation of a microfluidic device for the study of the effects of cavitation microstreaming on biological samples. Chapter IV focused on the effects of microbubble-based ultrasound treatments on the hydration and permeability of phospholipid membrane models. Chapter V focused on quantifying streaming within giant vesicles as a result of exposure to different conditions, and also provides a proof of concept on how the analysis could be extended to biological cells. The aim of the present chapter is to evaluate the experimental findings, summarise the overall conclusions of the work and provide recommendations and insights on future experimental steps that could be undertaken.

2.0 Summary of findings

In Chapter I, it was found that 1,2-dioleoyl-sn-glycero-3-phosphatidylcholine giant unilamellar vesicles could be prepared readily on stainless steel electrodes at a fraction of the cost of existing methods. No evidence of transition metal leaching, lipid oxidation or hydrolysis was observed within the instrumentation detection limits.

In Chapter II, a novel microfluidic acoustic resonator based on the “thin-reflector” mode was presented. The microscope-compatible acoustofluidic chamber enables simultaneous ultrasound exposure at therapeutic frequencies of 513 and 908 kHz, monitoring of acoustic emissions using a PVDF film and optical microscope observation, including compatibility with high-speed imaging. The device was used to observe and quantify sonoporation in cancer cells. In addition, the acoustic response and microstreaming patterns produced by three cavitation agents (SonoVue® gas-filled microbubbles, perfluorocarbon droplets, and polymer nanocups) were characterised acoustically and microscopically in the same device. It was found that the temperature rise as a result of one minute of operation was small at both frequencies ($\Delta T<1°C$). Microbubbles were found to produce acoustic emissions at integer

harmonics of the driving frequency at low acoustic pressures and fractional harmonics at higher pressures. Gas-trapping polymeric cups produced primarily broadband emissions. Using a high speed camera, the radial expansions of cavitating microbubbles could be readily monitored in real time. Similarly, the cavitation microstreaming fields could be captured and quantified by using fluorescent beads as tracers. Streaming velocities of up to 1000 μm/s were recorded. These results demonstrated the effectiveness of the device as a tool for investigating cavitation processes and microbubble-cell interactions in ultrasound mediated therapy.

Chapter III focused on quantifying the changes in membrane hydration as a result of various therapeutically relevant exposure regimes. When exposed to ultrasound, the degree of lipid packing of DOPC:Chol phospholipid vesicles decreased accordingly. Similar disordering effects were recorded as a result of exposure to pressure-driven flow. In some cases, ultrasound and microbubbles combined also led to a decrease in packing, which was hypothesised to be due to the microstreaming flows caused by cavitating microbubbles. The vesicle membrane packing only increased in the presence of microbubbles, indicating the lipid transfer and incorporation of highly saturated DSPC lipids from the microbubble shell to the vesicle bilayer. This hypothesis was substantiated by fluorescence microscopy, showing fluorescent DSPE-PEG2000-Rhodamine from the microbubble shell transferred to the vesicle bilayer. It was also found that exposure to PEG40s, a common microbubble constituent, caused the dehydration of the bilayer membranes. These changes in lipid packing promoted the uptake of a fluorescent model drug molecule, fluorescein sodium salt, indicating an increase in the bilayer's permeability. Under all conditions except exposure to free PEG40s, the fluorescence within the vesicles increased. It was also shown that DSPC debris on the vesicle bilayer led to an increase in uptake of fluorescein, in accordance to other studies in the literature.

Chapter IV demonstrated that when cholesterol-doped DOPC vesicles were exposed to pressure-driven flow, ultrasound, microbubbles, and their combination thereof, streaming flows of the order of a few μm/s were induced within the vesicle lumen. In the case of steady

flow, the effect was attributed to the transfer of momentum to the phospholipid membrane, which in turn transfers momentum to the vesicle lumen. In the case of ultrasound, the effect was attributed to the acoustic streaming flows generated within the fluid channel of the device. For ultrasound and microbubbles combined, the streaming velocities were higher compared to ultrasound alone, potentially because of the cavitation streaming flows caused by cavitating microbubbles.

Furthermore, an experimental proof-of-concept to extend the work on giant vesicles to cells was presented. The findings of this chapter provide new insights into the momentum transfer across phospholipid membranes in ultrasound mediated microbubble-based exposures. Alteration of the intracellular trafficking within cells may have significant safety and treatment implications, as outlined in Section 5.3.5.

3.0 Limitations and future work

In Chapter II, a method to produce GUVs in a sucrose solution was presented. However, it is of great interest to produce GUVs at physiological ion concentrations (~300 mOsm/L), to better mimic *in vivo* conditions. Future work could therefore include modification of the proposed method e.g. by using non-conductive glass electrodes and inducing an external electric field as described by Okomura and colleagues[214]. Previous studies have also shown that pure charged lipid films could be electroformed into vesicles using electroformation on ITO[416]. Moreover, to overcome the challenge of long sedimentation times, a microfluidic concentrator similar to that developed by Carugo et al.[95] could be incorporated in the electroformation chamber.

In Chapter III, the effects of different therapeutically relevant conditions on the lipid packing and permeability of GUVs was assessed. Two main limitations were identified for the device presented in Chapter III. The first is related to the image acquisition, as only the mid-plane of the vesicles was taken into consideration in the analyses presented, possibly ignoring effects

that occur in the luminal and apical sections of the cell/vesicle membrane. However, the mitigation of this limitation is particularly challenging, due to the necessity of using confocal spectral imaging to acquire generalised polarisation data. This limitation could be addressed by performing spectral z-stacks of vesicles before, during, and after the application of the treatment, while accounting for photobleaching effects.

The second limitation relates to the effect of an oil-immersion objective in contact with the glass slide on the acoustic field within the acoustofluidic device. While in the simulations presented in Chapter III it was assumed that the ultrasound wave was reflected by the glass-air interface, this effect may be altered by the contact of immersion oil and objective on the glass slide. This could be accounted for by adding an immersion oil layer and objective to the layers configuration of the device in the 1D and 2D models, in order to characterise the effects on the ultrasound field and related US-RA behaviour.

In addition, the effects of varying the substrate properties on the behaviour of ultrasound-responsive agents could also be investigated, following the work done by Glynne-Jones and colleagues[417]. Initially, this could potentially be achieved by coating the glass layer using biologically relevant materials such as gels. Furthermore, the effect of distance from the thin-reflector layer may be also be investigated by capturing microbubbles in optical traps at different positions within the fluid layer of the device.

A further step to improve the analyses presented in this chapter would be to repeat the work done on giant unilamellar vesicles on giant plasma membrane vesicles (GPMVs) derived from endothelial cells, as they retain the composition of the cell membrane from which they are derived[154] and therefore represent a more realistic membrane model. Moreover, to better mimic physiological conditions, the work could potentially be extended to 3D cell cultures.

Chapter IV focused on quantifying the streaming within giant unilamellar vesicles *in vitro*. The limitations associated with this study include the inability to fully decouple the contributions of ultrasound and acoustic streaming to the flow within vesicles. This limitation

may be addressed by performing numerical simulations, or by embedding the GUV is agar gel in order to suppress extravesicular flow. Moreover, the study may be extended to three dimensional particle tracking using defocusing microscopy[163]. Further work may also focus on using more biomimetic vesicles that include cytoskeletal fibers[168] and proteins.[418]

Experimental difficulties also lie in tracking vesicles in the 3D space with sufficient spatial and temporal resolution, as well as accounting for the movement of cells as they migrate and undergo reproduction. The tradeoff between intensity of the signal, spatial and temporal resolution, and phototoxic effects was a major limiting factor to account for in the data acquisition in this chapter and throughout this thesis. These challenges can be partially addressed by exposing samples to laser excitation limited to the focal plane, pulsed laser exposures, and a more efficient optimisation of acquisition parameters such as frame size, gain, and scanning mode. Furthermore, the bioeffects and dynamics of ultrasound cavitation may be related to the associated acoustic emissions with the use of the PVDF passive cavitation detection setup described in Chapter III.

4.0 Final remarks

The work presented in this thesis has demonstrated that giant unilamellar vesicles are useful models to study cell-microbubble interactions. Vesicles can be employed as a minimal system to understand the effects of ultrasound-mediated ultrasound therapy on phospholipid membranes in the absence of other membrane constituents and active phenomena. The studies presented emphasise the concurrent nature of mechanical and chemical effects across wide spatial and temporal length scales, underlining the need for simpler approaches to characterisation.

Overall, this thesis has addressed several of the challenges that hinder progress in sonoporation studies. A new tool to fabricate vesicles rapidly, cheaply and reproducibly has been developed. The μLAR acoustofluidic device provides a versatile microscopy-compatible

platform that allows the concurrent monitoring of cavitation dynamics, acoustic emission, and sonoporation activity for researchers in the *in vitro* cell-microbubble field. The study on the effects of ultrasound and microbubble provides insight on the physical and chemical mechanisms involved in microbubble-mediated drug delivery. Lastly, the preliminary work presented on the dynamics of the intracellular space will hopefully promote further investigations in a relatively underexplored area of biomedical ultrasound studies.

Appendix A

1.0 Uncertainty analysis on layer thickness (1D simulations)

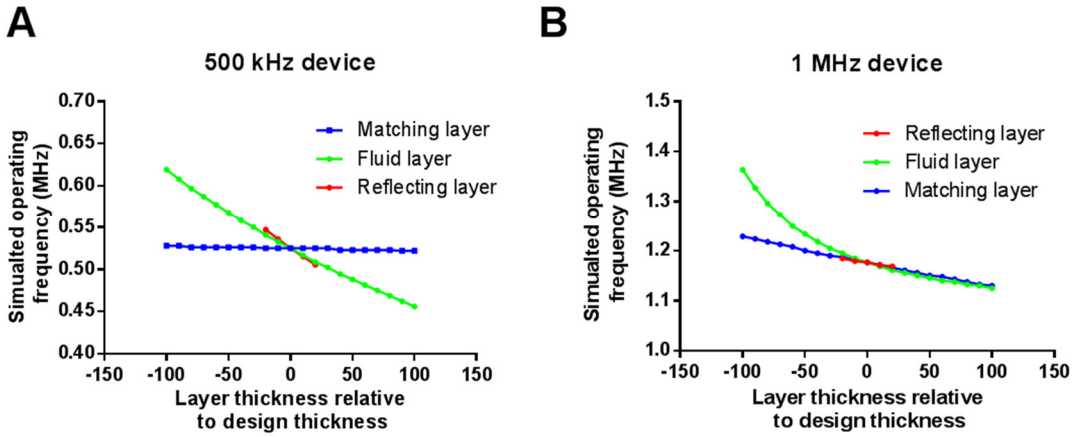


Figure 59 - The simulated effect of different layer thicknesses on the operating frequency of both the A. 0.5 MHz and B. 1 MHz μLARs.

The plots in Figure 59 show how the simulated resonant frequencies of both the 0.5 MHz μLAR and the 1MHz μLAR change when the layer thicknesses differ from the design thicknesses. The design thicknesses can be found in Table 1). The production tolerance for the MACOR sheet was ± 20%. All parts were machined using a computer numerical control (CNC) machine.

2.0 Particle streak velocimetry

A particle streak velocimetry (PSV) algorithm was written in MATLAB. Image processing was performed on each frame in the videos (Figure 60A) to generate binarised images containing only streaks (Figure 60B). Image processing involved a series of intensity-based operations as well as morphological filtration using functions available in the MATLAB image processing toolbox.

Images were first sharpened by subtracting a blurred version of the image from itself. This facilitated the detection of particle streaks by enhancing contrast around edges in the image. Contrast was further enhanced by mapping the grayscale intensities such that 1% of the values were saturated at the minimum and maximum intensities respectively.

Minimum and maximum intensity threshold levels were then determined. Fluorescent tracer particles tend to accumulate toward the centres of vanished cavitation microstreaming patterns. This manifests as bright regions in the images that make thresholding by a single level ineffective. In these cases, a manually determined low-pass intensity threshold was applied to remove regions with far greater intensity than the streaks. A high-pass intensity threshold was then determined automatically by Otsu's method[419].
Following thresholding, connected-component labelling was performed on the binarised image[420]. Connected-components were then optionally filtered by area using a manually set lower and upper bound (Figure 60B). They were then additionally filtered by eccentricity such that only objects with an eccentricity greater than 0.97 (i.e: very close to a line segment in shape) were kept. Here, eccentricity is determined using the lengths of the major (M1) and minor (M2) axes of the ellipses with the same second-moments as the connected-components such that the eccentricity, e, is defined as:

$$e = \sqrt{1 - \left(\frac{M_2}{M_1}\right)^2} \qquad \textit{Equation 18}$$

The remaining objects which should, at this point, contain only particle streaks, were then thinned to a single pixel width[421] prior to determining their arc-lengths (Figure 60D). The single pixel width objects were then fitted with 1st and 2nd order polynomials (Figure 60E). The best fitting as determined by the adjusted correlation coefficient was then used to calculate the arc-length. Each streak length was then converted to an average velocity at the centre of the streak using the pixel-to-micron conversion and the exposure time of the image. A representative output for the image in Figure 60A is shown in Figure 60F.

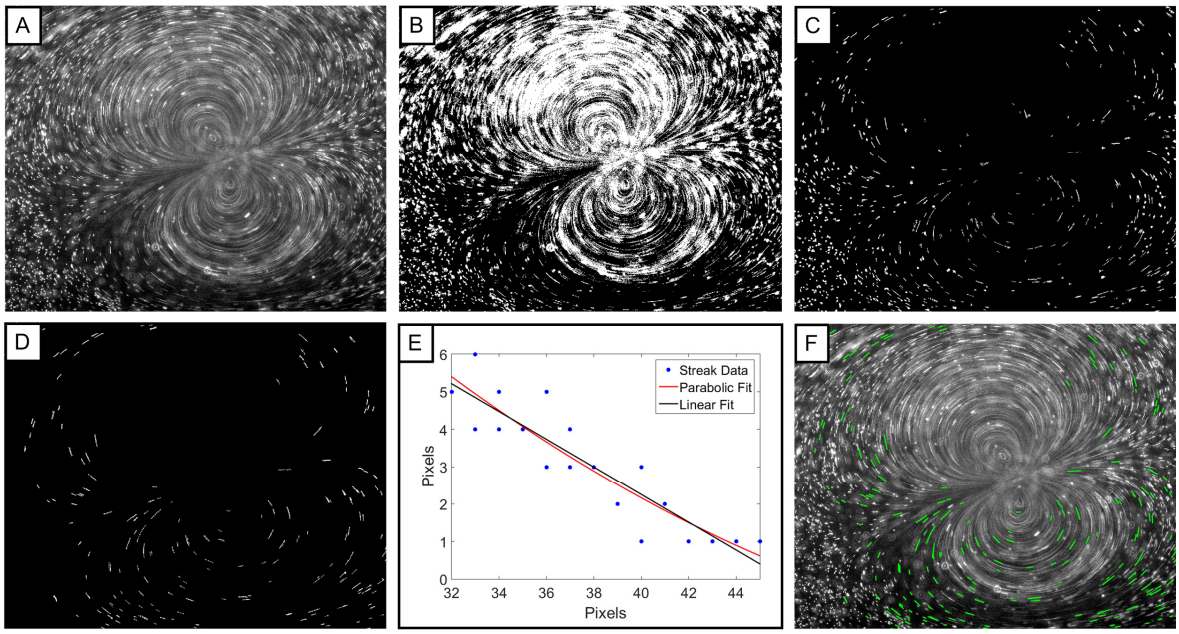


Figure 60 - The particle streak velocimetry image analysis routine. A) A raw microscope image of cavitation microstreaming produced by a SonoVue microbubble. B) The thresholded image. C) The size-filtered image. D) The eccentricity-filtered image. E) A representative streak fitted with a 1st and 2nd order polynomial. F) The detected and measured headless velocity vectors overlaid on the raw microscopy image.

2.1. Particle streak velocimetry algorithm performance

One limitation of PSV is that the sense of the velocity vectors is unknown such that the curl (for vorticity) and the divergence of the velocity field, for instance, cannot be determined from a single frame. Cross-correlation between successive frames or input of the axes, extents, and direction of the vortices could be employed to assign senses to each velocity vector. The shear stress and shear stress exposure over time that cells are exposed to in the μLAR can nonetheless be determined using PSV, by assuming a no-slip condition at the reflector layer and by using confocal microscopy to limit the depth-of-field.

The performance of the Matlab particle streak velocimetry (PSV) image processing algorithm was assessed by analysis of synthetic particle streak images with known particle streak lengths and distributions. Synthetic streak images were generated by adapting the methods used by Lazar et. al[422] and Raffel et. al[423]. The sensitivity of the PSV analysis to both streak density and gaussian noise was determined. This is especially important for streaks near the center of the

cavitation microstreaming patterns where the streak density and noise variance is highest. To generate synthetic PSV images, the intensity distribution of a single, stationary particle was determined by the following equation:

$$I_{xy} = I_{\max} q e^{\left(8\frac{-x^2-y^2}{d_p^2}\right)} \qquad \textit{Equation 19}$$

where I(x,y) is the pixel intensity at position (x,y), Imax is the the peak intensity of that particle, q is the particle's light scattering efficiency, dp is the particle diameter. This equation assumes that the intensity distribution is approximately a Gaussian bell and that roughly 95% of the scattered light is found within the particle diameter. To create each individual streak, a particle intensity distribution with a random position, diameter and peak intensity was translated by a random amount. The synthetic images (334 x 334 pixels) were approximately 1/10 of the size of the experimentally captured cavitation microstreaming images (1126 x 902 pixels) to increase the speed of image generation. The simulation streak lengths, thicknesses and peak intensities (0-75 pixels, 3-6 pixels and 51-128 respectively) were representative of cavitation microstreaming streaks produced by 2 μm diameter flow tracer particles captured using a 4x objective and an exposure time of 220 ms.

To investigate the effect of streak density on PSV performance, the number of streaks in each image was increased until the synthetic images closely resembled the areas of cavitation microstreaming images containing the greatest number of flow tracers. Assuming an imaging plane of 1000μm x 1000μm x 50μm (typical of a 4x objective), the range of streaks tested corresponds to an experimental concentration of flow tracers between 10×10^6 and 180×10^6 flow tracers/mL. 30 sets of images were generated and analysed to reduce stochastic variation in PSV performance between synthetic streak images. Studying the effect of noise on PSV performance was carried out by using the MATLAB function 'wgn' was used to overlay 40 synthetic images, each containing 400 streaks with a matrices of white Gaussian noise with linearly increasing power. Figure 61b and Figure 61C show synthetic images containing 500 streaks and 900 streaks respectively. Neither of these images have had any Gaussian noise

added. Figure 61d shows a synthetic image with the maximum tested amount of noise applied. A real cavitation microstreaming image is shown in Figure 61a for comparison.

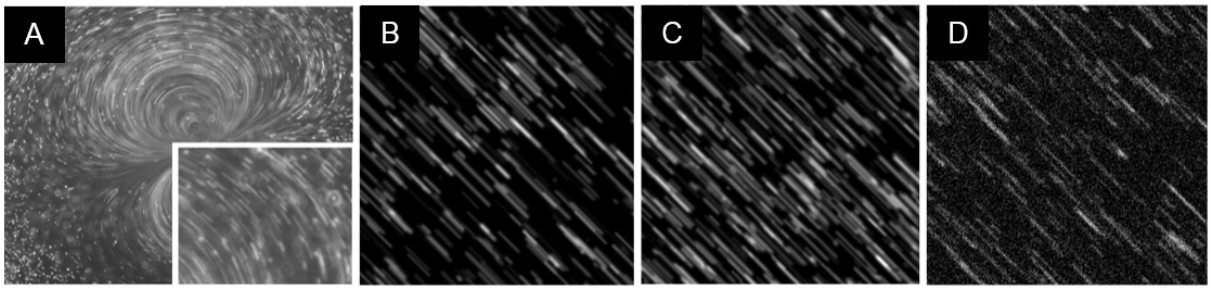


Figure 61 – A. Experimental cavitation microstreaming image, B. Synthetic PSV image containing 500 streaks, C. Synthetic PSV image containing 900 streaks, D. Synthetic PSV image containing 400 streaks with white Gaussian noise applied.

Increasing the number of streaks in synthetic images causes the mean streak length measured to increase (up to a maximum of 5 pixels, 12.5% error) over the full length of streak densities tested (Figure S10A). This is because the synthetic streaks overlap more and more and therefore appear to get longer on average. Increasing the power of the white Gaussian noise on synthetic streak images causes the mean streak length measured to decrease as the PSV algorithm begins to measure parts of the noise as small streaks (Figure 62B). This indicates that experimental images with low streak density and low noise are required for accurate PSV.

By design, the PSV analysis rejects objects that are in the wrong size range or do not have high enough eccentricity or contrast. Thus, at extreme streak densities and/or noise variances, the result would simply be null. This point is reinforced in Figure 62C and S10D which show the percentage of the total streaks in each synthetic image detected by the PSV algorithm. As the noise or streak density increases, the proportion of total streaks detected also decreases but the accuracy is maintained. It was found that for high noise variance or high streak density synthetic images, the PSV algorithm tends to detect only the brightest streaks. This was observed for experimental images as well. For the examples included the paper, only successive images in which the flow field of interest was steady to a visual approximation were analysed. Furthermore, changes in the velocity field throughout the depth-of-field of the

image (~55 μm) were not taken into account. This limitation is, however, not inherent to the device.

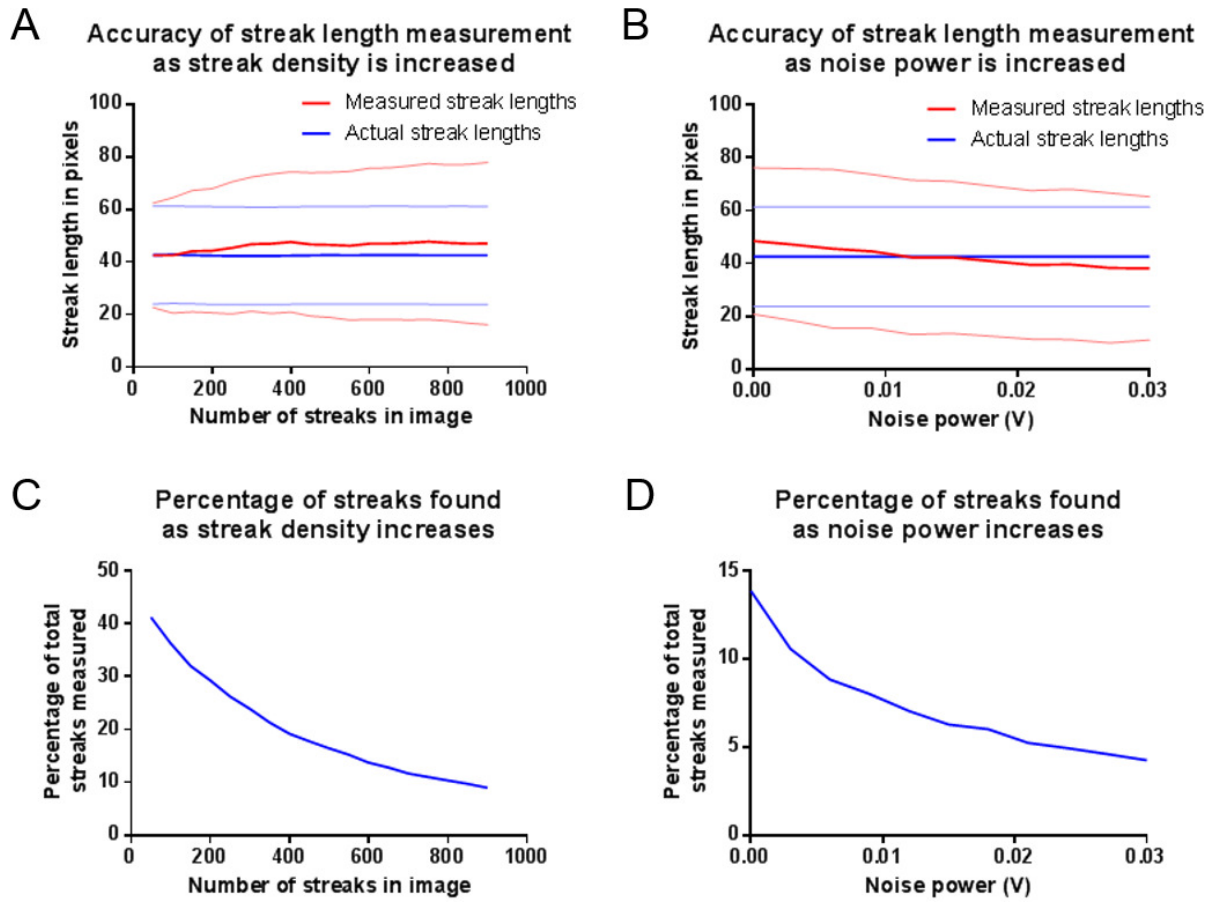


Figure 62 - The effect of streak density and noise on the PSV algorithm's ability to measure the mean streak length accurately are shown in A. and B., respectively. The error bars represent ± one standard deviation of the spread of streak lengths. The percentage of total streaks in the image found and measured by the PSV algorithm as the streak density and noise increases are shown in C. and D. All noise analysis was carried out on images containing 400 streaks.

Appendix B

Link to Supporting Videos

Supporting videos can be found online at the following link:

http://dx.doi.org/10.5287/bodleian:ZVxVBGne9

References

(1) Bray, F.; Ren, J. S.; Masuyer, E.; Ferlay, J. *Int. J. Cancer* **2013**, *132* (5), 1133–1145.

(2) Torre, L. A.; Bray, F.; Siegel, R. L.; Ferlay, J.; Lortet-tieulent, J.; Jemal, A. *CA a cancer J. Clin.* **2015**, *65* (2), 87–108.

(3) H.P. Rang. *Elsevier Churchhill Livingstone* **2012**, *7th*, 417.

(4) Allen, T. M.; Cullis, P. R. *Science (80-.).* **2004**, *303* (5665), 1818–1822.

(5) Lighthill, S. J. *J. Sound Vib.* **1978**, *61* (3), 391–418.

(6) van Wamel, A.; Kooiman, K.; Harteveld, M.; Emmer, M.; ten Cate, F. J.; Versluis, M.; de Jong, N. *J. Control. Release* **2006**, *112* (2), 149–155.

(7) Mitragotri, S. *Nat. Rev. Drug Discov.* **2005**, *4* (3), 255–260.

(8) Ng, K.; Liu, Y. *Med. Res. Rev.* **2002**, *22* (2), 204–223.

(9) Postema, M.; Gilja, O. H. *Curr. Pharm. Biotechnol.* **2007**, *8* (6), 355–361.

(10) Pitt, W. G.; Husseini, G. A.; Staples, B. J. *Expert Opin. Drug Deliv.* **2004**, *1* (1), 37–56.

(11) Lentacker, I.; De Cock, I.; Deckers, R.; De Smedt, S. C.; Moonen, C. T. W. *Adv. Drug Deliv. Rev.* **2014**, *72*, 49–64.

(12) Blomley, M. J. K. *Bmj* **2001**, *322* (7296), 1222–1225.

(13) Gorce, J. M.; Arditi, M.; Schneider, M. *Invest. Radiol.* **2000**, *35* (11), 661–671.

(14) Quaia, E.; Bartolotta, T. V. *Contrast media in ultrasonography basic principles and clinical applications*; Springer, 2005.

(15) Coussios, C. C.; Farny, C. H.; ter Haar, G.; Roy, R. A. *Int. J. Hyperth.* **2007**, *23* (2), 105–120.

(16) Miller, D. L.; Pislaru, S. V.; Greenleaf, J. F. *Somat. Cell Mol. Genet.* **2002**, *27* (1–6), 115–134.

(17) Suslick, K. S. *Science (80-.).* **1988**, *247* (4949), 1439.

(18) Stride, E. P.; Coussios, C. C. *Proc. Inst. Mech. Eng. Part H J. Eng. Med.* **2010**, *224* (2), 171–191.

(19) Provost, J.; Papadacci, C.; Arango, J. E.; Imbault, M.; Fink, M.; Gennisson, J. L.; Tanter, M.; Pernot, M. *Phys. Med. Biol.* **2014**, *59* (19), L1–L13.

(20) Stride, E. *Cerebrovasc. Dis.* **2009**, *27* (SUPPL. 2), 1–13.

(21) Coviello, C.; Kozick, R.; Choi, J.; Gyöngy, M.; Jensen, C.; Smith, P. P.; Coussios, C.-C. *J. Acoust. Soc. Am.* **2015**, *137* (5), 2573.

(22) Cox, B.; Beard, P. *Nature* **2015**, *527* (7579), 451–452.

(23) Stride, E. P.; Coussios, C. C. *Proc. Inst. Mech. Eng. Part H J. Eng. Med.* **2010**, *224* (2), 171–191.

(24) Marmor, J. B.; Hahn, G. M. *Cancer* **1980**, *46* (9), 1986–1991.

(25) Lyon, P. C.; Gray, M. D.; Mannaris, C.; Folkes, L. K.; Stratford, M.; Campo, L.; Chung, D. Y. F.; Scott, S.; Anderson, M.; Goldin, R.; Carlisle, R.; Wu, F.; Middleton, M. R.; Gleeson, F. V; Coussios, C. C. *Lancet Oncol.* **2018**, *0* (0).

(26) Stewart, E. A.; Rabinovici, J.; Tempany, C. M. C.; Inbar, Y.; Regan, L.; Gastout, B.;

Hesley, G.; Kim, H. S.; Hengst, S.; Gedroye, W. M. *Fertil. Steril.* **2006**, *85* (1), 22–29.

(27) Madersbacher, S.; Kratzik, C.; Szabo, N.; Susani, M.; Vingers, L.; Marberger, M. *Eur. Urol.* **1993**, *23 Suppl 1* (1), 39–43.

(28) Zhou, Y.-F. *World J. Clin. Oncol.* **2011**, *2* (1), 8.

(29) Coussios, C. C.; Farny, C. H.; ter Haar, G.; Roy, R. A. *Int. J. Hyperth.* **2007**, *23* (2), 105–120.

(30) Elias, W. J.; Huss, D.; Voss, T.; Loomba, J.; Khaled, M.; Zadicario, E.; Frysinger, R. C.; Sperling, S. A.; Wylie, S.; Monteith, S. J.; Druzgal, J.; Shah, B. B.; Harrison, M.; Wintermark, M. *N. Engl. J. Med.* **2013**, *369* (7), 640–648.

(31) Tyler, W. J. *Neuroscientist* **2011**, *17* (1), 25–36.

(32) Binaschi, M.; Bigioni, M.; Cipollone, A.; Rossi, C.; Goso, C.; Maggi, C.; Capranico, G.; Animati, F. *Curr. Med. Chem. Agents* **2001**, *1* (2), 113–130.

(33) Hynynen, K. *Expert Opin. Drug Deliv.* **2007**, *4* (1), 27–35.

(34) Riganti, C.; Voena, C.; Kopecka, J.; Corsetto, P. A.; Montorfano, G.; Enrico, E.; Costamagna, C.; Rizzo, A. M.; Ghigo, D.; Bosia, A. *Mol. Pharm.* **2011**, *8* (3), 683–700.

(35) Lawler, S. E.; Speranza, M.-C.; Cho, C.-F.; Chiocca, E. A. *JAMA Oncol.* **2017**, *3* (6), 841.

(36) Banchereau, J.; Palucka, K. *Nat. Rev. Clin. Oncol.* **2017**, *15* (1), 9–10.

(37) Dewhirst, M. W.; Secomb, T. W. *Nat. Rev. Cancer* **2017**, *17* (12), 738–750.

(38) Chan, W. C. W. *Acc. Chem. Res.* **2017**, *50* (3), 627–632.

(39) Kwan, J. J.; Myers, R.; Coviello, C. M.; Graham, S. M.; Shah, A. R.; Stride, E.; Carlisle, R. C.; Coussios, C. C. *Small* **2015**, *11* (39), 5305–5314.

(40) Fukumura, D.; Jain, R. K. *J. Cell. Biochem.* **2007**, *101* (4), 937–949.

(41) Yang, B.; Han, X.; Ji, B.; Lu, R. *Curr. Drug Deliv.* **2016**, *13* (8), 1261–1274.

(42) Hartlev, L. B.; Boeje, C. R.; Bluhme, H.; Palshof, T.; Rehling, M. *Eur. J. Nucl. Med. Mol. Imaging* **2012**, *39* (9), 1478–1482.

(43) Yang, H.; Xiong, X.; Zhang, L.; Wu, C.; Liu, Y. *Int. J. Nanomedicine* **2011**, *6*, 2043–2051.

(44) Nakamura, Y.; Mochida, A.; Choyke, P. L.; Kobayashi, H. *Bioconjug. Chem.* **2016**, *27* (10), 2225–2238.

(45) Wilhelm, S.; Tavares, A. J.; Dai, Q.; Ohta, S.; Audet, J.; Dvorak, H. F.; Chan, W. C. W. *Nat. Rev. Mater.* **2016**, *1* (5), 16014.

(46) Lieleg, O.; Baumgärtel, R. M.; Bausch, A. R. *Biophys. J.* **2009**, *97* (6), 1569–1577.

(47) Wiig, H.; Tenstad, O.; Iversen, P.; Kalluri, R.; Bjerkvig, R. *Fibrogenesis Tissue Repair* **2010**, *3* (1), 12.

(48) Lipinski, C. A.; Lombardo, F.; Dominy, B. W.; Feeney, P. J. *Adv. Drug Deliv. Rev.* **2012**, *64* (SUPPL.), 4–17.

(49) Lipinski, C. A. *Drug Discov. Today Technol.* **2004**, *1* (4), 337–341.

(50) Lee, C. M.; Tannock, I. F. *Br. J. Cancer* **2006**, *94* (6), 863–869.

(51) Gillet, J.-P.; Gottesman, M. M. In *Methods in molecular biology (Clifton, N.J.)*; 2010; Vol. 596, pp 47–76.

(52) Shen, F.; Chu, S.; Bence, A. K.; Bailey, B.; Xue, X.; Erickson, P. A.; Montrose, M. H.; Beck, W. T.; Erickson, L. C. *J. Pharmacol. Exp. Ther.* **2007**, *324* (1), 95–102.

(53) Eug, M.; Cruz, M.; Isabel, S.; Lu, M.; Maria, B.; Martins, F. *Drug Deliv. nanoparticles Formul. Charact.* **2009**, No. 7, 35–49.

(54) Akbarzadeh, A.; Rezaei-Sadabady, R.; Davaran, S.; Joo, S. W.; Zarghami, N.; Hanifehpour, Y.; Samiei, M.; Kouhi, M.; Nejati-Koshki, K. *Nanoscale Res. Lett.* **2013**, *8* (1), 1–8.

(55) Graham, S. M. Ultrasound-triggered drug release from liposomes using nanoscale cavitation nuclei, University of Oxford, 2014.

(56) Deshpande, P. P.; Biswas, S.; Torchilin, V. P. *Nanomedicine* **2013**, *8* (9), 1509–1528.

(57) Artzi, N.; Oliva, N.; Puron, C.; Shitreet, S.; Artzi, S.; Bon Ramos, A.; Groothuis, A.; Sahagian, G.; Edelman, E. R. *Nat. Mater.* **2011**, *10* (9), 704–709.

(58) Wong, A. D.; Ye, M.; Ulmschneider, M. B.; Searson, P. C. *PLoS One* **2015**, *10* (5), e0123461.

(59) Hobbs, S. K.; Monsky, W. L.; Yuan, F.; Roberts, W. G.; Griffith, L.; Torchilin, V. P.; Jain, R. K. *Proc. Natl. Acad. Sci.* **1998**, *95* (8), 4607–4612.

(60) Peer, D.; Karp, J. M.; Hong, S.; Farokhzad, O. C.; Margalit, R.; Langer, R. *Nat. Nanotechnol.* **2007**, *2* (12), 751–760.

(61) Cheng, Z.; Al Zaki, A.; Hui, J. Z.; Muzykantov, V. R.; Tsourkas, A. *Science (80-.).* **2012**, *338* (6109), 903–910.

(62) Wu, T. C. *Cancer Res.* **2007**, *67* (13), 6003–6006.

(63) Arvanitis, C. D.; Bazan-Peregrino, M.; Rifai, B.; Seymour, L. W.; Coussios, C. C. *Ultrasound Med. Biol.* **2011**, *37* (11), 1838–1852.

(64) Jain, K. K. *Nanobiotechnology and personalized medicine*; Elsevier Science, 2011; Vol. 104.

(65) Swietach, P.; Vaughan-Jones, R. D.; Harris, A. L.; Hulikova, A. *Philos. Trans. R. Soc. B Biol. Sci.* **2014**, *369* (1638), 20130099–20130099.

(66) Schellmann, N.; Deckert, P. M.; Bachran, D.; Fuchs, H.; Bachran, C. *Mini-Reviews Med. Chem.* **2010**, *10* (10), 887–904.

(67) Roy, D.; Cambre, J. N.; Sumerlin, B. S. *Prog. Polym. Sci.* **2010**, *35* (1–2), 278–301.

(68) Dan, M.; Bae, Y.; Pittman, T. A.; Yokel, R. A. *Pharm. Res.* **2015**, *32* (5), 1615–1625.

(69) Chung, Y. E.; Kim, K. W. *Ultrasonography* **2014**, *34* (1), 3–18.

(70) ter Haar, G.; Coussios, C. *Int. J. Hyperth.* **2007**, *23* (2), 89–104.

(71) Kneidl, B.; Peller, M.; Winter, G.; Lindner, L. H.; Hossann, M. *Int. J. Nanomedicine* **2014**, *9*, 4387–4398.

(72) Lucky, S. S.; Soo, K. C.; Zhang, Y. *Chem. Rev.* **2015**, *115* (4), 1990–2042.

(73) Vyšniauskas, A.; Qurashi, M.; Kuimova, M. K. *Chem. - A Eur. J.* **2016**, *22* (37), 13210–13217.

(74) Wan, G.-Y.; Liu, Y.; Chen, B.-W.; Liu, Y.-Y.; Wang, Y.-S.; Zhang, N.; Wan, G.-Y.; Liu, Y.; Chen, B.-W.; Liu, Y.-Y.; Wang, Y.-S.; Zhang, N. *Cancer Biol. Med.* **2016**, *13* (3), 325–338.

(75) Beguin, E.; Sheng, J.; Nesbitt, H.; Owen, J.; McHale, A.; Callan, J.; Stride, E. P. *J. Acoust. Soc. Am.* **2016**, *140* (4), 3026–3026.

(76) Kooiman, K.; Vos, H. J.; Versluis, M.; De Jong, N. *Adv. Drug Deliv. Rev.* **2014**, *72*, 28–48.

(77) Graham, S. M.; Carlisle, R.; Choi, J. J.; Stevenson, M.; Shah, A. R.; Myers, R. S.; Fisher, K.; Peregrino, M. B.; Seymour, L.; Coussios, C. C. *J. Control. Release* **2014**, *178* (1), 101–107.

(78) Husseini, G. A.; Diaz De La Rosa, M. A.; Richardson, E. S.; Christensen, D. A.; Pitt, W. G. *J. Control. Release* **2005**, *107* (2), 253–261.

(79) Kennedy, J. E.; Ter Haar, G. R.; Cranston, D. *Br. J. Radiol.* **2003**, *76* (909), 590–599.

(80) Azhari, H. *Basics of Biomedical Ultrasound for Engineers*; 2010.

(81) Claudon, M.; Cosgrove, D.; Albrecht, T.; Bolondi, L.; Boslo, M.; Calliada, F.; Correas, J. M.; Darge, K.; Dietrich, C.; D'Onofrio, M.; Evans, D. H.; Filice, C.; Greiner, L.; Jäger, K.; De Jong, N.; Leen, E.; Lencioni, R.; Lindsell, D.; Martegani, A.; Meairs, S.; Nolsøe, C.; Piscaglia, F.; Ricci, P.; Seidel, G.; Skjoldbye, B.; Solbiati, C.; Thorelius, L.; Tranquart, F.; Weskott, H. P.; Whittingham, T. *Ultraschall der Medizin* **2008**, *29* (1), 28–44.

(82) Schneider, M. *Echocardiography* **1999**, *16* (s1), 743–746.

(83) Borden, M. A.; Pu, G.; Runner, G. J.; Longo, M. L. *Colloids Surfaces B Biointerfaces* **2004**, *35* (3–4), 209–223.

(84) Zhang, P.; Sun, F.; Liu, S.; Jiang, S. *J. Control. Release* **2016**, *244*, 184–193.

(85) Garay, R. P.; El-Gewely, R.; Armstrong, J. K.; Garratty, G.; Richette, P. *Expert Opin. Drug Deliv.* **2012**, *9* (11), 1319–1323.

(86) Sirsi, S. R.; Borden, M. A. *Bubble Sci. Eng. Technol.* **2009**, *1* (1–2), 3–17.

(87) Chong, W. K.; Papadopoulou, V.; Dayton, P. A. *Abdom. Radiol.* **2018**, *43* (4), 762–772.

(88) Vos, H. J.; Dollet, B.; Bosch, J. G.; Versluis, M.; de Jong, N. *Ultrasound Med. Biol.* **2008**, *34* (4), 685–688.

(89) Flynn, H. G. *J. Acoust. Soc. Am.* **1982**, *72* (6), 1926.

(90) Stride, E. Characterisation and Design of Ultrasound Contrast Agent Particles, University College London, 2005.

(91) de Jong, N.; Emmer, M.; van Wamel, A.; Versluis, M. *Med. Biol. Eng. Comput.* **2009**, *47* (8), 861–873.

(92) Leighton, T. G.; Walton, A. J.; Pickworth, M. J. W. *Eur. J. Phys.* **1990**, *11* (1), 47–50.

(93) Wiklund, M.; Hertz, H. M. *Lab Chip* **2006**, *6* (10), 1279.

(94) Gor'kov, L. P. *Sov. Physics-Doklady* **1962**, *6* (9), 773–775.

(95) Carugo, D.; Octon, T.; Messaoudi, W.; Fisher, A. L.; Carboni, M.; Harris, N. R.; Hill, M.; Glynne-Jones, P. *Lab Chip* **2014**, *14* (19), 3830–3842.

(96) Stride, E.; Saffari, N. *IEEE Trans. Ultrason. Ferroelectr. Freq. Control* **2005**, *52* (12), 2332–2345.

(97) Evander, M.; Nilsson, J. *Lab Chip* **2012**, *12* (22), 4667.

(98) Carugo, D.; Octon, T.; Messaoudi, W.; Fisher, A. L.; Carboni, M.; Harris, N. R.; Hill, M.; Glynne-Jones, P. *Lab Chip* **2014**, *14* (19), 3830–3842.

(99) Grenvall, C.; Antfolk, C.; Bisgaard, C. Z.; Laurell, T. *Lab Chip* **2014**, *14* (24), 4629–4637.

(100) Lenshof, A.; Magnusson, C.; Laurell, T. *Lab Chip* **2012**, *12* (7), 1210.

(101) Lei, J.; Hill, M.; Glynne-Jones, P. *Lab Chip* **2014**, *14* (3), 532–541.

(102) Wiklund, M.; Green, R.; Ohlin, M. *Lab Chip* **2012**, *12* (14), 2438.

(103) Lei, J.; Glynne-Jones, P.; Hill, M. *Lab Chip* **2013**, *13* (11), 2133.

(104) Muller, P. B.; Rossi, M.; Marín, A. G.; Barnkob, R.; Augustsson, P.; Laurell, T.; Kähler, C. J.; Bruus, H. *Phys. Rev. E - Stat. Nonlinear, Soft Matter Phys.* **2013**, *88* (2), 23006.

(105) Davidson, B. J.; Riley, N. *J. Sound Vib.* **1971**, *15* (2), 217–233.

(106) Wu, J.; Nyborg, W. L. *Adv. Drug Deliv. Rev.* **2008**, *60* (10), 1103–1116.

(107) Gormley, G.; Wu, J. *J. Acoust. Soc. Am.* **1998**, *104* (5), 3115–3118.

(108) Collis, J.; Manasseh, R.; Liovic, P.; Tho, P.; Ooi, A.; Petkovic-Duran, K.; Zhu, Y. *Ultrasonics* **2010**, *50* (2), 273–279.

(109) Tho, P. *J. Acoust. Soc. Am.* **2005**, *122* (October), 3051.

(110) Helfield, B. L.; Leung, B. Y. C.; Goertz, D. E. *Phys. Med. Biol.* **2014**, *59* (7), 1721–1745.

(111) Wiedemair, W.; Tuković, Ž.; Jasak, H.; Poulikakos, D.; Kurtcuoglu, V. *Phys. Med. Biol.* **2012**, *57* (4), 1019–1045.

(112) Sassaroli, E.; Hynynen, K. *Phys. Med. Biol.* **2005**, *50* (22), 5292–5305.

(113) Qin, S.; Ferrara, K. W. *Phys. Med. Biol.* **2006**, *51* (20), 5065–5088.

(114) Caskey, C. F.; Stieger, S. M.; Qin, S.; Dayton, P. A.; Ferrara, K. W. *J. Acoust. Soc. Am.* **2007**, *122* (2), 1191–1200.

(115) Chen, H.; Kreider, W.; Brayman, A. A.; Bailey, M. R.; Matula, T. J. *Phys. Rev. Lett.* **2011**, *106* (3), 34301.

(116) Wu, J.; Ross, J. P.; Chiu, J.-F. *J. Acoust. Soc. Am.* **2002**, *111* (3), 1460–1464.

(117) Green, R. Microscale Fluid Flows: The Application of Acoustic Streaming to Biomedical Research, University of Southampton, **2013**.

(118) Ward, M.; Wu, J. *J. Acoust. Soc. Am.* **1999**, *106* (4), 2230–2230.

(119) van Wamel, A.; Kooiman, K.; Harteveld, M.; Emmer, M.; ten Cate, F. J.; Versluis, M.; de Jong, N. *J. Control. Release* **2006**, *112* (2), 149–155.

(120) Collis, J.; Manasseh, R.; Liovic, P.; Tho, P.; Ooi, A.; Petkovic-Duran, K.; Zhu, Y. *Ultrasonics* **2010**, *50* (2), 273–279.

(121) Juffermans, L. J. M.; Kamp, O.; Dijkmans, P. A.; Visser, C. A.; Musters, R. J. P. *Ultrasound Med. Biol.* **2008**, *34* (3), 502–508.

(122) Van Wamel, A.; Bouakaz, A.; Versluis, M.; De Jong, N. *Ultrasound Med. Biol.* **2004**, *30* (9), 1255–1258.

(123) Chen, X.; Leow, R. S.; Hu, Y.; Wan, J. M. F.; Yu, A. C. H. *J. R. Soc. Interface* **2014**, *11* (95), 20140071–20140071.

(124) Wang, M.; Zhang, Y.; Cai, C.; Tu, J.; Guo, X.; Zhang, D. *Sci. Rep.* **2018**, *8* (1), 3885.

(125) Hu, Y.; Wan, J. M. F.; Yu, A. C. H. *Ultrasound Med. Biol.* **2013**, *39* (12), 2393–2405.

(126) Kinoshita, M.; Hynynen, K. *Proc. - IEEE Ultrason. Symp.* **2006**, *1* (4), 852–855.

(127) van Rooij, T.; Skachkov, I.; Beekers, I.; Lattwein, K. R.; Voorneveld, J. D.; Kokhuis, T. J. A.; Bera, D.; Luan, Y.; van der Steen, A. F. W.; de Jong, N.; Kooiman, K. *J. Control. Release* **2016**, *238*, 197–211.

(128) Karshafian, R.; Bevan, P. D.; Williams, R.; Samac, S.; Burns, P. N. *Ultrasound Med. Biol.* **2009**, *35* (5), 847–860.

(129) Meijering, B. D. M.; Juffermans, L. J. M.; Van Wamel, A.; Henning, R. H.; Zuhorn, I. S.; Emmer, M.; Versteilen, A. M. G.; Paulus, W. J.; Van Gilst, W. H.; Kooiman, K.; De Jong, N.; Musters, R. J. P.; Deelman, L. E.; Kamp, O. *Circ. Res.* **2009**, *104* (5), 679–687.

(130) Carugo, D.; Ankrett, D. N.; Glynne-Jones, P.; Capretto, L.; Boltryk, R. J.; Zhang, X.; Townsend, P. A.; Hill, M. *Biomicrofluidics* **2011**, *5* (4).

(131) De Cock, I.; Zagato, E.; Braeckmans, K.; Luan, Y.; de Jong, N.; De Smedt, S. C.; Lentacker, I. *J. Control. Release* **2015**, *197*, 20–28.

(132) Fekri, F.; Delos Santos, R. C.; Karshafian, R.; Antonescu, C. N. *PLoS One* **2016**, *11* (6), e0156754.

(133) Leow, R. S.; Wan, J. M. F.; Yu, A. C. H. *J. R. Soc. Interface* **2015**, *12* (105), 20150029–20150029.

(134) Kooiman, K.; Van Der Steen, A. F. W.; De Jong, N. *IEEE Trans. Ultrason. Ferroelectr. Freq. Control* **2013**, *60* (9), 1811–1815.

(135) Carlisle, R.; Choi, J.; Bazan-Peregrino, M.; Laga, R.; Subr, V.; Kostka, L.; Ulbrich, K.; Coussios, C.-C.; Seymour, L. W. *JNCI J. Natl. Cancer Inst.* **2013**, *105* (22), 1701–1710.

(136) Hallow, D. M.; Seeger, R. A.; Kamaev, P. P.; Prado, G. R.; LaPlaca, M. C.; Prausnitz, M. R. *Biotechnol. Bioeng.* **2008**, *99* (4), 846–854.

(137) Miller, D. L. *Ultrasound Med. Biol.* **1987**, *13* (8), 443–470.

(138) Marmottant, P.; Hilgenfeldt, S. *Nature* **2003**, *423* (6936), 153–156.

(139) Ibsen, S.; Shi, G.; Schutt, C.; Shi, L.; Suico, K. D.; Benchimol, M.; Serra, V.; Simberg, D.; Berns, M.; Esener, S. *Ultrasonics* **2014**, *54* (8), 2090–2098.

(140) De Cock, I.; Lajoinie, G.; Versluis, M.; De Smedt, S. C.; Lentacker, I. *Biomaterials* **2016**, *83*, 294–307.

(141) Alonso, M. A.; Millán, J. *J. Cell Sci.* **2001**, *114* (Pt 22), 3957–3965.

(142) Spector, A. A.; Yorek, M. A. *J. Lipid Res.* **1985**, *26* (9), 1015–1035.

(143) Riske, K. A.; Sudbrack, T. P.; Archilha, N. L.; Uchoa, A. F.; Schroder, A. P.; Marques, C. M.; Baptista, M. S.; Itri, R. *Biophys. J.* **2009**, *97* (5), 1362–1370.

(144) McEwan, C.; Kamila, S.; Owen, J.; Nesbitt, H.; Callan, B.; Borden, M.; Nomikou, N.; Hamoudi, R. A.; Taylor, M. A.; Stride, E.; McHale, A. P.; Callan, J. F. *Biomaterials* **2016**, *80*, 20–32.

(145) Di, L.; Artursson, P.; Avdeef, A.; Ecker, G. F.; Faller, B.; Fischer, H.; Houston, J. B.; Kansy, M.; Kerns, E. H.; Krämer, S. D.; Lennernäs, H.; Sugano, K. *Drug Discov. Today* **2012**, *17* (15–16), 905–912.

(146) Lee, A. G. *Biochim. Biophys. Acta - Biomembr.* **2004**, *1666* (1–2), 62–87.

(147) Simons, K.; Toomre, D. *Nat. Rev. Mol. Cell Biol.* **2000**, *1* (1), 31–39.

(148) Rothman, J. E. *Nature* **1994**, *372* (6501), 55–63.

(149) Singer, S. J.; Nicolson, G. L. *Science (80-.).* **1972**, *175* (4023), 720–731.

(150) Khan, S. *Choice Rev. Online* **2011**, *48* (5), 48-2433-48–2433.

(151) Schwille, P. In *The Minimal Cell: The Biophysics of Cell Compartment and the Origin of Cell Functionality*; Springer Netherlands: Dordrecht, 2011; pp 231–253.

(152) Korlach, J.; Schwille, P.; Webb, W. W.; Feigenson, G. W. *Proc. Natl. Acad. Sci.* **1999**, *96* (15), 8461–8466.

(153) Kaiser, H.-J.; Lingwood, D.; Levental, I.; Sampaio, J. L.; Kalvodova, L.; Rajendran, L.; Simons, K. *Proc. Natl. Acad. Sci.* **2009**, *106* (39), 16645–16650.

(154) Sezgin, E.; Kaiser, H.-J.; Baumgart, T.; Schwille, P.; Simons, K.; Levental, I. *Nat. Protoc.* **2012**, *7* (6), 1042–1051.

(155) Veatch, S. L.; Keller, S. L. *Biophys. J.* **2003**, *85* (5), 3074–3083.

(156) Fidorra, M.; Duelund, L.; Leidy, C.; Simonsen, A. C.; Bagatolli, L. A. *Biophys. J.* **2006**, *90* (12), 4437–4451.

(157) Sun, T. L.; Sun, Y.; Lee, C. C.; Huang, H. W. *Biophys. J.* **2013**, *104* (9), 1923–1932.

(158) Nishimura, K.; Matsuura, T.; Sunami, T.; Fujii, S.; Nishimura, K.; Suzuki, H.; Yomo, T. *RSC Adv.* **2014**, *4* (66), 35224.

(159) Nappini, S.; Al Kayal, T.; Berti, D.; Nord Èn, B.; Baglioni, P. *J. Phys. Chem. Lett.* **2011**, *2* (7), 713–718.

(160) Staykova, M.; Lipowsky, R.; Dimova, R. *Soft Matter* **2008**, *4* (11), 2168.

(161) Méléard, P.; Bagatolli, L. A.; Pott, T. *Methods Enzymol.* **2009**, *465* (C), 161–176.

(162) Fenz, S. F.; Sengupta, K. *Integr. Biol.* **2012**, *4* (9), 982.

(163) Sebastian, B.; Favero, T.; Dittrich, P. S. *J. Phys. Chem. Lett.* **2017**, *8* (24), 6128–6134.

(164) Sezgin, E.; Gutmann, T.; Buhl, T.; Dirkx, R.; Grzybek, M.; Coskun, Ü.; Solimena, M.; Simons, K.; Levental, I.; Schwille, P. *PLoS One* **2015**, *10* (4), e0123930.

(165) Silvius, J. R. *Biochim. Biophys. Acta - Biomembr.* **2003**, *1610* (2), 174–183.

(166) Montes, L. R.; Alonso, A.; Goñi, F. M.; Bagatolli, L. A. *Biophys. J.* **2007**, *93* (10), 3548–3554.

(167) Levental, K. R.; Levental, I. In *Current Topics in Membranes*; 2015; Vol. 75, pp 25–57.

(168) Brüggemann, D.; Frohnmayer, J. P.; Spatz, J. P. *Beilstein J. Nanotechnol.* **2014**, *5* (1), 1193–1202.

(169) Schwille, P. In *The Minimal Cell: The Biophysics of Cell Compartment and the Origin of Cell Functionality*; Springer Netherlands: Dordrecht, 2011; pp 231–253.

(170) Parasassi, T.; De Stasio, G.; Ravagnan, G.; Rusch, R. M.; Gratton, E. *Biophys. J.* **1991**, *60* (1), 179–189.

(171) Aron, M.; Browning, R.; Carugo, D.; Sezgin, E.; Bernardino de la Serna, J.; Eggeling, C.; Stride, E. *BMC Bioinformatics* **2017**, *18* (1), 254.

(172) Hosny, N. A.; Mohamedi, G.; Rademeyer, P.; Owen, J.; Wu, Y.; Tang, M.-X.; Eckersley, R. J.; Stride, E.; Kuimova, M. K. *Proc. Natl. Acad. Sci.* **2013**, *110* (23), 9225–9230.

(173) König, B.; Dietrich, U.; Klose, G. *Langmuir* **1997**, *13* (3), 525–532.

(174) Sezgin, E.; Sadowski, T.; Simons, K. *Langmuir* **2014**, *30* (27), 8160–8166.

(175) Barucha-Kraszewska, J.; Kraszewski, S.; Ramseyer, C. *Langmuir* **2013**, *29* (4), 1174–1182.

(176) Levitt, J. A.; Kuimova, M. K.; Yahioglu, G.; Chung, P. H.; Suhling, K.; Phillips, D. *J. Phys. Chem. C* **2009**, *113* (27), 11634–11642.

(177) Przybylo, M.; Sýkora, J.; Humpolíčová, J.; Benda, A.; Zan, A.; Hof, M. *Langmuir* **2006**, *22* (22), 9096–9099.

(178) Dodes Traian, M. M.; Flecha, F. L. G.; Levi, V. *J. Lipid Res.* **2012**, *53* (3), 609–616.

(179) Yamamoto, K.; Ando, J. *J. Cell Sci.* **2013**, *126* (5), 1227–1234.

(180) Yu, W.; So, P. T.; French, T.; Gratton, E. *Biophys. J.* **1996**, *70* (2), 626–636.

(181) Sanchez, S. A.; Tricerri, M. A.; Gunther, G.; Gratton, E. *Mod. Res. Educ. Top. Microsc.* **2007**, *2*, 1007–1014.

(182) Sezgin, E.; Waithe, D.; Bernardino De La Serna, J.; Eggeling, C. *ChemPhysChem* **2015**, *16* (7), 1387–1394.

(183) Parasassi, T.; De Stasio, G.; Ravagnan, G.; Rusch, R. M.; Gratton, E. *Biophys. J.* **1991**, *60* (1), 179–189.

(184) Lingwood, D.; Simons, K. *Science* **2010**, *327* (5961), 46–50.

(185) Bagatolli, L. a; Gratton, E. *Biophys. J.* **2000**, *79* (1), 434–447.

(186) Dietrich, C.; Bagatolli, L. a; Volovyk, Z. N.; Thompson, N. L.; Levi, M.; Jacobson, K.; Gratton, E. *Biophys. J.* **2001**, *80* (3), 1417–1428.

(187) Korlach, J.; Schwille, P.; Webb, W. W.; Feigenson, G. W. *Proc. Natl. Acad. Sci. U. S. A.* **1999**, *96* (15), 8461–8466.

(188) Feigenson, G. W.; Buboltz, J. T. *Biophys. J.* **2001**, *80* (6), 2775–2788.

(189) Veatch, S. L.; Keller, S. L. *Biophys. J.* **2003**, *85* (5), 3074–3083.

(190) Sun, T. L.; Sun, Y.; Lee, C. C.; Huang, H. W. *Biophys. J.* **2013**, *104* (9), 1923–1932.

(191) Nishimura, K.; Matsuura, T.; Sunami, T.; Fujii, S.; Nishimura, K.; Suzuki, H.; Yomo, T. *RSC Adv.* **2014**, *4* (66), 35224.

(192) Staykova, M.; Lipowsky, R.; Dimova, R. *Soft Matter* **2008**, *4* (11), 2168.

(193) Fenz, S. F.; Sengupta, K. *Integr. Biol.* **2012**, *4* (9), 982.

(194) Nappini, S.; Kayal, A.; Berti, D.; Nord En, B.; Baglioni, P. *J. Phys. Chem. Lett* **2011**, *2*, 713–718.

(195) Dubavik, A.; Sezgin, E.; Lesnyak, V.; Gaponik, N.; Schwille, P.; Eychm??ller, A. *ACS Nano* **2012**, *6* (3), 2150–2156.

(196) Bernardino de la Serna, J.; Perez-Gil, J.; Simonsen, A. C.; Bagatolli, L. A. *J. Biol. Chem.* **2004**, *279* (39), 40715–40722.

(197) Bernardino de la Serna, J.; Hansen, S.; Berzina, Z.; Simonsen, A. C.; Hannibal-Bach, H. K.; Knudsen, J.; Ejsing, C. S.; Bagatolli, L. A. *Biochim. Biophys. Acta - Biomembr.* **2013**, *1828* (11), 2450–2459.

(198) Heinrich, M. C.; Capraro, B. R.; Tian, A.; Isas, J. M.; Langen, R.; Baumgart, T. *J. Phys. Chem. Lett* **2010**, *1*, 3401–3406.

(199) López-Montero, I.; Rodríguez-García, R.; Monroy, F. *J. Phys. Chem. Lett.* **2012**, *3* (12), 1583–1588.

(200) Caschera, F.; Serna, J. B. de la; Löffler, P. M. G.; Rasmussen, T. E.; Hanczyc, M. M.; Bagatolli, L. A.; Monnard, P.-A. **2011**.

(201) Walde, P.; Cosentino, K.; Engel, H.; Stano, P. *ChemBioChem* **2010**, *11* (7), 848–865.

(202) Méléard, P.; Bagatolli, L. A.; Pott, T. *Methods Enzymol.* **2009**, *465*, 161–176.

(203) Dimova, R.; Aranda, S.; Bezlyepkina, N.; Nikolov, V.; Riske, K. a; Lipowsky, R. *J. Phys. Condens. Matter* **2006**, *18* (28), S1151-76.

(204) Reeves, J. P.; Dowben, R. M. *J. Cell. Physiol.* **1969**, *73* (1), 49–60.

(205) Angelova, M. I.; Dimitrov, D. S. *Faraday Discuss. Chem. Soc.* **1986**, *81*, 303.

(206) Pautot, S.; Frisken, B. J.; Weitz, D. a. *Langmuir* **2003**, *19* (7), 2870–2879.

(207) Yamada, A.; Le Berre, M.; Yoshikawa, K.; Baigl, D. *ChemBioChem* **2007**, *8* (18), 2215–2218.

(208) Stachowiak, J. C.; Richmond, D. L.; Li, T. H.; Liu, A. P.; Parekh, S. H.; Fletcher, D. a. *Proc. Natl. Acad. Sci. U. S. A.* **2008**, *105* (12), 4697–4702.

(209) Arriaga, L. R.; Datta, S. S.; Kim, S. H.; Amstad, E.; Kodger, T. E.; Monroy, F.; Weitz, D. a. *Small* **2014**, *10* (5), 950–956.

(210) Bagatolli, L. A.; Parasassi, T.; Gratton, E. *Giant phospholipid vesicles: Comparison among the whole lipid sample characteristics using different preparation methods - A two photon fluorescence microscopy study*; 2000; Vol. 105.

(211) Shimanouchi, T.; Umakoshi, H.; Kuboi, R. *Langmuir* **2009**, *25* (9), 4835–4840.

(212) Angelova, M.; Dimitrov, D. S. In *Trends in Colloid and Interface Science II*; Steinkopff: Darmstadt, 1988; pp 59–67.

(213) Politano, T. J.; Froude, V. E.; Jing, B.; Zhu, Y. *Colloids Surfaces B Biointerfaces* **2010**, *79* (1), 75–82.

(214) Okumura, Y.; Zhang, H.; Sugiyama, T.; Iwata, Y. *J. Am. Chem. Soc.* **2007**, *129* (6), 1490–1491.

(215) Aimon, S.; Manzi, J.; Schmidt, D.; Poveda Larrosa, J. A.; Bassereau, P.; Toombes, G. E. S. *PLoS One* **2011**, *6* (10), e25529.

(216) Fidorra, M.; Duelund, L.; Leidy, C.; Simonsen, A. C.; Bagatolli, L. A. *Biophys. J.* **2006**, *90* (12), 4437–4451.

(217) Sezgin, E.; Sadowski, T.; Simons, K. *Langmuir* **2014**, *30* (27), 8160–8166.

(218) Sezgin, E.; Waithe, D.; Bernardino de la Serna, J.; Eggeling, C. *Chemphyschem* **2015**, *16* (7), 1387–1394.

(219) E. G. Bligh; W. J. Dyer. *Can. J. Biochem. Physiol.* **1959**, *37*.

(220) Buell, S. L.; Demas, J. N. *J. Phys. Chem.* **1983**, *87* (23), 4675–4681.

(221) McIntyre, J. C.; Sleight, R. G. *Biochemistry* **1991**, *30* (51), 11819–11827.

(222) Gruber, H. J.; Schindler, H. *BBA - Biomembr.* **1994**, *1189* (2), 212–224.

(223) Montes, L.; Alonso, A.; Goni, F. M.; Bagatolli, L. A. *Biophys. J.* **2007**, *93* (10), 3548–3554.

(224) Lecuyer, S.; Ristenpart, W. D.; Vincent, O.; Stone, H. a. *Appl. Phys. Lett.* **2008**, *92* (10).

(225) Bi, H.; Yang, B.; Wang, L.; Cao, W.; Han, X. *J. Mater. Chem. A* **2013**, *1* (24), 7125.

(226) Herold, C.; Chwastek, G.; Schwille, P.; Petrov, E. P. *Langmuir* **2012**, *28* (13), 5518–5521.

(227) Silvius, J. R. *Biochim. Biophys. Acta - Biomembr.* **2003**, *1610* (2), 174–183.

(228) Veatch, S. L.; Keller, S. L. *Phys. Rev. Lett.* **2002**, *89* (26), 268101.

(229) Söderlund, T.; Alakoskela, J. M. I.; Pakkanen, A. L.; Kinnunen, P. K. J. *Biophys. J.* **2003**, *85* (4), 2333–2341.

(230) Lis, L. J.; Lis, W. T.; Parsegian, V. a; Rand, R. P. *Biochemistry* **1981**, *20* (7), 1771–1777.

(231) Suwalsky, M.; Castro, R.; Villena, F.; Sotomayor, C. P. *J. Inorg. Biochem.* **2008**, *102* (4), 842–849.

(232) Binder, H.; Zschörnig, O. *Chem. Phys. Lipids* **2002**, *115* (1–2), 39–61.

(233) Ohki, S.; Düzgünes, N. *BBA - Biomembr.* **1979**, *552* (3), 438–449.

(234) Stohs, S. J.; Bagchi, D. *Free Radic. Biol. Med.* **1995**, *18* (2), 321–336.

(235) Ayuyan, A. G.; Cohen, F. S. *Biophys. J.* **2006**, *91* (6), 2172–2183.

(236) Mills, J. K.; Needham, D. *Biochim. Biophys. Acta - Biomembr.* **2005**, *1716* (2), 77–96.

(237) Fuller, N.; Rand, R. P. *Biophys. J.* **2001**, *81* (1), 243–254.

(238) Sparling, M. L.; Zidovetzki, R.; Muller, L.; Chan, S. I. *Anal. Biochem.* **1989**, *178* (1), 67–76.

(239) Nieva-Echevarr??a, B.; Goicoechea, E.; Manzanos, M. J.; Guill??n, M. D. *Food Chem.* **2015**, *179*, 182–190.

(240) Kriat, M.; Vion-Dury, J.; Confort-Gouny, S.; Favre, R.; Viout, P.; Sciaky, M.; Sari, H.; Cozzone, P. J. *J. Lipid Res.* **1993**, *34*, 1009–1019.

(241) MacKenzie, A.; Vyssotski, M.; Nekrasov, E. *J. Am. Oil Chem. Soc.* **2009**, *86* (8), 757–763.

(242) Wood, A. K. W.; Sehgal, C. M. *Ultrasound Med. Biol.* **2015**, *41* (4), 905–928.

(243) Aryal, M.; Arvanitis, C. D.; Alexander, P. M.; McDannold, N. *Adv. Drug Deliv. Rev.* **2014**, *72*, 94–109.

(244) Azagury, A.; Khoury, L.; Enden, G.; Kost, J. *Adv. Drug Deliv. Rev.* **2014**, *72*, 127–143.

(245) Ferrara, K.; Pollard, R.; Borden, M. *Annu. Rev. Biomed. Eng.* **2007**, *9* (1), 415–447.

(246) Sirsi, S. R.; Borden, M. A. *Adv. Drug Deliv. Rev.* **2014**, *72*, 3–14.

(247) Lee, J. Y.; Carugo, D.; Crake, C.; Owen, J.; De Saint Victor, M.; Seth, A.; Coussios, C.; Stride, E. *Adv. Mater.* **2015**, *27* (37), 5484–5492.

(248) Crake, C.; Owen, J.; Smart, S.; Coviello, C.; Coussios, C. C.; Carlisle, R.; Stride, E. *Ultrasound Med. Biol.* **2016**, *42* (12), 3022–3036.

(249) Korpanty, G.; Carbon, J. G.; Grayburn, P. A.; Fleming, J. B.; Brekken, R. A. *Clin. Cancer Res.* **2007**, *13* (1), 323–330.

(250) Li, Z. G.; Liu, A. Q.; Klaseboer, E.; Zhang, J. B.; Ohl, C. D. *Lab Chip* **2013**, *13* (6), 1144.

(251) De Cock, I.; Lajoinie, G.; Versluis, M.; De Smedt, S. C.; Lentacker, I. *Biomaterials* **2016**, *83*, 294–307.

(252) Carugo, D.; Aron, M.; Sezgin, E.; Bernardino de la Serna, J.; Kuimova, M. K.; Eggeling, C.; Stride, E. *Biomaterials* **2017**, *113*, 105–117.

(253) Juffermans, L. J. M.; van Dijk, A.; Jongenelen, C. A. M.; Drukarch, B.; Reijerkerk, A.; de Vries, H. E.; Kamp, O.; Musters, R. J. P. *Ultrasound Med. Biol.* **2009**, *35* (11), 1917–1927.

(254) Collis, J.; Manasseh, R.; Liovic, P.; Tho, P.; Ooi, A.; Petkovic-Duran, K.; Zhu, Y. *Ultrasonics* **2010**, *50* (2), 273–279.

(255) Li, W.; Juan, T.; Guo, X. S.; Di, X.; Dong, Z. *Chinese Phys. B* **2014**, *23* (12), 124302.

(256) Lajoinie, G.; De Cock, I.; Coussios, C. C.; Lentacker, I.; Le Gac, S.; Stride, E.; Versluis, M. *Biomicrofluidics* **2016**, *10* (1), 11501.

(257) Lukinavičius, G.; Umezawa, K.; Olivier, N.; Honigmann, A.; Yang, G.; Plass, T.; Mueller, V.; Reymond, L.; Corrêa, I. R.; Luo, Z. G.; Schultz, C.; Lemke, E. A.; Heppenstall, P.; Eggeling, C.; Manley, S.; Johnsson, K. *Nat. Chem.* **2013**, *5* (2), 132–139.

(258) Di Rienzo, C.; Gratton, E.; Beltram, F.; Cardarelli, F. *Proc. Natl. Acad. Sci.* **2013**, *110* (30), 12307–12312.

(259) López-Duarte, I.; Vu, T. T.; Izquierdo, M. A.; Bull, J. A.; Kuimova, M. K. *Chem. Commun.* **2014**, *50* (40), 5282–5284.

(260) Owen, D. M.; Rentero, C.; Magenau, A.; Abu-Siniyeh, A.; Gaus, K. *Nat. Protoc.* **2012**, *7* (1), 24–35.

(261) De Cock, I.; Zagato, E.; Braeckmans, K.; Luan, Y.; de Jong, N.; De Smedt, S. C.; Lentacker, I. *J. Control. Release* **2015**, *197*, 20–28.

(262) Carugo, D.; Owen, J.; Crake, C.; Lee, J. Y.; Stride, E. *Ultrasound Med. Biol.* **2015**, *41* (7), 1927–1937.

(263) Marmottant, P.; Raven, J. P.; Gardeniers, H.; Bomer, J. G.; Hilgenfeldt, S. *J. Fluid Mech.* **2006**, *568*, 109–118.

(264) Carugo, D.; Ankrett, D. N.; Glynne-Jones, P.; Capretto, L.; Boltryk, R. J.; Zhang, X.; Townsend, P. A.; Hill, M. *Biomicrofluidics* **2011**, *5* (4), 44108.

(265) Meng, L.; Cai, F.; Jiang, P.; Deng, Z.; Li, F.; Niu, L.; Chen, Y.; Wu, J.; Zheng, H. *Appl. Phys. Lett.* **2014**, *104* (7).

(266) Longsine-Parker, W.; Wang, H.; Koo, C.; Kim, J.; Kim, B.; Jayaraman, A.; Han, A. *Lab Chip* **2013**, *13* (11), 2144.

(267) Yuan, F.; Sankin, G.; Zhong, P. *J. Acoust. Soc. Am.* **2011**, *130* (5), 3339–3346.

(268) Wiklund, M.; Brismar, H.; Önfelt, B. *Lab Chip* **2012**, *12* (18), 3221.

(269) Evander, M.; Nilsson, J. *Lab Chip* **2012**, *12* (22), 4667.

(270) Ozcelik, A.; Ahmed, D.; Xie, Y.; Nama, N.; Qu, Z.; Nawaz, A. A.; Huang, T. J. *Anal. Chem.* **2014**, *86* (10), 5083–5088.

(271) Bertin, N.; Spelman, T. A.; Combriat, T.; Hue, H.; Stéphan, O.; Lauga, E.; Marmottant, P. *Lab Chip* **2017**, *17* (8), 1515–1528.

(272) Orbay, S.; Ozcelik, A.; Lata, J.; Kaynak, M.; Wu, M.; Huang, T. J. *J. Micromechanics Microengineering* **2017**, *27* (1), 15008.

(273) Marmottant, P.; Hilgenfeldt, S. *Nature* **2003**, *423* (6936), 153–156.

(274) Marmottant, P.; Hilgenfeldt, S. *Proc. Natl. Acad. Sci.* **2004**, *101* (26), 9523–9527.

(275) Rallabandi, B.; Wang, C.; Hilgenfeldt, S. *J. Fluid Mech.* **2013**, *739*, 57–71.

(276) Ohlin, M.; Iranmanesh, I.; Christakou, A. E.; Wiklund, M. *Lab Chip* **2015**, *15* (16), 3341–3349.

(277) Gedge, M.; Hill, M. *Lab Chip* **2012**, *12* (17), 2998.

(278) Wiklund, M.; Green, R.; Ohlin, M. *Lab Chip* **2012**, *12* (14), 2438.

(279) Glynne-Jones, P.; Boltryk, R. J.; Hill, M.; Harris, N. R.; Baclet, P. *J. Acoust. Soc. Am.* **2009**, *126* (3), EL75-EL79.

(280) Carugo, D.; Octon, T.; Messaoudi, W.; Fisher, A. L.; Carboni, M.; Harris, N. R.; Hill, M.; Glynne-Jones, P. *Lab Chip* **2014**, *14* (19), 3830–3842.

(281) Hill, M.; Wood, R. J. K. *Ultrasonics* **2000**, *38* (1), 662–665.

(282) Hahn, P.; Schwab, O.; Dual, J. *Lab Chip* **2014**, *14* (20), 3937–3948.

(283) Glynne-Jones, P.; Démoré, C. E. M.; Ye, C.; Qiu, Y.; Cochran, S.; Hill, M. *IEEE Trans. Ultrason. Ferroelectr. Freq. Control* **2012**, *59* (6), 1258–1266.

(284) Hill, M.; Townsend, R. J.; Harris, N. R. *Ultrasonics* **2008**, *48* (6–7), 521–528.

(285) van Rooij, T.; Skachkov, I.; Beekers, I.; Lattwein, K. R.; Voorneveld, J. D.; Kokhuis, T. J. A.; Bera, D.; Luan, Y.; van der Steen, A. F. W.; de Jong, N.; Kooiman, K. *J. Control. Release* **2016**, *238*, 197–211.

(286) Kooiman, K.; Foppen-Harteveld, M.; Der Steen, A. F. W. Van; De Jong, N. *J. Control. Release* **2011**, *154* (1), 35–41.

(287) Mannaris, C.; Averkiou, M. A. *Ultrasound Med. Biol.* **2012**, *38* (4), 681–691.

(288) Kolb, J.; Nyborg, W. L. *J. Acoust. Soc. Am.* **1956**, *28* (6), 1237–1242.

(289) Lötters, J. C.; Olthuis, W.; Veltink, P. H.; Bergveld, P. *J. Micromechanics Microengineering* **1997**, *7* (3), 145–147.

(290) Feshitan, J. A.; Chen, C. C.; Kwan, J. J.; Borden, M. A. *J. Colloid Interface Sci.* **2009**, *329* (2), 316–324.

(291) Kwan, J. J.; Graham, S.; Myers, R.; Carlisle, R.; Stride, E.; Coussios, C. C. *Phys. Rev. E - Stat. Nonlinear, Soft Matter Phys.* **2015**, *92* (2), 23019.

(292) Lajoinie, G.; De Cock, I.; Coussios, C. C.; Lentacker, I.; Le Gac, S.; Stride, E.; Versluis, M. *Biomicrofluidics* **2016**, *10* (1), 11501.

(293) Chin, C. T.; Lancée, C.; Borsboom, J.; Mastik, F.; Frijlink, M. E.; De Jong, N.; Versluis, M.; Lohse, D. *Rev. Sci. Instrum.* **2003**, *74* (12), 5026–5034.

(294) Forbes, M. M.; O'Brien, W. D. *J. Acoust. Soc. Am.* **2012**, *131* (4), 2723–2729.

(295) Li, Y. S. J.; Haga, J. H.; Chien, S. *J. Biomech.* **2005**, *38* (10), 1949–1971.

(296) Tarbell, J. M. *Cardiovasc. Res.* **2010**, *87* (2), 320–330.

(297) Hosseinkhah, N.; Goertz, D. E.; Hynynen, K. *IEEE Trans. Biomed. Eng.* **2015**, *62* (5), 1293–1304.

(298) Doinikov, A. A.; Bouakaz, A. *J. Acoust. Soc. Am.* **2010**, *128* (1), 11–19.

(299) Verhaagen, B.; Boutsioukis, C.; van der Sluis, L. W. M.; Versluis, M. *J. Acoust. Soc. Am.* **2014**, *135* (4), 1717–1730.

(300) Bolaños-Jiménez, R.; Rossi, M.; Rivas, D. F.; Kähler, C. J.; Marin, A. *J. Fluid Mech.* **2017**, *820* (May), 529–548.

(301) Coussios, C. C.; Farny, C. H.; ter Haar, G.; Roy, R. A. *Int. J. Hyperth.* **2007**, *23* (2), 105–120.

(302) McDannold, N.; Vykhodtseva, N.; Hynynen, K. *Proc. - IEEE Ultrason. Symp.* **2005**, *2* (4), 1249–1252.

(303) Kwan, J. J.; Graham, S.; Myers, R.; Carlisle, R.; Stride, E.; Coussios, C. C. *Phys. Rev. E - Stat. Nonlinear, Soft Matter Phys.* **2015**, *92* (2).

(304) Kumon, R. E.; Aehle, M.; Sabens, D.; Parikh, P.; Han, Y. W.; Kourennyi, D.; Deng, C. X. *Ultrasound Med. Biol.* **2009**, *35* (3), 494–506.

(305) Chen, X.; Leow, R. S.; Hu, Y.; Wan, J. M. F.; Yu, A. C. H. *J. R. Soc. Interface* **2014**, *11* (95), 20140071–20140071.

(306) Nwokeoha, S.; Carlisle, R.; Cleveland, R. O. *Ultrasound Med. Biol.* **2016**, *42* (10), 2478–2492.

(307) Rahim, A.; Taylor, S. L.; Bush, N. L.; ter Haar, G. R.; Bamber, J. C.; Porter, C. D. *Ultrasound Med. Biol.* **2006**, *32* (8), 1269–1279.

(308) Cafarelli, A.; Verbeni, A.; Poliziani, A.; Dario, P.; Menciassi, A.; Ricotti, L. *Acta Biomater.* **2017**, *49*, 368–378.

(309) Wang, C.; Jalikop, S. V.; Hilgenfeldt, S. *Appl. Phys. Lett.* **2011**, *99* (3).

(310) Barnett, S. B.; Ter Haar, G. R.; Ziskin, M. C.; Rott, H. D.; Duck, F. A.; Maeda, K. *Ultrasound Med. Biol.* **2000**, *26* (3), 355–366.

(311) Walde, P.; Cosentino, K.; Engel, H.; Stano, P. *ChemBioChem* **2010**, *11* (7), 848–865.

(312) Olbrich, K.; Rawicz, W.; Needham, D.; Evans, E. *Biophys. J.* **2000**, *79* (1), 321–327.

(313) Sezgin, E.; Levental, I.; Mayor, S.; Eggeling, C. *Nat. Rev. Mol. Cell Biol.* **2017**, *18* (6), 361–374.

(314) Mouritsen, O. G.; Bloom, M. *Annu. Rev. Biophys. Biomol. Struct.* **1993**, *22* (1), 145–171.

(315) Gullingsrud, J.; Schulten, K. *Biophys. J.* **2004**, *86* (6), 3496–3509.

(316) Zhang, Y. L.; Frangos, J. A.; Chachisvilis, M. *Biochem. Biophys. Res. Commun.* **2006**, *347* (3), 838–841.

(317) Hassan, M. A.; Campbell, P.; Kondo, T. *Drug Discov. Today* **2010**, *15* (21–22), 892–906.

(318) Park, J.; Fan, Z.; Kumon, R. E.; El-Sayed, M. E. H.; Deng, C. X. *Ultrasound Med. Biol.* **2010**, *36* (7), 1176–1187.

(319) Pereno, V.; Carugo, D.; Bau, L.; Sezgin, E.; Bernardino De La Serna, J.; Eggeling, C.; Stride, E. *ACS Omega* **2017**, *2* (3), 994–1002.

(320) Kuhn, P.; Eyer, K.; Robinson, T.; Schmidt, F. I.; Mercer, J.; Dittrich, P. S. *Integr. Biol.* **2012**, *4* (12), 1550.

(321) Sennoga, C. A.; Mahue, V.; Loughran, J.; Casey, J.; Seddon, J. M.; Tang, M.; Eckersley, R. J. *Ultrasound Med. Biol.* **2010**, *36* (12), 2093–2096.

(322) Sanchez, S. A.; Tricerri, M. A.; Gunther, G.; Gratton, E. *Mod. Res. Educ. Top. Microsc.* **2007**, *2*, 1007–1014.

(323) Booth, R.; Noh, S.; Kim, H. *Lab Chip* **2014**, *14* (11), 1880–1890.

(324) Chiu, J.-J.; Chien, S. *Physiol. Rev.* **2011**, *91* (1), 327–387.

(325) Yang, F.; Gu, N.; Chen, D.; Xi, X.; Zhang, D.; Li, Y.; Wu, J. *J. Control. Release* **2008**, *131* (3), 205–210.

(326) Teimouri, M.; Farzadfar, F.; Alamdari, M. S.; Hashemi-Meshkini, A.; Alamdari, A.; Rezaei-Darzi, E.; Varmaghani, M.; Zeynalabedini, A. *Iranian Journal of Pharmaceutical Research.* **2016**; Vol. 15.

(327) Róg, T.; Pasenkiewicz-Gierula, M.; Vattulainen, I.; Karttunen, M. *Biochim. Biophys. Acta - Biomembr.* **2009**, *1788* (1), 97–121.

(328) Kapoor, S.; Werkmüller, A.; Denter, C.; Zhai, Y.; Markgraf, J.; Weise, K.; Opitz, N.; Winter, R. *Biochim. Biophys. Acta - Biomembr.* **2011**, *1808* (4), 1187–1195.

(329) Prieto, M. L.; Oralkan, Ö.; Khuri-Yakub, B. T.; Maduke, M. C. *PLoS One* **2013**, *8* (10).

(330) Mendelsohn, R.; Sunder, S.; Bernstein, H. J. *BBA - Biomembr.* **1976**, *419* (3), 563–569.

(331) De Cock, I.; Lajoinie, G.; Versluis, M.; De Smedt, S. C.; Lentacker, I. *Biomaterials* **2016**, *83*, 294–307.

(332) Sebastian, B.; Dittrich, P. S. **2013**, No. October, 1695–1697.

(333) Honerkamp-Smith, A. R.; Woodhouse, F. G.; Kantsler, V.; Goldstein, R. E. *Phys. Rev. Lett.* **2013**, *111* (3), 38103.

(334) Yamada, A.; Lee, S.; Bassereau, P.; Baroud, C. N. *Soft Matter* **2014**, *10* (32), 5878.

(335) Steshenko, O.; Andrade, D. M.; Honigmann, A.; Mueller, V.; Schneider, F.; Sezgin, E.; Hell, S. W.; Simons, M.; Eggeling, C. *Biophys. J.* **2016**, *110* (11), 2441–2450.

(336) Yamamoto, K.; Ando, J. *Am. J. Physiol. - Hear. Circ. Physiol.* **2015**, *309* (7), H1178–H1185.

(337) Yamamoto, K.; Ando, J. *J. Cell Sci.* **2013**, *126* (5), 1227–1234.

(338) Abkarian, M.; Lartigue, C.; Viallat, A. *Phys. Rev. Lett.* **2002**, *88* (6), 4.

(339) Skotheim, J. M.; Secomb, T. W. *Phys. Rev. Lett.* **2007**, *98* (7).

(340) Honerkamp-Smith, A. R.; Woodhouse, F. G.; Kantsler, V.; Goldstein, R. E. *Phys. Rev. Lett.* **2013**, *111* (3), 38103.

(341) Simunovic, M.; Prévost, C.; Callan-Jones, A.; Bassereau, P. *Philos. Trans. R. Soc. A Math. Phys. Eng. Sci.* **2016**, *374* (2072), 20160034.

(342) Luan, Y.; Lajoinie, G.; Gelderblom, E.; Skachkov, I.; van der Steen, A. F. W.; Vos, H. J.; Versluis, M.; De Jong, N. *Ultrasound Med. Biol.* **2014**, *40* (8), 1834–1846.

(343) Der Loughian, C.; Muleki Seya, P.; Pirat, C.; Inserra, C.; Béra, J.-C.; Rieu, J.-P. *Soft Matter* **2015**, *11* (17), 3460–3469.

(344) Tirosh, O.; Barenholz, Y.; Katzhendler, J.; Priev, A. *Biophys. J.* **1998**, *74* (3), 1371–1379.

(345) Dutheil, D.; Underhaug Gjerde, A.; Petit-Paris, I.; Mauco, G.; Holmsen, H. *J. Chem. Biol.* **2009**, *2* (1), 39–49.

(346) Silvander, M.; Bergstrand, N.; Edwards, K. *Chem. Phys. Lipids* **2003**, *126* (1), 77–83.

(347) Tirosh, O.; Barenholz, Y.; Katzhendler, J.; Priev, A. *Biophys. J.* **1998**, *74* (3), 1371–1379.

(348) Garbuzenko, O.; Barenholz, Y.; Priev, A. *Chem. Phys. Lipids* **2005**, *135* (2), 117–129.

(349) Zhao, J.; Wu, J.; Heberle, F. A.; Mills, T. T.; Klawitter, P.; Huang, G.; Costanza, G.; Feigenson, G. W. *Biochim. Biophys. Acta - Biomembr.* **2007**, *1768* (11), 2764–2776.

(350) Pereno, V.; Aron, M.; Vince, O.; Mannaris, C.; Seth, A.; de Saint Victor, M.; Lajoinie, G.; Versluis, M.; Coussios, C.; Carugo, D.; Stride, E. *Biomicrofluidics* **2018**, *12* (3), 34109.

(351) Dunn, K. W.; Kamocka, M. M.; McDonald, J. H. *AJP Cell Physiol.* **2011**, *300* (4), C723–C742.

(352) Small, E. F.; Dan, N. R.; Wrenn, S. P. *Langmuir* **2012**, *28* (40), 14364–14372.

(353) Lawaczeck, R.; Kainosho, M.; Chan, S. I. *BBA - Biomembr.* **1976**, *443* (3), 313–330.

(354) Small, E. F.; Willy, M. C.; Lewin, P. A.; Wrenn, S. P. *Colloids Surfaces A Physicochem. Eng. Asp.* **2011**, *390* (1–3), 40–47.

(355) Clerc, S. G.; Thompson, T. E. *Biophys. J.* **1995**, *68* (6), 2333–2341.

(356) Mathai, J. C.; Tristram-Nagle, S.; Nagle, J. F.; Zeidel, M. L. *J. Gen. Physiol.* **2008**, *131* (1), 69–76.

(357) Nagle, J. F.; Mathai, J. C.; Zeidel, M. L.; Tristram-Nagle, S. *J. Gen. Physiol.* **2008**, *131* (1), 77–85.

(358) Dodes Traian, M. M.; Flecha, F. L. G.; Levi, V. *J. Lipid Res.* **2012**, *53* (3), 609–616.

(359) Ohno, H.; Sakai, T.; Tsuchida, E.; Honda, K.; Sasakawa, S. *Biochem. Biophys. Res. Commun.* **1981**, *102* (1), 426–431.

(360) Haidekker, M. A.; L'Heureux, N.; Frangos, J. A. *Am. J. Physiol. Heart Circ. Physiol.* **2000**, *278* (4), 1401–1406.

(361) Gervasio, O. L.; Phillips, W. D.; Cole, L.; Allen, D. G. *J. Cell Sci.* **2011**, *124* (21), 3581–3590.

(362) Gudi, S.; Nolan, J. P.; Frangos, J. A. *Proc. Natl. Acad. Sci.* **1998**, *95* (5), 2515–2519.

(363) Martynov, S.; Kostson, E.; Saffari, N.; Stride, E. *J. Acoust. Soc. Am.* **2011**, *130* (5), 2700–2708.

(364) Hosseinkhah, N.; Chen, H.; Matula, T. J.; Burns, P. N.; Hynynen, K. *J. Acoust. Soc. Am.* **2013**, *134* (3), 1875–1885.

(365) Sanchez, S. A.; Tricerri, M. A.; Gunther, G.; Gratton, E. *Mod. Res. Educ. Top. Microsc.* **2007**, *2*, 1007–1014.

(366) Collis, J.; Manasseh, R.; Liovic, P.; Tho, P.; Ooi, A.; Petkovic-Duran, K.; Zhu, Y. *Ultrasonics* **2010**, *50* (2), 273–279.

(367) Hu, Y.; Wan, J. M. F.; Yu, A. C. H. *Ultrasound Med. Biol.* **2013**, *39* (12), 2393–2405.

(368) Prentice, P.; Cuschieri, A.; Dholakia, K.; Prausnitz, M.; Campbell, P. *Nat. Phys.* **2005**, *1* (2), 107–110.

(369) Nyborg, W. L. *J. Acoust. Soc. Am.* **1958**, *30* (4), 329–339.

(370) Wu, J. *Prog. Biophys. Mol. Biol.* **2007**, *93* (1–3), 363–373.

(371) Prosperetti, A.; Crum, L. A.; Commander, K. W. *J. Acoust. Soc. Am.* **1988**, *83* (2), 502–514.

(372) Bose, N.; Carugo, D.; Maiti, T. K.; Zhang, X.; Chakraborty, S. *15th Int. Conf. Miniaturized Syst. Chem. Life Sci.* **2011**, 1743–1745.

(373) Yu, H.; Xu, L. *J. Control. Release* **2014**, *174* (1), 151–160.

(374) Zhong, W.; Sit, W. H.; Wan, J. M. F.; Yu, A. C. H. *Ultrasound Med. Biol.* **2011**, *37* (12), 2149–2159.

(375) Yamamoto, K.; Ando, J. *Am. J. Physiol. - Hear. Circ. Physiol.* **2015**, *309* (7), H1178–H1185.

(376) Yamamoto, K.; Ando, J. *J. Cell Sci.* **2013**, *126* (5), 1227–1234.

(377) McPherson, P. S.; Ritter, B.; Wendland, B. *Trafficking Inside Cells: Pathways, Mechanisms and Regulation*; Landes Bioscience, 2009; Vol. 1.

(378) Schlicher, R. K.; Radhakrishna, H.; Tolentino, T. P.; Apkarian, R. P.; Zarnitsyn, V.; Prausnitz, M. R. *Ultrasound Med. Biol.* **2006**, *32* (6), 915–924.

(379) Tang, Y.; Olufemi, L.; Wang, M.-T.; Nie, D. *Front. Biosci.* **2008**, *13* (13), 759–776.

(380) Dugani, C. B.; Klip, A. *EMBO Rep.* **2005**, *6* (12), 1137–1142.

(381) Wu, G.; Yussman, M. G.; Barrett, T. J.; Hahn, H. S.; Osinska, H.; Hilliard, G. M.; Wang, X.; Toyokawa, T.; Yatani, A.; Lynch, R. A.; Robbins, J.; Dorn, G. W. *Circ. Res.* **2001**, *89* (12), 1130–1137.

(382) Janka, G. E. *Eur. J. Pediatr.* **2007**, *166* (2), 95–109.

(383) Lin Chua, C. E.; Tang, B. L. *J. Cell. Mol. Med.* **2006**, *10* (4), 828–837.

(384) Donaldson, J.; Segev, N. In *Regulation*; Springer New York: New York, NY, 2009; pp 329–341.

(385) Šlotová, J.; Kaepfel, Z.; Hrazdira, I. *Biol. Plant.* **1967**, *9* (1), 49–55.

(386) Miller, M. W.; Ciaravino, V.; Allen, D.; Jensen, S. *Int. J. Radiat. Biol.* **1976**, *30* (3), 217–222.

(387) Miller, D. L. *Environ. Exp. Bot.* **1983**, *23* (1), 1–27.

(388) Miller, D. L. *Ultrasound Med. Biol.* **1987**, *13* (8), 443–470.

(389) Dyer, H. J.; Miller, D. L.; Nyborg, W. L.; Nyborg, W. L. *J. Acoust. Soc. Am.* **1976**, *59*.

(390) Wilson, W. L.; Wiercinski, F. J.; Nyborg, W. L.; Schnitzler, R. M.; Sichel, F. J. *J. Acoust. Soc. Am.* **1966**, *40* (6), 1363–1370.

(391) Johnsson, A.; Lindvall, A. *Naturwissenschaften* **1969**, *56* (1), 40.

(392) Lorz, B.; Simson, R.; Nardi, J.; Sackmann, E. *Europhys. Lett.* **2000**, *51* (4), 468–474.

(393) Skotheim, J. M.; Secomb, T. W. *Phys. Rev. Lett.* **2007**, *98* (7), 78301.

(394) Lindken, R.; Rossi, M.; Große, S.; Westerweel, J. *Lab Chip* **2009**, *9* (17), 2551.

(395) Arakawa, T.; Haniu, M.; Narhi, L. O.; Miller, J. A.; Talvenheimo, J.; Philo, J. S.; Chute, H. T.; Matheson, C.; Carnahan, J.; Louis, J. C.; Yan, Q.; Welcher, A. A.; Rosenfeld, R. *J. Biol. Chem.* **1994**, *269* (45), 27833–27839.

(396) Bhatia, T.; Cornelius, F.; Brewer, J.; Bagatolli, L. A.; Simonsen, A. C.; Ipsen, J. H.; Mouritsen, O. G. *Biochim. Biophys. Acta - Biomembr.* **2016**, *1858* (6), 1390–1399.

(397) Genova, J.; Ulrih, N.; Kralj-Iglič, V.; Iglič, A.; Bivas, I. *Life* **2015**, *5* (2), 1101–1110.

(398) Bouvrais, H.; Pott, T.; Bagatolli, L. A.; Ipsen, J. H.; Méléard, P. *Biochim. Biophys. Acta - Biomembr.* **2010**, *1798* (7), 1333–1337.

(399) Yamada, A.; Lee, S.; Bassereau, P.; Baroud, C. N. *Soft Matter* **2014**, *10* (32), 5878.

(400) Keller, S. R.; Skalak, R. *J. Fluid Mech.* **1982**, *120* (1), 27–47.

(401) Pommella, A.; Brooks, N. J.; Seddon, J. M.; Garbin, V. *Sci. Rep.* **2015**, *5*, 13163.

(402) Oglęcka, K.; Rangamani, P.; Liedberg, B.; Kraut, R. S.; Parikh, A. N. *Elife* **2014**, *3*, e03695.

(403) Portet, T.; Dimova, R. *Biophys. J.* **2010**, *99* (10), 3264–3273.

(404) Rawicz, W.; Smith, B. A.; McIntosh, T. J.; Simon, S. A.; Evans, E. *Biophys. J.* **2008**, *94* (12), 4725–4736.

(405) Wang, E.; Goldman, R. D. **1978**, *79* (December).

(406) Costaguta, G.; Payne, G. S. In *Trafficking Inside Cells: Pathways, Mechanisms and Regulation*; Springer New York: New York, NY, 2009; pp 105–118.

(407) Segev, N. *Trafficking Inside Cells*; 2009.

(408) Gal, N.; Weihs, D. *Cell Biochem. Biophys.* **2012**, *63* (3), 199–209.

(409) Williams, A. R. *J. Acoust. Soc. Am.* **1972**, *52* (2B), 688–693.

(410) Wang, E.; Goldman, R. D. *J. Cell Biol.* **1978**, *79* (3), 708–726.

(411) Dyer, H. J.; Nyborg, W. L. *IRE Trans. Med. Electron.* **1960**, *ME-7* (3), 163–165.

(412) Noguchi, H.; Gompper, G. *Phys. Rev. E - Stat. Nonlinear, Soft Matter Phys.* **2005**, *72* (1).

(413) Abkarian, M.; Lartigue, C.; Viallat, A. *Phys. Rev. Lett.* **2002**, *88* (6), 4.

(414) Doinikov, A. A.; Bouakaz, A. *J. Acoust. Soc. Am.* **2010**, *128* (1), 11–19.

(415) Skachkov, I.; Luan, Y.; Van Der Steen, A. F. W.; De Jong, N.; Kooiman, K. *IEEE Trans. Ultrason. Ferroelectr. Freq. Control* **2014**, *61* (10), 1661–1667.

(416) Li, Q.; Wang, X.; Ma, S.; Zhang, Y.; Han, X. *Colloids Surfaces B Biointerfaces* **2016**, *147*, 368–375.

(417) Glynne-Jones, P.; Boltryk, R. J.; Hill, M.; Harris, N. R.; Baclet, P. *J. Acoust. Soc. Am.* **2009**, *126* (3), EL75-EL79.

(418) Varnier, A.; Kermarrec, F.; Blesneac, I.; Moreau, C.; Liguori, L.; Lenormand, J. L.; Picollet-D'Hahan, N. *J. Membr. Biol.* **2010**, *233* (1–3), 85–92.

(419) Otsu, N. *IEEE Trans. Syst. Man. Cybern.* **1979**, *9* (1), 62–66.

(420) Haralick, R.; Shapiro, L. *Computer and Robot Vision*; Addison-Wesley Pub. Co, 1992; Vol. I.

(421) Lam, L.; Lee, S. W. *IEEE Trans. Pattern Anal. Mach. Intell.* **1992**, *14* (9), 869–885.

(422) Lazar, E.; DeBlauw, B.; Glumac, N.; Dutton, C.; Elliott, G. In *27th AIAA Aerodynamic Measurement Technology and Ground Testing Conference*; American Institute of Aeronautics and Astronautics: Reston, Virigina, 2010.

(423) Raffel, M.; Willert, C. E.; Wereley, S. T.; Kompenhans, J. *Particle Image Velocimetry: A Practical Guide.*; Springer, 1998.